HIGH-RESOLUTION SPECTROSCOPIC STUDIES IN GLASS-BLOWN AND MICRO-FABRICATED CELLS FOR MINIATURE RUBIDIUM ATOMIC CLOCKS

Thèse présentée à la

Faculté des Sciences

de l'Université de Neuchâtel

pour l'obtention du grade de

Docteur ès Sciences

par:

Matthieu Pellaton

M. Sc. en Physique de l'Université de Neuchâtel

Acceptée le 19 Mai 2014 sur proposition du jury:

Prof. assoc. Gaetano Mileti, UniNE, Neuchâtel, Directeur de thèse
Prof. Nico de Rooij, EPFL, Neuchâtel, Rapporteur
Dr. Christoph Affolderbach, UniNE, Neuchâtel, Rapporteur
Dr. John Kitching, NIST, Boulder, Colorado (USA), Rapporteur
Dr. Pierre Waller, ESTEC, Noordwijk (NL), Rapporteur

Université de Neuchâtel, Juin 2014

Faculté des sciences
Secrétariat-décanat de Faculté
Rue Emile-Argand 11
2000 Neuchâtel - Suisse
Tél: + 41 (0)32 718 2100
E-mail: secretariat.sciences@unine.ch

IMPRIMATUR POUR THESE DE DOCTORAT

La Faculté des sciences de l'Université de Neuchâtel autorise l'impression de la présente thèse soutenue par
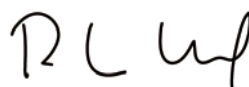
Monsieur Matthieu PELLATON

Titre:

High-resolution spectroscopic studies in glass-blown and micro-fabricated cells for miniature Rubidium atomic clocks

sur le rapport des membres du jury composé comme suit :

- Prof. associé Gaetano Mileti, LTF-IPH, Université de Neuchâtel, directeur de thèse
- Prof. Nico F. de Rooij, Ecole Polytechnique Fédérale de Lausanne
- Dr John Kitching, NIST, Boulder (CO), USA
- Dr Pierre Waller, ESA-ESTEC, Noordwijk, The Netherlands
- Dr Christoph Affolderbach, LTF-IPH, Université de Neuchâtel

Neuchâtel, le 2 juin 2014   Le Doyen, Prof. P. Kropf

Abstract

Keywords: Miniature atomic clock, double-resonance, rubidium vapour cells, anti-relaxation wall-coating, frequency stability, metrology.

Nowadays, buffer-gas alkali vapour cells form the heart of essentially all types of compact or miniaturized atomic clocks. They reliably hold and confine a vapour of alkali atoms, that provides the atomic transition frequency serving as stable reference for the clock oscillator. The desire to bring atomic clock stability to portable applications such as telecommunication and navigation increased the need for more compactness and lower power consumption. This motivated the present thesis work on the cells miniaturization and the novel clocks that could be realized with such cells.

In the frame of this thesis, more than 150 glass blown cells were produced and tested and more than 30 microfabricated cells evaluated. We present the fabrication process for each type of them. We restrict ourselves to the spectroscopic analysis of certain cell types only, which are more oriented towards the miniaturization of an atomic clock. Nonetheless, it is worth to mention that, among the cells produced, cells having a volume of $\simeq 12$ cm^3 are at the basis of atomic clocks exhibiting short-term stabilities better than $2 \times 10^{-13}\tau^{-1/2}$.

An excellent control of the cell fabrication process is essential, and can only be achieved through a thorough characterization. We developed and performed spectroscopic tests to validate the (micro-) cells fabrication processes elaborated at the LTF and SAMLAB in Neuchâtel. In particular, the buffer gas mixture characterization with a resolution of $\pm$ 1%, and the leak rate detection with a limit of 1.5×10^{-13} mbar l/s were achieved. This allowed the validation of two distinct sealing processes: the classic anodic bonding, and an innovative low temperature sealing technique using thermocompression of indium.

As an alternative to the buffer gas, the use of certain types of wall coating also allows the atomic polarization preservation. Four different types have been used: Parylen C and N, Tetracontane and OTS. While the Parylene appears to be inadequate for use with rubidium atoms, excellent antirelaxing properties are obtained with tetracontane and OTS. The successful in-house fabrication of wall coated cells allowed the observation of the ripening process by double resonance

spectroscopy. The results are presented and an interpretation is given. A microfabricated OTS wall coated cell was produced at Neuchâtel too, by R. Straessle at SAMLAB. We present its spectroscopic analysis and demonstrate truly antirelaxing properties of the coating in a 4.2 mm^3 vapour volume.

Finally, a spectroscopic and metrologic study of an innovative "cell-microwave resonator" assembly is presented. Both the cell and the resonator are microfabricated. The cell vapour volume is of the order of 50 mm^3 only. Systematic shifts limiting the metrologic performances are characterized, with a focus on the light shift. A detailed, theoretical and analytical, analysis is presented in both, the D1 and D2, lines and for various optical pumping schemes. Frequency light shift is found to be one of the main stability limiting factor in the medium to long term regime. The limit is at a level of few 10^{-12}. We demonstrate fractional frequency stability below 10^{-11} from 1 s up to one day of integration time with a resonator physics package volume of less than 0.9 cm^3. This represents a factor of five in terms of volume reduction compared to European commercial clocks with similar short term stability performances. An alternative interrogation scheme, suppressing completely the light shift, is discussed to improve the medium to long term performances. This scheme would allow the fabrication of an atomic clock extremely compact with highly competitive stability performances.

This work was done in the Laboratoire Temps-Fréquence at the University of Neuchâtel, in close collaboration with laboratories from the Ecole Polytechnique Fédérale de Lausanne (EPFL), in particular, the Sensors, Actuators and Microsystems LABoratory (SAMLAB) for the microfabricated cells, and the Laboratory of ElectroMagnetics and Acoustics (LEMA) for the miniature microwave cavity.

Résumé

Mots-clés: Horloge atomique miniature, double-resonance, cellules à vapeur de rubidium, revête-ment anti-relaxant, stabilité de fréquence, métrologie.

De nos jours, les cellules à vapeur d'atomes alkalin et gaz tampon sont au coeur de presque toutes les horloges atomiques commerciales compactes ou miniatures. Elles contiennent une vapeur d'atomes alkalin dont une des frequences de transition atomique sert de reference stable à l'oscillateur de l'horloge. Ce travail de recherche porte sur l'étude des phénomènes physiques se déroulant dans ces cellules et plus particulièrement des effets de miniaturization sur la vapeur d'atomes, en vue de la réalisation d'une horloge miniature. Il est motivé par le besoin croissant d'horloges stables, encore plus compactes et moins gourmandes en énergie pour des applications portables telles que les télécommunications ou la navigation.

Dans le cadre de cette thèse, plus de 150 cellules en verre soufflé ont été produites et caracterisées et plus de 30 cellules micro fabriquées ont été évaluées. On présentera les méthodes de productions de chacune d'entre elles, et on se restreindra sur l'évaluation spectroscopique de certains type seulement, orientés vers la miniaturisation. Néanmoins, il est important de signaler que certaines cellules produites (d'un volume de $\simeq 12$ cm^3) sont au coeur d'horloges compactes affichant des instabilités à court terme meilleures que $2 \times 10^{-13} \tau^{-1/2}$.

Un excellent contrôle des processus de fabrication des cellules est essentiel, et n'est possible qu'avec une charactérisation minutieuse. On présentera les différents tests spectroscopiques per-mettant de valider les processus de (micro-) fabrication développés à Neuchâtel pour des cellules de référence d'horloges atomiques miniatures. Notamment, la caractérisation par spectroscopie du taux de mélange de gaz tampon avec une résolution de $\pm$ 1% ainsi que la détection de fuites aussi petites que 1.5×10^{-13} mbar l/s ont été rendues possible. Ceci a permis de valider deux pro-cessus de fabrication de cellule : le "classique" anodic-bonding ainsi qu'une technique innovante de scellage à basse temperature par thermocompression d'indium.

L'utilisation de certains revêtements antirelaxants permet également de s'astreindre du gaz tam-pon pour la préservation du spin des atomes; quatre types différents ont été testés: Parylene N et C, tetracontane et Octadecyl-Trichloro-Silane (OTS). Alors que les parylenes N et C s'avèrent

inadéquats en tant que revêtements anti-relaxants, d'excellentes propriétés anti-relaxantes sont obtenues pour le tetracontane, validant ainsi la méthode ainsi que le système de production développé au LTF pour des cellules en verre soufflé. La fabrication au sein même du LTF a également permis l'observation du phénomène dit de ripening d'une cellule revêtue de tetracontane par spectroscopie double résonance. Les résultats sont présentés, et une explication physique est donnée. L'expérience acquise avec les cellule en verre soufflé a permis la validation spectroscopique par double résonance d'une cellule micro-fabriquée avec revêtement OTS. Les résultats sont présentés et les propriétés antirelaxantes du revêtement sont démontrées pour un volume de vapeur de rubidium de 4.2 mm^3.

Finalement, une évaluation spectroscopique et métrologique d'un assemblage "résonateur micro-onde-cellule" novateur et micro fabriqué d'un volume inférieur à 0.9 cm^3 est présentée. Le volume de la vapeur de rubidium et de gaz tampon est de l'ordre de 50 mm^3 seulement. Les déplacements de fréquence systématiques limitant les performances métrologiques sont caractérisés, avec une attention particulière pour le déplacement radiatif (light shift). Une analyse détaillée, théorique et expérimentale, de ce dernier, dans les lignes D1 (795 nm) et D2 (780 nm) et pour chaque variante de pompage optique est donnée. le déplacement de fréquence lié aux variations de puissance micro-onde (power shift) ainsi que le déplacement radiatif en fréquence s'avèrent être les principaux facteurs limitant la stabilité à moyen-long terme à un niveau de quelques 10^{-12}. On démontre également des performances d'instabilité d'horloge relative meilleure que 10^{-11} de 1 seconde à une journée de temps d'intégration. Une variante d'interrogation supprimant totalement le déplacement radiatif est proposée. Cette dernière permet d'envisager une horloge rubidium extrêmement compact avec des performances hautement competitives.

Ce travail a été effectué au sein du Laboratoire Temps-Fréquence (LTF) de l'Université de Neuchâtel, en étroite collaboration avec plusieurs laboratoires de l'Ecole Polytechnique Fédérale de Lausanne (EPFL), dont le Sensors, Actuators and Microsystems LABoratory (SAMLAB) pour les cellules micro-fabriquées et le Laboratory of ElectroMagnetics and Acoustics (LEMA) pour la cavité micro-onde miniature.

"Les portes du succès sont bardées de chaines qu'on attaque à la lime à ongles..."

Alain Tempoulthet

Acknowledgments

Alone, we're nothing...

I would like to thank all the people who have guided, helped and supported me during the realization of this thesis:

- First, I would like to thank my supervisor, Prof. Gaetano Mileti, who offered me the opportunity to realize this research. Master of diplomacy and management he found the way to reorient my (sometimes) chaotic working line. He also taught me how to trust my work and to better sell it. I would also like to thank him for giving me the opportunity to be his assistant for his theoretical physics lectures and for the CUSO lectures on atomic clocks.

- A particular thank goes also to Christoph Affolderbach, who has followed my studies as closely as Gaetano did. Whenever I needed some help or had questions his door was always open for a friendly discussion. His support, explanations and hints were really helpful, without forgetting to mention his help to improve my writing skills. Still waiting for a sailing evening...

- I would also like to thank all the jury members, Prof. Nico de Rooij, Dr. John Kitching and Dr. Pierre Waller, for their valuable time devoted to the reading and evaluation of this manuscript.

- Several results presented in this thesis couldn't be obtained without the contributions of our technical staff and our partners. I particularly would like to thank the SAMLAB, EPFL and Rahel Straessle and Yves Pétremand for the fabrication of the MEMS cells, as well as the LEMA, EPLFL and Maddalena Violetti for the µ-LGR. I also would like to thank: Patrick Scherler, for the CAD design, his expertise with the magnetron cavity and his sense of perfection for the realization of the various assemblies used for these studies, Marc Durrenberger for his invaluable electronic devices for laser and PP control, Daniel Varidel for everything related to network, computer and for taking care of our time lab. Thank you also to the mechanical workshop people, Christian Hêche, André Cornu with a special attention to Isidro Fernandez who taught me the basics of a lathe machine.

- A very special thank goes to Muriel who managed with style her secretariat duties. Her everyday smile was always welcome.

- Some colleagues have became friends, and that is invaluable. Thank you Thejesh for your patience, serenity and help on so many levels. I miss our endless discussions. Florian, your laser heads rock, but thanks for the fun sport activities. Nikola, what to say... You're sitting on my chair! Thank you for forcing me to get out of my confidence zone. And miss pretty, Danijela, thank you for having brought some feminine mood in our office and gossips. Bertrand, merci pour les p'tites pauses clopes, and Martin, thank you for the sportive motivation. I wish I could have spent more time sailing or kiting or whatever! Thank you Renaud for the chocolate and your support.

- Being one of the last survivor of the first bunch of PhD students of the LTF I would like to warmly thank my very first colleagues who left (or are leaving) but gave me their moral support until the end. Lionel, Laurent, Vladimir, thank you for creating this nice and friendly working atmosphere. I would also like to thank all the newcomers who brought additional fun on the physics floor: Prof. Thomas Südmeyer, Salman, Sargis, Clément, Kutan, Loïc, Clara, Maxime, Nayara and Antoine. Sorry for having been so busy. Some of you already know, for the rest enjoy as long as you can!

- I would not have been able to reach this point without the support, love and affection I received from my family and friends. Work is one very important thing but life would have no meaning without you. I want to address my heartfully thanks to my parents for their love and support I have received. To my friends: sorry the list is too long, but simply thank you for having supported me in all my mood phases, especially my grumpiness.

- Thank you Christelle for being my beloved one and my best friend at the same time. I don't know how I would have reach this point without you and all the love you gave me.

Table of Contents

List of Figures

List of Tables

Author's Contributions

Articles in peer-reviewed journals

[A.1]   R. Straessle, M. Pellaton, C. Affolderbach, Y. Pétremand, D. Briand, G. Mileti, and N. F. de Rooij, "Microfabricated alkali vapor cell with anti-relaxation wall coating," *accepted for publication in Appl. Phys. Lett.*, 2014.

[A.2]   M. Violetti, M. Pellaton, C. Affolderbach, F. Merli, J.-F. Zürcher, G. Mileti, and A. K. Skrivervik, "The Micro Loop-Gap Resonator: A Novel Miniaturized Microwave Cavity for Double-Resonance Rubidium Atomic Clocks," *accepted for publication in the IEEE Sensors Journal*, 2014.

[A.3]   A. Horsley, G.-X. Du, M. Pellaton, C. Affolderbach, G. Mileti, and P. Treutlein, "Imaging of relaxation times and microwave field strength in a microfabricated vapor cell," *Phys. Rev. A*, vol. 88, p. 063 407, Dec. 2013.

[A.4]   R. Straessle, M. Pellaton, C. Affolderbach, Y. Pétremand, D. Briand, G. Mileti, and N. F. de Rooij, "Low-temperature indium-bonded alkali vapor cell for chip-scale atomic clocks," *Journal of Applied Physics*, vol. 113, no. 6, p. 064 501, 2013.

[A.5]   M. Pellaton, C. Affolderbach, Y. Pétremand, N. F. de Rooij, and G. Mileti, "Study of laser-pumped double-resonance clock signals using a microfabricated cell," *Physica Scripta*, vol. 2012, no. T149, p. 014 013, 2012.

[A.6]   Y. Pétremand, C. Affolderbach, R. Straessle, M. Pellaton, D. Briand, G. Mileti, and N. F. de Rooij, "Microfabricated rubidium vapour cell with a thick glass core for small-scale atomic clock applications," *J. Micromech. Microeng.*, vol. 22, no. 2, p. 025 013, 2012.

[A.7]   C. Stefanucci, T. Bandi, F. Merli, M. Pellaton, C. Affolderbach, G. Mileti, and A. K. Skrivervik, "Compact microwave cavity for high performance rubidium frequency standards," *Review of Scientific Instruments*, vol. 83, no. 10, p. 104 706, 2012.

[A.8]   F. R. Giorgetta, E. Baumann, R. Théron, M. L. Pellaton, D. Hofstetter, M. Fischer, and J. Faist, "Short wavelength (4 μm) quantum cascade detector based on strain compensated InGaAs/InAlAs," *Appl. Phys. Lett.*, vol. 92, no. 12, p. 121 101, Mar. 2008.

International conferences with proceedings

[P.1]   A. Horsley, G.-X. Du, M. Pellaton, C. Affolderbach, G. Mileti, and P. Treutlein, "Spatially Resolved Measurement of Relaxation Times in a Microfabricated Vapor Cell," in *proc. of the 2013 Joint UFFC, EFTF and PFM Symp.*, 2013.

[P.2]   M. Pellaton, C. Affolderbach, M. Violetti, J.-F. Zurcher, A. K. Skrivervik, and G. Mileti, "Double resonance spectroscopic studies using a new generation of microfabricated microwave cavity," in *proc. of the 2013 Joint UFFC, EFTF and PFM Symp.*, 2013, pp. 582–5.

[P.3]   T. Bandi, M. Pellaton, D. Miletic, C. Affolderbach, F. Gruet, R. Matthey, and G. Mileti, "Double resonance in alkali vapor cells for high performance and miniature atomic clocks," in *Proc. of the IEEE International Frequency Control Symp. (IFCS)*, Baltimore, USA, May 2012.

[P.4]   F. Gruet, C. Affolderbach, M. Pellaton, T. Bandi, R. Matthey, and G. Mileti, "Compact and frequency stabilised laser heads for rubidium atomic clocks," in *Proc. of the International Conference on Space Optics (ICSO)*, ICSO 2012, Ajaccio, Corse, France, Oct. 2012.

[P.5]   M. Pellaton, R. Straessle, C. Affolderbach, D. Briand, N. F. de Rooij, and G. Mileti, "Wall-coated cells for rb atomic clocks: study of the ripening process by double-resonance spectroscopy," in *Proc. of the 26th European Frequency and Time Forum (EFTF)*, Göteborg, Apr. 2012.

[P.6]   R. Straessle, M. Pellaton, Y. Pétremand, D. Briand, C. Affolderbach, G. Mileti, and N. de Rooij, "Low-temperature Indium hermetic sealing of alkali vapor-cells for chip-scale atomic clocks," in *Proceedings of the 25th IEEE International Conference on Micro Electro Mechanical Systems (MEMS)*, Paris, France, 2012, pp. 361–4.

[P.7]   R. Straessle, Y. Pétremand, D. Briand, N. F. de Rooij, M. Pellaton, C. Affolderbach, and G. Mileti, "Towards wall-coated micro-fabricated cells: Alkali vapor-cells using thin-film low-temperature bonding," in *Proc. of the 26th European Frequency and Time Forum (EFTF)*, Göteborg, Apr. 2012.

[P.8] R. Straessle, Y. Pétremand, D. Briand, N. de Rooij, M. Pellaton, C. Affolderbach, and G. Mileti, "Micro-fabricated alkali vapor cells sealed at low temperatures with thin-film metallic bonding," in *Proc. of the IEEE International Frequency Control Symp. (IFCS)*, IEEE International Frequency Control Symposium, Baltimore, USA, May 2012, pp. 127–30.

[P.9] M. Violetti, F. Merli, J.-F. Zürcher, A. K. Skrivervik, M. Pellaton, C. Affolderbach, and G. Mileti, "New Miniaturized Microwave Cavity for Rubidium Atomic Clocks," in *proceedings of IEEE Sensors conference*, proc. IEEE Sensors 2012, 2012.

[P.10] M. Pellaton, Y. Pétremand, C. Affolderbach, N. F. de Rooij, and G. Mileti, "Laser-pumped double-resonance clock using a micro-fabricated cell," in *Proc. of the 2011 Joint Conference of the IEEE International Frequency Control Symp. (IFCS) and the European Frequency and Time Forum (EFTF)*, Joint Conference of the IEEE International Frequency Control Symposium and European Frequency and Time Forum, Jun. 2011, pp. 604–6.

[P.11] Y. Pétremand, R. Straessle, N. F. de Rooij, M. Pellaton, C. Affolderbach, and G. Mileti, "Multiple stack anodic bonded 4 mm thick Rb vapor cell," in *Proc. of the 2011 Joint Conference of the IEEE International Frequency Control Symp. (IFCS) and the European Frequency and Time Forum (EFTF)*, Joint Conference of the IEEE International Frequency Control Symposium and European Frequency and Time Forum, Jun. 2011, pp. 233–5.

[P.12] S. Micalizio, A. Godone, F. Levi, E. K. Bertacco, C. Calosso, F. Gruet, M. Pellaton, T. Bandi, C. Affolderbach, and G. Mileti, "Pulsed Optically Pumped Rb Clock with Optical detection: First Results," in *Proc. of the 24th European Frequency and Time Forum (EFTF)*, 2010, p116.

Oral/Poster Presentations without proceedings

[O.1] T. Bandi, C. Affolderbach, M. Pellaton, F. Gruet, C. Stefanucci, F. Merli, A. K. Skrivervik, C. E. Calosso, and G. Mileti, "Compact, high-performance cw double-resonance rb frequency standard: present status," Oral presentation by T. Bandi at the 2013 Joint UFFC, EFTF and PFM Symp., Prague, Jul. 2013.

[O.2]   G.-X. Du, A. Horsley, M. Pellaton, C. Affolderbach, G. Mileti, and P. Treutlein, "Microwave field imaging using microfabricated vapor cells," Oral presentation by G.-X. Du at DPG Frühjahrstagung, Hannover, Germany, Mar. 2013.

[O.3]   A. Horsley, G.-X. Du, M. Pellaton, C. Affolderbach, G. Mileti, and P. Treutlein, "Microfabricated Vapor Cells for Atomic Clock and Microwave Field Sensing Applications," Oral presentation by A. Horsley at the Young Atom Opticians conference 2013 (YAO 2013), Birmingham, UK, Apr. 2013.

[O.4]   C. Affolderbach, M. Pellaton, Y. Pétremand, N. F. de Rooij, and G. Mileti, "Laser-microwave double-resonance spectroscopy in mm-scale Rb vapour cells for atomic clocks," Oral presentation by C. Affolderbach at the Joint Annual Meeting of the Austrian Physical Society and Swiss Physical Society, Lausanne, Switzerland, Jun. 2011.

[O.5]   M. Pellaton, C. Affolderbach, Y. Pétremand, N. F. de Rooij, and G. Mileti, "Study of laser-pumped double-resonance clock signals using a micro-fabricated cell," Poster presentation at the International School and Conference on Photonics, Photonica, Belgrade, Serbia, Sep. 2011.

[O.6]   M. Pellaton, Y. Pétremand, C. Affolderbach, N. F. de Rooij, and G. Mileti, "Laser-pumped double-resonance atomic clock using a micro-fabricated Rubidium cell," Oral presentation by M. Pellaton at the European Conference on Lasers and Electro-Optics and the XIIth European Quantum Electronics Conference (CLEO/Europe-EQEC), Munich, May 2011.

[O.7]   F. Gruet, T. Bandi, M. Pellaton, C. Affolderbach, R. Matthey, J. D. Francesco, and G. Mileti, "Compact stabilized laser heads for frequency standards and spectroscopy," Poster presentation by F. Gruet at the Workshop on Optical Clocks, Istituto Nazionale di Ricerca Metrologica (INRIM), Torino, Dec. 2010.

[O.8]   C. Schori, M. Pellaton, S. Jeanneret, G. Bergonzi, Y. Pétremand, N. F. de Rooij, and G. Mileti, "Spectroscopy of micro-fabricated Rubidium vapour cells for atomic clocks," Poster presentation by C. Schori at Atelier LEA-Microtechnique d'Arc-et-Senans, Arc-et-Senans, Sep. 2008.

In preparation

[I.1]   A. Horsley, G.-X. Du, M. Pellaton, C. Affolderbach, G. Mileti, and P. Treutlein, "Imaging rb-wall interactions and microwave fields in vapor cells," *submitted for presentation at 28th European Frequency and Time Forum (EFTF) in Neuchâtel*, Jun. 2014.

[I.2]   K. Masuda, M. Pellaton, J.-C. Diels, L. Arissian, and G. Mileti, "Push-pull optical pumping with mode-locked laser," *submitted for presentation at 28th European Frequency and Time Forum (EFTF) in Neuchâtel*, Jun. 2014.

[I.3]   M. Pellaton, R. Straessle, C. Affolderbach, Y. Pétremand, D. Briand, N. F. de Rooij, and G. Mileti, "Spectroscopy in a micro-fabricated rb cell with anti-relaxation wall-coating," *submitted for presentation at 28th European Frequency and Time Forum (EFTF) in Neuchâtel*, Jun. 2014.

Projects involved

This thesis work was performed within the frame of, and financed by four main projects: MACQS, NPI, FNS-Rb and FNS-REQUIP. The cells realized contributed also to the success of several other side projects: mUSO, ESA-LARC, ESA-POP, SQUATOS, MClocks and DLR. We briefly describe these projects here below:

- **MACQS** (2009-2013): Miniature atomic clocks and quantum sensors, Swiss National Science Foundation (SNF) Sinergia contract 122693. This project aimed at the development of innovative miniature atomic clocks and quantum sensors from a multi-group approach. The groups involved were:

  - Laboratoire Temps-Fréquence (LTF), Université de Neuchâtel (UniNe). PhD student: *M. Pellaton*, under the direction of Prof. *G. Mileti*.

  - Sensors, Actuators and Microsystems LABoratory (SAMLAB), Ecole Polytechnique Fédérale de Lausanne (EPFL). PhD student: Dr. *R. Straessle* [1], under the direction of Dr. *D. Briand*.

  - Laboratory of ElectroMagnetics and Acoustics (LEMA), Ecole Polytechnique Fédérale de Lausanne (EPFL). PhD student: Dr. *M. Violetti* [2], under the direction of Prof. *A. K. Skrivervik*.

  - Laboratory of Microengineering for Manufacturing (LPM), Ecole Polytechnique Fédérale de Lausanne (EPFL). PhD student: Dr. *F. Vecchio* [3], under the direction of Dr. *T. Maeder*.

  - Microsystems for Space Technologies Laboratory (LMTS), Ecole Polytechnique Fédérale de Lausanne (EPFL). PhD student: Dr. *V. Venkatraman* [4], under the direction of Prof. *H. Shea*.

  This project represents the core of the studies presented in this manuscript. Our research line was to perform fundamental spectroscopic studies on existing glass-blown and miniature atomic vapour cells and other innovative components developed by LTF and the project partners (see Chapters 4, 5 and 6). The study on innovative wall coatings and miniature

wall coated cells was also part of the research line and is presented in the Chapter 5. The Chapter 6 presents the realization of a clock based on a miniature atomic resonator presenting significant gains in term of volume ($\sim$8X) for similar stability performances ($\sigma_y(\tau) = 1 \times 10^{-11}\tau^{-1/2}$).

- **NPI** (2010-2013): Networking/Partnering Initiative (NPI), Co-Sponsored PhD on Advanced vapour cells for future atomic clocks, ESTEC contract No.4000101390. The scope of the activities was the investigation, implementation and validation of advanced vapour cells for future on-board atomic clocks. The objective was to improve, by at least a factor 5, current clock performances (stability over mass-volume-power-cost ratio). As for the MACQS project, the results are presented in Chapters 4, 5 and 6.

- **FNS-Rb** (2008-2014): Precision double resonance spectroscopy and metrology with stabilised lasers and atomic vapours: applications for atomic clocks and magnetometers, SNF Project funding (Div. I-III) contracts 118062, 130381 and 140681. The main research topic is precision laser-based spectroscopy and metrology (double resonance and coherent population trapping) of alkali atoms in, respectively, wall-coated and micro-fabricated buffer gas cells, for application in atomic clocks and magnetometers.

- **FNS-REQUIP** (2010-2012): Alkali cells wall-coating systems for atomic clocks, SNF R'EQUIP contract 128704. This project financed the update of the LTF cell filling system to allow the fabrication of wall-coated vapour cells for high performance and miniature atomic clocks. The cell filling is described in the present chapter, and the studies on the successfully produced cells are presented in the Chapter 5.

- **mUSO** (2007-2010): Miniature Ultra Stable Oscillators for Secure Telecommunications, ESTEC contract 20794/07/NL/GLC. Prime : Spectratime SA (at time of proposal : TEMEX NEUCHATEL TIME SA). subcontractors: UniNe-LTF, EPFL-SAMLAB, EPFL-ESPLAB. (at time of proposal all UniNe-IMT). The project objective was the development of a new generation of portable and low power miniature Ultra Stable Oscillators (mUSO). The interrogation scheme was based on Coherent Population Trapping (CPT) of ^{85}Rb. Although the size of the cell is beyond the limit of the glass blowing technique in terms of geometry and optical quality control, promising short term stabilities of $7 \times 10^{-11}\tau^{-1/2}$ have been obtained with the smallest cells (6 mm diameter) realized with the LTF cell filling system [5].

- **ESA-LARC** (2005-2011): Gas cell laser clock technologies for atomic frequency standards, ESTEC contract 19392/05/NL/CP. Contractor: UniNe-LTF (no partners). The project aimed at the development of Laser-pumped Atomic Rubidium Clock (LARC) for space. The use of laser-pumping instead of lamp-pumping brought a significant short-term improvement, but required a new recipe for the buffer gas filling of the cells, to compensate for the light-shift and the temperature shift. This drove the implementation of an innovative gas mixing technique. Moreover, evacuated cells were required for the laser frequency stabilization. Several cells have been produced to validate the modified cell filling system and to finally produce the demonstrator's cells(buffer gas filled and evacuated) showing a short-term stability of $5.3 \times 10^{-13} \tau^{-1/2}$ [6]. More information at http://telecom.esa.int/telecom/www/object/index.cfm?fobjectid=30855.

- **ESA-POP** (2008-2011): Next Generation Compact Atomic Clocks, ESTEC contract 21504/08/NL/GLC. Prime: Istituto Nazionale di Ricerca Metrologica (INRIM). Subcontractors: UniNe-LTF, Galileo Avionica SpA, Spectratime SA. This project focused on the development of the next generation of vapour-cells based compact atomic clocks having the performance of a passive Hydrogen-Maser but a mass-volume-consumption similar to the commercial compact rubidium atomic frequency standards. Two research lines have been followed: Continuous DR by our laboratory in 25 mm diameter cells [7] and the pulsed optically pumped (POP) interrogation by the INRIM in the 22.66 mm diameter quartz cells [8]. Both interrogation techniques have demonstrated state-of-the-art stabilities for vapour cell atomic clocks exhibiting $\sigma_y(\tau) < 2 \times 10^{-13} \tau^{-1/2}$ using cells fabricated within this research work.

- **SQUATOS** (2011-2012): Space QUalified Assembly Technique for Optical Systems, funded by the Swiss Space Office in the frame of Swiss Space Positioning Measures, call 2010. Project coordinator: CSEM SA. Partners: Micos Engineering GmbH, Hexagon Technology Center, GmbH, UniNe - LTF. This project aimed at the assessment of the Three Dimensional Miniaturized Optical Surface Mounted Device (TRIMO-SMD) technology performance in various environmental conditions, identification of the technology's limits in space applications, definition of the roadmap toward space qualification of the TRIMO-SMD. A fibre-coupled stabilization setup at 780 nm using a TRIMO-SMD assembling technique [9] was developed and realized (see [10] and Figure 2.7). This realization benefited from the high quality evacuated cells (10 mm diameter) produced.

- **Rb-laser** (2010-2012): Compact and stabilized laser head for innovative Rubidium clock, funded by the Swiss Space Office in the frame of Swiss Space Positioning Measures, call 2010. Partners: UniNe-LTF and Spectratime SA. This project aimed at an update of the compact and frequency-stabilized laser heads developed by LTF. The goal was to miniaturize and fully integrate into the redesigned laser head the laser control electronics. This project also benefited from the high quality evacuated cells (10 mm diameter) produced.

- **MClocks** (2013-2016): EMRP[1] (European Metrology Research Programme, Programme of Euramet) project IND55-Mclocks : Compact and high-performing microwave clocks for industrial Applications. Prime: Istituto Nazionale di Ricerca Metrologica (INRIM). Partners: Observatoire de Paris - System de Reference Temps Espace, France; Turkiye Bilimsel ve Teknolojik Arastirma Kurumu TUBITAK, Turkey; Université de Franche Comté - Laboratoire National de Metrologie d'Essai, France; Muquans, France. Associated Research excellence Grant (REG) : UniNe-LTF. Started in 2013, this project aims at a vapour cell clock that combines compactness, reliability, low cost and power consumption, with the frequency stability close to that of a H-maser. High quality evacuated cells (10 mm diameter) are required for laser frequency stabilization [11]. The project will also benefit from the excellent buffer gas control achieved with the updated cell filling system and the high quality of the produced clock reference cells. More information at `http://www.inrim.it/Mclocks/`.

- **DLR** (2013-): Optical Filtering for Onboard LIDAR Calibration, ESTEC contract N° 4000106330/12/NL/EM. The objective of the project is to study optical filtering technologies for onboard LIDAR calibration and to demonstrate suitable techniques using breadboards and their experimental validation. The CO_2 measurement requirements with an IPDA LIDAR are considered as reference for the activity. The part of LTF concerns the development of a laser system for frequency calibration of the LIDAR laser transmitter. This realization benefited from the high quality evacuated cells (10 mm diameter) produced.

---

[1]The EMRP is jointly funded by the EMRP participating countries within EURAMET and the European Union.

Abbreviations

AB	**A**nodic **B**onding
AOM	**A**cousto-**O**ptic Modulator
BG	**B**uffer **G**as
ECDL	**E**xternal **C**avity **D**iode **L**aser
EIT	**E**lectromagnetically **I**nduced **T**ransparency
ESA	**E**uropean **S**pace **A**gency
EMRP	**E**uropean **M**etrology **R**esearch **P**rogramme
FNS	**F**ond **N**ational **S**uisse
FOF	**F**ield **O**rientation **F**actor
FoM	**F**igure **o**f **M**erit
FWHM	**F**ull **W**idth at **H**alf **M**aximum
HV	**H**igh **V**acuum
UHV	**U**ltra **H**igh **V**acuum
CF	**C**on**F**lat
CPT	**C**oherent **P**opulation **T**rapping
CSAC	**C**hip **S**cale **A**tomic **C**lock
CW	**C**ontinuous **W**ave
DFB	**D**istributed **F**eed**B**ack
DR	**D**ouble **R**esonance
LARC	**L**aser-pumped **A**tomic **R**ubidium **C**lock
LH	**L**aser **H**ead
LIAD	**L**ight **I**nduced **A**tomic **D**esorption
LEMA	**L**aboratory of **E**lectrom**a**gnetics and **A**coustics
LMTS	**M**icrosystems for **S**pace **T**echnologies **L**aboratory
LPM	**L**aboratoire de **P**roduction **M**icrotechnique
LTF	**L**aboiratoire **T**emps-**F**réquence
LS	**L**ight **S**hift
µ-LGR	**M**icro **L**oop **G**ap **R**esonator

MEMS	Micro-Electro-Mechanical Systems
mUSO	miniature Ultra Stable Oscillators
NPI	Networking/Partnering Initiative
OTS	OctadecylTrichloroSilane
POP	Pulsed Optically Pumped
PP	Physics Package
PrS	Pressure Shift
PS	Power Shift
SAM	Self-Assembled-Monolayer
SAMLAB	Sensors, Actuators and Microsystems Laboratory
SERF	Spin Exchange Relaxation Free
SNF	Swiss National Science Foundation
SQUATOS	Space QUalified Assembly Technique for Optical Systems
TRIMO-SMD	Three Dimensional Miniaturized Optical Surface Mounted Device
TS	Temperature Shift
VCSEL	Vertical Cavity Surface Emitting Laser

Physical Constants[1]

Speed of Light	c	$=$	$299\ 792\ 458\ \text{ms}^{-1}$
Free electron's Landé g-factor	g_S	$=$	$2.002\ 0319\ 304\ 361\ 53(53)$
Magnetic Constant	μ_0	$=$	$4\pi \times 10^{-7}\ \text{NA}^{-2}$
Electric constant	ϵ_0	$=$	$8.854\ 187\ 817... \times 10^{-12}\ \text{Fm}^{-1} = (\mu_0 c^2)^{-1}$
Bound electron's Landé g-factor ($5^2\text{S}_{1/2}$) [13]	g_J	$=$	$2.002\ 331\ 13(20)$
^{87}Rb Nucleus' Landé g-factor [13]	$g_{I_{87}}$	$=$	9.95141×10^{-4}
^{85}Rb Nucleus' Landé g-factor [13]	$g_{I_{85}}$	$=$	2.93640×10^{-4}
Bohr magneton $\frac{e\hbar}{2m_e}$	μ_B	$=$	$9.274\ 009\ 68(20) \times 10^{-26}\ \text{JT}^{-1}$
Electron elementary charge	e	$=$	$1.602\ 176\ 565(35) \times 10^{-19}\ \text{C}$
Electron mass	m_e	$=$	$9.109\ 382\ 91(40) \times 10^{-31}\ \text{kg}$
Plank constant $\frac{h}{2\pi}$	$\hbar$	$=$	$1.054\ 571\ 726(47) \times 10^{-34}\ \text{Js}$
Rb Second order Zeeman constant	K_C	$=$	$575.15\ \text{HzG}^{-2}$

---

[1] if not specified, the constants are taken from: Mohr et al., "CODATA recommended values of the fundamental physical constants: 2010", Rev. Mod. Phys., vol. 84, 2012 [12]

Information on the notations used:

Symbol	Description	units
ω, Ω	angular frequencies	s^{-1} or $\frac{\mathrm{rad}}{\mathrm{s}}$
ν	frequencies	Hz
Γ	rates and/or linewidths (FWHM) in the angular frequency domain	s^{-1} or $\frac{\mathrm{rad}}{\mathrm{s}}$
γ	linewidth (FWHM) in the frequency domain	Hz

Introduction

Mastering the time is still beyond human reach today but mastering its measurement has inspired the humankind since ages. As for every quantity, the measurement of time needs a reference. Historically, the natural day-night cycle served as the first reference to quantify longer cycles such as the moon phases and the seasons. This gave rise to the calendars. The need to measure shorter time scale initiated the clock era[1]. The first clock is attributed to the Egyptian civilization with what we call now the shadow clock. It was then followed by the water clock (clepsydra) and the sand clock which allowed the transport of the time reference and the measurement of time at night as well. A first revolution happened with the use of oscillating systems such as the pendulum, and a mechanical system to maintain and count the oscillations. But the main revolution for our domain came in the beginning of the 20th century, with the use of electric or magnetic resonances in the frequency domain. The first quartz clock [15] in the 30's and the first atomic clock [16], in the 40's were built. Rapidly, the performances achieved by the atomic clocks surpassed the ones of the quartz and in 1967 the second was redefined during the 13th *Conférence Générale des Poids et Mesures (CGPM)*. Initially defined as 1/86'400 of a mean solar day, the definition of the second became "the duration of 9 192 631 770 periods of the radiation corresponding to the transition between the two hyperfine levels of the ground state of the caesium 133 atom". The mission of timekeeping was transferred from the stars to the caesium atoms.

The innovations were not stopped by that definition and various types of clock have been developed since the first caesium beam clocks was realized in 1955 [17]. These clocks strongly differ, from their working principle, performances and thus their applications fields. The state-of-the-art clocks in terms of precision and accuracy today are the fountain clocks, optical-lattices clocks, and ion-traps clocks. The time uncertainty is of the order of 1 to 10 ps per day, or 10^{-17} to 10^{-16} relative. Their volume, cost of production and power consumption are prohibitive for any commercial applications, and restrict their use to international time keeping [18] or laboratory fundamental researches, such as the quantification of the variations of fundamental constants like the fine structure constant [19], or the electron-to-proton mass ratio [20]. The precision

---

[1]According to Lombardi [14], a clock is an instrument that measures time intervals shorter than a day.

and accuracy achieved are so good that the relativistic effects become significant and have to be corrected [21].

The commercial needs, less demanding in terms of precision and accuracy, have driven the development of more compact, and cheaper clocks. These clocks can be grouped into four different types: active and passive hydrogen masers, caesium thermal beams and vapour-cell based clocks. The masers and the caesium thermal beams, having an accuracy of the order of the nano second per day, or 10^{-14} relative, represent a niche market due to their high price and volume. The applications range from radio astronomy and accurate measurement of the continental drift, Global Navigation Satellite Systems (GNSS), time keeping, and fundamental physics [22]. The mass production of smaller and less expensive clocks (several tens of thousands per year [23]) is represented by the vapour cell based clocks. These clocks answer to the need for reliable, small, portable and low power consumption clocks with still competitive stability performances and a moderate price. The time error varies from few nanosecond per day, or 10^{-14} relative, for the high performances rubidium clock [24] to the microsecond per day, or 10^{-11} relative inaccuracy, for the smallest clocks [25]. As a comparison, the time error for temperature stabilized quartz oscillators is of the order of one millisecond per day, or 10^{-8} relative inaccuracy. This error rises up to the second per day, or 10^{-5} relative inaccuracy for the quartz used in our wristwatches. The commercial atomic clocks cover a wide range of applications such as network synchronization for telecommunication, power grids synchronization, precise timing for financial markets, laboratory timing, GNSS and secured communication [22]. Most of the current applications for the vapour cell clock are station-based, but the demand for lower volume, mass and power consumption for highly portable applications, such as portable GNSS receiver, or distributed underground or underwater geophysical sensors [26], is increasing. The need for improved and miniature vapour cells for such applications motivated this thesis work.

In the past recent years, two opposite research lines were followed in the field of vapour cells clock optimization, either the miniaturization, or the improvement of the clock stability performances:

- An extreme miniaturization down to an atomic resonator volume of few cm^3 was achieved by exploiting micro-fabrication techniques for cell fabrication [27] and by using the coherent population trapping (CPT)[28], [29] as interrogation scheme [25], [30]–[32]. The cost for such an extreme miniaturization is a significant degradation in terms of the short-term frequency stability performances up to $\sigma_y(\tau) \sim 1 \times 10^{-10}\tau^{-1/2}$ [25] in terms of Allan

deviation. Most of these studies were carried out in the United States under the Chip-Scale Atomic Clock (CSAC) project initiated in 2002 and financed by the Defence Advanced Research Projects Agency (DARPA). The objectives were a frequency stability below 10^{-11} at one hour for a 1 cm^3 atomic resonator [22]. Two independent projects were also developed in Neuchâtel [32], [33].

- The stability improvement in compact ($\sim$1 litre) cell clocks was exploiting the significantly improved clock performances obtained with a laser instead of a lamp in the double resonance (DR)[34] interrogation scheme. Both, the continuous wave [6], [7] and the pulsed approach [8] were employed. The short-term clock frequency stability could be improved down to $\sigma_y(\tau) < 2 \times 10^{-13} \tau^{-1/2}$ for a compact but non-negligible volume of <1500 cm^3 [7].

For this thesis work, we decided to follow both approaches simultaneously: a moderate miniaturization allowing a significant size reduction along with a moderate stability degradation, and the laser-pumped DR interrogation scheme which is more efficient than the classical lamp-pumped DR interrogation schemes for similar cell sizes [35], [36]. This interrogation scheme is expected to allow the compensation of the stability degradation induced by the miniaturization. Beside the interrogation scheme, the cell fabrication, its alkali vapour and the methods employed to prevent the depolarization of the alkali atoms also affect the potential stabilities of the clock.

Historically, the researches were carried out using rubidium for one essential reason, its optical spectral characteristic. Indeed, under proper conditions, the optical spectrum of the ^{85}Rb partially overlaps the one of the ^{87}Rb. This allows a selective optical pumping of the ground state levels, using only a rubidium spectral lamp; and renders the required inversion of population of the ground state levels feasible without the use of an appropriate laser, non-existent in the early decades of atomic clocks. With the venue of suitable lasers, other alkali atoms, such as caesium, might also be convenient for DR. But, ^{87}Rb still appears more efficient, as its reduced number of ground states allows a more efficient optical pumping. It is therefore chosen for this work.

Two methods are reported for preventing the depolarization of the alkali atoms due to the collisions with the inner cell wall: the buffer-gas [37] and the wall-coating [38]. While the buffer gas method prevents the atoms to collide directly with the inner walls of the cell by strongly reducing their mean free path, the wall-coating significantly reduces the depolarization probability of the collisions with the walls. These two methods were investigated.

Based on these considerations, the Miniature Atomic Clocks and Quantum Sensors (MACQS) project started in 2009. It was funded by the Sinergia project fund of the Swiss National Science Foundation. The objective of the MACQS project was to develop and test new technologies in order to miniaturize the key building blocks of an atomic sensors based on the DR scheme: the cell, the microwave resonator and the pump-light source. Both, laser and micro-fabricated spectral lamp [39], [40] were envisaged as the pump-light source. Five Swiss research groups were involved and many key components have been produced and tested. Among others, miniature microfabricated cells sealed by anodic bonding or indium bonding with different geometries, an innovative miniaturized microfabricated magnetron cavity and wall coated cells were fabricated. This thesis reports on the spectroscopic studies realized on these different components.

This work was also co-financed by two other funds: the European Space Agency's Networking/-Partnering Initiative (NPI) with the *"Advanced Vapour Cells for Future Atomic Clocks"* project and the Swiss national science foundation with the *"Precision double resonance spectroscopy and metrology with stabilised lasers and atomic vapours: applications for atomic clocks and magne-tometers"* project.

This document is split in six chapters as follow:

Chapter 1

This part presents the theoretical basis required to understand the interaction of an atom with electromagnetic fields. A short overview of the atomic structure and the diverse splitting, as well as optical and magnetic pumping through their respective dipole interactions, is given. This is followed by the presentation of the basic DR principle and its theoretical model for a 3-level system. Finally the notion of clock frequency stability is discussed, and the limiting factors for clock stability are detailed.

Chapter 2

We present here the different experimental configurations and setups used for the spectroscopy analysis. The building blocks of our laboratory atomic clock, laser head and physics package, are described in detail.

Chapter 3

We present in this chapter the fabrication methods employed for the fabrication of all the cells studied and presented in this manuscript. The accent is put on the glass-blown cell technology and the filling techniques, from the evacuated cells to the wall coated cells, passing by the buffer-gas filled cells. The micro fabrication techniques are also presented more briefly.

Chapter 4

This chapter treats the spectroscopic characterizations methods, employed to evaluate the newly developed micro fabrication processes for evacuated and buffer gas filled cells. From the linear absorption spectroscopy to the double resonance spectroscopy, different methods are used to quantify leak rates, contamination level and control of the fillings of the cells produced.

Chapter 5

In a similar way to the Chapter 4, this chapter presents evaluations of the produced wall-coated cells. Four coatings are treated. While Parylen N, Parylen C and tetracontane are tested in centimetric glass-blown cells, OTS was employed for the realization of a microfabricated wall-coated cell with a proven operational wall-coating. The real-time observation and monitoring of the well-known ripening process in coated cell by double resonance spectroscopy is also presented.

Chapter 6

This chapter is dedicated to the metrological study of a newly designed physics package for a miniature atomic clock. This physics package consists of an innovative subwavelength microwave resonator, and a thick glass core microfabricated cell. Both are micro-fabricated and allow a significant size reduction compared to commercially available high performances clocks, without compromising too much on the stability. The systematic shifts are measured and optimized and the ultimate performances are evaluated. A clock frequency measurement over 6 months is presented and its stability analysis is confronted to the different instability sources. An alternative

interrogation scheme, potentially improving the long term regime, is also discussed.

Summary and conclusions

Finally the conclusions and future prospects are discussed in this last part.

Chapter 1

Double resonance rubidium atomic clock: basic principles

A clock exploits the resonance phenomenon of an oscillating system (resonator) that provides a frequency reference. Typically, this system can be mechanical, like a pendulum, a balance wheel, or electro-mechanical like a quartz oscillator. In the case of a microwave atomic clock, an ensemble atoms-microwave magnetic field serves as a reference for a quartz oscillator; the resonance phenomenon is a chosen atomic hyperfine transition that occurs when the frequency of the electromagnetic field, generated by the quartz oscillator, is resonant with the transition's Bohr frequency. For a transition between two quantum states of energy eigenvalues, E_1 and E_2, the Bohr frequency is expressed as:

$$\nu_B = \frac{E_2 - E_1}{h}. \tag{1.1}$$

where h is the Planck's constant.

This study is on double resonance (DR) rubidium atomic clocks, or rubidium clocks. They belongs to the class of passive frequency standards, in which the microwave field serves as a probe for the resonance[1]: a quartz oscillator, at the basis of the microwave generation, is locked in frequency to the atomic resonance by an electronic servo-loop (see Figure 1.1). In a rubidium clock, the atomic resonator represents the heart of the clock, and is composed of two key elements: a vapour cell, confining the atoms, and a microwave cavity sustaining the probing field.

---

[1]By opposition to active resonators that produce the resonant field through stimulated emission radiation

This atomic resonator structure presents already strong advantages in terms of cost, size, power consumption, and reliability, and is widely used for the synchronisation of satellite navigation systems and telecommunication networks. Yet, it is actually not small enough for highly portable systems, such as mobile phone, navigation system receiver. The scope of this study is on further
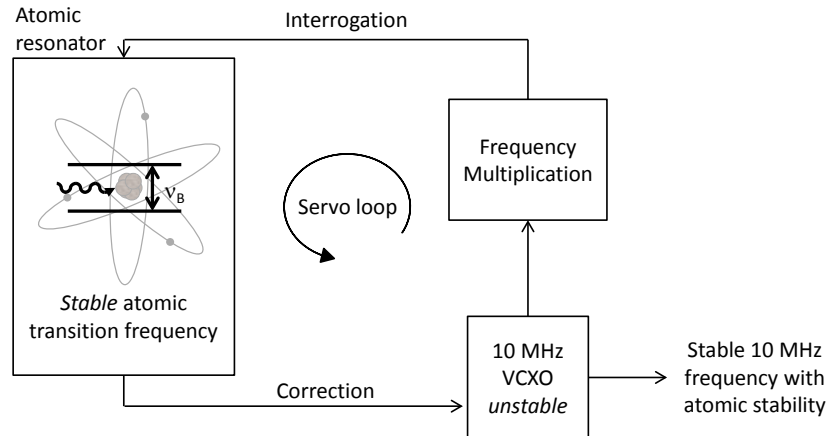
FIGURE 1.1: Clock principle of a passive atomic resonator.

miniaturization of this atomic resonator, and more particularly the cell. The atoms, confined in the cell, are continuously moving, undergo many collisions and are constantly subject to electromagnetic perturbations. These effects give rise to shifts and broadening of the atomic resonance that may be stressed by the cell size reduction. Since the short- and medium- to long-term stabilities of an atomic clock are intrinsically related to the properties of the resonance line (see Chapter 1.7) a thorough understanding of these various physical effects appears essential for the choice and the control required of the experimental conditions minimizing these effects.

In this chapter, we introduce the double resonance principle and the basic physics describing the various mechanisms involved in it. The structure and the intrinsic splitting of the energy levels of the rubidium atom is discussed followed by a semi-classical treatment of the effects induced by the atom-field interaction: Zeeman effect, magnetic dipole transition and electric dipole transition. Finally, the two types of spectra present in a rubidium clock, the optical absorption spectrum and the optical-microwave DR spectrum, are discussed. The respective shifts and broadening and their origins are discussed in details and quantitative predictions are drawn. A new phenomenological description of the AC-Stark shift is also developed.

1.1 Motivation

Atomic structure and atom-field interactions are quantum physics problems taught in undergraduate courses, and the practical case usually concerns the hydrogen atom (see for example Cohen-Tannoudji's "Quantum mechanics" [41]). For the general case, and especially the rubidium, other authors like D. A. Steck [42], J. Vanier [37] or A. Corney [43] propose detailed treatments of the subject. However, the presentation is highly theoretical and relevant information for the experimentalist in double resonance spectroscopy is sometimes not straightforward. The purpose of this chapter is to restrict the theory to the interactions and transitions of interest for a rubidium clock only. In particular, we calculate all the transition probabilities for the magnetic dipole interaction. We also redefine a pure magnetic field polarization since the standard electromagnetic polarization definition, based on the electric field only (see [43]), is not precise enough for an unambiguous description of the magnetic field orientation.

1.2 Double resonance principle

The high resolution spectroscopic studies in this thesis are based on the double resonance principle: consider an ensemble of three levels systems (as shown on Figure 1.2) confined in an absorption cell. We name levels 1 and 2, lower and upper ground state levels, and level 3 the excited level. At thermal equilibrium, the two ground states can be considered equally populated and the excited state empty. Indeed, for ^{87}Rb at 60°C, the ratios of the populations, n_1, n_2 and n_3, of the states given by the Boltzmann distribution are:

$$\frac{n_1}{n_2} = e^{-(E_2 - E_1)/k_B T} \approx 0.999 \qquad \frac{n_3}{n_2} = e^{-(E_3 - E_2)/k_B T} \approx 1.2 \times 10^{-24} \qquad (1.2)$$

with $((E_2 - E_1)/h \approx 6.8 \text{ GHz}) \ll (k_B T/h \approx 6.9 \text{ THz}) \ll ((E_3 - E_2)/h \approx 380 \text{ THz})$. Consider also two oscillating electromagnetic fields interacting with the atoms. The first, in the optical domain (780 nm/384 THz or 795 nm/377 THz) is resonant with the transition 2-3. The second, in the microwave domain (6.834 GHz), can be frequency swept across the Bohr frequency of the transition 1-2, defined as the clock transition.

The double resonance principle resides in the simultaneous interaction of these two resonant fields with the atomic population. Figure 1.3 shows the typical interrogation scheme for the

DR spectroscopy. The resonant optical field, produced by a laser diode, travels through the cell containing the atomic vapour in which it is partially absorbed ; the cell's transmission is recorded with a photo-detector. The optical interaction induces and maintains a ground state polarization by depleting the level 2 in favour of the level 1 through the unstable level 3. This process is called optical pumping and the transmission of the cell is increased under its effect. The oscillating magnetic field sustained by a microwave cavity fed by a microwave synthesizer, is used as a *frequency interrogator* for the transition 1-2, or clock transition. Indeed, out of the resonance the magnetic field doesn't interact with the atoms, and the population stays in the optically polarized state. On the contrary, when at resonance, the magnetic field induces transitions between the ground state levels, *refilling* the depleted level, and thus reducing the transmission of the optically pumped cell. These *pumping* effects are illustrated in Figure 1.2.

Typically, the transmission as a function of the microwave frequency, has a Lorentzian lineshape with a linewidth of few kHz; it is known as the DR signal (see section 1.6). In the case of rubidium atoms, the approximation by the three levels systems holds but requires the use of an additional constant magnetic field, the C-field, to lift the degeneracy of the hyperfine ground states (see section 1.4.2). The states 1 and 2 are associated with the atomic states $|5^2S_{1/2}; F_g = 1, m_F = 0\rangle$, respectively $|5^2S_{1/2}; F_g = 2, m_F = 0\rangle$. The state 3 is associated either with the $|5^2P_{3/2}\rangle$ (D$_2$ line) or $|5^2P_{1/2}\rangle$ (D$_1$ line) depending on the chosen optical wavelength. The clock transition is therefore the ground state $|F_g = 1, m_F = 0\rangle \leftrightarrow |F_g = 2, m_F = 0\rangle$ transition of 0-0 transition, with an unperturbed transition frequency or clock frequency of 6 834 682 610.90429(9) Hz[44].
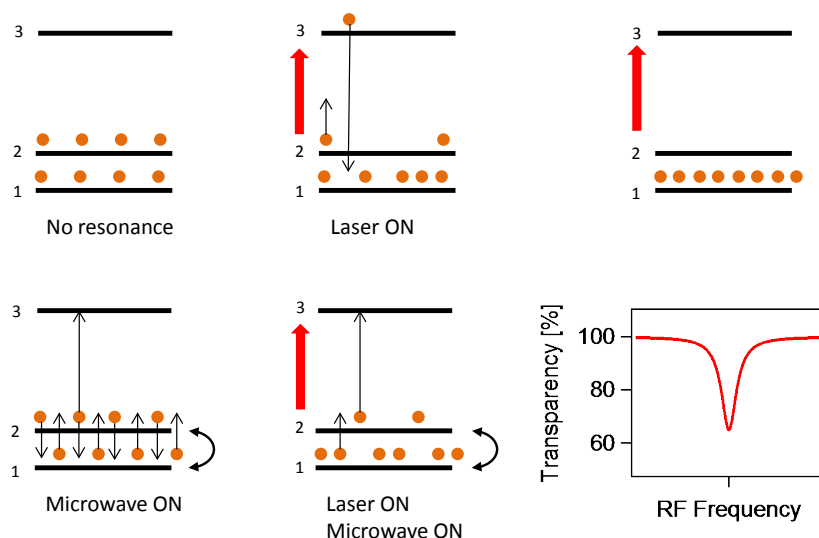
FIGURE 1.2: Schematic representation of the interactions involved in the DR interrogation scheme. Top left, the atoms are at rest, they equally populate the two ground states due to the Boltzmann distribution, the vapour is 50% transparent (first term of eq. 1.74); top centre, beginning of the optical interaction only resonant with the transition 2→3. the level 3 being unstable the atoms "fall" back randomly in the ground states 1 and 2, the level 2 is being emptied and the transmission of the vapour increases (second term of eq. 1.74); top right, without relaxation within the ground states, the inversion of population is total and the vapour is 100% transparent; bottom left, magnetic interaction only, the RF field resonant with the transition 1↔2, induces an oscillation of the populations between the two states. On a time average, states 1 and 2 are equally populated, the vapour transparency is 50%; bottom centre, double interaction with the two fields at resonances. Optical interaction empties the state 2 which is repopulated by the magnetic interaction and the transmission of the vapour decreases (last term of eq. 1.74); bottom right, DR spectrum. The transparency of the vapour is shown as a function of the RF frequency.
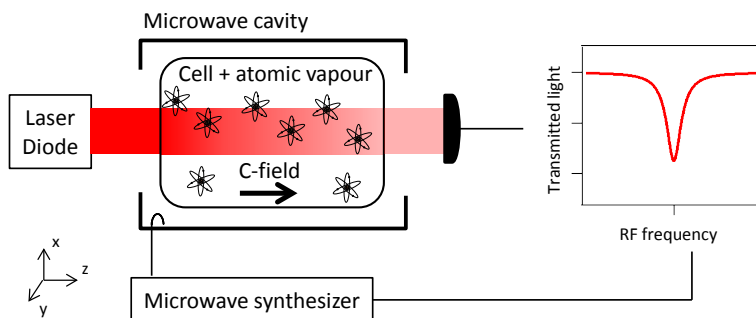
FIGURE 1.3: Double-resonance interrogation scheme. The graphic shows the typical transmitted intensity (DR signal) as a function of the microwave frequency. The z-axis is chosen parallel to the C-field.

1.3   Structure of the Rb atom at rest: intrinsic splittings

The rubidium atom (Z=37) is a hydrogen-like atom: the 36 first electrons are completely filling the atomic subshells as follow: $(1s^2, 2s^2, 2p^6, 3s^2, 3p^6, 4s^2, 3d^{10}, 4p^6)$, where the superscript indicates the degeneracy, i.e. the number of electrons, of the subshell; the first number corresponds to the principal quantum number n and the letter to the azimutal quantum number l as follow: $s \leftrightarrow l = 0; p \leftrightarrow l = 1, d \leftrightarrow l = 2$. These electrons act as a negatively charged shield with no angular momentum around the nucleus, and the average charge seen by the valence electron is $+e$. The central field approximation [41] allows the separation of variables and the same method as for the hydrogen atom can be applied. The angular part of the Hamiltonian can be expressed as follow:

$$\boldsymbol{H}_0 = \kappa_{nl} + \epsilon_{nl}\vec{\boldsymbol{L}}^2 + \xi_{nl}\vec{\boldsymbol{L}} \cdot \vec{\boldsymbol{S}} + \mathscr{A}_{nl}\vec{\boldsymbol{I}} \cdot \vec{\boldsymbol{J}} \tag{1.3}$$

where $\vec{\boldsymbol{L}}$, $\vec{\boldsymbol{S}}$, $\vec{\boldsymbol{J}} = \vec{\boldsymbol{L}} + \vec{\boldsymbol{S}}$ and $\vec{\boldsymbol{I}}$ are the operators for the orbital angular momentum, the electron spin angular momentum, the total electron angular momentum, and the nucleus spin angular momentum, respectively. κ_{nl}, ϵ_{nl}, ξ_{nl}, and $\mathscr{A}_{nl}$ are constants arising from the separation of variables including also relativistic effects and the vacuum fluctuations [41]. The third element is called spin-orbit term and is responsible for the atomic fine structure. The last term arises from the coupling of the nucleus spin with the total electron momentum and induces the hyperfine structure of the atom. These effects on the energy levels are shown on Figure 1.4. The energy states are named using the F, m_F notation, where F and m_F are the quantum numbers associated to the total angular momentum operator of the atom, $\vec{\boldsymbol{F}} = \vec{\boldsymbol{J}} + \vec{\boldsymbol{I}}$, and $|F, m_F\rangle$ the eigenstates.

1.4   Weak electromagnetic interactions

The interaction of the atom with an electromagnetic field is treated here semi-classically[1] as a perturbation, and the total interaction Hamiltonian is approximated by:

$$\boldsymbol{H} = \boldsymbol{H}_0 + \boldsymbol{W}, \tag{1.4}$$

where $\boldsymbol{H}_0$ is the unperturbed Hamiltonian of the atom, and $\boldsymbol{W}$ the perturbation. In the case of a static field, this perturbation is constant and only modifies the eigen energies of the eigenstates.

---

[1]the atoms are treated quantum-mechanically but the electromagnetic fields classically.
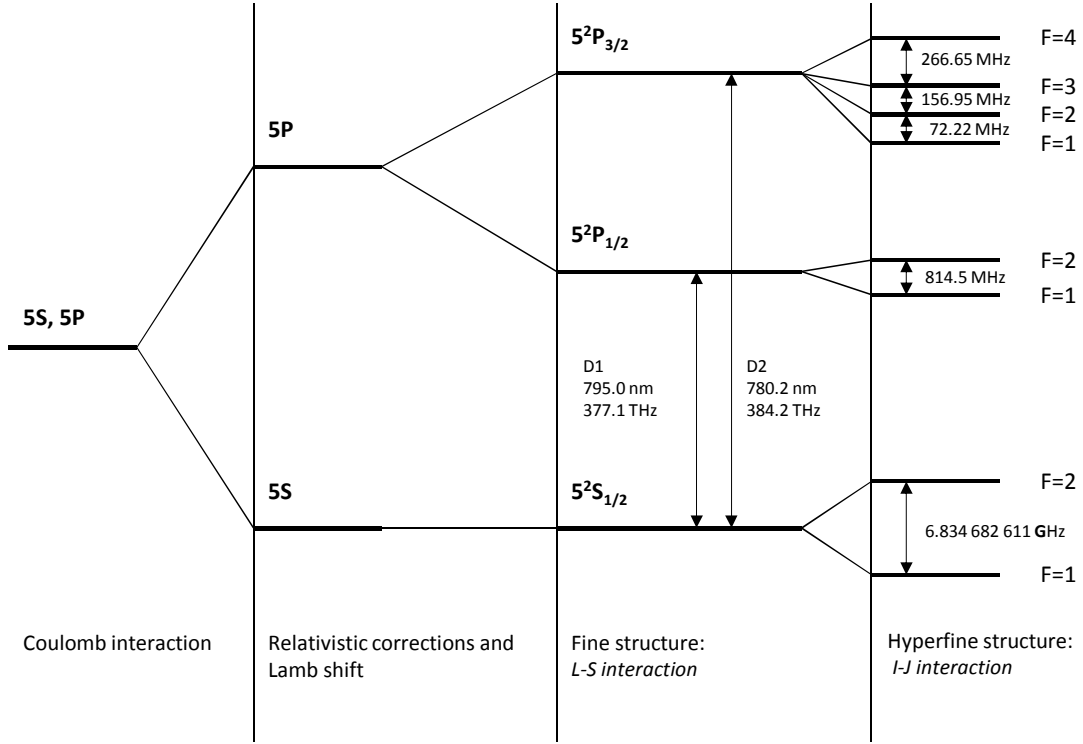
FIGURE 1.4: Splitting of the ^{87}Rb energy levels $(J = \frac{3}{2})$ in absence of external fields.

This effect is known as the Zeeman effect for a static magnetic field (see section 1.4.2), or Stark effect for a static electric field. In the case of an oscillating field resonant with ω_0, the Bohr frequency of two of its states $|i\rangle$ and $|f\rangle$, the atom makes cyclic transitions between these states. The angular frequency of this cycle is called the Rabi frequency or Ω_{if}, and is expressed as follow:

$$\Omega_{if} = \frac{|W_{fi}|}{\hbar} \tag{1.5}$$

where W_{fi} is the matrix element of the amplitude $\tilde{\boldsymbol{W}}$ of the oscillating perturbation Hamiltonian $\boldsymbol{W}$:

$$W_{fi} = \langle f| \, \tilde{\boldsymbol{W}} \, |i\rangle \,. \tag{1.6}$$

When the lifetime of the excited state is short as compared to the period of the Rabi oscillation, another quantity, the transition rate, becomes relevant. It is given by the following expression

(see [37] for a complete derivation):

$$\Gamma_{if}(\omega) = \left(\frac{\Omega_{if}}{2}\right)^2 2\pi g(\omega - \omega_{if}).$$

(1.7)

where $g(\omega - \omega_{if})$ is a normalized distribution, centred at ω_{if}, the frequency corresponding to the energy splitting of the two coupled states.

1.4.1 Perturbation Hamiltonian

We saw in section 1.2, that the DR principle involves the interaction between the rubidium atoms and three different types of electromagnetic fields: a static magnetic field, called C-field, a microwave magnetic field, and a near infra-red optical field. All these interactions are described by the same interaction Hamiltonian, but the final expression of the perturbation $\boldsymbol{W}$, issued from a second order approximation of $\boldsymbol{H}$ strongly depends on the type of field considered.

1.4.1.1 Magnetic field

In the case of a pure magnetic field, the perturbation Hamiltonian can simply be written as [41],

$$\boldsymbol{W}_M(t) = -\vec{\boldsymbol{\mu}} \cdot \vec{B}_0 \cos(\omega t),$$

(1.8)

where $\vec{\boldsymbol{\mu}}$ is the magnetic moment operator of the atom, given by $\vec{\boldsymbol{\mu}} = -\mu_B(\vec{\boldsymbol{L}} + g_J\vec{\boldsymbol{J}} - g_I\vec{\boldsymbol{I}})$, and $\vec{B}_0 \cos(\omega t)$ the magnetic field. In a rubidium clock, the focus is only on the ground state levels of the atom, for which $l = 0$. Therefore, the radial part of the total interaction Hamiltonian can be reduced to:

$$\boldsymbol{H}_M = \boldsymbol{H}_0 + \boldsymbol{W}_M = \mathscr{A}_{n0}\vec{\boldsymbol{I}} \cdot \vec{\boldsymbol{S}} + \mu_B(g_J\vec{\boldsymbol{S}} - g_I\vec{\boldsymbol{I}}) \cdot \vec{B}(t).$$

(1.9)

1.4.1.2 Light field

In the case of light interaction, both fields interact with the atom through magnetic and electric dipole interaction, and higher orders terms. For the transitions of interest, we only consider

the electric dipole term, since it is the dominant perturbation term by more than four orders of magnitude (the electric dipole approximation). The perturbation Hamiltonian is therefore:

$$\boldsymbol{W_L} = -\vec{\boldsymbol{d}} \cdot \vec{E}_0(\omega) \cos(\omega t) \tag{1.10}$$

$$= -E_0(\omega)\vec{\boldsymbol{d}} \cdot \vec{e}_\lambda \cos(\omega t) \tag{1.11}$$

where $E_0(\omega)$ is the amplitude of the electric field. $\vec{\boldsymbol{d}} = -e \cdot \vec{\boldsymbol{r}}$ is the dipole operator with e the charge of the electron, and $\vec{e}_\lambda$ the polarization vector of the field.

1.4.2 Rubidium in a static magnetic field: ground states Zeeman splitting

For a static magnetic field oriented along the z direction[1], defined from now on as C-field (with C_0 as its amplitude), equation (1.9) is reduced to:

$$\boldsymbol{H}_C = \mathscr{A}_{n0}\vec{\boldsymbol{I}} \cdot \vec{\boldsymbol{S}} + (g_J\mu_B\boldsymbol{S_z} - g_I\mu_B\boldsymbol{I_z})C_0. \tag{1.12}$$

For low C-field strength, typically below 100 mG, $(g_J\mu_B\boldsymbol{S_z} - g_I\mu_B\boldsymbol{I_z})C_0$ is considered as a small perturbation to $\mathscr{A}_{n0}\vec{\boldsymbol{I}} \cdot \vec{\boldsymbol{S}}$, and the basis $\{F_g, m_F\}$ is still a good approximation. The eigen energies for the states $|F, m_F\rangle$ are given by the Breit-Rabi formula [37], [45]:

$$E(F_g, m_F) = -\frac{\mathscr{A}_{n0}}{4} - g_I\mu_B C_0 m_F \pm \frac{\mathscr{A}_{n0}}{4}(2I + 1)\left(1 + \frac{4m_F}{2I + 1}x + x^2\right)^{1/2} \tag{1.13}$$

where

$$x = \frac{2(g_J + g_I)\mu_B C_0}{\mathscr{A}_{n0}(2I + 1)}, \tag{1.14}$$

with the convention that the plus sign applies for $F = I + 1/2$, and the minus one for $F = I - 1/2$. In rubidium clocks, the C-fields used are of the order of 100 mG or below, and $\mathscr{A}$ of 10^{-24} J. Therefore $\frac{\mu_B C_0}{\mathscr{A}} \ll 1$; in addition, for the rubidium atoms, $\frac{g_I}{g_J} < 5 \times 10^{-4}$, so the equation (1.13) can be approximated by:

$$E(F_g, m_F) = \mathscr{A}_{n0}(2I + 1)\left(\frac{-1}{4(2I + 1)} \pm \frac{1}{4}\right) \pm m_F \frac{g_J\mu_B}{2I + 1}C_0 \pm \frac{(g_J\mu_B)^2}{2\mathscr{A}_{n0}(2I + 1)}C_0^2 \tag{1.15}$$

---

[1]In most practical cases, the orientation of the static field determines the z axis, or in other words, the quantization axis. For a non homogeneous field, this quantization axis is only valid locally.

or

$$E(F_g, m_F) = \frac{\mathscr{A}_{n0}}{4}\left(-1 \pm 4\right) \pm m_F \frac{g_J \mu_B}{4}C_0 \pm \frac{(g_J \mu_B)^2}{8\mathscr{A}_{n0}}C_0^2 \qquad (1.16)$$

for the ^{87}Rb case ($I = 3/2$). The selection rules for the hyperfine magnetic dipole transitions impose a change of the magnetic quantum number, $\Delta m_F = 0, \pm 1$ (see section 1.4.3). The corresponding Bohr frequencies of the allowed transitions are thus given by:

$$\frac{E(F_g = 2, m_F) - E(F_g = 1, m_F)}{h} = \frac{2\mathscr{A}_{n0}}{h} + (m_{F_1} + m_{F_2})\frac{g_J \mu_B}{4h}C_0 + \frac{(g_J \mu_B)^2}{4h\mathscr{A}_{n0}}C_0^2 \qquad (1.17)$$

The first term of the equation (1.17) induces the hyperfine splitting ($E_{HFS}/h = 2\mathscr{A}_{n0}/h = 6\ 834\ 682\ 610.90429(9)$ Hz [44]), and the two remaining terms are responsible for the Zeeman splitting (see Figure 1.5). The corresponding linear and quadratic frequency shift coefficients, with respect to the magnetic field amplitude, are $(m_{F_1} + m_{F_2})0.7$ MHz/G and 575.14 Hz/G^2, respectively. For the low C-field strength, (100 mG or below), the linear coefficient spreads equidistantly all the allowed magnetic transition frequencies over a range of ± 420 kHz centred around the hyperfine frequency. In first order, the $|F_g = 1, m_F = 0\rangle \leftrightarrow |F_g = 2, m_F = 0\rangle$ transition frequency is unperturbed by the magnetic field. This first order insensitivity defines this transition as the clock transition and the two considered states as clock states. A quadratic frequency shift is present and is $\sim$5.8 Hz at 100 mG. Though it is at least four orders of magnitude smaller than any other allowed magnetic transition frequency shift, it still has to be considered as a frequency perturbation (see Chapter 1.7).

1.4.3 Magnetic dipole transitions

In the case of an atom in a RF magnetic field oscillating at frequency ω_M, combining equations (1.5), (1.7) and (1.8), gives the corresponding transition rate:

$$\Gamma_{M_{if}}(\omega_M) = \frac{|\langle f|\vec{\mu} \cdot \vec{B}_{RF}|i\rangle|^2}{4\hbar^2} 2\pi g(\omega_M - \omega_{if}). \qquad (1.18)$$

The previous section showed that an additional static magnetic field only shifts the energies of the eigenstates, and has an impact only on the Bohr frequencies of the transitions considered. It also breaks the isotropy of the problem and generates a quantization axis. Therefore, we split
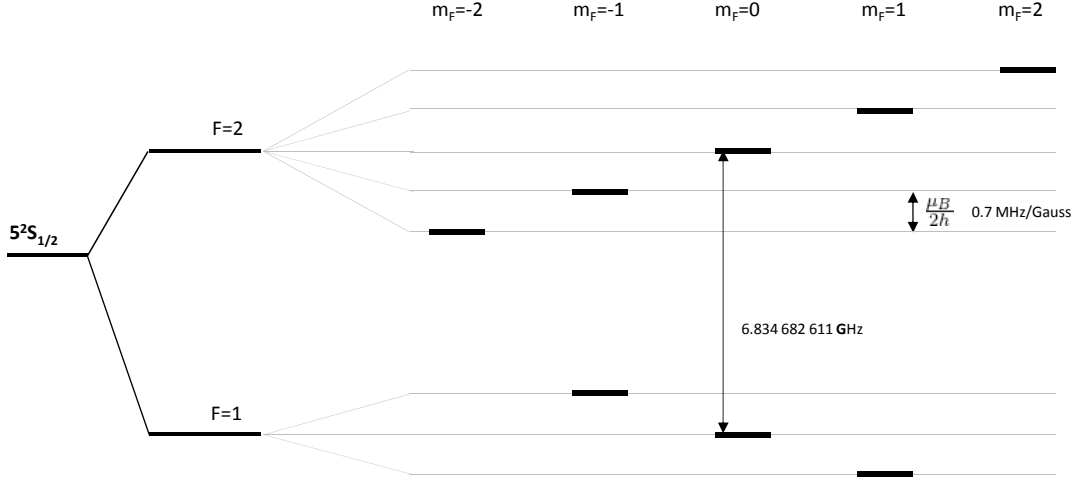
FIGURE 1.5: Schematic weak field Zeeman splitting of the ^{87}Rb ground state energy levels. The drawing is not to scale with respect to the hyperfine splitting.

$\vec{B}_{RF}$ in a parallel field, $\vec{B}_{\parallel}$, and an orthogonal one $\vec{B}_{\perp}$ fields with respect to the local C-field and consider them separately:

$$\vec{B}_{RF}(t) = (\vec{B}_{\parallel} + \vec{B}_{\perp})\cos(\omega_M t) \text{ with } \begin{cases} \vec{B}_{\parallel} = \frac{\vec{B}_{RF} \cdot \vec{C}_0}{||\vec{C}_0||} \frac{\vec{C}_0}{||\vec{C}_0||} \\ \vec{B}_{\perp} = \vec{B}_{RF} - \vec{B}_{\parallel} \end{cases} \tag{1.19}$$

Locally, we choose to fix $\vec{e}_z$ along the C-field, and $\vec{e}_x$ along $\vec{B}_{\perp}$. Using equations (1.9 and 1.19), the fact that $\frac{g_I}{g_J} < 5 \times 10^{-4}$ and that $g_J \approx 2$, the transition rates finally become:

$$\Gamma_{M_{if}}(\omega_M) = \left(\frac{B_{\parallel}\mu_B}{\hbar}\right)^2 2\pi g(\omega_M - \omega_{if}) \underbrace{|\langle f| \boldsymbol{S}_z |i\rangle|^2}_{(\mu_{if}^{\pi})^2}$$

$$+ \left(\frac{B_{\perp}\mu_B}{\hbar}\right)^2 2\pi g(\omega_M - \omega_{if}) \underbrace{|\langle f| \boldsymbol{S}_x |i\rangle|^2}_{(\mu_{if}^{\sigma})^2} \tag{1.20}$$

As can be seen in Table 1.1, μ_{if}^{π} and μ_{if}^{σ} are non null only for transitions with $\Delta m_F = 0$ and $\Delta m_F = \pm 1$, respectively.

TABLE 1.1: Magnetic dipole matrix elements, μ_{if}^π, left table and μ_{if}^σ, right table, within the ground state $5^2\mathrm{S}_{1/2}$. We use: $i \leftrightarrow m_{F=1}$, and $f \leftrightarrow m_{F=2}$.

$m_{F=1}$ \ $m_{F=2}$	-2	-1	0	1	2
-1	0	$\frac{\sqrt{3}}{4}$	0	0	0
0	0	0	$\frac{1}{2}$	0	0
1	0	0	0	$\frac{\sqrt{3}}{4}$	0

$$\mu_{if}^\pi$$

$m_{F=1}$ \ $m_{F=2}$	-2	-1	0	1	2
-1	$\frac{\sqrt{3}}{4}$	0	$\frac{1}{4\sqrt{2}}$	0	0
0	0	$\frac{\sqrt{3}}{4\sqrt{2}}$	0	$\frac{\sqrt{3}}{4\sqrt{2}}$	0
1	0	0	$\frac{1}{4\sqrt{2}}$	0	$\frac{\sqrt{3}}{4}$

$$\mu_{if}^\sigma$$

From now on, we use the following definition for a dipole transition: a π-transition is a transition with $\Delta m_F = 0$ and a σ-transition is a transition with $\Delta m_F = \pm 1$. On the contrary to the definition, based only on the polarization vector of the electric field for any transition [43], this definition distinguishes the type of transition from the change of the magnetic quantum number and imposes clear and stringent conditions on the field inducing the transitions:

- In the case of an *electric* dipole transition, a $\pi(\sigma)$-transition is induced by an electric field parallel (orthogonal) to the local C-field; this is equivalent to the standard definition.

- In the case of a *magnetic* dipole transition, a $\pi(\sigma)$-transition is induced by an magnetic field parallel (orthogonal) to the local C-field; this differ from the standard definition.

Using equations (1.7) and (1.20), the magnetic Rabi frequencies are finally defined as:

$$\Omega_{M_{if}}^\pi = \frac{2B_\parallel \mu_B}{\hbar} \mu_{if}^\pi \tag{1.21}$$

$$\Omega_{M_{if}}^\sigma = \frac{2B_\perp \mu_B}{\hbar} \mu_{if}^\sigma \tag{1.22}$$

and especially:

$$\Omega_{M_{00}}^\pi = \frac{B_\parallel \mu_B}{\hbar} \tag{1.23}$$

which is the Rabi frequency of the 0-0 transition.
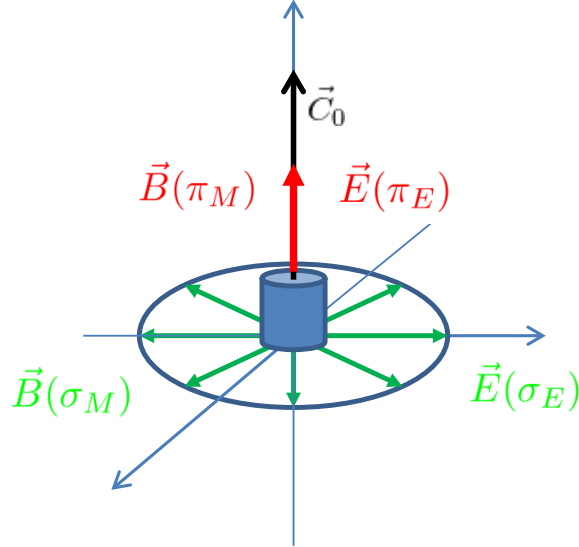
FIGURE 1.6: Scheme of the type of polarizations encountered. Indices specify whether a magnetic or an electric coupling is involved. It is important to note that in this manuscript, the name of the field polarization (π, σ) depends on the type of interaction considered.

It is interesting to note that:

$$\frac{1}{(B_\parallel)^2} \sum_i (\Omega^\pi_{M_{ii}})^2 = \frac{1}{(B_\perp)^2} \sum_{i \neq j} (\Omega^\sigma_{M_{ij}})^2 \tag{1.24}$$

Reflecting the fact that neither σ nor π transitions are intrinsically favoured. Thus, only the direction of the RF magnetic field compared to the C-field weights these transitions.

1.4.4 Electric dipole transitions

In the case of an atom interacting with a light field at an optical frequency ω, combining equations (1.5), (1.7) and (1.10), gives the following transition rate for a fixed field frequency:

$$\Gamma_{if}(\omega) = \frac{\pi E_0(\omega)^2}{2\hbar^2} |\langle f| e\vec{r} \cdot \vec{e}_\lambda |i\rangle|^2 g(\omega - \omega_{if}). \tag{1.25}$$
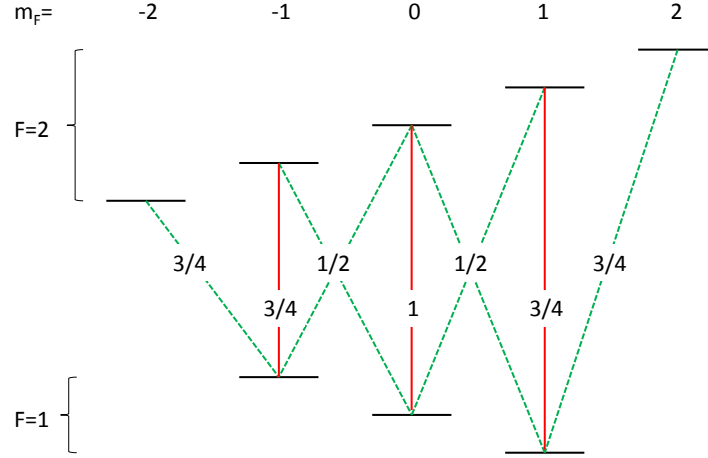
FIGURE 1.7: Magnetic transition rates in the ^{87}Rb $5^2S_{1/2}$ state expressed as multiple of $\left(\frac{B_{\parallel}\mu_B}{\hbar}\right)^2$ for the π-transitions, in solid red, and $\left(\frac{B_{\perp}\mu_B}{\hbar}\right)^2$ for the σ-transitions, in dashed green.

For a physical light source, the transition rate becomes:

$$\Gamma_{if} = \int d\omega g(\omega - \omega_{if})\frac{\pi I(\omega)}{2c\epsilon_0\hbar^2}|\langle f|e\vec{r}\cdot\vec{e}_\lambda|i\rangle|^2 \tag{1.26}$$

where $I(\omega) = \epsilon_0 c E_0^2(\omega)$ is the light intensity spectrum. Here we have to consider the fact that the light is a travelling wave and the atoms are moving, therefore, the Doppler effect. Indeed, in the laboratory frame of reference, the Bohr frequency of an atom is shifted by $\Delta\nu = -\nu\frac{v_z}{c}$, where v_z is the relative speed with respect to the light source. The frequency distribution of the atomic transition becomes:

$$g'(\nu) = g(\nu - \Delta\nu). \tag{1.27}$$

Since the atoms are in thermal vapour phase, their speeds follow the Maxwell-Boltzmann distribution. The probability for an atom to have a speed $\vec{v}$ is [46]:

$$P(\vec{v})d\vec{v} = (\frac{m}{2\pi k_B T})^{\frac{3}{2}}Exp(-\frac{m\vec{v}^2}{2k_B T})d\vec{v} \tag{1.28}$$

by integrating over $dv_x dv_y$ we find the probability for an atom to have a speed v_z(it is the only relevant speed for the Doppler shift):

$$P(v_z)dv_z = (\frac{m}{2\pi k_B T})^{\frac{1}{2}} Exp(-\frac{mv_z^2}{2k_B T})dv_z \tag{1.29}$$

It is a normalized distribution with a FWHM of $2\sqrt{2\ln 2}\sqrt{\frac{k_B T}{m}}$. Integrating the product of equation (1.27) and (1.29), we obtain the average lineshape for the whole atomic population

$$\tilde{g}(\nu) = \int g(\nu - \Delta\nu)P(v_z)dv_z. \tag{1.30}$$

Which is in fact the convolution between the two distributions. For a lorentzian absorption profile and a gaussian distribution of speeds, the result is called a Voigt distribution: $Voigt[\sigma_L, \sigma_G](\nu)$. (It is not an analytical function but a precise expression can be found in [47]). σ_L is the half width at half maximum (HWHM) of the Lorentzian lineshape and $\sigma_G = \frac{c}{\nu}\sqrt{\frac{k_B T}{m_{Rb}}}$ the standard deviation of the Gaussian distribution. It is normalized due to the properties of the convolution, and its FWHM is well approximated with an accuracy of 0.02% by [48]:

$$FWHM_{Voigt} \approx 0.5346\gamma_L + \sqrt{0.2166\gamma_L^2 + \gamma_G^2} \tag{1.31}$$

where $\gamma_L = 2\sigma_L$ and $\gamma_G = 2\sqrt{2\ln 2}\,\sigma_G$ are the FWHM of the Lorentzian and Gaussian distributions.

In the case of a distributed feedback (DFB) laser source, the absorption lineshape is much broader ($\Delta\nu_{\text{Doppler}} \approx 500$ MHz, $\Delta\nu_{\text{BG}} > 500$ MHz[1]) than the emission spectrum of the laser itself (typically $\Delta\nu_L \approx 5$ MHz). For simplicity, we consider the laser as monochromatic, i.e., $I(\omega) = I_0\delta(\omega - \omega_L)$, and the pumping rate becomes[2]:

$$\Gamma_{if} = \pi\tilde{g}(\omega_L - \omega_{if})\frac{I_0}{2c\epsilon_0\hbar^2}|\langle f|\,e\vec{r}\cdot\vec{e}_\lambda\,|i\rangle|^2 \tag{1.32}$$

The pumping rate is the probability for a irradiated atom to leave its initial state $|F, m_F\rangle$ to any reachable excited state $|F_e, m_{F_e}\rangle$; it is naturally the sum of all the non zero transition probabilities. For the low C-field considered, the Zeeman splitting is not resolved by simple laser spectroscopy, and we treat the substates, $|F_e, m_{F_e}\rangle$, of the hyperfines states, $|F_e\rangle$, as degenerated.

---

[1] see section 1.5.1

[2] This would not be possible for a vertical-cavity surface-emitting lasers (VCSEL) which has typically $\Delta\nu_L < 100$ MHz. Taking the laser linewidth into account would induce an additional broadening through the convolution process.

We thus define

$$|F_e\rangle = \sum_{m_{F_e}} |F_e, m_{F_e}\rangle \tag{1.33}$$

$$|\mu\rangle = |F_g = 1, \mu\rangle \tag{1.34}$$

$$|\mu'\rangle = |F_g = 2, \mu'\rangle . \tag{1.35}$$

A schematic representation of these states and the corresponding pumping rates are shown on Figure 1.8). These definitions have the advantage to simplify the expression of an averaged pumping rate $\Gamma_{\mu F_e}$ for every Zeeman sub state of a given hyperfine state of the ground state[1]. Using equations (1.32) and (1.33)-(1.35)we get:

$$\Gamma_{F_e} = \pi \tilde{g}(\omega_L - \omega_{\mu F_e}) \frac{I_0}{2c\epsilon_0 \hbar^2} \frac{1}{\mathscr{G}_{F=1}} \sum_{\mu} \sum_{m_{F_e}} |\langle F_e, m_{F_e}| e\vec{r} \cdot \vec{e}_\lambda |\mu\rangle|^2 \tag{1.36}$$

$$\Gamma'_{F_e} = \pi \tilde{g}(\omega_L - \omega_{\mu' F_e}) \frac{I_0}{2c\epsilon_0 \hbar^2} \frac{1}{\mathscr{G}_{F=2}} \sum_{\mu'} \sum_{m_{F_e}} |\langle F_e, m_{F_e}| e\vec{r} \cdot \vec{e}_\lambda |\mu'\rangle|^2 \tag{1.37}$$

The optical frequencies of the hyperfine transitions, $\omega_{\mu F_e}$ and $\omega_{\mu' F_e}$ are given in Table 1.2, and the dipole matrix elements, $|\langle F_e, m_{F_e}| e\vec{r} \cdot \vec{e}_\lambda |F = i, m_F\rangle|^2$ in Appendix D. Using these coefficients, and for a light σ-polarized[2], the average pumping rates become:

$$\Gamma_{F_e} = \pi g(\omega_L - \omega_{\mu F_e}) \frac{I_0}{2c\epsilon_0 \hbar^2} S_{F=1, F_e} \frac{2}{3} |\langle J_e| |e\boldsymbol{r}| |J\rangle|^2 \tag{1.38}$$

$$\Gamma'_{F_e} = \pi g(\omega_L - \omega_{\mu' F_e}) \frac{I_0}{2c\epsilon_0 \hbar^2} S_{F=2, F_e} \frac{2}{3} |\langle J_e| |e\boldsymbol{r}| |J\rangle|^2 \tag{1.39}$$

$$\tag{1.40}$$

where $|\langle J_e| |e\boldsymbol{r}| |J\rangle|^2$ is the reduced dipole matrix element and $S_{F F_e}$ the relative hyperfine transition strength factors (given in Table 1.2) [13].

---

[1]we made the approximation that for a given hyperfine substate, $\omega_{\mu m} = \omega_{\nu m}$ for all μ and ν.

[2]i.e. the light propagates parallel to the quantization axis with an arbitrary polarization.

In turn, the reduced dipole matrix element can be expressed as a function of the intrinsic excited atom lifetime τ:

$$\frac{1}{\tau} = \frac{\omega_0^3}{3\pi\epsilon_0\hbar c^3} \frac{2J+1}{2J_e+1} |\langle J_e||e\boldsymbol{r}||J\rangle|^2 = \begin{cases} 26.2348(77)\text{ns} & \text{for the D2 line [13]} \\ 27.679(27)\text{ns} & \text{for the D1 line [13].} \end{cases} \tag{1.41}$$

It results for the pumping rates Γ_{F_e} (for $\Gamma'_{F_e}, F = 2$):

$$\Gamma_{F_e} = S_{F=1,F_e} \frac{I_0}{\hbar\omega_0} \pi\tilde{g}(\omega_L - \omega_{\mu F_e}) \frac{2J_e+1}{2J+1} \frac{\pi c^2}{\omega_0^2\tau} \tag{1.42}$$

$$= S_{F=1,F_e} \mathscr{I}_0 2\pi\tilde{g}(\omega_L - \omega_{\mu F_e}) \frac{2J_e+1}{2J+1} \frac{\sigma_0}{12\tau} \tag{1.43}$$

$$= \mathscr{I}_0 \sigma_{F=1,F_e}(\omega_L - \omega_{\mu F_e}) \tag{1.44}$$

In which $\mathscr{I}_0$ is the photon flux, $\sigma_0 = \frac{6\pi c^2}{\omega_0^2}$, and

$$\sigma_{F=1,F_e}(\omega - \omega_{\mu F_e}) = S_{F=1,F_e} \frac{2J_e+1}{2J+1} 2\pi g(\omega - \omega_{\mu F_e}) \frac{\sigma_0}{12\tau}, \tag{1.45}$$

the absorption cross section[1]. Note that σ_0 depends on the average optical frequency of the line, ω_0. For the D1 line it is $\sigma_0 \approx 2.91 \times 10^{-13}$ m^2, and $\sigma_0 \approx 3.02 \times 10^{-13}$ m^2 for the D2 line.

1.5 Optical absorption spectrum

According to Beer's law, the variation of intensity of a light beam travelling through an absorptive medium of length z is:

$$\frac{dI(\omega, z)}{dz} = -\alpha(\omega, z)zI(\omega, z). \tag{1.46}$$

In the case the light intensity is low enough so that the optical pumping is negligible, the absorption coefficient doesn't vary with the intensity. Therefore, $\alpha(\omega, z) = \alpha(\omega)$ and the solution of equation (1.46) becomes:

$$I(\omega, z) = I(\omega, z_0)(1 - e^{-\alpha(\omega)}) \tag{1.47}$$

---

[1]Γ'_{F_e} differs from Γ_{F_e} only by the Bohr frequencies $\omega_{\mu F_e}$, and the hyperfine transition strength factors S_{FF_e}
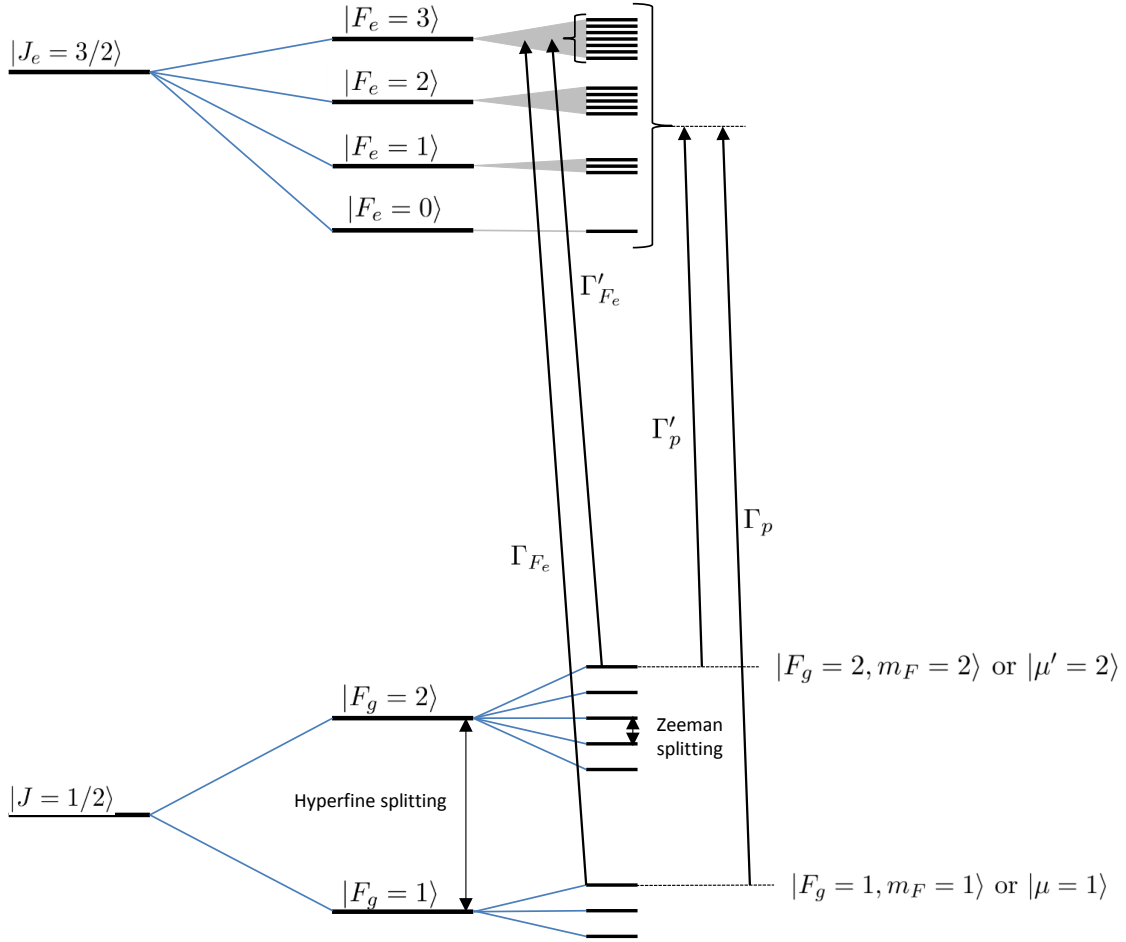
FIGURE 1.8: Schematic representation of the different pumping rates in the D2 line of the ^{87}Rb. the ' denotes rates for the upper ground states.

For a vapour of ^{87}Rb at thermal equilibrium, using equation (1.45), the absorption coefficient, α is given by:

$$\alpha(\omega) = n_{Rb}(T) \sum_{F} \sum_{F_e} \frac{\mathscr{G}_F}{\mathscr{G}_J} \sigma_{FF_e}(\omega - \omega_{\mu F_e}) \tag{1.48}$$

where $\mathscr{G}_J$ and $\mathscr{G}_F$ are the degeneracy of the fine ground state level $|J\rangle$ and the hyperfine state level $|F\rangle$, respectively, and $n_{Rb}(T)$ is the rubidium vapour density that is given in m^{-3} by [49]:

$$n_{Rb}(T) = \begin{cases} \dfrac{10^{(9.863-4215/T)}}{k_B T} & \text{for} \quad T < 312.5\mathrm{K} \\ \dfrac{10^{(9.318-4040/T)}}{k_B T} & \text{for} \quad T \geq 312.5\mathrm{K}. \end{cases} \tag{1.49}$$

Figure 1.9 shows the spectrum of the absorption coefficient at room temperature. The overlap is due to the small hyperfine splitting compared to the Doppler broadening.
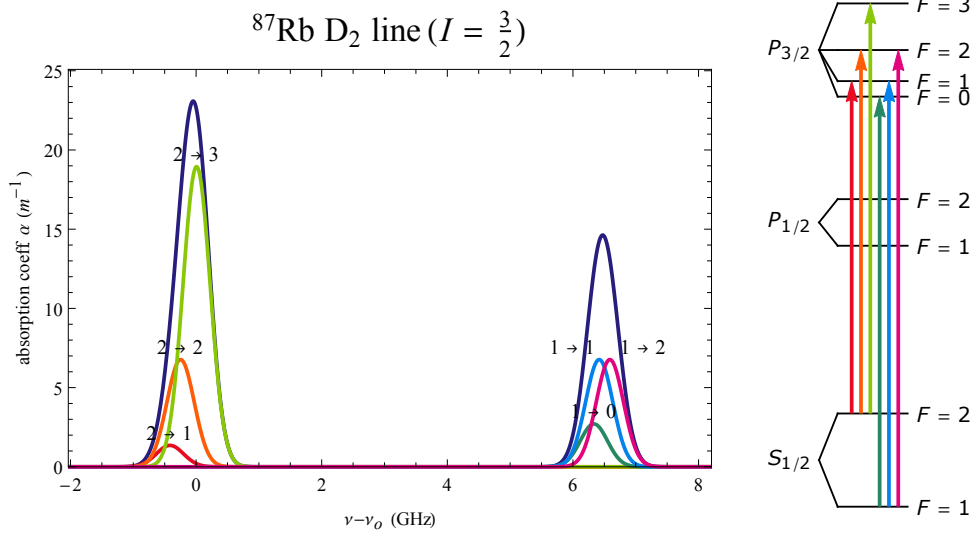
FIGURE 1.9: Absorption spectrum of the ^{87}Rb in the D2 line with hyperfine transitions identifications. From [50]

1.5.1 Buffer gas shift and broadening of optical transitions

In equation (1.7) $g(\omega)$ was defined as a normalized lineshape; it is related to the finite lifetime of the atomic state as follow:

$$FWHM_{g(\omega)} = \Gamma^* = 2\pi\gamma = \frac{1}{\tau} \tag{1.50}$$

TABLE 1.2: Frequency offsets (upper lines) from 384 228 115.20 MHz in MHz, and relative hyperfine transition strength factors, S_{FF_e} (lower lines) in the D2 line.

^{87}**Rb**	F=1	F=2
F'=3	-	0 14/20
F'=2	6568.03 5/12	-266.65 5/20
F'=1	6411.08 5/12	-423.6 1/20
F'=0	6338.86 2/12	-

^{85}**Rb**	F=2	F=3
F'=4	-	1126.49 81/126
F'=3	4041.58 28/90	1005.85 35/126
F'=2	3978.18 35/90	942.45 10/126
F'=1	3948.81 27/90	-

This finite lifetime of the atom in the excited state is due to the random vacuum fluctuations of the electromagnetic field [51]. In addition, confined rubidium atoms within a cell filled with buffer gases undergo many collisions with the buffer gas atoms; The collisions with the cell walls are not relevant here since the average time between two collisions, typically few microseconds, is much bigger than the intrinsic excited lifetime of ∼30 ns. These collisions strongly perturb the excited states. It results in an increase of the de-excitation rate, inducing a broadening of the lineshape, as well as a shift of the Bohr frequencies. This phenomenon has been extensively studied by several authors [47], [52]–[60] who showed that the induced shifts and broadening factors are linear along with the pressure and depend on the gas type. The relevant coefficients are listed in Table 1.3.

The equivalent broadening cross section is given by:

$$\sigma_{BG} = \frac{\gamma_{BG}}{n_{BG}\bar{v}_{rel}} \tag{1.51}$$

where γ_{BG} is the pressure broadening, n_{BG}, the density of the buffer gas, and $\bar{v}_{rel}$ the average relative speed between a rubidium atom and a buffer gas atom:

$$\bar{v}_{rel} = \sqrt{\frac{8k_BT}{\pi\mu}} \tag{1.52}$$

with k_B the Boltzmann constant, and μ the reduced mass of Rb and the buffer gas, atom or molecule considered. A comparison with other cross sections, such as quenching and kinetic gas

TABLE 1.3: Pressure Broadening and shift coefficients (γ and δ) for the optical D2 line of rubidium induced by collisions with Nitrogen and Argon buffer gases.

Author	N_2 shift [MHz/mbar]	N_2 Broad. [MHz/mbar]	Ar Shift [MHz/mbar]	Ar Broad. [MHz/mbar]
C. Ottinger et al. [52]			-6.09	13.91
S. L. Izotova et al. [53]–[55]			-4.27	13.5
P. Y. Kantor et al. [56]	-6.15	14.21	-5.34	14.89
M. Têtu et al. [57]	-4.64	18.8		
G. Mileti [47]	-3.55	22.2		
M. D. Rotondaro et al. [58], [59]	-4.34	13.7	-4.32	13.3
M. V. Romalis et al. [60]	-4.51	13.8		
Average value ± std. deviation	**-4.64±0.95**	**16.55±3.8**	**-5.01±0.87**	**13.9±0.7**

TABLE 1.4: Cross sections and corresponding rates of different relaxation mechanism between the $5^2P_{3/2}$ and $5^2S_{1/2}$ states ($\sigma_0 = \pi(R_{Rb} + R_{N_2})^2$ with $R_{Rb} = 4$Å and $R_{N_2} = 3.7$Å[58]).

process	cross section [m^2]		Broad. factor [MHz/mbar]	
N_2-Rb quenching [37]	σ_q	4.3×10^{-19}	$\tilde{\gamma}_q$	0.91
Ar-Rb gas kinetic collision [58]	$\sigma_{0_{Ar}}$	1.72×10^{-18}	$\tilde{\gamma}_{0_{Ar}}$	3.20
N_2-Rb gas kinetic collision [58]	$\sigma_{0_{N_2}}$	1.86×10^{-18}	$\tilde{\gamma}_{0_{N_2}}$	3.93
Ar-Rb Pressure broadening	$\sigma_{BG_{Ar}}$	7.48×10^{-18}	$\tilde{\gamma}_{BG_{Ar}}$	13.9
N_2-Rb Pressure broadening	$\sigma_{BG_{N_2}}$	7.84×10^{-18}	$\tilde{\gamma}_{BG_{N_2}}$	16.55

collisions is given in Table 1.4.

1.5.2 Generalized optical absorption spectrum and optical pumping rates

The theoretical absorption spectra of a rubidium vapour with and without buffer gases are plotted using equation (1.48) and the Voigt profile $Voigt[\sigma_L, \sigma_G](\nu)$ as the absorption lineshape. Considering a cell with a 4 mm long vapour volume, at 80°C, and filled with:

- rubidium: 91% of ^{87}Rb and 9% of ^{85}Rb
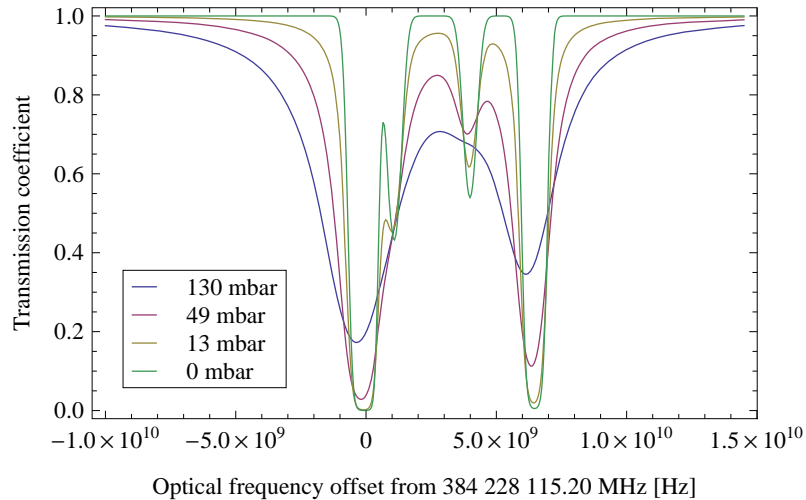
FIGURE 1.10: Transmission spectra computed for identical conditions except the buffer gas pressure.

- Nitrogen-Argon buffer gas mixture: 42% N_2 and 58% Ar (the broadening and shift coefficients for a mixture are the weighted sum of the corresponding average coefficients given in Table 1.3; in the present case, $\tilde{\gamma}_{BG} = 15.44 \frac{\text{MHz}}{\text{mbar}}$ and $\tilde{\delta}_{BG} = 4.8 \frac{\text{MHz}}{\text{mbar}}$)

the transmission lineshapes of Figure 1.10 are obtained. A clear reduction of the absorption coefficient of the cell along with the increase of BG pressure is observed: without buffer gas, the cell is opaque at 80°C while the same cell filled with 130 mbar of buffer gas in identical conditions shows a transmission of ~20%. In addition to the increase of the cell transmission, the broadening allows the overlap of two lines of the ^{87}Rb and ^{85}Rb spectra, which is at the origin of the lamp pumped rubidium clocks.

1.5.2.1 Average optical pumping rates

Figure 1.11 shows the pumping rates spectra. In a similar way to the absorption coefficient, the increase of the BG pressure reduces the pumping efficiency, and the hyperfine structure is completely hidden by the broadening mechanisms.

Since the hyperfine splitting is not resolved, Vanier [37] and also Mileti [47], deduce average pumping rates, Γ_p and Γ'_p, assuming that all the optical transitions share the same average
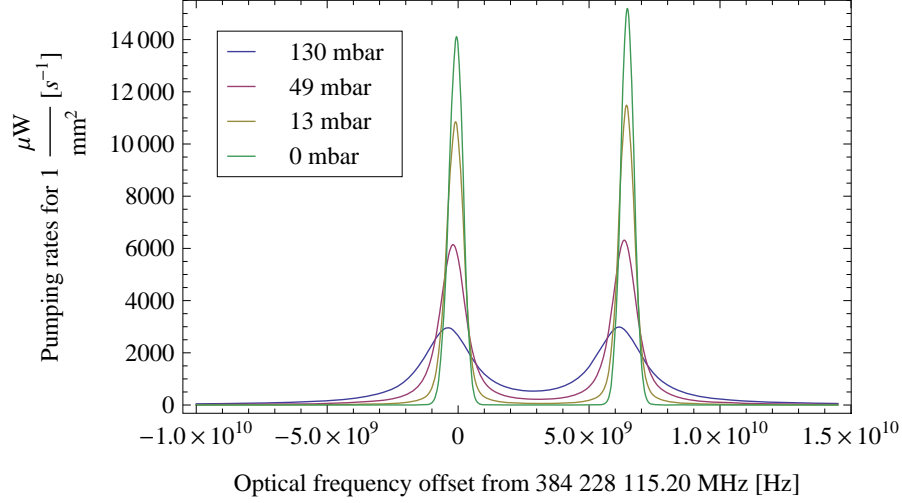
FIGURE 1.11: Pumping rate spectra computed for different buffer gas pressure.

frequency $\omega_{\mu J'}$. These pumping rates couple every single state $|\mu\rangle$ or $|\mu'\rangle$, to all the excited sub states $|F_e\rangle$ of the $|J_e\rangle$ state (see Figure 1.8). They are expressed as follow:

$$\Gamma_p(\omega_L) = \sum_{F_e} \Gamma_{F_e}(\omega_L) \tag{1.53}$$

$$= \mathscr{I}_0 \frac{2J_e + 1}{2J + 1} \frac{\sigma_0}{12\tau} 2\pi \tilde{g}(\omega_L - \omega_{\mu J_e}) \tag{1.54}$$

For practical purposes we consider a pure lorentzian lineshape [34],

$$\Gamma_p(\omega_L) = \left(\frac{\Omega_L}{2}\right)^2 \frac{\Gamma^*}{(\omega_L - \omega_{\mu J_e})^2 + (\Gamma^*/2)^2} \tag{1.55}$$

$$= \frac{(\Omega_L)^2}{\Gamma^*} \text{ at resonance,} \tag{1.56}$$

where Γ^* is the excited state decay rate; typically this rate is, $\Gamma^* \approx 2 \times 10^9$ s^{-1} for the pressures considered in this manuscript.

Finally, using equation (1.7) and (1.54), a simple expression for the Rabi frequencies in the D2 line is obtained:

$$\Omega_L = \Omega_L' = \sqrt{\mathscr{I}_0}\sqrt{\frac{2\sigma_0}{3\tau}} \tag{1.57}$$

$$= 2.72 \times 10^{-3}\sqrt{\mathscr{I}_0 \left[\frac{\text{Photons}}{\text{s m}^2}\right]} \tag{1.58}$$

$$= 5.39 \times 10^6\sqrt{I_0 \left[\frac{\mu\text{W}}{\text{mm}^2}\right]} \tag{1.59}$$

1.6   Optical-microwave double resonance spectrum

We have considered up to now the magnetic and the electric interactions separately. In an atomic clock, both interactions act simultaneously on a huge number of atoms. In addition to the quantum probabilities of each atom, one has to consider the statistical distribution of the atomic population among the quantum states. Therefore, we use the density matrix formalism for which the evolution of the whole system is governed by Liouville's equation:

$$\frac{d}{dt}\rho = \frac{1}{i\hbar}[\tilde{\boldsymbol{H}},\rho]. \tag{1.60}$$

ρ is the density operator in the interaction representation and $\tilde{\boldsymbol{H}}$ the total interaction Hamiltonian. This equation contains $n(n+1)/2$ coupled linear differential equations, where n is the number of states considered. Ideally, the system consists of a total of 24 states in the D2 line of ^{87}Rb (3+5 in the $5^2\text{S}_{1/2}$ and 7+5+3+1 in the $5^2\text{P}_{3/2}$), so potentially 300 coupled differential equations. Under proper hypothesis (see below), the number of states can be strongly reduced, and we follow here a simplified three level approximation based on Vanier's paper, "The passive optically pumped Rb frequency standard: the laser approach" [34]. It provides a good and qualitative understanding of the various phenomena observed. The extension to a nine-levels analysis, taking into account the multiplicity of each ground state level, is developed and discussed in [37], [61], and [47]. It mainly results in an alteration of the pumping rates and a reduction of the resonant atomic population. Figure 1.12 shows a schematic representation of these models.

Hyp. 1 The clock cell is filled with Nitrogen. The purpose of Nitrogen is to strongly reduce
the lifetime of the excited states $|F_e\rangle$, and to quench the spontaneous emission of light
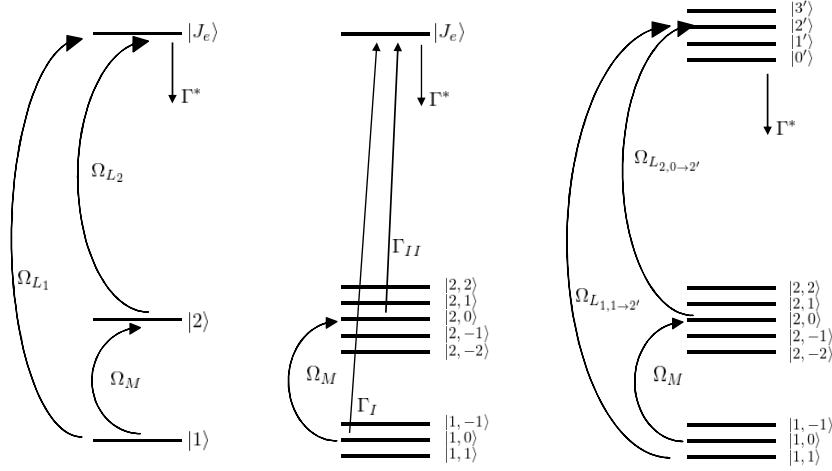
FIGURE 1.12: DR models; left, Vanier's [34] 3-level approach; centre, Mileti's [47] and Vanier's [37] 9-level approach; right, ideal approach. Straight arrows represent pumping rates, curved arrows, Rabi oscillations inducing coherences.

that is normally emitted by the excited Rb atoms decaying back to the ground states. The reduction of the excited lifetime results in an overlap of the optical resonances justifying the use of a single excited state $|J_e\rangle$ and the corresponding average pumping rate calculated in section 1.5.2.1).

Hyp. 2 The excited Rb atom de-excitation takes place only via collisions with Nitrogen. The selection rules of this relaxation process are not known and we assume they randomly fill the ground state levels with equal probability. We name this rate of de-excitation Γ^*. It is of the order of $2 - 5 \times 10^9$ s^{-1} for the pressure considered in this study.

Hyp. 3 The use of buffer gas significantly reduces the mean free path of the rubidium atoms so that the nature of motion is a diffusion. The atoms are restricted to a region much smaller than the wavelength of the microwave, and for our purposes appear motionless. Thus, the Doppler broadening almost completely disappears. This effect is named after Dicke who analysed it first [62].

Hyp. 4 The laser light is monochromatic and σ-polarized (see section 1.4.4). It couples only one of the two hyperfine level of the S state to the P state. The light intensity is uniform across the beam.

31

Hyp. 5 Within the ground state, different mechanisms such as wall collisions, buffer gas collisions, and Rb-Rb collisions among others tend to equilibrate the populations of all the different ground state levels. We treat them in a phenomenological way and characterize them by two relaxation rates, Γ_1 and Γ_2 for the populations and the magnetic coherences, respectively.

With these hypothesis and the Vanier's model, equation (1.60) takes the following form:

$$\frac{d\rho_{11}}{dt} = \frac{1}{i\hbar}[\boldsymbol{H}, \boldsymbol{\rho}]_{11} + \frac{\Gamma^*}{2}\rho_{J_e J_e} - \Gamma_1(\rho_{11} - 1/2) \tag{1.61}$$

$$\frac{d\rho_{22}}{dt} = \frac{1}{i\hbar}[\boldsymbol{H}, \boldsymbol{\rho}]_{22} + \frac{\Gamma^*}{2}\rho_{J_e J_e} - \Gamma_1(\rho_{22} - 1/2) \tag{1.62}$$

$$\frac{d\rho_{J_e J_e}}{dt} = \frac{1}{i\hbar}[\boldsymbol{H}, \boldsymbol{\rho}]_{J_e J_e} - \Gamma^*\rho_{J_e J_e} \tag{1.63}$$

$$\frac{d\rho_{12}}{dt} = \frac{1}{i\hbar}[\boldsymbol{H}, \boldsymbol{\rho}]_{12} - \Gamma_2\rho_{12} \tag{1.64}$$

$$\frac{d\rho_{1J_e}}{dt} = \frac{1}{i\hbar}[\boldsymbol{H}, \boldsymbol{\rho}]_{1J_e} - \frac{\Gamma^*}{2}\rho_{1J_e} \tag{1.65}$$

$$\frac{d\rho_{2J_e}}{dt} = \frac{1}{i\hbar}[\boldsymbol{H}, \boldsymbol{\rho}]_{2J_e} - \frac{\Gamma^*}{2}\rho_{2J_e} \tag{1.66}$$

where $\boldsymbol{H} = \boldsymbol{W}_L + \boldsymbol{W}_M$ is the interaction Hamiltonian of the optical and RF fields.

This system of equations is solved in details in [34], from which is extract the following solution for the state being depopulated at optical resonance:

$$\rho_{11} = \frac{1}{2}\frac{\Gamma_1}{\Gamma_1'} + \Gamma_{L_1}\frac{S}{4}\frac{(\Gamma_2')^2}{\Gamma_1'}\frac{1}{(\omega_M - \omega_{12}')^2 + (\Gamma_2')^2(S+1)} \tag{1.67}$$

where

$$\Gamma_1' = \Gamma_1 + \frac{\Gamma_{L_1}}{2} \tag{1.68}$$

$$\Gamma_2' = \Gamma_2 + \frac{\Gamma_{L_1}}{2} \tag{1.69}$$

$$\omega_{12}' = \omega_{12} - \Delta\omega \tag{1.70}$$

$$S = \frac{\Omega_M^2}{\Gamma_1'\Gamma_2'} \tag{1.71}$$

Γ_{L_1} is the optical pumping rate given by equation (1.56), Ω_M the clock transition's Rabi frequency (see equation (1.23)), ω_M the microwave frequency and $\Delta\omega$ an additional frequency shift to the unperturbed Bohr frequency ω_{12} (see section 1.7.2). S is called the saturation factor.

These equations are valid locally. Therefore, the total absorption of the vapour for a resonant light field, is given by equation (1.48):

$$\frac{dI(z)}{dz} = -\alpha(z)\rho_{11}(z)I(z) \tag{1.72}$$

This is a non linear equation, and has to be solved numerically; This point is discussed in [34]. For the present manuscript, we assume the intensity to be much lower than the saturation intensity of the rubidium ($I_{sat} \approx 17\mu W/mm^2$ [13]), and ρ_{11} and α constant along the beam. The following expression for the transmitted intensity is then obtained:

$$I_{out} = I_0 e^{-\alpha\rho_{11}\Delta z} \approx I_0(1 - \alpha\rho_{11}\Delta z) \tag{1.73}$$

$$\approx I_0\left(1 - \alpha\Delta z\left(\frac{1}{2} - \frac{\Gamma_{L_1}}{4\Gamma_1} + \frac{S}{4}\frac{\Gamma_{L_1}}{\Gamma_1'}\frac{(\Gamma_2')^2}{(\omega_M - \omega_{12}')^2 + (\Gamma_2')^2(S+1)}\right)\right). \tag{1.74}$$

The second term describes the absorption of the vapour as a function of the optical and magnetic fields; it is the DR signal. Its first term represents the absorbed light by the atomic population at rest. The second term, the *optical depumping*, is a correction term and describes the effect of optical pumping: for significant optical pumping rates Γ_{L_1} with respect to the longitudinal relaxation rate Γ_1, the state being pumped out is depopulated and the transmission increases. The last term, the *magnetic repumping* can be seen as a correction term of the optical depumping: the magnetic interaction repopulates the state being emptied, and the transmission decreases. The DR signal has a lorentzian lineshape characterized by four quantities: amplitude (A), background level (Bck), central frequency ($\nu_{clock} = \frac{\omega_{12}'}{2\pi}$) and linewidth, or full width at half maximum ($FWHM$). The linewidth is expressed as:

$$FWHM_\omega = 2\Gamma_2'\sqrt{S+1} \ [\text{rad/s}] \tag{1.75}$$

$$\text{or } FWHM_\nu = \frac{\Gamma_2'}{\pi}\sqrt{S+1} \ [\text{Hz}]. \tag{1.76}$$

Using equations (1.68), (1.69) and (1.71) we obtain:

$$FWHM_\nu = \frac{\left(\Gamma_2 + \frac{\Gamma_L}{2}\right)}{\pi}\sqrt{\frac{\Omega_M^2}{(\Gamma_2 + \frac{\Gamma_L}{2})(\Gamma_1 + \frac{\Gamma_L}{2})} + 1}\,. \qquad (1.77)$$

For a small microwave Rabi frequency compared to the population and coherence relaxations rates and the optical pumping rate, equation (1.77) can be approximated by:

$$FWHM_\nu \approx \frac{\Gamma_2}{\pi} + \frac{\Gamma_L}{2\pi} = \frac{\Gamma_2}{\pi} + \frac{2.9 \times 10^{13}}{\Gamma^*}I\left[\frac{\mu W}{mm^2}\right], \qquad (1.78)$$

which shows a linear behaviour as a function of the optical pumping rate, Γ_L. Equations (1.56) and (1.59) have been used for the right hand side of the equality. The first term represents the intrinsic linewidth of the DR signal,

$$FWHM_{\nu_{Intr}} = \frac{\Gamma_2}{\pi} \qquad (1.79)$$

and shows the equivalence between the intrinsic linewidth and the coherence relaxation rate within a factor of π. The second term shows the optical pumping as a complementary loss process for the coherence, as it induces additional broadening to the DR signal. It is proportional to the light intensity.

The Amplitude of the DR signal is given by

$$A = I_0 \frac{\Gamma_{L_1}}{4(\Gamma_1 + \frac{\Gamma_{L_1}}{2})}\frac{\Omega_M^2}{\Omega_M^2 + (\Gamma_2 + \frac{\Gamma_L}{2})(\Gamma_1 + \frac{\Gamma_L}{2})} \qquad (1.80)$$

and its background level,

$$Bck = I_0\left(\frac{\Gamma_{L_1}}{4\Gamma_1} - \frac{1}{2}\right). \qquad (1.81)$$

When it comes to atomic clock evaluation, the Figure-of-Merit (FoM) is the parameter to optimize (see section 1.7). It is defined as:

$$FoM = \frac{C}{FWHM_\nu} \qquad (1.82)$$

where C is the contrast of the DR signal given by the ratio between the amplitude and the background level: $C = A/Bck$.

Figure 1.13 shows the evolution of the DR signal parameters along with the laser intensity for various microwave power. Although only three levels are considered, and the non linearity of equation (1.72) is not considered, the predictions of this model are valid qualitatively. Indeed, in his comparison between the 3-levels and 9-levels models, Mileti [47] demonstrated typical corrections factors of the order 5/8 for the amplitude and the background level. The central frequency and the intrinsic linewidth are not affected by the multiplicity of the ground state levels.

The signal amplitude shows a peaking as a function of the light intensity. This peaking is accentuated for the contrast and the FoM by the linewidth and background increases. The light intensities required are typically one order of magnitude smaller than the saturation intensity of the rubidium which complies with the hypothesis made for the linearisation of equation (1.72).

The graphic of the linewidth shows the limits of validity of the linear approximation made for the equation (1.78) at low intensities dominated by the RF power broadening (see equation (1.77)). Nevertheless, a linear behaviour is still observed at higher intensities, and a linear extrapolation of this portion to zero light intensity provides overestimated values of the coherence relaxation rate, Γ_2. This overestimation becomes smaller as the RF power is reduced.

As opposed to the contrast which shows a peaking along with the light intensity only, the FoM shows a peaking as a function of the RF power too. This implies to optimize the light intensity and the RF power simultaneously, since optimizing only one parameter at a time doesn't guarantee the determination of the global optimal condition.

Note for the evacuated and wall coated cells: The hypothesises 1-3 are not valid in the case of a pure vapour of rubidium which is typically encountered in wall coated or evacuated cells: the atoms are moving freely from wall to wall at an average speed of 300 m/s, and the quenching cannot occur. No particular theoretical treatment exist for this situation, so we extend phenomenologically the Lorentzian lineshape and the trends of its parameters (Amplitude, Linewidth, FoM) to the evacuated and wall coated cells. We limit this extension for a standing microwave wave, and a cell smaller than $\lambda_{RF}/2 \sim 2$ cm to ensure a proper Dicke narrowing [62]. Otherwise, the Doppler effect comes into picture and creates a typical pedestal below the lorentzian lineshape as observed in [63].
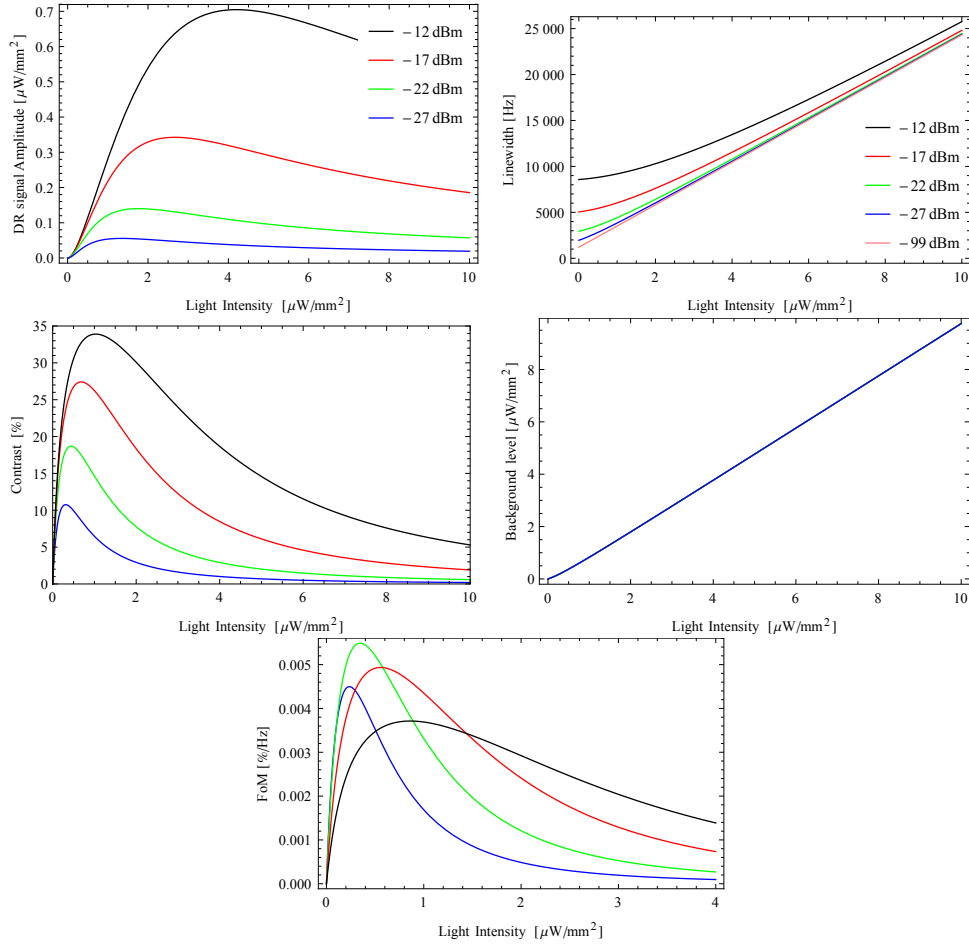
FIGURE 1.13: Three-level model's qualitative predictions of the various measurable parameters. Top left: amplitude; top right: linewidth; middle left: contrast; middle right: background level; bottom: figure-of-merit. The population and coherence relaxation rates are $\Gamma_1 = \Gamma_2 = \pi \times 1200\text{s}^{-1}$.

1.6.1 Relaxation mechanisms: homogeneous line broadening

In the fifth hypothesis of section 1.6, we have introduced phenomenologically the population and coherence relaxation rates, Γ_1 and Γ_2. These rates have well defined physical origins and are consequences of various collision types the rubidium atoms undergo. The type depends on the confinement method. From equations (1.61),(1.62) or (1.64), the relaxation rates are additive quantities. Therefore, the equivalent rate of two independent relaxation processes is the sum of the individual broadenings.

At first, we present the spin exchange (SE) broadening present in all practical cases. The discussion is then extended to the confinement of the atoms inside an evacuated cell with non negligible wall depolarization probability. It is followed by the buffer gas case, in which the cell containing the Rb vapour is additionally filled with buffer gases (this is the only case satisfying the hypothesises 1-3 of section 1.6). Finally the case of a cell having walls coated with antirelaxation material is treated.

1.6.1.1 Spin exchange broadening

Due to the thermal nature of the vapour, the rubidium atoms collide with each other. During such a collision the atoms can exchange their spin states [37]. This process is called spin-exchange (SE) and in the case of the 0-0 transition, this exchange is equivalent to an electron-randomizing collision [64]. Therefore the relaxation rates are similar to the collisional rate obtained from the gas theory. The population and coherence SE relaxation rates, $\Gamma_{i_{SE}}$ are expressed as follow [65]:

$$\Gamma_{1_{se}} = n\overline{v}_{rel}\sigma_{se} \tag{1.83}$$

$$\Gamma_{2_{se}} = \frac{6I+1}{8I+4}\Gamma_{1_{se}} = \frac{5}{8}\Gamma_{1_{se}} \tag{1.84}$$

where n is the density of the rubidium vapour, $I = 3/2$ the nuclear spin for the ^{87}Rb, $\sigma_{se} = 1.6 \times 10^{-18}$ m^2 [66], the ^{87}Rb-^{87}Rb spin exchange cross section, and $\overline{v}_{rel} = \sqrt{16k_BT/(\pi M)}$ the relative mean velocity between the colliding rubidium atoms of mass M. As a comparison, the elastic collisional cross section is one order of magnitude bigger: 13.97×10^{-18} m^2 [37]. It was observed that σ_{se} does not vary much with the temperature [37], and we consider it constant. Nevertheless, due to their atomic density dependency, the relaxation rates become significant as the temperature is raised. At temperatures of 50, 70 and 90°C the contributions to the linewidth of the clock signal ($FWHM_\nu = \Gamma_{2_{se}}/\pi$) are calculated to be 18 Hz, 95 Hz and 412 Hz, respectively.

1.6.1.2 Bare wall broadening

Collisions of the rubidium atoms with the bare walls of the container, typically made of glass or quartz, have a significant probability, ϵ [67], to fully randomize the polarization of the ground

state of atom. The associated relaxation rate is defined as the bare wall relaxation rate, $\Gamma_{i_{bw}}$. From the kinetic gas theory, the mean free path inside a pure rubidium vapour is of the order of few cm at the temperatures considered[1]. The rubidium atoms move therefore freely from wall to wall inside a cell of size below the centimetre. And the rate of collisions with the walls of the cell, Γ_w, is given by the inverse of the average wall-to-wall time of flight, $\overline{\tau}_w$ [37]:

$$\Gamma_w = \frac{1}{\overline{\tau}_w} \tag{1.85}$$

where, for a cylindrical cell,

$$\overline{\tau}_w = \frac{4V}{vA} \tag{1.86}$$

A denotes the inner surface of the container, and V its volume. The atom's mean velocity $\overline{v}$ is given by the Maxwell-Boltzmann distribution:

$$\overline{v} = \sqrt{\frac{8k_BT}{\pi M}} \tag{1.87}$$

and is of the order of $\overline{v} = \sim 290$ m/s for the range of temperature considered (60-90°C).

Taking into account the probability of depolarization per collisions, the coherence and population relaxation rates are finally expressed:

$$\Gamma_{1_{bw}} = \Gamma_{2_{bw}} = \Gamma_w = \frac{\epsilon}{\overline{\tau}_w}. \tag{1.88}$$

ϵ was measured to be $\epsilon = 0.5$ for Na-glass and Cs-glass collisions [67], [68] and only $\epsilon = 0.05$ for Rb-silicon collisions [69]. No precise data exists for Rb-glass collisions and we will assume for this manuscript $0.5 \leq \epsilon \leq 1$. The corresponding broadenings are tens of kHz for sub-centimetric cells, and scale linearly with the characteristic length of the cell $l_{cell} = 4V/A$. Table 1.5 summarizes the calculated collision rates and their corresponding broadening for the four different cell geometries studied in this thesis (see Chapter 3). Compared to typical DR linewidths on the order of 100 Hz to few kHz, these broadenings are more than one order of magnitude bigger. Circumventing this issue requires to reduce either the collision rate, $\overline{\tau}_w$, by the use of a buffer gas, or the ϵ factor

---

[1]$\sim$3 cm at 80°C assuming a collisional cross section of 1397×10^{-20} m^2 [37]

by the use antirelaxation coatings. Consequences of these methods are discussed in the following sections.

TABLE 1.5: Atom wall collision rates and correspond relaxations rates for bare walls.

| Cell type | l_{cell} | Coll. rate | $\gamma_{i_{bw}}$ (FWHM$_\nu$) | |
| | | | $\epsilon = 1$ | $\epsilon = 0.5$ |
	[mm]	[kHz]	[kHz]	[kHz]
2D-In[a]	1.2	243	77	39
2D-AB[b]	2.2	130	41	21
3D[b]	2.7	108	34	17
14 mm[c]	8.0	35	11	6

[a]Indium bonding
[b]Anodic bonding
[c]Glass-blown

1.6.1.3 Buffer gas broadening

The use of buffer gases prevents the atoms to collide directly with the inner walls of the cell by strongly reducing their mean free path: from few cm in a pure Rb vapour down to few µm or even below in a BG at the pressures considered. On the one hand, these collisions prevent electron randomization collisions on the walls of the container through the diffusion motion, while on the other hand, they perturb the ground-state wave function of the valence electron of the alkali-metal atom [70]. This perturbation induces relaxations in the population difference and in the coherence of the ground state clock transition. The corresponding relaxation rates are given by [37], [47]:

$$\Gamma_{1_{BG}} = \kappa_{cell} D_0 \frac{P_0}{P} + \overline{v}_{rel} \sigma_{1_{BG}} \frac{n_0 P}{P_0} \tag{1.89}$$

$$\Gamma_{2_{BG}} = \kappa_{cell} D_0 \frac{P_0}{P} + \overline{v}_{rel} \sigma_{2_{BG}} \frac{n_0 P}{P_0}. \tag{1.90}$$

κ_{cell} is a geometrical factor depending on the shape of the cell, D_0 the diffusion constant of the ^{87}Rb atoms ($D_0 = 35 \times 10^{-6} \frac{\text{m}^2}{\text{s}}$) [1], P_0 the standard atmospheric pressure, P the pressure of the BG, n_0 the Loschmidt constant ($n_0 = 2.6867774 \times 10^{25} \text{m}^{-3}$), and $\sigma_{i_{BG}}$ the relaxation

---

[1]For simplicity we consider here an average diffusion constant for a mixture of Nitrogen and Argon at 60°C. The diffusion constants are both $16 \times 10^{-6} \frac{\text{m}^2}{\text{s}}$ for Argon and Nitrogen at 32°C, and scale with $T^{3/2}$ [37].

cross section (see Table 1.6). For a cylindrical cell, the geometrical factor is expressed as $\kappa_{cell} = \frac{1}{D^2}\left((4.81)^2 + \pi^2\frac{D^2}{L^2}\right)$, where D is the diameter of the cell, and L its length.

The first terms of equation (1.89) and (1.90) correspond to the relaxation rate due to the remaining collisions of the rubidium atoms with the cell walls; it scales down with the total buffer gas pressure. The second parts represent the effect of the Rb atoms' collisions with the BG atoms or molecules on the population and the coherence within the rubidium vapour; it scales up with the total buffer gas pressure. These opposed trends with respect to the pressure impose a non zero minimum for the relaxation rate. The optimal buffer gas pressure and the corresponding minimum relaxation rates depend on the cell geometry. Figure 1.14 shows the theoretical behaviour of the BG contribution to the DR signal linewidth as a function of the total pressure of the BG for the four different cell geometries used in this thesis (see Chapter 3). The predicted optimal pressures minimizing the linewidth for each cell geometry are presented in Table 1.7 along with their corresponding linewidths.
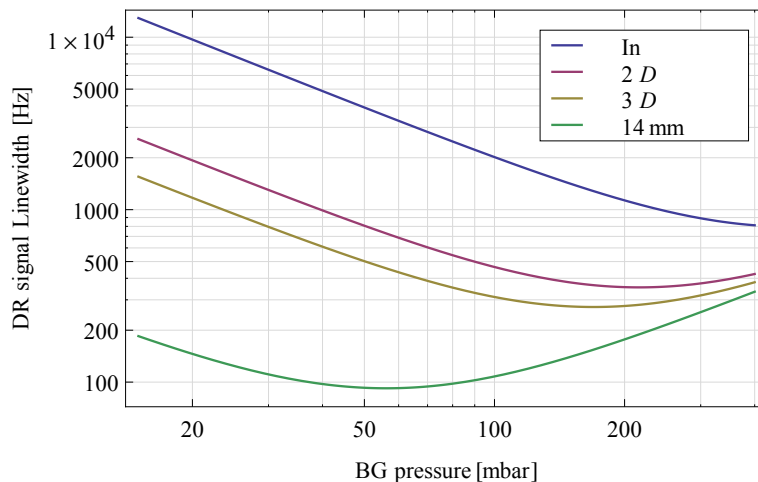
FIGURE 1.14: theoretical behaviour of the BG contribution to the DR signal linewidth as a function of the total BG pressure, for three typical cell geometries studied in this thesis. The mixture used is 58%Ar and 42%N$_2$. Diameter and length in mm of the cells are: In(5;0.78), 2D(5;2), 3D(4;4.05), 14 mm(12;12).

1.6.1.4 Broadening in wall coated cells

The use of a proper wall coating can significantly reduce the depolarization probability, ϵ_{coat}, or the longitudinal relaxation rate, of a rubidium atom during a *collision* with the wall of the

TABLE 1.6: Cross sections for the coherence and the populations relaxations, respectively σ_2 and σ_1, for ^{87}Rb in Argon and Nitrogen gases from [37], [71].

[m^2]	Argon	Nitrogen
σ_1	49×10^{-27}	8.0×10^{-27}
σ_2	37×10^{-27}	350×10^{-27}

TABLE 1.7: Optimal pressures and linewidths for buffer gas filled cylindrical cells.

Cell type	Diameter [mm]	Height [mm]	Optimized Presure [mbar]	Linewidth contribution [Hz]
2D-In	5	0.78	486	796
2D-AB	5	2	216	354
3D	4	4.05	168	275
14 mm	12	12	92	56

cell. Values down to 10^{-6} for an alkene [72], 10^{-4} [73] for a paraffin and 3×10^{-2} for a self-assembled-monolayer- (SAM) octadecyltrichlorosilane (OTS)[1] coating [75] have been reported so far.

The resulting coating electron randomization relaxation rate,

$$\Gamma_{er_{coat}} = \frac{\epsilon_{coat}}{\overline{\tau}_w}, \tag{1.91}$$

contributes to a linewidth well below 10 Hz, for alkene and alkane, and below 3 kHz for SAM-OTS in any of the cells considered in Table 1.5. As a comparison, in our experimental conditions, the spin exchange linewidth contribution is of the order of few hundreds Hz (see section 1.6.1.1).

Although the details of atom-coating interaction are not yet fully understood [76], the relevant features of a coated cell are well described by qualitative analysis given by Goldenberg [77], Bouchiat and Brossel [38], [73] and Vanier and Audoin [37]. All analysis are similar and based on the fact that the atom gets adsorbed momentarily (about 40 ns [77]) on the coated surface before being released back in the vapour.

---

[1] A value of 5×10^{-4} has been reported for a thick OTS film, but potassium instead of rubidium was used [74].

The average time the atom spends adsorbed on the coating surface, τ_{ad}, is related to the adsorption energy E_{ad} through the following relation [78]:

$$\tau_{ad} = \tau_0 e^{\frac{E_a}{k_B T}} \tag{1.92}$$

where τ_0 is the period of vibration of the adsorbed atom in the wall potential typically having a value $\sim 10^{-12}$ s, k_B the Boltzmann constant, and T the temperature of the coating. Typical values of adsorption energies for rubidium on paraffin are of the order of few tens meV (see Table 5.2).

During the adsorption process, the attractive van der Waals forces perturb the ground-state wave function of the valence electron inducing a negative phase shift to the atom [37]. The average phase shift per collision, $\overline{\Phi}_{coat}$, is expressed as follows:

$$\overline{\Phi}_{coat} = \delta\omega_{ad}\tau_{ad} \tag{1.93}$$

where $\delta\omega_{ad}$ is the difference between the resonant hyperfine frequency while the Rb is absorbed on the surface and that in free space [79]. For paraffin coatings, the average phase shifts are found to be negative and of the order of few tens of $\frac{\text{mrad}}{\text{coll}}$ [63], [78], [80], [81].

Due to the statistical nature of the adsorption, a dispersion of the average phase shifts among the atomic population is created, inducing a coherence loss. The induced broadening is called adiabatic broadening, and its equivalent relaxation rate is expressed as follow [78]:

$$\Gamma_{2_{ad}} = 2\frac{(\overline{\Phi}_{coat})^2}{\overline{\tau}_w}. \tag{1.94}$$

where $\overline{\tau}_w$ is the average atom wall-to-wall time-of-flight defined in section 1.6.1.2. Typical values for the adiabatic broadening are few tens of Hz (see Table 1.14).

In addition to the coating electron randomization relaxation rate, and the adiabatic relaxation rate, other processes contribute to the relaxation rate of the coherence of the atomic population. We identify and describe them here below:

- Polarized atoms can be absorbed into the coating for a sufficiently long time that all polarization is destroyed [78]. Since the vapour is saturated, the adsorbed atoms are replaced

by "new" random atom from the reservoir to balance the pressure of the vapour with the saturation pressure. This gives rise to the adsorption losses rate, $\Gamma_{loss_{ads}}$.

- The covering of the coating may not be 100%, resulting in bare glass surfaces. Collisions with such surfaces is equivalent to a loss process, although the atom is not replaced. We call this process the covering factor effect [82]. a_{cov} being the total uncovered surface, the covering factor rate is given by:

$$\Gamma_{cov} = \frac{\overline{v}a_{cov}}{4V} \tag{1.95}$$

- Polarized atoms can enter the reservoir of the cell. Similarly to the adsorption loss, they are replaced by "new" random atoms from the reservoir. This process is called reservoir or hole effect [83]. a_{hole} being the surface of the reservoir's hole, the hole effect rate is expressed as follow:

$$\Gamma_{hole} = \frac{\overline{v}a_{hole}}{4V} \tag{1.96}$$

- The collision with metallic rubidium droplet present in the interrogation chamber is similar to the hole effect since the metallic rubidium act as a reservoir. Using a_{met}, as the total metallic surface in the interrogation chamber, we obtain for the metallic droplet relaxation rate:

$$\Gamma_{met} = \frac{\overline{v}a_{met}}{4V} \tag{1.97}$$

V is the volume of the cell, and $\overline{v}$ is the average thermal speed of the rubidium atoms.

Although these processes have different physical origins, they are completely equivalent for the population and the coherence; from an experimental point of view and for a given cell, they are undistinguishable.

1.6.1.5 Broadening in wall coated cell with buffer gas

Mixing antirelaxing coating and buffer gases might appear as an interesting idea. A study by Masnou-Seeuws and Bouchiat [84] concluded a potential reduction of the population relaxation rate along with a moderate buffer gas pressure [37]. This effect was confirmed experimentally by Boulanger [85] and more recently by Knappe and Robinson [86]. Nevertheless, these two other studies focused as well on the coherence relaxation rate, responsible for the DR lineshape

broadening (see equation (1.78)). They measured an increase of the broadening even at moderate pressure, and attribute this effect to the existence of two classes of atoms accumulating different phase shifts [86]. At higher buffer gas pressure, the relaxations appears to be dominated by the collisions with the buffer gas, and no significant difference between coated and uncoated cell was observed. As a conclusion, the improvement of the coating with a buffer gas does not appear efficient. On the contrary this technique might be interesting for reducing the buffer gas pressure required in microfabricated cells, by reducing the contribution of the walls in the buffer gas model.

1.7 Atomic Clock frequency stability

An atomic frequency standard, or atomic clock is quantitatively characterized by its frequency (in)accuracy and (in)stability. The accuracy represents how close from an ideal frequency the produced frequency is, while the stability is the ability of the clock to produce the same frequency over a given time scale. Since it is not caesium based, a rubidium clock does not realize the SI-definition of the second, hence it is considered as a secondary frequency standard and requires a proper calibration against a primary frequency standard (e.g. caesium fountain). The clock accuracy becomes the accuracy of the calibration and is not considered in this study. The key parameter of a rubidium clock is therefore its stability. Since the clock output is the quartz frequency stabilized to the DR signal of the atomic resonator (see Figure 1.1), the frequency stability of the clock reflects that of the DR clock signal. Therefore, understanding the underlying physical effects causing instabilities to the clock transition is essential to improve the clock frequency stability and identify the limiting factors.

In this section, we present the mathematical tool commonly used for the clock frequency stability analysis, the overlapping Allan deviation. We then discuss in details the sources of the instabilities in the short-term (1-100 s) and in the medium- to long-term regimes ($100 - 10^5$ s), which are respectively the line broadening and the clock frequency shift instabilities, conceptually introduced in equations (1.70) and (1.77).

1.7.1 Overlapping Allan deviation

A clock frequency analysis allows to distinguish the different noise processes present in its frequency output. Such analysis is typically done in the time domain in terms of frequency deviation. The phase of the clock, $x(t)$, is measured at regular time intervals of length τ_0, and the mean clock fractional frequency y_i, is given by:

$$y_i = \frac{1}{t_{i+1} - t_i} \left(x(t_{i+1}) - x(t_i) \right) = \frac{1}{\tau_0} \left(x_{i+1} - x_i \right). \tag{1.98}$$

The standard deviation of the clock mean frequencies is not adapted to the analysis of a clock stability, since it diverges for the common noise processes present in frequency sources. The problem arises from the average value, which is not constant for processes other than white frequency noise [87]. That problem is overcome by the use of the two-sample deviation or Allan deviation [88] which allows to distinguish between various frequency noise processes such as white, flicker and random walk frequency noise (see Figure 1.15). It is expressed as follow:

$$\sigma_y(\tau)_{Allan} = \sqrt{\frac{1}{2} \langle (y_{i+1} - y_i)^2 \rangle} = \sqrt{\frac{1}{2(N-1)} \sum_{i=1}^{N-1} (y_{i+1} - y_i)^2} \tag{1.99}$$

In order to extend to longer averaging time τ and improve the statistical confidence, a variant of the Allan deviation is commonly used: the overlapping Allan deviation. As its name indicates it considers a set of overlapping subsets of samples instead of consecutive ones. It is defined as follow [87]:

$$\sigma_y(\tau) = \sigma_y(m\tau_0) = \sqrt{\frac{1}{2m^2(N-2m+1)} \sum_{j=1}^{N-2m+1} \sum_{i=j}^{j+m-1} (y_{i+m} - y_i)^2} \tag{1.100}$$

where N is the total number of samples, and $m = \frac{\tau}{\tau_0}$ the size of a subset of samples. Figure 1.15 shows the behaviours of most typical frequency noises present in a rubidium clock in term of overlapping Allan deviation along with a simulated data set. The white frequency noise deviation is proportional to $\tau^{-1/2}$ and the flicker frequency noise deviation is constant; it is commonly called *Flicker floor*. The deviations due to a drift (1×10^{-16} /s on Figure 1.15) and a random walk frequency noise process, are proportional to τ. The simulated data also include a periodic frequency oscillation (2×10^{-12} of relative amplitude and a period of 5000 s) creating the *bump* around 2000 s.
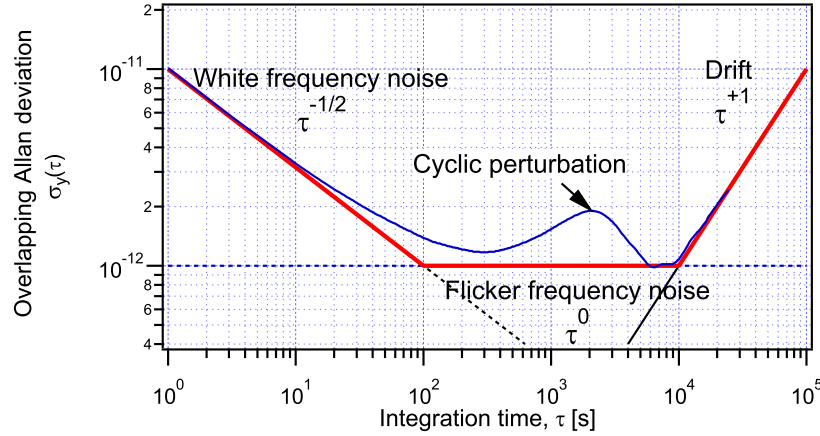
FIGURE 1.15: Thick red: typical behaviour of a clock frequency presenting white frequency noise at a level of $10^{-11} \times \tau^{-1/2}$, flicker frequency noise at a level of 10^{-12} and a linear drift of $1 \times 10^{-16}/\tau$, in terms of overlapping Allan deviation. Thin blue: overlapping Allan deviation of a simulated data set including an additional periodic frequency oscillation.

We split the frequency stability of a clock into two regimes: the short-term stability, based on averaging time scales between 1 and 100 seconds, and the medium to long term stability, based on averaging time scales comprised between 100 up to 10^5 seconds ($\sim$ one day). The short term regime is dominated by the white frequency noise process, it is equivalent to a statistical averaging of the frequencies: the longer the data set, the more precise the mean frequency is. While the medium- to long-term is degraded by random or "slow" frequency fluctuations and drifts.

1.7.1.1 Short-term frequency stability

The short term frequency (in)stability in term of Allan deviation ($\sigma_y(\tau)$), is governed by the DR signal lineshape and the detection noise. It is estimated by [89]:

$$\sigma_y(\tau) = \frac{N \cdot L}{\sqrt{2} \cdot A \cdot \nu_{Rb}} \tau^{-1/2} \tag{1.101}$$

where N is the total detection noise power spectral density within the feedback loop, A the amplitude of the clock signal, L, the DR signal linewidth and ν_{Rb} the frequency of the clock transition. For a detection noise approximated to be proportional to the background level, the instability becomes:

$$\sigma_y(\tau) \propto \frac{1}{FoM} \tau^{-1/2} \tag{1.102}$$

where FoM is the figure of merit defined by equation (1.82).

The detection noise is intrinsically lower limited by the stochastic properties of the light. The corresponding shot-noise current noise density is expressed as,

$$N_{shot} = \sqrt{2eI_{DC}}, \tag{1.103}$$

where e is the charge of the electron, and I_{DC} the photocurrent of the DR signal at half amplitude. Combining equations (1.101) and (1.103) one obtains the intrinsic shot noise limit of the short term stability:

$$\sigma_{Shot}(\tau) = \frac{\sqrt{eI_{DC}} \cdot L}{A \cdot \nu_{Rb}} \tau^{-1/2} \tag{1.104}$$

providing an ultimate lower limit of the clock short term stability.

1.7.1.2 Medium- to long-term frequency stability

The medium- to long-term frequency stability region concerns the slow fluctuations/drift of the clock transition frequency. It is dominated by the different unstable physical processes inducing a shift to the clock transition. By a simple error propagation and assuming the fluctuations are uncorrelated we have:

$$\sigma_y(\tau) = \sqrt{\sum_i \sigma_{y_i}(\tau)^2} = \sqrt{\sum_i \left(\frac{\partial y}{\partial p_i} \sigma_{p_i}(\tau) \right)^2}, \tag{1.105}$$

where y is the fractional clock frequency, and $\sigma_{p_i}(\tau)$ the overlapping Allan deviation of the parameter p_i in subscript. Improving the medium- to long-term frequency stability of a clock requires to reduce either the individual fluctuations of the various parameters through a better control, or the relative sensitivity of the clock transition frequency to the parameter fluctuation, $\frac{\partial y}{\partial p_i}$.

1.7.2 Clock frequency shifts and corresponding coefficients

In equation (1.70) we introduced $\Delta\omega$ as an additional frequency shift to the unperturbed Bohr frequency ω_{12}. This total shift has well defined and additive physical origins that we list and

TABLE 1.8: Order of magnitude of the spin exchange shifts and temperature sensitivity for ^{87}Rb at different vapour temperature. $\Delta = -1/3$ corresponds to an ideal population imbalance when the vapour is optically pumped from $|F_g = 2\rangle$ state and $\Delta \approx -0.07$ to a typical population imbalance reached in clock operation [65].

	Δ	Shift $\Delta\nu_{SE}$ [Hz]	Temperature sensitivity TC_{SE}	
			[Hz/K]	[K^{-1}]
50°C	-1/3	-0.5	0.05	6.7×10^{-12}
	-0.07	-0.1	0.01	1.4×10^{-12}
70°C	-1/3	-2.7	0.2	3.1×10^{-11}
	-0.07	-0.6	0.04	6.5×10^{-12}
90°C	-1/3	-11.9	0.8	1.2×10^{-10}
	-0.07	-2.5	0.17	2.5×10^{-11}

describe here below. An estimation of each relative shift coefficient is also given. At first, we mention the spin exchange (SE) shift present in every case. The discussion is then extended to the shift induced by the confinement method (buffer gas shift or wall coating). Finally the shifts induced by the various electromagnetic fields are also treated.

1.7.2.1 Spin exchange shift

In addition to a broadening, Rb-Rb collisions also induce a small shift to the atomic magnetic moment that results in a global shift of the clock transition. This shift is expressed as follow [65], [66]:

$$\Delta\nu_{SE} = -\frac{1}{8}n_{Rb}\overline{v}_{rel}\lambda_{SE}\Delta, \qquad (1.106)$$

where n_{Rb} is the density of the Rb (see equation (1.49)), $\lambda_{SE} = 6.9 \times 10^{-19}$ m^2 [65], [66], the collisional cross section characterizing the frequency shift, and Δ the difference in population between the two clock levels: ideally, when the atoms are completely pumped from $|F_g = 2\rangle (|F_g = 1\rangle)$, $\Delta = -1/3$ (1/5). Table 1.8 summarizes the calculated value for the SE shift, $\Delta\nu_{SE}$, and its temperature sensitivity, $TC_{SE} = \frac{\partial\Delta\nu_{SE}}{\partial T}$, for the typical operating temperatures and population difference ($\Delta \approx -0.07$ [65]) found in this manuscript.

1.7.2.2 Buffer gas shift and temperature coefficient

The clock frequency shift induced by the collisions with a buffer gas has been extensively studied from both experimental and theoretical points of view [90]–[98]. It depends on both the temperature of the vapour and the density of the BG, and can be expressed for a single BG as follow:

$$\Delta\nu_{BG} = P(\beta + \delta(T - T_0) + \gamma(T - T_0)^2) \tag{1.107}$$

where P is the pressure at the sealing temperature, T the temperature of the cell, T_0 a reference temperature set at 60°C, and α, β, γ the pressure shift coefficient, the linear temperature shift coefficient and the quadratic temperature shift coefficient of the gas, respectively. These coefficients are given in Table 1.9 for the two gases (N_2 and Ar) commonly used in Rb clocks.

The sensitivity coefficient to the temperature, or BG temperature coefficient, TC_{BG} is calculated from equation (1.107) as:

$$TC_{BG}^{(1)}(P,T) = \frac{\partial\Delta\nu_{BG}}{\partial T} = P(\delta + 2\gamma(T - T_0)) \tag{1.108}$$

For a single buffer gas, this coefficient is zero at a given temperature: around 300°C for Nitrogen and below -200°C for the Argon. The interest in mixing these two gases, comes from the fact that the temperature at which $TC_{BG}^{(1)}$ is zero (this temperature is called the inversion temperature, or T_{inv}) can be steered to the usual temperature of operation for a rubidum atomic clock (see Figure 1.16). For a given gas mixture, the equivalent shift coefficients are the weighted sum of the respective gas coefficients according to their relative densities [93]. For a two gas mixture, these are written as:

$$\beta \quad = p\beta_{Ar} + (1 - p)\beta_{N_2} \tag{1.109}$$

$$\delta \quad = p\delta_{Ar} + (1 - p)\delta_{N_2} \tag{1.110}$$

$$\gamma \quad = p\gamma_{Ar} + (1 - p)\gamma_{N_2} \tag{1.111}$$

TABLE 1.9: Buffer gas shift coefficient for ^{87}Rb in Argon and Nitrogen gases. [93]

	$\beta \left[\frac{\text{Hz}}{\text{mbar}}\right]$	$\delta \left[\frac{\text{Hz}}{\text{mbar K}}\right]$	$\gamma \left[\frac{\text{Hz}}{\text{mbar K}^2}\right]$
Argon	-49.93	-0.255	-4.265×10^{-4}
Nitrogen	400	0.401	-9.075×10^{-4}

TABLE 1.10: Order of magnitude of the Buffer gas shifts and first and second order temperature sensitivities at different buffer gas pressure. The mixture is chosen to be 59% Ar and 41% N$_2$ and the temperature is set 1 K off the inversion temperature.

59% Ar $T = T_{inv} \pm 1$ K	Shift $\Delta\nu_{BG}$ [kHz]	Temperature sensitivity			
		$TC_{BG}^{(1)}$		$TC_{BG}^{(2)}$	
		[Hz/K]	[K^{-1}]	[Hz/K^2]	[K^{-2}]
60 mbar	8	0.075	1.1×10^{-11}	0.037	5.5×10^{-12}
100 mbar	13.5	0.12	1.8×10^{-11}	0.062	9.1×10^{-12}
150 mbar	20.2	0.19	2.7×10^{-11}	0.094	1.4×10^{-11}

where p is the fraction of Argon in the mixture. From equation (1.108) the inversion temperature is then given by:

$$T_{inv} = T_0 - \frac{\delta}{2\gamma} \tag{1.112}$$

$$= T_0 - \frac{p(\delta_{Ar} - \delta_{N_2}) + \delta_{N_2}}{2\left(p(\gamma_{Ar} - \gamma_{N_2}) + \gamma_{N_2}\right)}. \tag{1.113}$$

In optimized condition, the first order temperature coefficient being null, we have to consider the second term of the Taylor expansion of equation (1.107) given by :

$$TC_{BG}^{(2)}(P) = P(p\gamma_{Ar} + (1-p)\gamma_{N_2}) \tag{1.114}$$

Table 1.10 summarizes the calculated value for the BG shift, $\Delta\nu_{BG}$, and its linear and quadratic temperature sensitivities, $TC_{BG}^{(1)}$ and $TC_{BG}^{(2)}$, respectively. The mixture and pressure are chosen to be similar to the one used for the clock demonstrator (see Chapter 6). The temperature is set 1 K off the inversion temperature to enhance the consequences of a poor determination of the inversion temperature.
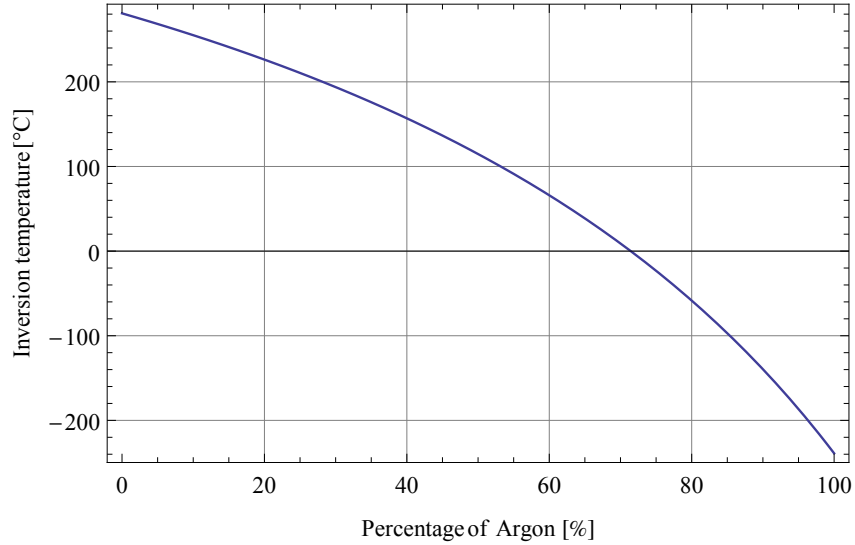
FIGURE 1.16: Theoretical buffer gas inversion (Argon-Nitrogen) temperature as a function of the percentage of Argon.

1.7.2.3   Wall coating shift

The average phase shift the atoms undergo during their adsorption time (see equation 1.93, and Table 5.2) induces a shift to the clock transition frequency:

$$\Delta\nu_{coat} = \frac{\overline{\Phi}_{coat}}{2\pi\overline{\tau}_w} \tag{1.115}$$

For the known efficient coatings, this phase shift is negative as a consequence of the predominance of the attractive van der Waals forces between the alkali atom and those of the coating [37]. Typical values are found to be of the order of few tens of $\frac{\text{mrad}}{\text{coll}}$ (see Table 5.2).

From the temperature dependence of the adsorption time (see equation (1.92)) a temperature sensitivity is induced to the total shift of the clock transition frequency. The corresponding coating temperature coefficient is given by:

$$TC_{coat} = \frac{d(\Delta\nu_{coat})}{dT} = -\frac{E_a}{k_B T^2}\Delta\nu_{coat} \tag{1.116}$$

Typical values are found to be of the order of $TC_{coat} \approx 1\,\frac{\text{Hz}}{\text{K}}$. Within the allowable experimental temperature this sensitivity factor is intrinsic to the coating properties only, and cannot be

minimized. However, Rahman and Robinson [79] observed two turnover points in the temperature dependence close to the melting point of the coating. But this temperature is not viable for long term operation of the coating since its quality quickly degrades [76].

1.7.2.4   Second order Zeeman shift

The second order Zeeman shift has already been treated in section 1.4.2. We recall here its numerical expression for the completeness of this section. The second order Zeeman shift of the clock transition is given by:

$$\Delta\nu_{Zeem}(C_0) = K_C \cdot C_0^2 \tag{1.117}$$

with $K_C = 575.14 \left[\frac{\text{Hz}}{\text{G}^2}\right]$, and C_0 the C-field amplitude. For a C-field generated by a current I through a coil of length L with N turns, the second order Zeeman shift of the clock transition becomes:

$$\Delta\nu_{Zeem}(I) = K_C \left(\frac{\mu_0 N}{L}\right)^2 I^2 \tag{1.118}$$

The first order sensitivity coefficient to the magnetic field, or magnetic coefficient MC_{Zeem} is calculated from equation (1.117) as:

$$MC_{Zeem} = \frac{\partial \Delta\nu_{Zeem}}{\partial C_0} = 2 \cdot K_C \cdot C_0 \tag{1.119}$$

and a similar derivation of equation (1.118) provides the sensitivity coefficient to the current, or current coefficient CC_{Zeem}:

$$CC_{Zeem} = \frac{\partial \Delta\nu_{Zeem}}{\partial I} = 2 \cdot K_C \left(\frac{\mu_0 N}{L}\right)^2 I = 2 \cdot K_C \cdot C_0 \left(\frac{\mu_0 N}{L}\right) \tag{1.120}$$

Table 1.11 summarizes the calculated value for the Zeeman shift, and its sensitivities to the magnetic field and current, MC_{Zeem} and CC_{Zeem}, respectively. The conditions are chosen to be similar to the one used for the clock demonstrator (see Chapter 6).

TABLE 1.11: Order of magnitude of the Zeeman shift and sensitivities to magnetic field and current for the clock demonstrator of Chapter 6: $C_0 = 125$ mG, $N = 35$, $L = 7$ mm, $I = 2$ mA.

Quadratic Shift $\Delta\nu_{Zeem}$ [Hz]	Magnetic sensitivity MC_{Zeem}		Current sensitivity CC_{Zeem}	
	[Hz/G]	[G^{-1}]	[Hz/mA]	[A^{-1}]
9	144	2.1×10^{-4}	9.1	1.3×10^{-6}

1.7.2.5 Light induced shift

The light shift (LS) effect, or AC Stark shift, is a well known process, and is one of the main sources of instability in the different types of atomic frequency standards [99]. It is a consequence of the states' energy shifts induced by the coupling through the electric dipole operator. These energy shifts are induced by virtual transitions (off-resonance transitions) [34], [37], [100] allowed by the short lifetime of the excited state. A red shifted coupling pushes away from each other the coupled states, and the opposite effect occurs for a blue shifted coupling (see figure 1.17).

The theoretical expression we present here is similar to the one developed by Mathur et al. [101], but the hypothesises are slightly modified: instead of considering the average effect on the degenerated hyperfine states, we restrict ourselves to the clock states only. This leads to significant changes, especially on the dependency of the LS to the light polarization. The buffer gas shift and broadening are also considered, giving a global picture of the light shift effect in laser pumped vapour cell atomic frequency standards.

For a three-level system (see Figure 1.17), the LS is expressed as follow [34]:

$$\Delta\nu_{LS} = \left(\frac{\Omega_L}{4\pi}\right)^2 \left(\frac{\delta\nu'_L}{(\frac{\Gamma^*}{4\pi})^2 + (\delta\nu'_L)^2} - \frac{\delta\nu_L}{(\frac{\Gamma^*}{4\pi})^2 + (\delta\nu_L)^2}\right). \tag{1.121}$$

where Ω_L is the optical Rabi frequency, and Γ^* the intrinsic decay rate of the excited states. The frequency detunings, $\delta\nu_L$, are given by:

$$\delta\nu_L = \nu_L - \nu_0 \tag{1.122}$$

$$\delta\nu'_L = \nu_L - \nu'_0 \tag{1.123}$$

for which ν_L is the laser frequency, and ν_0, ν_0' are the optical frequencies for the atomic transitions $|F_g = 1\rangle \to |F_e\rangle$, $|F_g = 2\rangle \to |F_e\rangle$, respectively.

The first term of equation (1.121) represents the energy shift of the upper ground state $|2\rangle$ and the second terms the energy shift of the lower ground state $|1\rangle$. The opposite signs are due to the definition of the Bohr frequency of the clock transition (see equation 1.1; hence, a negative shift of the lower (upper) level results in a positive (negative) shift of the transition frequency, and vice versa. The Figure 1.17 illustrates this effect.
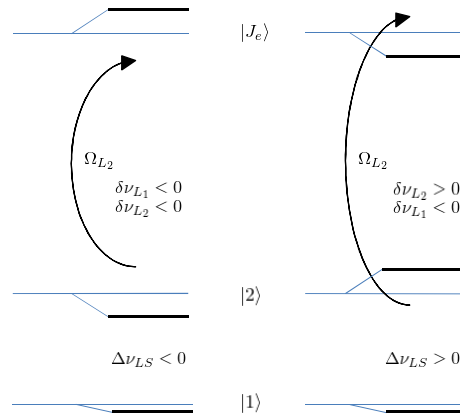
FIGURE 1.17: Effect of the optical detuning on the energies of a three level system.

Equation (1.121) gives a good insight of the phenomenon and allows for a qualitative understanding of the light shift effect. But in the case of the ^{87}Rb in vapour-cell frequency standards, the situation is more complex: the ground state clock levels ($|F_g = 1; m_F = 0\rangle$ and $|F_g = 2; m_F = 0\rangle$) are coupled to several partially resolved excited states, and the contribution of each has to be taken into account. Moreover, the light polarization comes into picture through the selection rules of the electric dipole transitions. Such complexity of the excited level was already considered by Happer and Mathur [102], Mathur et al. [101] and Arditi [103], but their theoretical expression stands for an average shift induced to the degenerated hyperfine ground states and not specifically to the clock states. It is expressed as follow (for clarity the Doppler shifts are here omitted):

$$\Delta \nu_{hfs} = \left(\frac{\Omega_L}{4\pi}\right)^2 \sum_{F_e} \left(\frac{\eta_{2F_e} \delta \nu_{L_{2F_e}}}{(\frac{\Gamma^*}{4\pi})^2 + (\delta \nu_{L_{2F_e}})^2} - \frac{\eta_{1F_e} \delta \nu_{L_{1F_e}}}{(\frac{\Gamma^*}{4\pi})^2 + (\delta \nu_{L_{1F_e}})^2}\right), \tag{1.124}$$

where

$$\eta_{F_g F_e} = 2(2F_e + 1)W^2(J_e\ I\ 1\ F_g; F_e\ \tfrac{1}{2}), \tag{1.125}$$

and

$$\delta\nu_{L_{F_g F_e}} = \nu_L - \nu_{F_g F_e}. \tag{1.126}$$

$W^2(J_e I 1 F_g; F_e\tfrac{1}{2})$ are the Racah coefficients [104], and $\nu_{F_g F_e}$, the optical frequency for the atomic transition $|F_g\rangle \rightarrow |F_e\rangle$.

This expression is insensitive to the light polarization. It allows a qualitative match between theory and experiment for ^{133}Cs, explaining the asymmetry observed in the experimental data [103], but fails in explaining recent measurements from our group in the D1 line [105] as well as the data presented in Chapter 6. We follow here the same approach, but consider only the allowed transitions from the ground state clock levels to the excited states' Zeemans sub levels, as Miao Zhu does [106]. The consequences are essentially changes in the η-coefficients, to include an induced dependence on the polarization of the pumping light:

$$\tilde{\eta}_{F_g F_e} = \sum_{i=-1}^{1} \epsilon_i \xi^i_{F_g m_F = 0 F_e}. \tag{1.127}$$

The i index corresponds to the polarization of the pumping light ($-1 : \sigma^-$, $0 : \pi$, $1 : \sigma^+$), ϵ_i is the proportion of that given polarization, and $\xi^i_{F_g m_F = 0 F_e}$ the relative transition strength factor for the transition $|F_g; m_F = 0\rangle \rightarrow |F_e; m_F = 0 + i\rangle$ expressed as multiple of $|\langle J = 1/2| |er| |J'\rangle|^2$. These factors are given in Table 1.12. It is worth to mention the following relation:

$$\frac{1}{F_g + 1}\sum_{m_F} \xi^i_{F_g m_F F_e} = \frac{1}{3}\eta_{F_g F_e} \qquad \forall i, \tag{1.128}$$

which explains why the polarization of the optical field has no incidence on equation (1.124).

We include here the effects of the buffer gases. As measured by Rotondaro [59] and others [52]–[55], [60], the use of buffer gases induces a shift as well as a broadening of the optical transitions.

TABLE 1.12: Relative transition strength factors expressed as multiples of $|\langle J = 1/2| |er| |J' = 1/2\rangle|^2$ and $|\langle J = 1/2| |er| |J' = 3/2\rangle|^2$ for the D1 and D2 line, respectively.

	$F_g = 1$			$F_g = 2$		
Δm_F	-1	0	1	-1	0	1
D1: $F_e = 1$	1/12	0	1/12	1/12	1/3	1/12
$F_e = 2$	1/4	1/3	1/4	1/4	0	1/4
D2: $F_e = 0$	1/6	1/6	1/6	-	-	-
$F_e = 1$	5/24	0	5/24	1/120	1/30	1/120
$F_e = 2$	1/8	1/6	1/8	1/8	0	1/8
$F_e = 3$	-	-	-	1/5	3/10	1/5

Both effects are proportional to the pressure. The broadening being a direct consequence of the excited state decay rate increase, it affects only the Γ^* parameter as follow:

$$^{BG}\Gamma^* = \Gamma^* + 2\pi\gamma_{BG}P_{BG}, \qquad (1.129)$$

where γ_{BG} is the pressure broadening coefficient, and P_{BG} the pressure of the buffer gas.

The shift itself affects only the optical transition Bohr frequencies as follow:

$$^{BG}\nu_{F_gF_e} = \nu_{F_gF_e} + \delta_{BG}P_{BG} \qquad (1.130)$$

where δ_{BG} is the pressure shift coefficient. In case of a buffer gas mixture, we consider the broadening and the shift induced by each gas weighted by its partial pressure. The coefficients for Argon and Nitrogen are given in Table 1.13.

TABLE 1.13: Optical pressure and shift coefficients for D1 and D2 line in MHz/mbar. From Rotondaro's thesis [58].

	D1		D2	
	δ	γ	δ	γ
Ar	-5.08	-13.6	-4.32	13.3
N2	-5.56	-12.2	-4.34	13.7

Including finally the Doppler effect, the total expression for the light shift becomes a weighted average over the whole population according to the Maxwell distribution. Combining equations (1.124), (1.127), (1.129), (1.130), and the Doppler shift ν_D, we obtain the following expression for the light shift:

$$\Delta\nu_{LS} = \left(\frac{\Omega_L}{4\pi}\right)^2 \sum_{F_e} \int d\nu_D g(\nu_D) \left(\frac{\tilde{\eta}_{2F_e}\delta\nu_{L_{2F_e}}}{(\frac{BG\Gamma^*}{4\pi})^2 + (\delta\nu_{L_{2F_e}})^2} - \frac{\tilde{\eta}_{1F_e}\delta\nu_{L_{1F_e}}}{(\frac{BG\Gamma^*}{4\pi})^2 + (\delta\nu_{L_{1F_e}})^2}\right), \quad (1.131)$$

where $g(\nu_D)$ is the Gaussian distribution of the frequencies. Figures 1.18 and 1.19 show the clock frequency light shift as a function of the laser frequency for an intensity of 1 µW/mm^2 and a pure σ-polarization. The comparison is made with Mathur's model in both, D1 and D2 lines. The similarity of both models prediction in the D2 line comes from the unresolved excited hyperfine splitting and a certain symmetry of the transition strength factors. This is not the case in the D1 line and the two models differ. Both models on both lines predict two laser frequencies at which the light shift is zero.
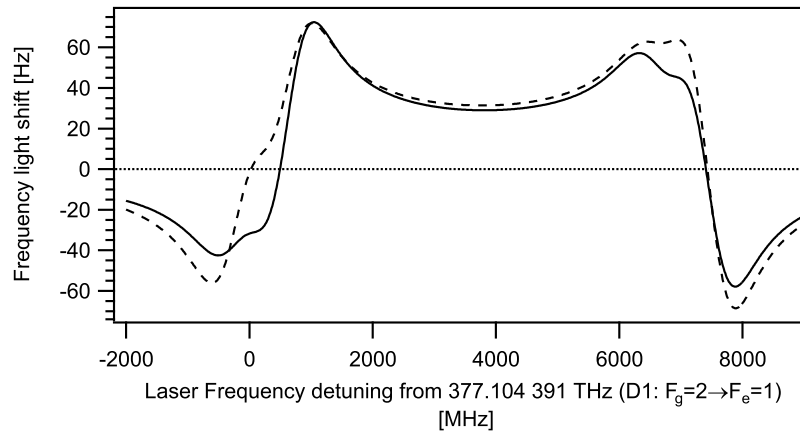
FIGURE 1.18: Theoretical frequency light shift predictions in the D1 line for a light intensity of 1 µW/mm^2 with a pure σ-polarization. Solid line: our model; dashed line: Mathur model.

The light intensity sensitivity coefficient, or α light-shift coefficient (α_{LS}) is calculated from equation (1.131) as:

$$\alpha_{LS}(\nu_L) = \frac{\partial\Delta\nu_{LS}}{\partial I_L} = \frac{\Delta\nu_{LS}}{I_L} \quad (1.132)$$

Using equation (1.59), this coefficient does not depend on the light intensity, I_L, but only on the laser frequency. It is null for the two same laser frequencies cancelling the total light shift.
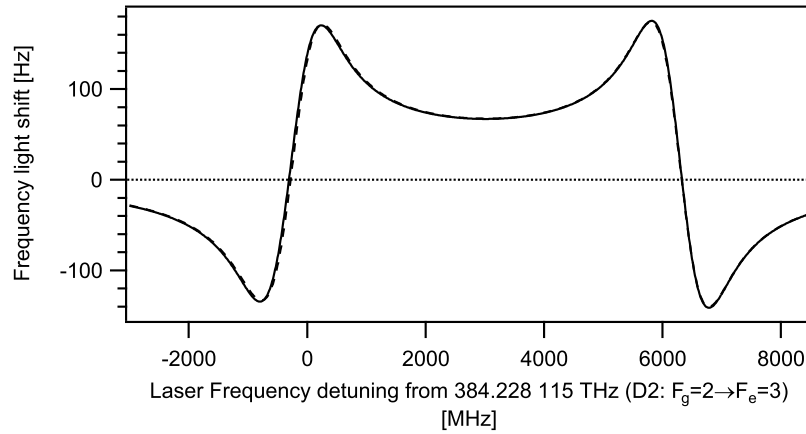
FIGURE 1.19: Theoretical frequency light shift predictions in the D2 line for a light intensity of $1\,\mu W/mm^2$ with a pure σ-polarization. Solid line: our model; dashed line: Mathur model.

The light frequency sensitivity coefficient, or β light-shift coefficient (β_{LS}) is calculated from equation (1.131) as:

$$\beta_{LS}(\nu_L, I_L) = \frac{\partial \Delta \nu_{LS}}{\partial \nu_L} = \frac{\partial \alpha_{LS}(\nu_L)}{\partial \nu_L} \cdot I_L \tag{1.133}$$

On the contrary to the α_{LS} coefficient the β_{LS} coefficient is proportional to the light intensity; it also depends on the light frequency, and cannot be cancelled close to the optical resonances for a σ-polarized light (see section 6.5).

1.7.2.6 Cavity Pulling

The cavity pulling effect arises when the resonant frequency of the cavity sustaining the microwave field is detuned from the atomic resonance. The frequency of the clock transition is "pulled" so that the offset is reduced. This effect is non negligible and transfers the temperature sensitivity of the microwave cavity frequency to the clock transition. The corresponding cavity pulling temperature coefficient (TC_{CP}) is expressed as follow [37]:

$$TC_{pulling} = \frac{d\Delta \nu_{CP}}{dT} \approx 3 \times 10^{-3} \frac{Q_L}{Q_a} \frac{d\Delta \nu_{cavity}}{dT} \tag{1.134}$$

where $\Delta \nu_{cavity}$ is the cavity detuning of the microwave cavity and Q_L and Q_a are the quality factor of the loaded cavity and of the atomic transition, respectively. $TC_{cavity} = \frac{d\Delta \nu_{cavity}}{dT}$ is the temperature shift coefficient of the cavity resonance frequency.

1.7.2.7   Microwave power shift

From the model used here, the clock frequency shows no dependency to the microwave power as opposed to the light. Nonetheless, microwave power sensitivity of the clock transition frequency is commonly reported for BG rubidium cells [7], [107]–[109]. This dependency, called the power shift, is most likely a consequence of field inhomogeneities within the cell, emphasized by the relative immobility of the atoms due to the BG. In other words, each atom has its own transition frequency defined by its local environment. Applying the microwave, or modifying its strength, modifies the local conditions, especially the absorption, thus the light intensity. Therefore any residual light shift will induce a power shift. This dependency was put in evidence recently by Bandi [7] who demonstrated a linear dependency of the microwave power shift coefficient to the light intensity. Two other methods were also proven to efficiently reduce the power shift: by introducing a C-field gradient along the quantization axis, Mileti [108] could reduce significantly the power shift sensitivity down to $3 \times 10^{-12}/\mu$W. Letting the atoms freely evolve by the use of wall coating vanishes the inhomogeneities through spatial average; with this method Risley et al. [80] demonstrated a complete suppression of the power shift.

1.7.2.8   External pressure shift

According to Riley, the variation of the external pressure induces a typical shift of about $1 \times 10^{-10}/$atm [110]. This phenomenon is attributed to the "oil-can" deflection of the end windows modifying the internal pressure of the buffer gas. This effect "scales with the 4th power of the cell diameter and inversely with the cube of the window thickness" [110]. Assuming the dimensions of the cell were 12 mm diameter and 1 mm thick (similar to the LARC cells, see Table 3.1), one obtains $1 \times 10^{-11}/$atm, or $1 \times 10^{-14}/$hPa for our 3D cell design (one has $(4/12)^4$ and $(1/0.5)^3$ as scaling factors for the window diameter, respectively thickness).

1.7.3   Summary of the broadenings and shift coefficients

Tables 1.14 and 1.15 show the summary of the intrinsic broadening mechanisms and the shift sensitivities to environmental parameters. The values for the broadening are purely theoretical.

The values for the sensitivity coefficients are typical for a BG cell in the experimental conditions encountered in Chapter 6.

TABLE 1.14: Summary of the various intrinsic broadening in buffer gas cells for four cell geometries.

Cell type	Dimensions		Spin exchange broadening	Bare glass broadening ($\epsilon = 1$)	BG + Wall broadening	Optimized pressure
	$\varnothing$ [mm]	h [mm]	[Hz]	[kHz]	[Hz]	[mbar]
2D-In (70°C)	5	0.78	95	77	796	486
2D-AB (70°C)	5	2	95	41	354	216
3D (70°C)	4	4.05	95	33	275	168
14 mm (50°C)	12	12	18	11.5	91	57

TABLE 1.15: Sumary of the perturbing shift coefficients for the 3D buffer gas cell. Light shift, microwave power shift are measured quantities (see Chapter 6).

Physical effect	sensitive variable	Coefficient	Approx. value	Rel. approx. value
Spin exchange		TC_{SE}	-0.04 Hz/K	-6.5×10^{-12} K^{-1}
Buffer gas		$TC_{BG}^{(1)}$	± 0.1 Hz/K	$\pm 1.5 \times 10^{-11}$ K^{-1}
	Temperature	$TC_{BG}^{(2)}$	-0.06 Hz/K^2	9×10^{-12} K^{-2}
Cavity pulling		TC_{CP}	± 0.03 Hz/K	$\pm 4.4 \times 10^{-12}$ K^{-1}
Light shift	Light intensity	α_{LS}	± 4 mHz/%	$\pm 5.9 \times 10^{-13}$ %$^{-1}$
	Light frequency	β_{LS}	± 0.35 Hz/MHz	$\pm 5.1 \times 10^{-11}$ MHz^{-1}
Zeeman	Magnetic field	MC_{Zeem}	+144 Hz/G	$+2.1 \times 10^{-4}$ G^{-1}
	C-field current	CC_{Zeem}	+9.1 kHz/A	$+1.3 \times 10^{-6}$ A^{-1}
Microwave power	Microwave power	PoC_{MW}	-0.17 Hz/dBm	-2.5×10^{-11} dBm^{-1}
Oil-can	External pressure	PrC_{Atm}	+70 µHz/hPa	$+1 \times 10^{-14}$ hPa^{-1}
N$_2$ leak (sct. 4.2.2)	N$_2$ int. pressure	PrC_{N_2}	+400 Hz/mbar	$+5.9 \times 10^{-8}$ mbar^{-1}

1.8   Conclusion

In this chapter, we covered the theoretical aspects required to explain the basic properties of a DR rubidium atomic clock. The models we introduced provide excellent qualitative prediction

TABLE 1.16: Summary of the main intrinsic broadening for three different coated cell geometries. The spin-exchange contribution at 100°C is FWHM$_{SE}$= 800 Hz.

	Volume	Wall surface	Reservoir hole surface	Spin Exchange broadening	Wall coll. broadening (Coll. rate)	Adiabatic broadening	Reservoir broadening	Sum (Measured)
	[mm³]	[mm²]	[mm²]	[Hz]	[Hz]	[Hz]	[Hz]	[Hz]
14 mm glass blown cell [a]	1357	679	0.79	18	<2 (35 k)	20	13	53 (63 ± 10)
KOH µ-fabricated cell (see Chapter 5)[b]	4.24	17.3	0.01	95	93.9 (295 k)	67	55	311 (8900 ± 100)[c]
3D µ-fabricated cell[d]	51	76	0.09	95	34 (108 k)	24	41	194

[a]Hole size: 1 mm diameter, tetracontane coated, $\Phi = -30$ [mrad/coll], $\epsilon = 1/10000$, 50°C
[b]Hole size: 0.1 x 0.1 mm², OTS coated, $\Phi = -19$ [mrad/coll], $\epsilon = 1/1000$, 70°C
[c]The significant difference is due to the reduced quality of the coating (covering, depolarization probability) that is not considered here
[d]Hole size: 0.3 x 0.3 mm², OTS coated, $\Phi = -19$ [mrad/coll], $\epsilon = 1/1000$, , 70°C

for the various interactions affecting the rubidium atoms, and their consequences on both the optical absorption spectrum and the DR spectrum. The discussion was focused on the induced broadening and shifts, providing powerful spectroscopic tools for the characterization of rubidium vapour cells. The origin of polarization types (π, $\sigma^\pm$) of the electromagnetic fields interacting with the atoms was redefined. The electric field orientation as well as the magnetic one are considered now whether the interaction is magnetic or electric. A $\Delta m_F = -1, 0, 1$ electric- (magnetic-) dipole transition defines respectively, a σ^-, π, σ^+ polarization of the corresponding field inducing the transition.

The notion of stability was introduced along with the statistical tool for its characterization, the Overlapping Allan deviation. The stability limiting factors were identified: broadenings of the DR spectrum limits the short term stability, and induced shift by fluctuating parameters restrict the medium- to long-term stability. A detailed description of all the significant broadening and shifts coefficients was presented with a particular focus on the light-shift effect: we proposed an innovative theoretical model which allows qualitative and quantitative predictions of the light-shift coefficients. The summary of all the potential shifts provides a simple and rapid tool for the evaluation of the required constrains imposed on the environmental parameters stabilities. As an example, for a 10^{-12} stability goal in the medium to long term regime, the linear BG frequency shift temperature coefficient, resulting from an operating temperature off by one K of the inversion temperature ($TC_{BG}^{(1)} = \pm 1.5 \times 10^{-11}$ K^{-1}), imposes a challenging temperature stability of ± 70 mK for the same time scale.

Chapter 2

The experimental setups

This chapter describes most of the spectroscopic experimental setups used in this thesis except the miniature double-resonance atomic clock presented in Chapter 6. The three spectroscopic schemes, linear absorption, Doppler-free saturated absorption and DR are described in detail, and their application briefly discussed. The two key components of the setup, the stabilized laser source and the atomic resonator, are introduced and detailed. The role of the laser head is double. It provides a tunable narrowband light source allowing the acquisition of optical spectra without the use of a spectrometer; it is also the light source for the optical pumping process in the DR scheme. The atomic resonator, or physics package, contains the cell under test and serves for the microwave interrogation. It also controls, when possible, the external environment of the cell, such as temperature and DC magnetic field.

The spectroscopy performed in this thesis serves two purposes. The first is analytical: the measured spectra allow, under certain hypothesises and within the theoretical frame developed in Chapter 1, to determine in a fast and non-destructive way the content of the cells under test and its evolution over the time. This aspect is essential for the validation of newly produced cells, especially in the case of the development of innovative fabrication processes, and is treated in Chapters 4 and 5. The second purpose is metrological: the spectroscopy of the cell under test is used to quantify the various induced shifts to the clock transition affecting the clock stability and to optimize the external experimental conditions and interrogating parameters in term of stability. This part is treated in the Chapter 6.

2.1   Linear optical absorption setup

In linear absorption spectroscopy, the laser beam, provided by a laser head (see section 2.4), passes through the rubidium vapour cell under test, and its transmission is recorded as a function of the laser frequency. The cell is heated to increase the rubidium vapour density, thus its optical density and the temperature is stabilized. The laser frequency is swept across the absorption lines of the rubidium atom, by ramping the bias current of the laser diode. Since the laser frequency depends linearly on the bias current, it can be calibrated using a known reference spectrum recorded simultaneously within the laser head. Figure 2.1 shows the experimental configuration for the linear configuration. The laser beam intensity is significantly reduced with neutral density filters so that optical pumping is negligible, and the transmission of the cell is measured. The obtained spectrum is Doppler broadened and the presence of buffer gas induces additional broadening and shift to the absorption lines, as described in Chapter 1.

We use this spectroscopy as a simple detection scheme for the presence of rubidium vapour inside the cell and for the estimation of significant buffer gas pressure through the collisional broadening induced (see Chapter 1). The achieved resolution for the buffer gas pressure is of the order of 10 millibar. It is limited by the relatively small collisional broadening ($\gamma_{N_2} \sim 16.55$ MHz/mbar) with respect to the Doppler broadening ($\Delta\nu_{\mathrm{Doppler}} \approx 500$ MHz). Nevertheless, under extremely well controlled experimental conditions and using a proper fitting procedure the linear absorption can be used to provide an optical measure of the Boltzmann constant, k_B with an uncertainty of few 10^{-6} only [111].
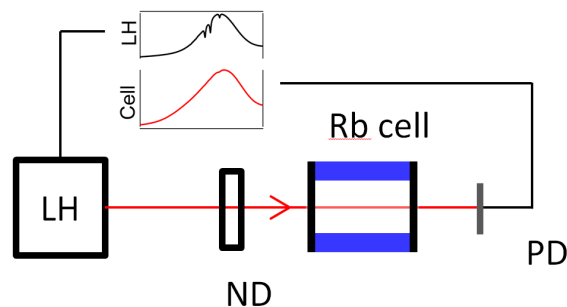
FIGURE 2.1: Schematic linear absorption setup. LH, Laser head; ND, Neutral density filter; PD, Photo-detector.

2.2 Doppler-free optical saturated absorption setup

Doppler-free saturated absorption spectroscopy [112] is operated similarly to the linear absorption spectroscopy, in the sense that the laser beam and reference spectrum are provided by a laser head, and the laser frequency is swept while the transmission of the cell under test is recorded. This spectroscopy is based on the velocity-selective saturation of the Doppler-broadened transitions [113]. Two laser beams of same frequency but different intensities counter propagate and overlap within the cell. The most intense beam is called the "pump"-beam, and the weakest, the "probe"-beam of which the transmission is recorded. From their opposite propagation directions, the pump and the probe beams interact with, and deplete, two longitudinal velocity classes of atoms due to the Doppler effect. When these classes are different, the transmission of the probe beam is identical to the linear absorption transmission since the class it probes is not affected by the pump beam. On the contrary, when these classes are identical, the population depletion induced by the pump beam reduces the absorption of the probe beam, inducing a narrow dip in the Doppler broadened spectrum. Such situation occurs when the laser frequency is at resonance with the atomic transitions and the class of atoms interacting with both lasers has a zero longitudinal velocity $v_z = 0$. We define this dip as a direct transition dip. This situation also occurs when, in the rest frame of a class of atoms having a negative velocity, $-v_z$, with respect to the pump beam source, the atoms are depleted by the blue shifted pump beam via a given atomic transition 1 of Bohr frequency ν_1 if $\nu_L(1 + \frac{v_z}{c}) = \nu_1$. The same class of atoms can be probed by the red shifted probe laser through a different atomic transition 2 of lower Bohr frequency, ν_2, if $\nu_L(1 - \frac{v_z}{c}) = \nu_2$. This imposes the laser frequency to be [114]:

$$\nu_L = \frac{\nu_1 + \nu_2}{2}. \tag{2.1}$$

Similarly, and for the same laser frequency, the class of atoms with a positive velocity, v_z, with respect to the pump beam source, are depleted by the red shifted pump beam via the transition 2 and probed by the blue shifted probe beam via the transition 1. The dip induced in the probe beam spectrum is called a crossover dip. Such spectroscopy is only achievable in low pressure and pure alkali vapours. Indeed, the narrow width of the dip, free from Doppler broadening, is sensitive to broadening by collisions unless the buffer gas pressure is quite low [115].

Figure 2.2 shows the experimental configuration for the realization of the Doppler-free saturated

absorption. The laser beam passes through the vapour cell as pump-beam. It is reflected back through the cell with a reduced intensity as the probe beam and is then deflected with the use of a beam splitter to be measured. This configuration differs from the commonly used ones where the laser beam is usually splitted before entering the cell [114], [116]–[118]. It presents a gain in terms of space and renders the alignment much easier.
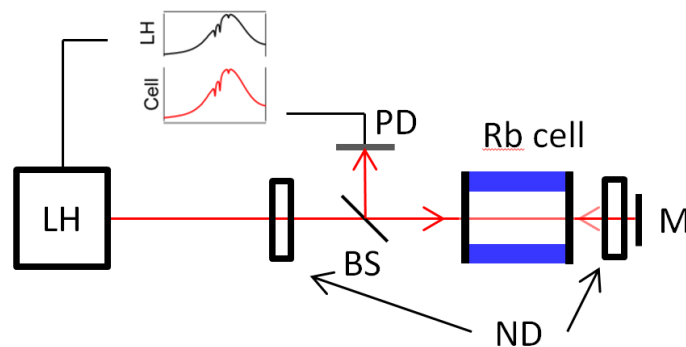
FIGURE 2.2: Schematic Doppler-free saturated absorption setup: LH, Laser head; BS, Beam splitter; ND, Neutral density filter; M, Mirror; PD, Photo-detector.

We use this spectroscopic method essentially for the realization of the reference spectra of the laser head. But its higher relative precision for the buffer gas broadening with respect to the sub-Doppler patterns ($\Delta\nu_{\text{sub-Doppler}} \approx 20$ MHz) allows also a ~ 20 times more precise estimation of a potential BG contamination in a nominally pure rubidium vapour cell.

2.3   Optical-microwave double-resonance setup

In DR spectroscopy, the transmission of the cell under test, or clock cell, is measured as a function of the applied microwave frequency while the pumping laser frequency is fixed. This provides the DR signal, of which the key parameters (amplitude, centre position, linewidth and background level) are measured as a function of the experimental parameters, which can be for example: laser intensity, laser frequency, laser polarization, microwave power, cell temperature, or C-field strength.
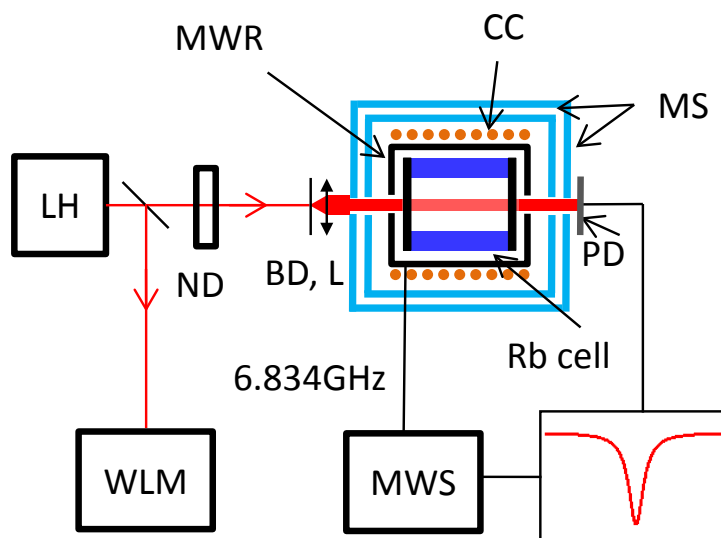
FIGURE 2.3: Schematic DR setup: LH, Laser Head; MWR, microwave resonator; CC, C-field Coil; MS, µ-metal Shield; ND, Neutral Density Filter; BD, Beam Diffuser; L, Lens; PD, Photo Detector; MWS, Microwave Source; WLM Wavelength meter.

A typical DR setup is depicted on Figure 2.3. The laser beam is provided by the laser head. A wavelength meter serves to measure the optical frequency of the free running un-swept laser frequency, since the reference spectrum of the laser head is only obtained for a swept laser. The laser beam passes through a beam diffuser-lens assembly before entering the cell, in order to homogenize its radial intensity distribution. The transmitted light power is measured with a photo detector. For ^{87}Rb, a 6.834 GHz microwave is generated by a commercial synthesizer and sent to a temperature stabilized resonant microwave resonator (MWR) which holds the clock cell and sustains the magnetic microwave field. The resonator is surrounded by a solenoid, or C-field coil, inducing the C-field along the laser beam propagation vector to isolate the clock transition by Zeeman splitting (see 1.4.2). The whole is finally surrounded by two layers of µ-metal magnetic shields to reduce the effect of external magnetic fields, and thermally isolated. The ensemble cell, resonator, coil, and shields is called the physics package or PP.

2.3.1 DR spectroscopic modes

We discuss here the three spectroscopic modes for the evaluation and optimization of the DR signal.

2.3.1.1 DC mode

The DC mode corresponds to the basic mode and provides the DR signal, $DR(\nu)$; the microwave frequency is swept and the laser transmission through the cell recorded. It allows a simple extraction of the DR signal parameters by a Lorentzian fit of the DC DR signal. Its precision is limited by the various noise processes, especially at low frequencies. The signal fluctuations occurring during the acquisition process deform the DR signal and bias the extracted fit parameter.

2.3.1.2 AC mode

The AC mode is a variant of the DC mode and provides the error signal, $e_{DR}(\nu)$, of the DR signal; the microwave is swept and frequency modulated (square modulation); a phase-sensitive detection of the modulated transmission is measured using a lock-in amplifier. The period, T_M, of the frequency modulation is chosen sufficiently large with respect to the relaxation times, T_1 and T_2, of the atomic population, so that the interrogation is quasi-static [37]. The frequency deviation, Δ_M, is chosen much smaller than the DR signal linewidth so that the error signal is at first order proportional to the derivative of the DR signal, i.e.:

$$\frac{e_{DR}(\nu)}{\Delta_M} \approx \frac{dDR(\nu)}{d\nu} \tag{2.2}$$

This mode allows to extract from the overwhelming noise very small DR signals. Moreover, the problematic signal fluctuations observed in the DC mode are suppressed and the precision in the determination of DR signal parameters is significantly improved for small and broad signals. The DR parameters are extracted from a derivative Lorentzian fit of the scaled error signal. The background level is measured simultaneously.

2.3.1.3 Clock mode

The clock mode is the realization of a clock with the optically pumped PP as atomic resonator (see Figure 1.1). The servo loop consists of using the error signal of the AC mode processed by a proportional-integrator (PI) amplifier to servo the quartz frequency of the microwave generator. Besides the realization of the atomic clock, it allows a much more precise measure of the clock transition frequency than the DC and AC mode. The precision is limited by the stability of the clock, which is optimized for a frequency deviation of [37]:

$$\Delta_{M_{opt}} = \frac{FWHM}{2\sqrt{3}} \approx 0.29 \ FWHM. \tag{2.3}$$

While the DC and AC modes are used for the optimization of the clock signal, and the characterization of significant shift coefficients, the clock mode allows an improvement of more than one order of magnitude of the precision of the shift coefficients; but the DR parameters can no longer be extracted. In terms of buffer gas pressure evaluation, the relative precision of the shifts measured in the clock mode, limited by the short-term stability of the clock ($\sigma_y(1s) < 10^{-10}$) allows, for example, the determination of a pure Ar buffer gas pressure at the level of 0.02 mbar, given a pressure shift coefficient of -49 Hz/mbar (see 1.7.2.2).

2.4 Laser heads

In this section, we describe the laser heads used as optical light sources in this thesis. This section is highly inspired from a joint publication with F. Gruet as first author: "Compact and frequency stabilized laser heads for rubidium atomic clocks" [11].

The laser head consists of a distributed feedback (DFB) laser diode and a highly compact sub-Doppler spectroscopic setup [114] used for the laser frequency calibration and stabilization. The laser light produced is linearly polarized, has a narrow emission spectrum (< 5 MHz), is tunable in frequency and can be frequency stabilized within ± 8 kHz ($\sigma_y(\tau) < 2 \times 10^{-11}$ up to 10^4 s). Its tunability over a whole rubidium D line frequency range provides a simple spectroscopic tool for both linear and saturated absorption spectroscopy. In terms of DR, the laser pumping allows one order of magnitude improvement in term of shot noise limit when compared to lamp pumped

atomic clocks [47]. The intensity and frequency stabilities of the laser head have allowed the realization of laser pumped rubidium atomic clocks with stabilities $\sigma_y(\tau) < 2 \times 10^{-13}\tau^{-1/2}$ (in continuous wave (CW) pumping scheme [119] or in pulsed optical pumping (POP) scheme [8]). This represents a stability record for hot rubidium vapours [8].

Two types of laser head were designed. The "standard laser head", inspired by a previous design using Extended-Cavity Diode Lasers (ECDL), made in 2003 [120], [121], and an "AOM laser head" using an integrated Acousto Optical Modulator (AOM). All mechanical components as well as the rubidium cell (see Chapter 3) were manufactured and assembled at LTF.

2.4.1   Standard laser head

Figure 2.4 shows the standard laser head. The optical components are mounted on a thermally controlled baseplate. The laser module is composed of a DFB laser diode that emits at 780 nm or 795 nm, a collimation lens and a miniature optical isolator. The part of the laser beam that passes straight through the first beamsplitter is used to monitor dc optical power with a photo-detector. The reflected part of the beam falls on another beamsplitter where the reflected part is sent through the reference rubidium cell assembly for sub-Doppler spectroscopy [114]. The transmitted part goes out of the laser head and serves for the spectroscopy or optical pumping of the clock cells under test. The sub-Doppler absorption signal is monitored by a second photo-detector after being retro-reflected. It is used to stabilize the laser frequency to the saturated-absorption lines, using lock-in detection. The reference rubidium cell assembly is composed of the high purity rubidium vapour cell, surrounded by two heaters, a magnetic coil and two magnetic shields. This serves to control the magnetic conditions on the cell and its temperature. The laser module, cell assembly, and photo-detectors are controlled and/or monitored by laboratory electronics. The complete laser head has a volume of 0.63 dm^3.

2.4.2   AOM Laser head

The AOM laser head is similar to the standard laser head and is based on a 780 nm DFB laser diode. It differs only from the implemented AOM and the beam path. The AOM is used to induces a precise and stable shift to the laser frequency. It allows the production of frequency stabilized laser beam of which the frequency is detuned from the fixed reference Rb sub-Doppler
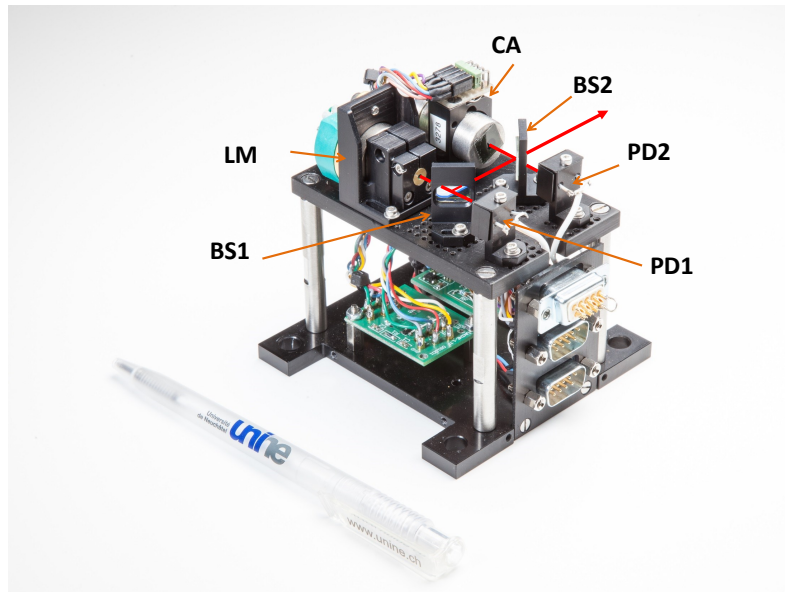
FIGURE 2.4: Photograph of the laser head. LM, Laser module; BS, beamsplitter; PD, photo-detectors; CA, rubidium cell assembly.

lines. This feature is particularly useful in order to minimize AC-Stark shift effect in Rb atomic clocks [122], as it will be explained in Chapter 6.

Figure 2.5 shows the assembled AOM laser head with the beam path highlighted. The laser module (LM) is identical to the ones used in the standard laser heads. A first beamsplitter allows part of the beam to directly go out of the laser head and be used for clock operation. A mirror sends the other part of the beam through a half-wave plate ($\lambda/2$) that allows selecting the beam polarization before the polarizing beamsplitter cube (PBC). Part of the beam makes a double-pass through the AOM using a set of mirrors and a quarter waveplate ($\lambda/4$). This single-shifted or double-shifted beam, depending on the order selected, will be used in the sub-Doppler absorption setup, and eventually enables laser frequency locking. Overall volume of the AOM laser head is 2.4 litres.

2.4.3 Reference rubidium cell

The rubidium vapour cell is a key element of the laser head, since it provides the optical reference spectrum. It consists of a 10 mm diameter, 19 mm length, glass blown cell filled with a pure
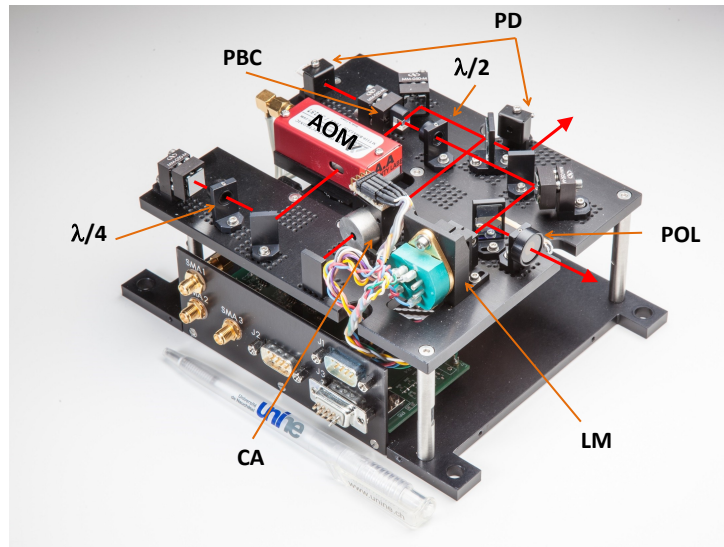
FIGURE 2.5: Photograph of the AOM laser head. In red: beam path. LM, Laser module; POL, polarizer; $\lambda/2$, half-wave plate; PBC, polarizing beamsplitter cube; $\lambda/4$, quarter waveplate; CA, rubidium cell assembly; PD, photo-detectors.

rubidium vapour. The purity of the rubidium vapour and the cleanliness of the cell are essential: for an uncontaminated cell, the Doppler-free saturated absorption spectroscopy produces high-contrast patterns with a linewidth below 20 MHz (see Figure 2.6a). This allows a strong laser frequency stabilization achieving frequency stability at one second of $5.2 \times 10^{-12} \tau^{-1/2}$. The slightest gas contamination broadens these patterns (see Figure 2.6b and section 1.5.1) and significantly reduces their contrast, resulting in a degradation of the achievable optical frequency stability. In the worst cases, the sub-Doppler patterns vanishes (Figure 2.6c). The development of a cleaning and filling method avoiding this contamination during and after the production phase, was a challenging part of this thesis. The method is described in Chapter 3).

In addition to their extensive use in the laser heads produced at LTF, these cells have also served for the realization of other optical frequency stabilization devices:

-Towards a space qualified miniaturized device, a fiber-coupled stabilization setup at 780 nm using TRIMO-SMD assembling technique (Three Dimensional Miniaturized Optical Surface Mounted Device)[9] was developed and realized (see Figure 2.7) in the frame of the SQUATOS[1]-projet [10].

---

[1] Space qualified assembly technique for optical systems.

-Study of the carbon dioxide proportion in the atmosphere requires a stable laser wavelength at 1572 nm. Such a stable wavelength can be achieved as follow; A 1560 nm laser is frequency stabilized through frequency doubling and stabilization on the sub-Doppler patterns of the rubidium vapour cell spectrum. It is then pulsed, or transformed into an optical comb so that one of the teeth has a 1572 nm wavelength. Such an optical frequency reference is developed within the frame of the DLR project: Optical Filtering for Onboard LIDAR Calibration (see page xxix) and exhibits a relative frequency stability of $\sigma_y < 5 \times 10^{-12}$ at one day.

(A) Excellent cell. (B) Slightly contaminated cell. (C) Contaminated cell.
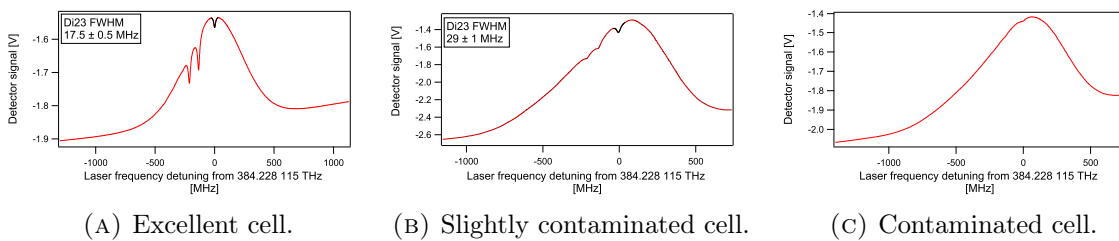
FIGURE 2.6: Comparison of three qualities of evacuated cells' saturated absorption spectra of the $|F_g = 2\rangle \rightarrow |F_e\rangle$ transition obtained with a D2 line DFB laser. The linewidth of the $|F_g = 2\rangle \rightarrow |F_e = 3\rangle$ sub-Doppler transition is 17.5±0.5 MHz for the excellent cell, 29±1 MHz for the middle one and not measurable for the contaminated.
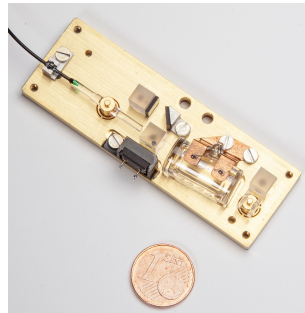
FIGURE 2.7: SQUATOS functional demonstrator. Dimensions of the base plate are 71 mm × 24 mm [10].

2.4.4 Laser heads characteristics and clock stability limits

The laser heads were extensively characterized, and we summarize here the most relevant parameters. Table 2.1 shows a comparison of the measured values for both laser head type as reported in [11]. The parameters of the laser heads are very similar in all points except in their intensity and frequency stabilities. The slight degradation observed for the AOM laser head as compared

to the D2 line laser head, comes from the use of the AOM. Indeed, the modified beam path, the added optical components and the reduction of the pump beam intensity for the sub-Doppler spectroscopy (reducing in turn the strength of the sub-Doppler dips) are factors participating to the degradation of the stabilities. In the case of the D1 line laser head, the short term frequency stability is degraded by a factor of six due to a lower contrast of the sub-Doppler absorption signals used to lock the laser; concerning the medium- to long-term stability, the absence (at the time of the measure) of thermal control of the reference cell is responsible for the one order of magnitude degradation factor.

Taking into account the light shifts coefficients given in Table 6.3, the clock frequency instabilities induced by the AOM laser head intensity and frequency instabilities, at 10^4 s, are of the order of $\sigma_{y_{I_L}} = 1.8 \times 10^{-14}$ and $\sigma_{y_{\nu_L}} 3.9 \times 10^{-13}$, respectively.

TABLE 2.1: Summary of the laser heads' most relevant parameters.

Parameter		(D1)D2 Standard Laser Head	D2 AOM Laser Head
$\frac{\partial \nu_L}{\partial I}$ [GHz/mA]		(-1)-1	-0.875
$\frac{\partial \nu_L}{\partial T}$ [GHz/K]		(-25)-25	-26.3
Output Power [mW]		$\sim$(5)5	$\sim$5
SMSR [dB]		>(45)40	>40
RIN [Hz^{-1}]		$< (2)5 \times 10^{-14}$ @ 300 Hz	7×10^{-14} @ 300 Hz
FM noise [kHz/$\sqrt{\text{Hz}}$]		(4)4 @ 300 Hz	5 @ 300 Hz
Linewidth [MHz]		$< (4)2.2$	4.6
Frequency stability	$\tau < 100$ s	$< (30)5 \times 10^{-12}\tau^{-1/2}$	$< 8 \times 10^{-12}\tau^{-1/2}$
	$100 < \tau < 4 \times 10^4$ s	$< (50)8 \times 10^{-12}$	$< 2 \times 10^{-11}$
Intensity stability	$\tau < 100$ s	$< (3)3 \times 10^{-5}$	$< 1 \times 10^{-4}$
	$100 < \tau < 4 \times 10^4$ s	$< (1)1 \times 10^{-4}$	$< 3 \times 10^{-4}$

2.5 Physics package based on the 14 mm magnetron-cavity

This section describes the laboratory PP and its microwave resonator cavity used in the DR characterizations of the various cells, of diameter equal or smaller than 14 mm, presented in the chapters 4 and 5.

The PP contains the atomic vapour cell and serves for applying the two magnetic fields used to prepare and interrogate the atoms. Two opposite openings allow the laser beam to enter, pass through the cell and be detected at the output of the PP. Moreover, the PP is used to control the temperature of the cell and isolate it from external temperature and magnetic fluctuations. Figure 2.8 shows the details of the laboratory PP and the types of cells that were characterized. This PP is made of concentric cylinders having a dedicated function. From the inner to the outer these are: the cell, a 14 mm magnetron cavity (see section 2.5.1 for the details), the C-field coil (240 turns, L=36 mm), a first magnetic shield ($\varnothing$=34 mm, L=45 mm), a Delrin® holder, and finally a second magnetic shield ($\varnothing$=100 mm, L=100 mm). The z-direction imposed by the orientation of the C-field corresponds to the symmetry axis of the cylinders, and the laser beam propagates along this axis. In such configuration, the light can only be sigma polarized (see Figure 1.6). Within the cell volume, the C-field is assumed uniform. The equivalent longitudinal shielding factor of the two combined shields is $S_L \sim$3000 [7].

2.5.1 14 mm physics package

Microwave cavity resonators are commonly used in atomic clocks exploiting magnetic resonances [37], [110], [123]. The high field density requiring a moderate input power, excellent field homogeneity, and compactness render the use of a cavity of particular interest for compact atomic clocks. Typically, the size of the cavity is of the order of half the wavelength of their resonant mode ($\lambda_{87Rb} = 4.4$ cm), but smaller realization are also possible (see Chapter 6). Various types of resonators allowing an efficient and homogeneous magnetic interrogation within the vapour cell, such as, split-ring [124], helicoïdal [125], slotted-tube [126]–[129] or lumped LC [130] resonators have been proposed. We focus here on the magnetron type cavity [131], [132], being also a loop-gap-resonator. It consists of electrodes forming a slotted tube, enclosed in a conductive cylindrical shield and inductively coupled by a loop (see Figure 2.9a). The design of this cavity was initially developed at the Observatoire Cantonal de Neuchâtel (ON) and is patented
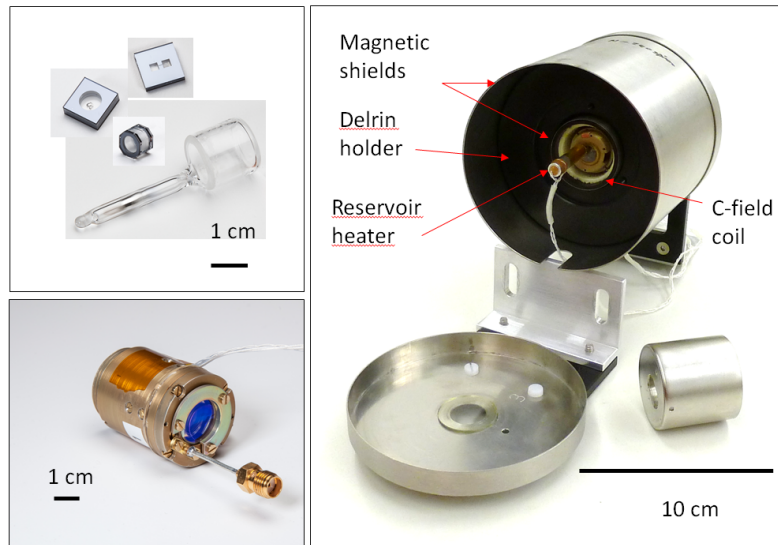
FIGURE 2.8: Details of the 14 mm PP. Left top, types of cell charaterized; left bottom, fully assembled magnetron cavity; right, fully assembled PP containing a wall-coated cell with reservoir.

[131]. It allows a fine tuning of the resonance frequency and a TE_{011}-like field mode. Such mode ensures the microwave magnetic field to be parallel to the symmetry axis, therefore inducing π-transitions (and hence the clock transition) only. This microwave cavity design was proven to be highly reliable (space qualified) since it is used in the clocks chosen for the Galileo mission [24]. In terms of clock performances it has allowed the realization of compact DR atomic clocks with outstanding short term stabilities of $\sigma_y(\tau) < 5 \times 10^{-13}\tau^{-1/2}$ [6].

The tuning of the cavity is realized by the insertion of the 14-mm cell within the electrodes: the presence of the higher dielectric constant of the glass in the vicinity of the electrodes gaps, results in a decrease of the resonance frequency of the cavity. When properly tuned, the cavity has a Q-factor of $Q_L < 350$ and a temperature shift coefficient of its resonance frequency of $TC_{cavity} \sim 40$ kHz/K [7]. This results in a cavity pulling temperature coefficient (see section 1.7.2.6) for a 1 kHz linewidth clock transition of $TC_{CP} = 6$ mHz/K.

As shown in Figure 2.8 this cavity was also used to characterize cells of dimensions smaller than 14 mm. To mimic the 14-mm cell and tune properly the cavity, the microfabricated cells were glued between two glass cylinders, as shown in Figure 2.9b, before being inserted into the cavity.
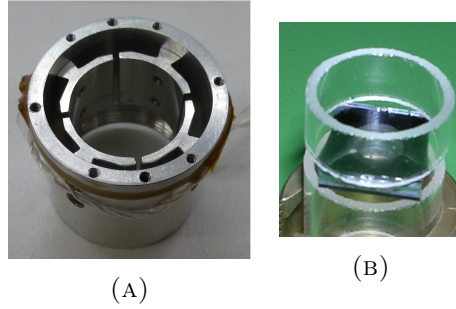
FIGURE 2.9: Details of the (A) 14-mm magnetron cavity and (B) dedicated assembly for the cavity tuning with microfabricated cells. The conductive shield length and inner diameter are 25 mm and $\sim$ 20 mm, respectively.

2.5.2 Characteristics 14 mm magnetron cavity-based assembly

Table 2.2 shows the summary of the most relevant parameters of the 14 mm PP.

TABLE 2.2: Summary of the most relevant parameters of the 14 mm magnetron cavity's physics package.

Parameter		Value
Magn. Shield. factor	S_L	$\sim$3000
C-field coil turns	N_{sp}	240
14 mm cavity		
Quality factor	Q_L	< 350
Resonance frequency temp. coeff.	TC_{cavity} [kHz/K]	40
Cavity pulling temp.coeff.	TC_{CP} [mHz/K]	6
FOF$_{exp}$ (see Chapter 6)	ξ_{exp}	0.993 [7]
Typ. cell volume	V_{cell} [cm^3]	3.5
Internal cavity volume	V_{int} [cm^3]	8
External cavity volume	V_{ext} [cm^3]	12.9

2.6 Physics package based on the micro-loop gap resonator (µ-LGR)

The detailed description of the miniature atomic resonator is given in Chapter 6, section 6.2.1.

2.7 Conclusion

In this chapter we described the three spectroscopic setups used for the characterization of rubidium vapour cells. As a comparison, the evaluation of a buffer gas pressure is discussed for the 3 schemes. The linear absorption allows a good estimation of the rubidium content and of a significant BG pressure with an uncertainty of 10 mbar. In a similar way, the sub-Doppler saturated absorption provides a 10 times more precise evaluation of the buffer gas pressure but is limited at contamination levels of few mbar only. Finally, the high resolution reached in DR spectroscopy allows a potential determination of a pure buffer gas pressure with an uncertainty of 0.02 mbar.

The two key components for the spectroscopy analysis performed within this thesis were explained in details. The laser head provides a stable, in terms of intensity, and frequency tunable coherent light field. When frequency-locked to a sub-Doppler pattern of the in-built sub-Doppler spectroscopic setup, the laser beam achieves, at 10^4 s, relative intensity and frequency stabilities of $\sigma_{I_L} < 3 \times 10^{-4}$ and $\sigma_{\nu_L} < 2 \times 10^{-11}$, respectively. The necessity of having a high rubidium vapour purity inside reference cells for laser stabilization was discussed. The clock physics package, based on a well-established 14 mm magnetron cavity [6], [24], [131], provides a temperature stabilized and well controlled electromagnetic environment for the vapour cell. The microwave field of the cavity has a TE_{011}-like mode aligned with the C-field and with the propagation vector of the laser beam. A dedicated assembly adaptor using glass cylinders allows the DR spectroscopic characterization of various types of cell of size inferior to 14 mm.

Chapter 3

Cells fabrication

Although the vapour cell is the simplest and the most compact method to confine the atoms where the electromagnetic interrogation takes place, its fabrication is quite critical: first, the alkali atoms are highly reactive, and must be handled under vacuum or controlled atmosphere. Second, the stability criteria imposed by the role of the cell as a clock reference are severe: the confinement must guarantee a highly stable inner atmosphere, in order to provide a stable frequency reference over the lifetime of the cell. It must also preserve the polarization and the coherence of the atomic vapour to guarantee a strong and narrow clock signal and must not react with the alkali vapour. So the cell must be hermetic, inert and must not liberate any gas by desorption, permeation or diffusion. It must also allow the use of buffer gas (BG) and/or anti-relaxing coatings. Finally, the precision and repeatability of the BG filling is also essential.

The choice of the container (material, shape, and manufacturability), its cleaning and sealing are critical factors for the fabrication of high quality cells. They differ depending on the size of the cell and its fabrication method: for cm-sized or bigger cells the conventional glass-blowing techniques [37] are employed, while for mm-scale cells, the silicon microfabrication techniques also used in micro-electro-mechanical systems (MEMS) are required [27]. The BG technique has been extensively used in both cell categories, but the use of coating has been restricted until recently to the glass blown cells only, as the known coatings did not withstand the relatively high temperatures employed in the MEMS sealing technologies [133]. However, an innovative

low-temperature In-bonding technique [134] has allowed recently the fabrication of a wall-coated microfabricated cell with proven functionality.

For buffer gas cells, the purity of the gases, the precise control of their partial pressures, and therefore the total pressure, are crucial for the short- and long-term performances of the reference cell. In the case of the coating, the quality (covering and purity) of the film deposited on the walls and the intrinsic properties of the coating itself dictate the performances of the cell (see Chapter 1).

In this chapter, we present the facilities (see Figure 3.1) and the various fabrication processes employed for the realization of the alkali vapour cells tested and used extensively in the frame of this thesis. The chapter is split into three parts. In the first part, the production and handling of the highly reactive alkali metal is discussed. The second part covers the production of glass-blown cells with our own facilities; the updated system is described and the recipes for the three types of cell, buffer gas, wall coated and evacuated are given. Finally, the fabrication of cells using MEMS technologies is discussed; anodic-bonding, low temperature indium-bonding and the fabrication process of an OTS-coated MEMS cell are presented. A summary of all the produced glass-blown cells is given at the end of the chapter.

3.1 Rubidium production and dispensing

Rubidium is an alkali metal highly reactive with oxygen and water. Therefore, it has to be manipulated either under high vacuum, or under a controlled atmosphere of inert or noble gases. This renders its manipulation difficult, and bringing the Rb inside the cell (dispensing it) is not straight forward. During the last decades, different methods have been proposed: the standard method consists of a metallic Rb ampoule with a breakable seal attached to a glass manifold including the cells [90], [135], [136]. Once the cell(s) is (are) cleaned the seal is broken and the Rb is chased, or distilled using a temperature gradient. Due to its high volatility, it evaporates from the hot region to condensate back at any cold point. This process is performed under high vacuum. Pipetting liquid metallic Rb is another solution that requires a non reactive atmosphere for the handling and a direct access to the reservoir of the cell; this can be done in an anaerobic glove box [137] or in liquid dodecane [138]. The chemical reaction of (meta-)stable compounds allows an "in-situ" production of metallic rubidium; the manipulation is much easier and allows

a precise control of the quantity of the rubidium. Moreover it renders affordable the use of isotopically enriched ^{87}Rb [139]. The following chemical reactions have been used successfully:

- $BaN_6 + AlkaliCl \rightarrow BaCl + 3N_2 + Alkali$ [137], [140]. This reaction takes place at 200°C.

- $AlkaliN_3 \rightarrow 2Alkali + 3N_2$ [141], [142]. This reaction takes place at 450°C or under UV light.

- $2RbCl + Ca \rightarrow 2Rb + CaCl_2$ [90]. This reaction takes place at 720°C.

- Electrolysis of Cs borate glass [143]. This reaction requires temperature above 500°C.

Although the two first reactions introduce non negligible safety issues, since the azides are highly toxic and explosive, they were demonstrated to be efficient for the in-cell alkali production, especially in the micro-fabrication processes. Other dispensing processes have also been demonstrated: the Rb dispensing pill [144], or the metal-wax micropackets [145], [146]. Both processes are laser activated: for the dispensing pill, the laser is used to raise the temperature of the pill

(A) LTF glass-blown cell filling system.

(B) LTF-SAMLAB micro-fabricated cell filling system (co-owned equipment by UniNE and EPFL). *Courtesy: Y. Pétremand.*

FIGURE 3.1: Cell filling systems employed for the fabrication of all the cells tested and extensively used in the frame of this thesis.

to 750°C for the chemical reaction of the components to take place[1]. Concerning the wax micropackets, the laser is used to ablate a silicon nitride membrane, and evaporate, within the cell, part of the wax until the Rb is released.

One of the main issues of the in-cell Rb production is due to the facts that either the reaction takes place at relatively high temperatures and/or releases other compounds, usually unwanted, than pure alkali vapour; especially N_2 is released with the use of azide compounds. This brings additional difficulties for buffer gas cells with controlled inversion temperature (see section 1.7.2.2), since this release must be anticipated and very well controlled. Moreover, the high temperatures required for the reaction represent a serious issue for coated cells, since the coatings are degraded above their melting temperature which is usually below 100°C, and for novel low temperature sealing such as In-bonding [1].

3.1.1 LTF method for rubidium dispensing in glass-blown cells

The chosen method consists of producing the metallic Rb within the manifold, or the cell ramp (see Figure 3.2), and under high vacuum, but out of the cells. The chemical reaction is similar to the one used by Missout and Vanier [90]. It has the advantage of using chemicals requiring only minor precautions. Contact with water and exposure to humidity must be reduced at its maximum and any contamination must be avoided. Thus the compounds are stocked in a dry atmosphere, and the use of glasses and gloves is mandatory. As mentioned before, this reaction takes place at 720°C, close to the glass softening point (825 °C). In addition, the rubidium reacts with the glass at elevated temperatures [37]. Therefore, care has to be taken not to heat the glass too much during the procedure.

After the reaction, most of the metallic rubidium produced will have condensated on the cold walls away from the reaction site, ready for the distillation process. Distilling the rubidium to the cells is done by heating the ramp with a flame torch, or wrapping it with heating elements, while keeping cold the regions on which we want the rubidium to condensate (e.g. the reservoirs of the cells).

---

[1]The pills are obtained by compressing the SAES getter alloys powder (See more at: http://www.saesgetters.com/it/pills-pieces). From the temperature of reaction, one might deduce that the powder is composed of RbCl and Ca.
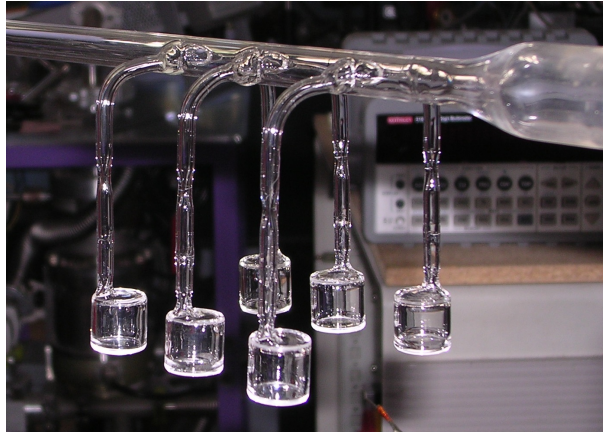
FIGURE 3.2: Typical cell ramp mounted on our cell filling system.

This ex-situ and under high vacuum production method doesn't present the drawback of by-products of the reaction: the potentially released gases are pumped away and the residues of the reaction are sealed off the manifold. Therefore, what is put inside the cells is extremely well controlled.

3.1.2 SAMLAB-LTF method for Rb dispensing in micro-fabricated cells

The micro-fabricated cells tested and studied in this thesis were produced at the wafer level, but filled with Rb individually. Since 2002, the condensation method has been also used: the metallic Rb is produced and evaporated from a heated dispenser. The vapour is then condensed inside the cooled cell body. This process is done in a vacuum chamber.

3.2 Glass blown cells and LTF cell filling system

The fabrication of glass-blown cells follows a conventional technique used by several research groups [37], [90], [136], [147]–[152], and industries: the container made out of borosilicate glass or quartz is attached to a glass manifold connected to a high-vacuum pumping system. A thorough cleaning is performed before the cell is filled with the alkali atoms and coating or buffer gas. The cell is sealed off the manifold by melting the attach point with a torch. This technique is not well adapted for small cells. The sub-centimetre sized cells are strongly limited by the

structural irregularities induced by the glass blowing technique. Nevertheless, millimetre sized cells are reported in the literature: we achieved the fabrication of a 6 mm diameter buffer gas cell showing competitive performances as a clock cell [5], Balabas retrieved non-linear magneto-optical-rotation signals in a 3 mm diameter paraffin coated cell [153], and the smallest all-glass cell reported has a volume of ~ 2 mm^3 and is made from a hollow-core glass fiber sealed with a CO_2 laser [152].

This conventional technique allows the fabrication of the three types of glass-blown cells commonly used in atomic clocks: the buffer gas cell, the wall-coated cell, both used as clock cell, and the pure alkali vapour cell (or evacuated cell) used exclusively as an optical frequency reference for laser stabilization (see section 2.4). The evacuated cell consist of a bare (uncoated) container containing ideally only the pure alkali vapour, and no buffer gas. Similar to the evacuated cell, the buffer gas cell is additionally filled with a precisely controlled amount of inert gas(es). Finally, the wall-coated cell consists of an evacuated cell of which the inner walls are coated with anti-relaxing material, but no buffer gas is used. A fourth kind can be envisaged, mixing the buffer gas technique and the wall-coating but could not be tested due to a lack of time.

Our cell filling system, initially developed for the production of evacuated and buffer gas cells only, has been modified to fabricate the four mentioned types of cells. We describe here its actual status and the fabrication methods for each type of cell. Since most of the fabrication processes are similar, we describe the production steps separately.

As already mentioned, the manufacture of these cells is quite critical. A high level of cleanliness is required and all the sealing processes are done at pressures well below the atmospheric pressure. Thus every sealing step increases the risk of breaking the vacuum, annihilating every previous step and resetting the whole process.

3.2.1 Cell body fabrication

The cell container fabrication is made by a professional glass blower. They are made out of borosilicate glass. The borosilicate glass has been used for a long time in our group and is proven to be compatible with the alkali vapours. The cell can be of arbitrary sizes and shapes, but usually a cylindrical geometry of few cm^3 is prefered (see Figure 3.3), imposed by the design of the microwave cavity (see section 2.5.1). Quartz was also used but presents additional handling

(A) 6 mm diameter and length borosilicate cell with no reservoir. Project: mUSO [5]

(B) 10 mm diameter and 19 mm length borosilicate cell with no reservoir. Projects: SQUATOS [10], ESA-LARC [6], ESA-POP [7], [8], Sinergia [154], FNS, EMRP, DLR.

(C) 25 mm diameter and length borosilicate cell with single reservoir. Project: ESA-POP [7].

(D) 20 mm diameter and length Quartz cell with two reservoirs. Made for a collaboration with INRIM (ESA-POP project [8])

FIGURE 3.3: Typical cell geometries produced and filled.

difficulties for the glass blower due to its higher melting temperature. The cells are then mounted on a ramp, or manifold (see Figure 3.2), which in turn is connected to our cell filling system. The tubes used to connect the cells to the ramp can be shortened during the sealing off or used later as reservoir for the metallic rubidium.

3.2.2 Cell filling system

The four types of cell mentioned here above can be fabricated on our cell filling system. To reach such a versatile system, a previous existing system from the "Observatoire de Neuchâtel" dedicated to the filling of BG cell has been updated. It now fulfils the following requirements:

- Reach a high vacuum as a grant of cleanliness for the cells' inner atmosphere. This prevents any gas contamination of the BG cells, or gas traces inducing broadening of optical lines in evacuated cells or uncontrolled properties in wall coated cells.

- Allow an excellent cleaning of the cells' walls to prevent ageing of the cells and deterioration of the coating properties.

- Allow the filling of glass-body cells with pure alkali metal

- Provide means and control instruments to fill the cells with a buffer gas, where the total pressure is controlled to within 1% of its value or better, in order to achieve low intensity-related light-shift for clock operation.

- Provide means and control instrumentation to prepare buffer gas mixtures, where the partial gas pressures are controlled to within 0.2% of their values or better, in order to obtain a low temperature-shift of the clock resonance within few Kelvin around a chosen operating temperature.

- Allow for coating the inner walls of the cell.

The cell filling system consists of two independent high vacuum systems sharing a common connection port for the cell ramp. One system (main system) is extremely clean and dedicated to the production of the evacuated and BG-filled cells exclusively. the second one (auxiliary system) is only dedicated to the fabrication of wall coated cells. The coating is made by vapour phase deposition and the whole vacuum system might be coated as well, reducing its level of cleanliness. A liquid nitrogen (LN) trap ensure the coating condenses elsewhere than in the pump. Turbo pumping groups (primary: scroll pump, secondary: turbo pump), coupled to ultra high vacuum (UHV) components (CF; ConFlat) nipples, tees and valves) allows a vacuum below 10^{-7} mbar. The connection of the cell ramp to any of the vacuum systems is also made using CF flanges. The use of CF flanges is driven by its resistance to relatively high temperatures required for the cleaning process; and by its vacuum characteristics: it is not permeable and doesn't outgas. The main system is connected to a gas mixing system. In contrary to standard method using an empty airlock chamber [90] (both gases mixing by diffusion), we use a gas mixer based on the principle of gas stream through super-sonic nozzles. It provides an extremely precise mixing of two gases (0.5% rel.). Such a precision is required for reproducibility in BG-cell fabrication (see section 3.2.4). Finally, the common connection port for the cell ramp, is located on top of a thermally isolated table. A scheme of the entire cell filling system is depicted in Figure 3.4.
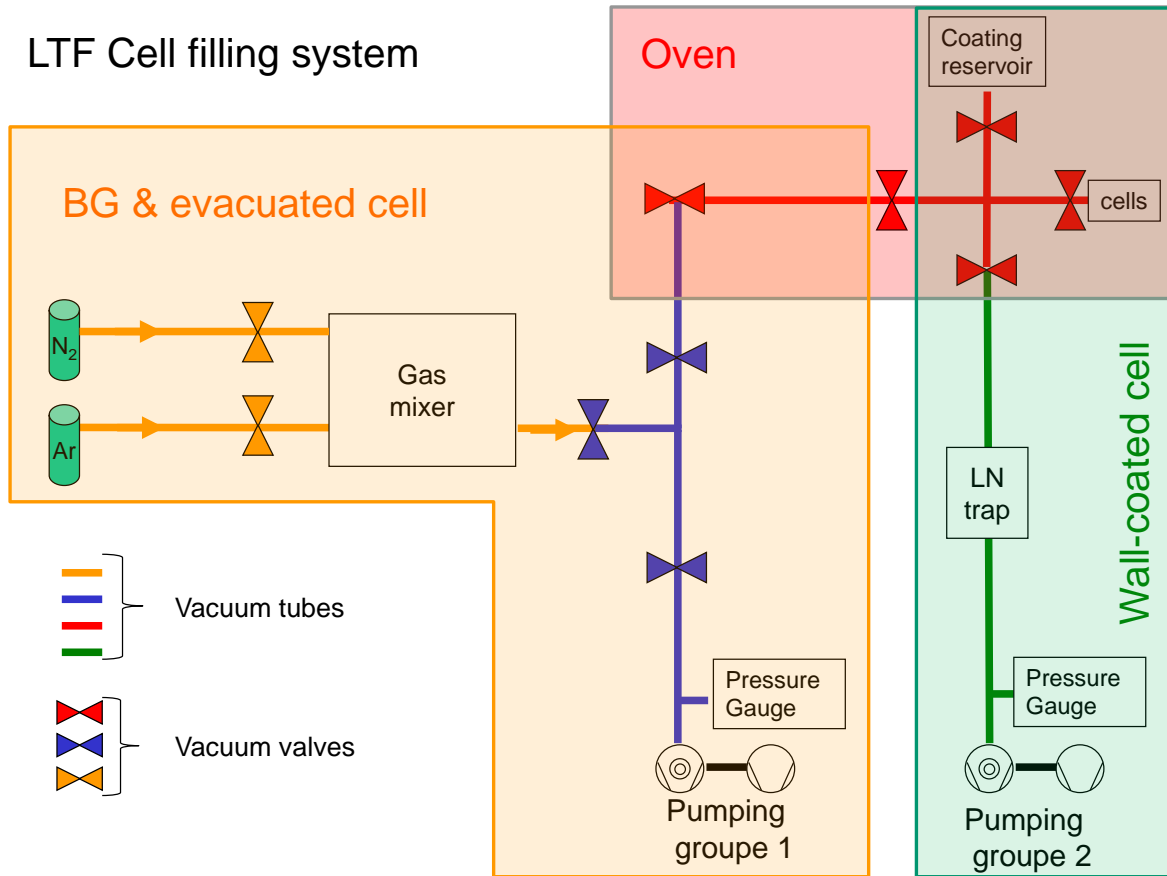
FIGURE 3.4: Scheme of the LTF cell filling system.

3.2.2.1   Cell cleaning

One of the most crucial steps in the production of the cells is their cleaning, especially for the evacuated cells. Our experience in the fabrication has shown that an insufficient cleaning can be responsible for the extremely low (null) production yield of evacuated cells. For the coated cells, as well it has been observed that a careful cleaning can dramatically reduce $\Gamma_{2_{ad}}$ [136]. The case of the BG-filled cells might be less sensitive to the cleaning, nevertheless no test has been carried out, and the same procedure is applied to all types of cells. We extensively use the most common cleaning procedures: the outgasing. The chemical cleaning (see for example [136]) is difficult to realize with the geometry of the ramps we use, moreover the chemicals used (piranha solution) present safety issues. The outgasing process consists of baking the system out while it is under

active high vacuum. It is similar to the ones used by Robinson [63] and Bouchiat [73]. The goal of the whole procedure is to desorb water and other adsorbed contaminants as well as pyrolyse organic substances that might have been introduced during the cell fabrication. Such procedure reduces the risks of potential gas releases once the cell is sealed.

3.2.2.2 Coating deposition

Two types of evaporative coating processes, *in-situ* and *ex-situ*, have been attempted for the 14 mm scale cells. Both differ from the "standard" paraffin coating procedures that use a removable central wax carrier [38], [63], [136] in the sense that the coating is not evaporated directly inside the cells but from a distant reservoir or source.

The *ex-situ* coating was performed by R. Straessle at SAMLAB for the Parylen and OTS coatings. A detailed description of the process is given in her thesis [1], and we give here only the main steps. The entire procedure takes place before the cells are mounted on the ramp. Since the standard cleaning procedure cannot be applied to the coated cells, a chemical pre-cleaning of the inner walls of the cells is done with liquid acids. The cells are then rinsed, dried and baked out before being then coated via a vapour deposition polymerisation process in a dedicated system from Comelec SA. The cells are then mounted on the ramp.

The *in-situ* coating deposition is similar to the rubidium distillation. It takes place directly within the cell filling system and was used for the deposition of tetracontane coating. This deposition has the advantage to benefit from the cleaning described in section 3.2.2.1 without exposing the cells to atmosphere after the cleaning step. The cleaned cells are cooled down while the rest of the ramp and the coating reservoir are heated well above the melting temperature of the coating. The coating is evaporated from a parallel reservoir and deposited on the cell walls by condensation. Once the coating is thick enough, the reservoir is removed, and the ramp is pumped out.

3.2.2.3 Buffer gas filling

The BG filling is much simpler than the process for coated cells. The buffer gas mixture is directly injected into the cell manifold. The internal pressure is slowly increased using a needle

valve until the desired pressure is reached. Since the pressures required are high enough, a capacitance gauge is used to monitor the pressure inside the system.

3.2.2.4 Cell sealing

The sealing procedure is a standard glass blowing procedure. The location of the seal along a glass tube is heated up to its melting temperature, and the two parts are pulled apart. When not under vacuum, pulling apart the pieces collapses the seal region, creating a hermetic seal on both pieces. Under vacuum, the procedure is identical, but care has to be taken not to heat to much the seal region; too soft glass will be "sucked" and ripped by the vacuum breaking this latter.

3.2.3 Evacuated cells

The production of these cells requires in the following order:

- cleaning procedure
- production and distillation of the rubidium
- cell sealing

It is the simplest, but the most critical procedure since the cells are sensitive to the slightest contamination (see section 2.4.3). A thorough cleaning and especially a proper sealing are crucial for a good cell. During the sealing off, the outgassing is enhanced by the high temperature of the process and the molten phase of the glass. A non-negligible quantity of gas can be released and eventually pollute the cell, resulting in a broadening and a contrast reduction of the sub-Doppler dips (see Figures 2.6). Therefore the sealing is done under "active" vacuum (the turbo pump is not isolated). This is a risky procedure for the pump and does not allow any failure, but is required for the good quality of the cell.

3.2.4 Buffer gas filled cell

The production of these cells is similar to the evacuated ones but requires an additional step:

- cleaning procedure

- production and distillation of the rubidium

- buffer gas filling

- cell sealing

Less critical to the sealing issues than the evacuated cells, this process is not easier. Indeed, the buffer gas control is crucial for the determination of the clock frequency and its sensitivity to the temperature fluctuations. As shown by equations 1.107 and 1.112 the microwave resonance frequency and its temperature sensitivity depend on both the pressure and the ratio of the buffer gases used. While the absolute resonance frequency is not critical for secondary frequency standards, its temperature sensitivity is. Since the temperature of operation in the clock is dictated by the atomic density required, it cannot be freely chosen to comply with a mixture not sufficiently well controlled. The inversion temperature for a N_2-Ar mixture being given by equation 1.112, its sensitivity to changes in the fraction of argon, p_{Ar} is expressed as follow:

$$\frac{\partial T_{inv}}{\partial p_{Ar}} = \frac{(\delta_{Ar} - \delta_{N_2})(p_{Ar}(\gamma_{Ar} - \gamma_{N_2}) + \gamma_{N_2}) - (\gamma_{Ar} - \gamma_{N_2})(p_{Ar}(\delta_{Ar} - \delta_{N_2}) + \delta_{N_2})}{2(p_{Ar}(\gamma_{Ar} - \gamma_{N_2}) + \gamma_{N_2})^2}.$$

Figure 3.5 shows the sensitivity, $\frac{\partial T_{inv}}{\partial p_{Ar}}$ of the inversion temperature as a function of the percentage of argon. For the mixture we aim at, this coefficient is of the order of 10 K/%. This imposes a control within $\pm 0.1\%$ of the fraction of Ar to control the inversion temperature of the clock frequency within ± 1 K. Such an accuracy is theoretically achieved by our cell filling facility, but experimentally, a scattering of ± 2 K is observed for cells with nominally identical BG mixture [155]. These variations are attributed to the sealing process. Due to the elevated temperatures reached during the seal off, strong local temperature gradients can modify the internal gas pressures, and thus the relative proportions.

3.2.5   Parylen N & C coated cell

The fabrication of parylen coated cells uses the *ex-situ* coating technique as described in section 3.2.2.2. Since the cells are already coated when mounted on the ramp, the filling procedure is similar to the evacuated cells, and only the cleaning procedures differ. The temperature limitation
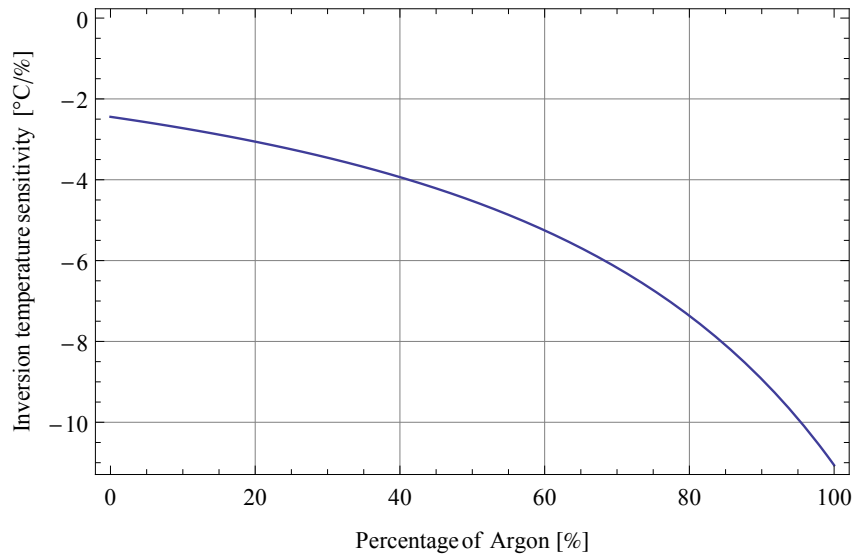
FIGURE 3.5: Theoretical sensitivity of the buffer gas inversion temperature (argon-nitrogen) as a function of the percentage of argon.

imposed by the coating doesn't allow the standard treatment, and outgassing is performed for few days, but at a moderate temperature of $\sim 80°C$ only.

3.2.6 Paraffin coated cell

The fabrication of paraffin coated cells is well reported in the literature by several research groups. Three methods of deposition are proposed: a resistive filament covered with tetracontane, is introduced inside the cell and a current is applied to heat, evaporate and deposit the coating on the cell walls. [38], [63], [136]. Phillips proposes also a wet deposition in which the tetracontane is dissolved in toluene [136]. The deposition from the evaporation of the coating from a side arm or reservoir of a single cell was introduced by Alexandrov and Balabas [72], [148], which has allowed the fabrication of alkene 1-nonadecene wall coated cells exhibiting Zeeman population lifetimes of about 3 seconds [150]. These methods allow only the production of one cell at a time, and Castagna et al. generalized the side arm evaporation method to a multiple cell manifold [149].

The works of Alexandrov [148], Castagna [149] and Phillips [136] were used as a basis to develop our own recipe. The production of wall coated cells requires the same level of cleanliness of

an evacuated cell, but the coating cannot sustain the elevated temperatures used for baking the cells. Therefore it has to be introduced post cleaning. Unlike the processes for evacuated or buffer gas cells, this recipe needs an additional volume, the coating reservoir. This reservoir must be independent from the cell manifold. Removing it from, or adding it to the system must not affect the cleanliness of the cells, and cleaning it must be done independently from the cells. To do so, an airlock system, with the help of three valves, was implemented on the filling systems. It allows the ramp, the coating reservoir and the pump to be independently and completely isolated from each other.

The fabrication procedure can be summarized as follow:

- cell cleaning procedure
- connecting and cleaning the coating reservoir
- *in-situ* coating by vapour phase deposition
- production and distillation of the rubidium
- cell sealing

The cleaning procedure slightly differs from the one described in section 3.2.2.1. The ramp and the empty coating reservoir are first cleaned using the standard outgassing procedure. The ramp is then isolated from the reservoir and the pump. The reservoir is filled with nitrogen, removed, filled with "flakes" of tetracontane (Sigma Aldrich, CAS Number 4181-95-7, assay > 95%), and put back onto the filling system. A second cleaning step, only for the reservoir and the coating, is performed. The parts in contact with air are briefly outgassed to remove adsorbed contaminants. The reservoir is then heated up above the boiling point of the tetracontane under vacuum while pumping for few minutes. The system is cooled down and the valves to the ramp are opened to allow the coating procedure.

The distillation of the rubidium is carefully performed to ensure a condensation in the reservoirs of the cells only and not on the coated walls. Thanks to the long reservoir, the sealing occurs sufficiently far from the rubidium and the coating locations and doesn't affect the quality of the cell. The ripening process is described in Chapter 5.

TABLE 3.1: List of produced glass-blown cell at LTF from April 2009 to December 2013.

Run #	Number of cells	Reservoir	Dimensions $\varnothing \times$ L [mm]	BG	Coating
1	2	Yes (Double)	22.66 × 22.66	Yes	No
2	10	No	10 × 19	No	No
3	4	No	14 × 23	No	No
4	10	No	6 × 6	Yes	No
5	10	Yes	14 × 16	Yes	No
6	10	No	10 × 19	No	No
7	10	No	14 × 23	Yes	No
8	10	No	14 × 23	Yes	No
9	5	No	14 × 23	No	No
10	10	No	10 × 19	No	No
11	2	Yes (Double)	22.66 × 22.66	Yes	No
12	6	Yes	25 × 25	Yes	No
13	10	No	6 × 6	Yes	No
14	10	No	14 × 23	Yes	No
15	10	Yes	14 × 14	No	Parylene N/C
16	2	Yes (Double)	22.66 × 22.66	Yes	No
17	10	Yes	14 × 14	No	Parylene N
18	10	No	10 × 19	No	No
19	6	Yes	14 × 14	No	Tetracontane
20	10	No	10 × 19 & 14 × 20	No & Yes	No

3.2.7 List of produced cells

A total of 157 cells have been produced in the frame of this thesis. Table 3.1 summarizes all of them with their filling and geometry.

3.3   micro-fabricated cells[1]

For miniature clocks, or other devices requiring millimetre-, or sub-millimetre-scaled cells, the glass blowing techniques reach their limits. Although it has been proven to be the state-of-the-art in cm-scale cells, the imperfections and the temperatures related to the melting process of the glass become too important when the size of the cell is shrunk down. Moreover, the residual stem from the sealing process has a size similar or bigger than the cell body (see for example [152], [153]). To circumvent these issues, Kitching et al. proposed in 2002 the idea of using micro-fabrication for vapour cell fabrication [27]. The MEMS technologies present an extremely high control of the dimensions, down to the micrometre level, which allows a precise and highly reproducible fabrication of sub-milimeter devices. Moreover, the possibility of batch fabrication at the wafer level and automation of the process enables the fabrication of hundreds identical samples at a same time for significantly lower overall cost of production. Several research groups have investigated these methods, developing innovative technologies for cell fabrication. The critical step for the fabrication of MEMS cells is the sealing process. Among the several existing MEMS packaging and wafer bonding [156], Glass-Silicon anodic bonding (AB) [157] has been the first successful technique employed for sub-millimetre-sized alkali vapour cell fabrication [137], [158]. It is now a standard for buffer gas vapour cell fabrication [159]–[164], but alternative sealing processes have also been proposed: glass fritt reflow [165], wax micropackets [145], Polymer bonding [166], low-temperature solder sealing [138], or low-temperature In bonding [134] (see [1], [139], [167] for more detailed reviews).

In the frame of this thesis, the reliable anodic bonding was chosen to fabricate buffer gas alkali vapour cells; but since the temperatures required for this sealing method ($>$ 250°C) are not compatible with the use of known wall coatings, the low-temperature In-bonding had been specifically developed for wall-coated cell. This development was the subject of another thesis [1], realized in collaboration with the present one in the frame of the MACQS project (see page xxix). We recall here the two sealing techniques and their related process flows for the fabrication of various types of cells. Their spectroscopic evaluations are presented in Chapters 4, 5 and 6.

---

[1]All cells were filled and sealed in the SAMLAB-LTF cell filling system (see Figure 3.1b) by R. Straessle and Y. Petremand.

3.3.1 Anodic bonding

Glass-to-silicon anodic bonding works as follow: elevated temperature (250-450°C) and a high voltage (200-1000 V) electrolyse the sodium oxide present in the glass; the O_2 anions migrate towards the interface and react with the silicon creating a thin layer of SiO_2; a strong bond is created. The fabrication process is then relatively straight forward, and two fabrication processes were developed.

The simplest one was used to produce what we call "2D" cells. This name comes from the fact that the ratio "thickness over width" is relatively small, the vapour is confined in a thin disk. The process is the following: The cells cavities are "drilled" out by deep reactive ion etching (DRIE) in a silicon wafer which is then anodically bonded to a glass wafer. The Si-wafer thickness is typically 1-2 mm and the glass wafer 500 µm. This wafer stack is then diced to obtain preforms, that are handled individually. A preform is filled with Rb (see section 3.1.2) before being sealed under an appropriate buffer gas atmosphere by anodic bonding with a 500 µm glass plate. The process flow is schemed in Figure 3.6a.

1.   Silicon wafer

2.   Photolithography and cavity etching by DRIE

3.   Wafer-level anodic bonding of Si with glass

4.   Dicing

5.   Rb deposition

6.   500 µm   Cell closing / anodic bonding After buffer-gas filling

(A) 2D cell fabrication process flow [168].   (B) 2D cell.

FIGURE 3.6: 2D cell fabrication process flow and final product.

A second process was developed in order to produce alkali cells having dimensions larger than standard micromachined but smaller than glassblown cells, for use in compact atomic devices [164]. These cells were designed in parallel of a new generation of microwave cavity developed at EPFL-LEMA (see Chapter 6) and are called "3D" cells, by opposition to the 2D's. The vapour is confined in a cylinder of 4.05 mm height × 4 mm diameter. The process flow is the following [164]: the cells cavities are "drilled" out mechanically in a 3 mm glass wafer which is then anodically bonded to a first DRIE patterned silicon wafer. A second DRIE patterned silicon wafer is in turn anodically bonded to the other side of the the previous wafer stack. A glass wafer is then anodically bonded to the 3 layer stack. Finally the 4-layer stack is diced to obtain preforms, that are then handled individually. A preform is filled with Rb before being sealed under an appropriate buffergas atmosphere by anodic bonding with a glass plate. The process flow is depicted in Figure 3.7a.

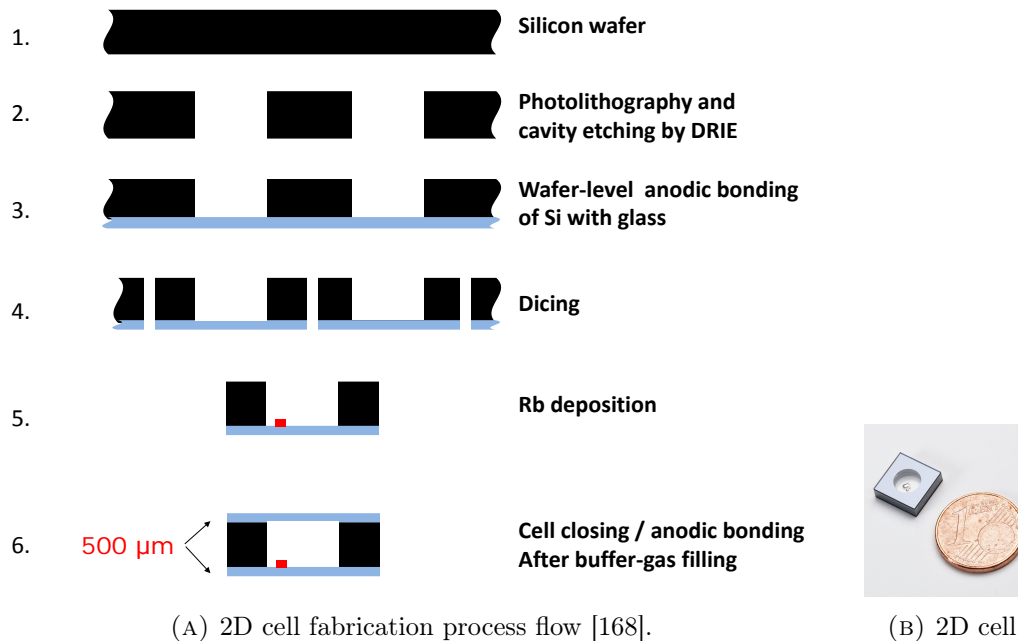(A) 3D cell fabrication process flow.   (B) 3D cell.
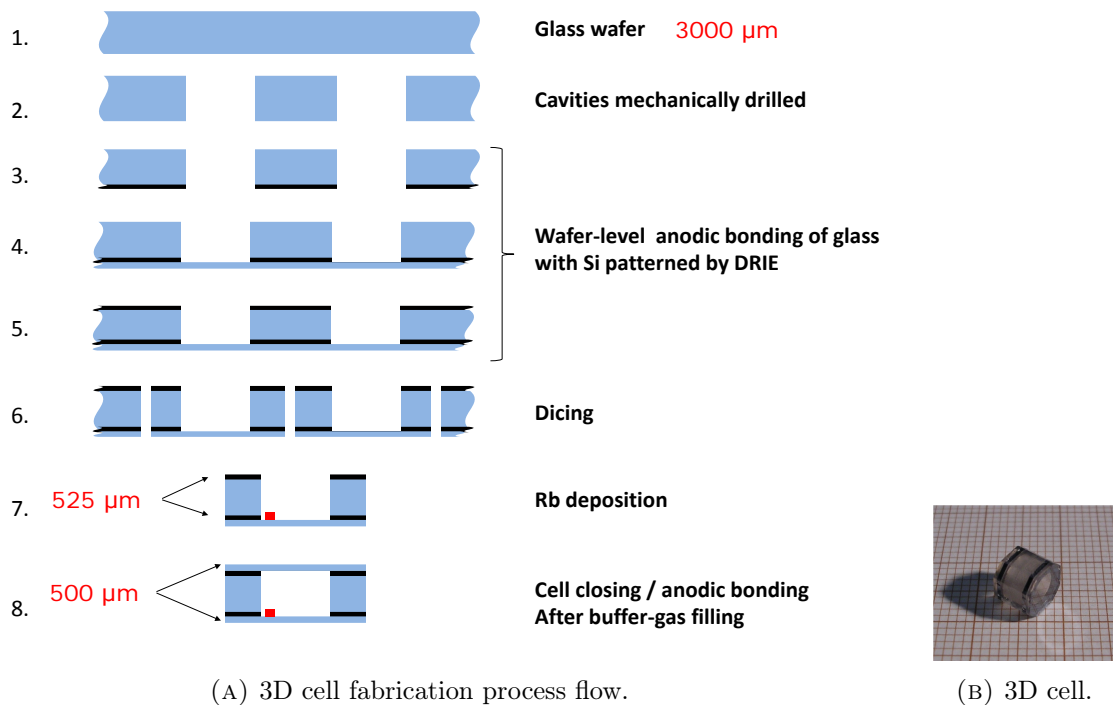
FIGURE 3.7: 3D cell fabrication process flow and final product.

For other type of cells, such as evacuated or wall coated cells, this technique reaches its limits. It

has been observed that gases were released inside the cell cavity during the bonding [1], degrading the high vacuum required for saturated absorption spectroscopy. Nonetheless, Knappe et al. showed that a careful baking of the preform and the glass cover before the anodic bonding, and the use of a getter, allow saturation dips below 35 MHz linewidth [169].

3.3.2 Low temperature indium-bonding

Clean, oxide-free indium has the property to cold weld to itself. This extremely interesting property has driven the interest of this bonding technique. The main problem is to obtain oxide-free indium. Indeed, indium is self-passivating and, in contact with air, forms an 80-100 Ångstroms thick and very hard oxide layer. Thermocompression of thick indium rings was proven to break this layer and is an efficient encapsulation technique [170]. The interaction between indium and alkali, even at low temperature, reduced considerably the lifetime of the cell, and minimizing the indium surface in contact with the alkali vapour was crucial. Another constraint arose from the limited tool pressure of the filling chamber. R. Straessle [1], [134] proposed to locate the bonding into grooves in order to isolate it from the alkali vapour; the tool pressure issue is solved by the thermocompression of multiple concentric high aspect ratio indium rings (12 µm-wide 8 µm-high) on one side with a 200 µm-wide 4 µm-height indium ring on the other side. The high aspect ratio of the indium rings helps for breaking up the indium oxide layers on both sides under moderate pressure, thus allowing a strong bond. The weak adhesion of indium on silicon is improved by using a chromium-gold adhesion intermediate layer. The fabrication process is depicted in Figure 3.8b and described in details in the thesis of R. Straessle [1].

3.3.2.1 OTS micro-fabricated cell

Thanks to this successful In-bonding technique developed at the SAMLAB, the wall coating and micro fabrication technologies could be merged together, and they could produce a micro-fabricated wall coated cell with proven antirelaxing properties (see Chapter 5). Nevertheless, due to the 140°C required for the bonding, Tetracontane could not be employed, and OTS was chosen instead. The cell consists of two chambers connected via a 100 µm × 100 µm channel. One chamber acts as a reservoir for the metallic rubidium it is not coated, the other one, OTS-coated, as interrogation chamber (see figure 3.9).

(A) In-bonded cell fabrication process flow [134]. *Courtesy: R.Straessle* [171].
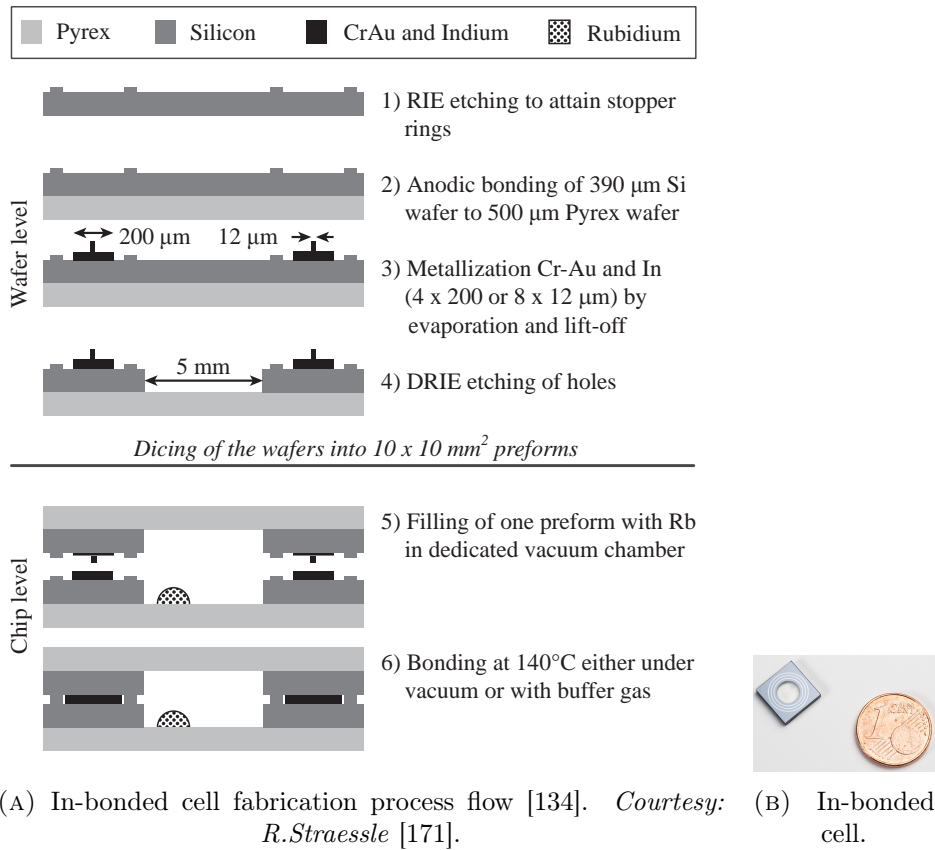
(B) In-bonded cell.

FIGURE 3.8: In-bonded cell fabrication process flow and final product.

FIGURE 3.9: Design of the micro-fabricated coated cell. *Courtesy: R.Straessle.*
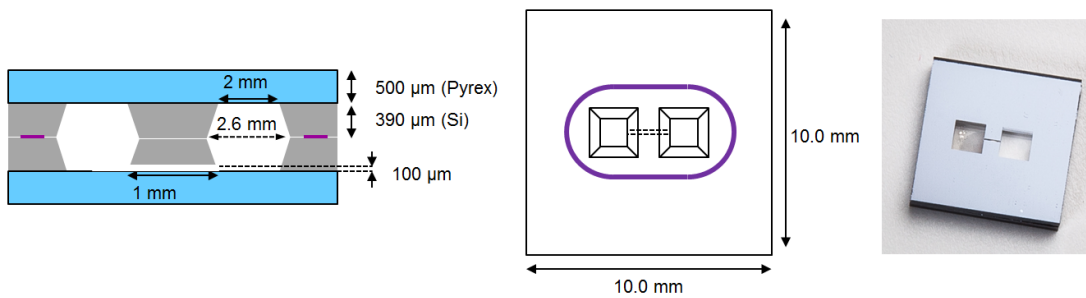
The interrogation chamber was subjected to an oxygen plasma, before the coating procedure is carried out at room temperature. The preforms were immersed in a solution of 2mM of OTS in toluene for 6 min to let the OTS coating build up on the walls. They were then rinsed in pure toluene and blow-dried with a nitrogen gun [1]. Before being filled and sealed together, the preforms were outgassed during 2 hours at 100°C. The reservoir chamber was then filled with natural rubidium before the cell was sealed with the In-bonding technique. A detailed description of the process of fabrication can be found in Straessle's Thesis. She deserves all the credit for the fabrication of this cell. The spectroscopic characterization is presented in Chapter 5, section 5.4.

3.4   Conclusion

In this chapter, we presented all the fabrication methods employed for the production of the cells studied in this thesis. A particular attention was given to the LTF cell filling system and the different methods used at LTF for glass blown rubidium vapour cells fabrication. The three types of cells, evacuated, buffer-gas filled and wall-coated, could be successfully produced, and total of more than 150 cells were fabricated within the 4 years duration of this thesis. They are listed on Table 3.1. The cell filling system was modified so that the fabrication of a fourth type of cell, mixing buffer gas and wall coating as antirelaxing technologies, could easily be envisaged without any modification. An overview of the existing Rb dispensing methods and MEMS sealing techniques was also given. The three MEMS fabrication processes employed for the production of the micro-fabricated cells employed in the frame of this thesis, including the first ever micro-fabricated wall-coated cell, were presented.

As stated by Vanier, "the manufacture of the cells is something of an art and the final success depends largely on recipes learned by past mistakes and successes" [37]. Accordingly, some of the cells produced were frustrations or missed shots, but also indispensable part of the development process. Sometimes a small hidden detail made the whole difference, sometimes fine tuning was required. But finally, all three types of cells, evacuated, BG-filled and Wall-coated could be successfully produced at the centimetre and the millimetre scale. Their spectroscopic characterizations are presented in the Chapters 4, 5 and 6.

Chapter 4

Spectroscopy as characterization tool for micro-fabricated cells and other type of cells

This chapter presents various non-destructive spectroscopic evaluation tools that will be used in the following chapter to validate the fabrication processes of various types of cells. In the present chapter, we focus on the evaluation of micro-fabricated cells and their fabrication processes developed at LTF and EPFL-SAMLAB in Neuchâtel using the equipments described in Chapter 3. The leak rate of the innovative In-bonding sealing (see Straessle's thesis [1]) is evaluated with three spectroscopic methods: linear absorption, sub-Doppler saturated absorption and double resonance. Contamination with and permeation of helium and other gases are discussed, as well as the consumption, or burning, of the alkali vapour. An evaluation of the buffer-gas filling accuracy of a cell produced with anodic-bonding using DR and CPT spectroscopy is also given.

4.1   Introduction

Inside the vacuum chamber of our cell filling system (see Figure 3.1a), the atmosphere can be extremely well controlled and monitored. The background pressure can be lowered below 10^{-7} mbar and with the gas mixer employed, the proportion of buffer gases and the total pressure can be

controlled within 0.1%. Such a control is expected to be transposed to the fabricated cells, but various mechanisms can alter the inner atmosphere during or after the sealing process. During the sealing, a contamination can occur through the outgassing of the materials of, and in the vicinity of, the cell. This phenomenon is enhanced by the relatively elevated temperature (typically well above 100°C) required for the sealing process. Moreover, the potentially large temperature gradients present during the sealing can alter locally the composition and the pressure of the gases, inducing bias to the nominal atmosphere composition. In addition to a potential residual outgassing, leaks and permeation can also alter the inner atmosphere of the cell after sealing. A leak could result from a non-hermetic sealing allowing the external atmosphere to enter the cell. The permeation is also a leak process since external gases can enter the cell, but its process is different: external gases get adsorbed on the external cell wall surface; they diffuse through the wall, and finally desorb from the inner walls [172].

These alterations of the cell's inner atmosphere are critical in view of clock applications and need to be thoroughly characterized. Indeed, the initial composition bias induced by the sealing can significantly modify the optimal operating temperature minimizing the temperature sensitivity of the clock (see section 1.7.2.2), and thus the overall performances of the clock. Moreover, the leaks are processes continuously modifying the inner atmosphere, inducing clock frequency drifts, and thus instabilities, or an accelerated oxidation (consumption) of the alkali metal. A very efficient method for inner atmosphere analysis consist of breaking the cell under vacuum and analyse its content by mass spectrometry or residual gas analysis (RGA) [173]. It has nevertheless two significant drawbacks: it is a destructive method, and it does not allow the precise quantification of potential leaks.

Here, we propose and demonstrate non-destructive spectroscopic methods for the analysis of various types of rubidium vapour cells. These methods exploit the different optical and microwave buffer gas shifts and broadenings introduced in Chapter 1 to determine, within certain assumptions, the content and the quality of the cell. Since this method avoids the destruction of the cell imposed by the RGA, it also allows the quantification of the leaks.

4.2   Evaluation of the In-bonding

In order to validate the potential of the newly developed In-bonding technique as an efficient sealing method for reference alkali cells, three spectroscopic methods were employed: linear optical absorption spectroscopy, saturated absorption spectroscopy, and laser-microwave DR spectroscopy. Two types of cells were characterized. The cells were fabricated by R. Straessle using the method described in section 3.3.2. Each cell consisted of a stack assembly of Pyrex-Silicon~Silicon-Pyrex. The '-' and '~' symbols represent anodic bonding and In bonding, respectively. Pyrex was 500 μm thick and Silicon 390 μm, resulting in an inner cylindrical vapour volume of 5 mm diameter and 780 μm thickness. One cell contained rubidium in natural isotopic abundance only, the other cell was additionally filled with 150 mbar of Ar and N_2 mixture. The BG ratio, P_{Ar}/P_{N_2} was 1.3. The studies reported in this section have been previously published in [134], that reports on the cells' realizations and evaluations.

4.2.1   Qualitative validation of the sealing: linear absorption spectroscopy

The D2 line absorption spectrum of each cell was measured by recording the transmission of the cell under test while the frequency of a monochromatic light source was swept across the absorption lines, as described in the section 2.1. To increase the absorption coefficient of the cell (see equation 1.48), and therefore the contrast of the lines, the temperature of the microfabricated In-bonded cell under test was raised and stabilized. The figures 4.1 and 4.2 show the D2 line absorption spectra of the BG cell at 70°C and the evacuated In-bonded cells, respectively, along with a calibration spectrum and the theoretical prediction discussed in section 1.5.2. The obtained absorption spectra testify the presence of a significant amount of rubidium vapour inside the cells and reject the possibility of a significant leak (see section 4.2.2 and 4.2.4.4). The In-bonding appears hermetic. The theoretical curves are calculated from eq. 1.47 and 1.48 taking into account every hyperfine transition. For both theoretical predictions, the isotopic ratio was adjusted at 40/60 of ^{87}Rb/^{85}Rb (natural ratio is 72.2/27.8 [13]) to fit at best the experimental data. Two values for the BG pressure are used for the predictions, at 125 mbar and 150 mbar. The Gaussian profile is used for the evacuated cell and the Voigt profile, issued from equation 1.30, for the BG cell. As it can be seen on both figures, 4.1 and 4.2, the predictions do not
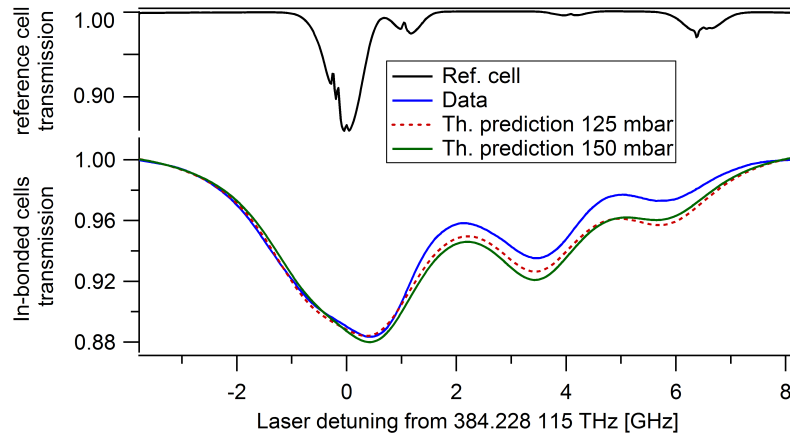
FIGURE 4.1: Experimental and predicted transmission spectra of an In-bonded BG filled cell. The cell is nominally filled with natural rubidium and a BG pressure and Ar-to-N_2 ratio of 150 mbar and 1.3, respectively. The two predictions use a 40/60 of ^{87}Rb/^{85}Rb isotopic ratio. The upper trace corresponds to the saturated absorption spectrum of the laser head's reference evacuated cell.
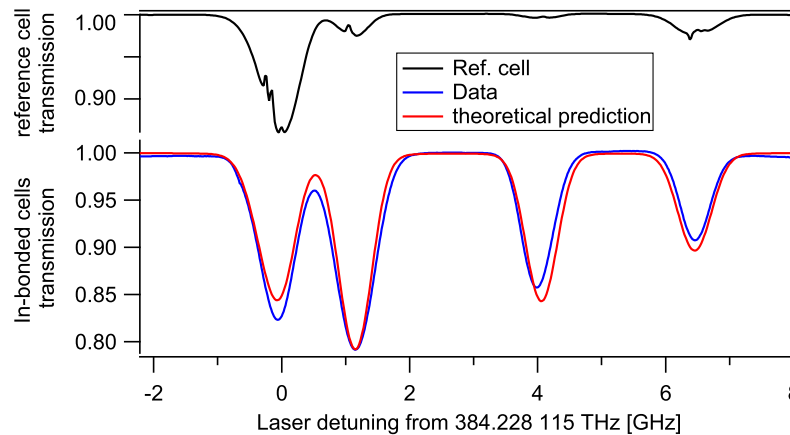
FIGURE 4.2: Experimental and predicted transmission spectra of an evacuated In-bonded cell. The cell is nominally filled with rubidium in natural isotopic abundance only. The prediction uses a 43/57 of ^{87}Rb/^{85}Rb isotopic ratio and a contamination of 1 mbar of N_2. The upper trace corresponds to the saturated absorption spectrum of the laser head's reference evacuated cell.

perfectly reproduce the acquired data. Nonetheless, some conclusions can be drawn from these measured data, initially performed to be only qualitative preliminary test:

- The obtained spectra prove that both cells contain rubidium in vapour phase. Moreover, the strengths of the absorption lines correspond qualitatively to the predicted ones. This

proves that the potential consumption of the rubidium by oxidation, or "burning" process, is sufficiently slow to let the pressure of the rubidium vapour build up until it reaches its saturation vapour pressure.

→ The cell is *hermetic*, but its tightness remains to be quantified.

- No significant broadening is visible for the evacuated cell (Figure 4.2), testifying the absence of a potential gas release during or after the sealing or a leak.

  → The fabrication process is "*clean*", and the cell does not outgas nor has a leak noticeable at this level.

- A clear broadening is observable for the BG cell spectrum, testifying the presence of a buffer gas inside the cell. Although the predictions are only qualitative, a better match is found for the 125 mbar trace which shows a similar resolution of the absorption peaks.

  → The buffer gas filling is *successful* but the inner pressure appears lower than the nominal 150 mbar pressure filled to the cell. This pressure default remains to be quantified.

4.2.2 Leak rate

A leak would results from a bad sealing letting the outer atmosphere enter the cell through cracks, channels or other ways. For the simplicity of the argument and since we are working in ambient air, we only consider an income of 21% of oxygen and 79% of N_2. The other components of the ambient atmosphere are only traces, and their effect would only consist of small corrections to the main effects induced by the nitrogen and oxygen. The oxygen income will instantaneously react with the alkali atoms, creating non volatile and useless oxides. This can partly or completely eliminate the cells' atomic rubidium content; this rubidium consumption is discussed in the section 4.2.4.4. Making now abstraction of this consumption, the leak will result, before the cell's rubidium vapour is completely oxidized, essentially in an increase of the internal BG pressure due to the gas inflow, assumed to be nitrogen only.

For a given leak rate, L, the inner pressure variation is proportional to the difference between the external (P_{out}) and the internal (P_{in}) pressures [134]:

$$\frac{dP_{in}}{dt} = \frac{L}{P_{ref}V}(P_{out} - P_{in}).$$ (4.1)

L is usually expressed in mbar·l·s^{-1}. P_{ref} is the atmospheric pressure and V the internal volume of the cell. The evolution of the inner pressure is therefore:

$$P_{in}(t) = P_{out} - (P_{out} - P_0) \cdot e^{-\frac{Lt}{VP_{ref}}} \tag{4.2}$$

where P_0 is the initial pressure inside the cell at t=0. Since we expect extremely small leak rates, and an initial pressure much smaller than the atmospheric pressure, some approximations can be made leading to a simpler expression for the leak rate:

$$L = V\frac{\Delta P}{\Delta t}. \tag{4.3}$$

As discussed in section 1.5.1, the broadening of the optical transitions is proportional to the pressure of gas present inside the cell. Therefore a variation of the nitrogen pressure induces a variation of the optical broadening of,

$$\frac{d\Delta\nu_{clock}}{dt} = \frac{\partial\Delta\gamma_{opt}}{\partial P_{N_2}}\frac{dP_{in}}{dt} \tag{4.4}$$

$$= \gamma_{opt_{N_2}}\frac{L}{P_{ref}V}(P_{out} - P_{in}) \tag{4.5}$$

$$\approx \gamma_{opt_{N_2}}\frac{L}{V}. \tag{4.6}$$

Similarly, the frequency shift of the double resonance signal is also proportional to the pressure of buffer gases present inside the cell (see equation 1.107). Therefore the variation of the clock frequency shift can be expressed as follow:

$$\frac{d\Delta\nu_{clock}}{dt} = \frac{\partial\Delta\nu_{clock}}{\partial P_{N_2}}\frac{dP_{in}}{dt} \tag{4.7}$$

$$= (\beta_{N_2} + \delta_{N_2}(T - T_0) + \gamma_{N_2}(T - T_0)^2)\frac{L}{P_{ref}V}(P_{out} - P_{in}) \tag{4.8}$$

$$\approx \beta_{N_2}\frac{L}{V}\frac{P_{out} - P_{in}}{P_{ref}} \approx \beta_{N_2}\frac{L}{V}. \tag{4.9}$$
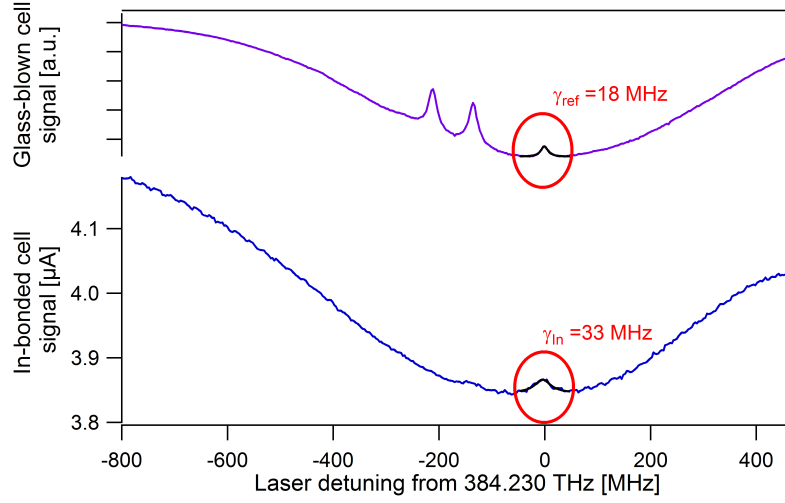
FIGURE 4.3: Saturated absorption spectra of (bottom trace) the evacuated In bonded cell along with (upper trace) the reference spectrum.

4.2.3 Quantitative validation of the sealing: saturated absorption spectroscopy of an evacuated cell

For a more precise determination of the buffer gas pressure from optical spectroscopy, the sub-Doppler saturated absorption spectroscopy was used (see section 2.2). Indeed, the good qualitative agreement between the theoretical model and the experiment seen on Figure 4.1, and the relatively small pressure broadening coefficient of the order of few MHz/mbar (see Table 1.3) with respect to the Doppler width of $\sim$500 MHz, does not allow to extract the inner pressure with a precision better than few tens of mbar. In contrast, the sub-Doppler saturated absorption spectroscopy presents Lorentzian patterns having widths of only few tens of MHz. This represents an improvement by at least a factor of ten in the relative precision, and thus allows the determination of inner contaminations at a level of the mbar precision. The figure 4.3 shows the saturated absorption spectrum of the evacuated In bonded cell along with the reference spectrum. This spectrum was recorded two month after the cell was sealed.

We focus our attention only on the $|F_g = 2\rangle \rightarrow |F_e = 3\rangle$ transition of the ^{87}Rb. For it is the most pronounced pattern, and has the advantage to be a direct and cyclic transition. Therefore its linewidth is not broaden by the contribution of another line (crossover) nor by the hyperfine

pumping [117]. Other mechanisms can also affect the linewidth and the depth of the sub-Doppler patterns, such as laser linewidth, geometrical (angle between pump and probe, cell size) collisional broadening. Since the two cells are operated under the same conditions, we only consider the additional broadening observed in the In-bonded cell, $\gamma_{add} = \gamma_{In} - \gamma_{ref} = 15 \pm 4$ MHz. This broadening can reasonably be attributed to the collisional broadening only, as the cell size is big enough. Indeed, the shortest distance in the cell between two collisions is 780 μm, much longer than the distance travelled by a thermal atom during its excited state lifetime, $\sim$10 μm. Considering helium and nitrogen, both having broadening coefficients of $\sim$15 MHz [58], the additional broadening may be explained by a $\sim$1 mbar gas contamination. The same measurement was repeated 5 months after fabrication and no further broadening was observed. From the 4 MHz uncertainty, the equation 4.9, and the coefficient from Table 1.3, an upper limit for the leak rate of 3×10^{-13} mbar l/s is estimated.

4.2.4 Quantitative validation of the sealing: double resonance spectroscopy of the buffer gas filled cell

Saturated absorption is not possible for a cell filled with several mbar of buffer gas, as the collisional broadening washes out the sub-Doppler patterns (see Figures 2.6). However, the presence of a sufficient buffer gas pressure allows the preservation of the ground state polarization and coherence, and the laser-pumped double-resonance spectroscopy can be used to analyse the pressure and its variation in the buffer gas filled cell.

4.2.4.1 Pressure evaluation

DC DR spectroscopic mode (see section 2.3.1.1) was used to measure the DR signal as a function of the laser intensity. Figure 4.4 shows its linewidth as a function of the laser intensity; the RF power is chosen low enough to not induce significant broadening. A linear extrapolation to zero light intensity provides an intrinsic linewidth of 2.022(7) kHz. This value is slightly higher than the predicted value of 1.4 kHz obtained using the equation 1.89 and a nominal pressure of 150 mbar. A reduced pressure of 100(1) mbar inside the cell could explain the experimental intrinsic linewidth. This agrees with the similar observation previously made on the linear absorption spectrum: the inner pressure appears lower than the nominal pressure filled

to the cell. A similar conclusion is drawn from the measured intrinsic shift (Figure 4.5): using the nominal gas pressure filled to the cell and equation 1.107 an offset of 21.5 kHz is expected. The measured value is only 16.88(1) kHz, corresponding to a reduced inner pressure of 117(7) mbar. The relatively big error bar arises from the uncertainty in the determination of the buffer gas mixture ratio of $\pm 2\%$ (see section 4.3).

Two independent methods, Doppler spectroscopy and DR spectroscopy show a significantly reduced inner pressure, with respect to the nominal gas pressure, of the BG In-bonded cell. This pressure reduction can be well explained by the way the nominal pressure is determined. Indeed, the gas pressure inside the filling chamber is measured far from the sealing zone and at room temperature. Since the cell is bonded at 140 °C, locally the buffer gas density is reduced, hence the equivalent inner pressure. From the perfect gas law, the inner pressure has to be corrected as follow:

$$P_{in} = P\frac{T_g}{T_s} \tag{4.10}$$

where $T_g = 313$ K is the temperature of the pressure gauge and $T_s = 413$ K the sealing temperature. A corrected nominal pressure of 114 mbar is found for the BG In-bonded cell, which is in excellent agreement with the pressures extracted from the intrinsic shift.

This is an important and non negligible effect that must be considered for the next generation of microfabricated buffer gas cells. For the glass-blown cells, a similar effect was also reported by Missout and Vanier due to the high glass sealing temperature [90], and could be solved by a proper control of the cell temperature and the double seal technique [90].
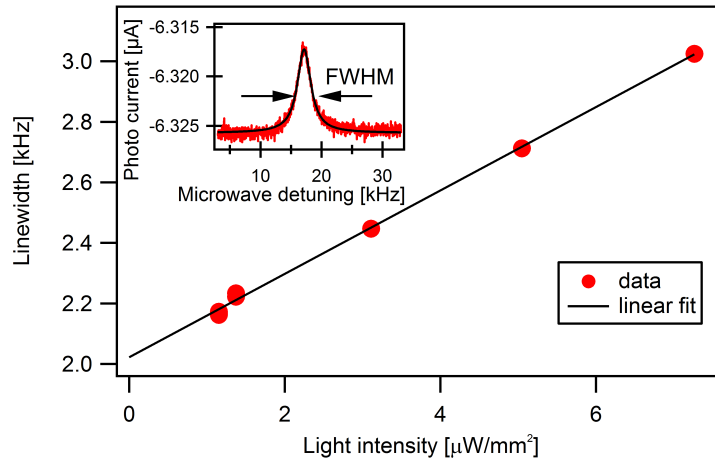
FIGURE 4.4: DR Linewidth of the In-bonded BG filled cell as a function of the light intensity. The intrinsic linewidth is measured to be 2.022(7) kHz.
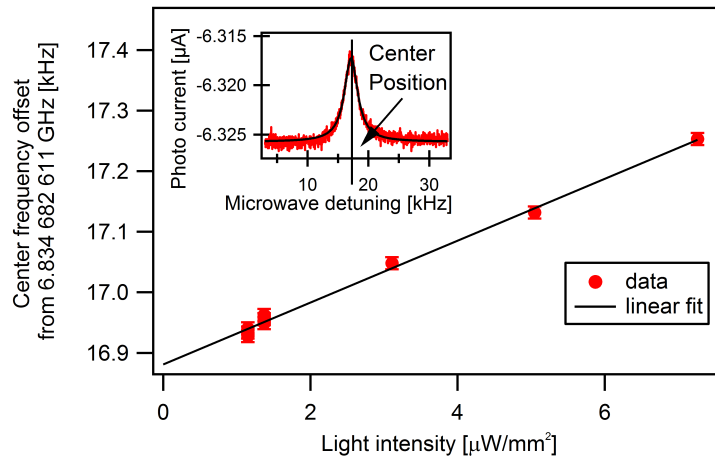
FIGURE 4.5: DR frequency shift of the In-bonded BG filled cell as a function of the light intensity. The intrinsic shift is measured to be 16.88(1) kHz.

4.2.4.2 Leak rate estimation

The intrinsic frequency shift of the BG In-bonded cell was measured four times over the timespan of one year (DC DR spectroscopic mode). Figure 4.6 shows the measured data along with their corresponding pressure variation from the initial pressure. Since for each measurement, the cell was reintroduced in the resonator, the microwave field might vary due to the positioning uncertainty of the cell inside the microwave resonator. Therefore, the error bars were increased

to take into account the systematic microwave power shifts. Assuming a cell contamination by nitrogen only, an upper limit for a potential leak rate of the cell is estimated. Using equation 4.9 and the nitrogen shift coefficient from Table 1.9, an average leak rate of $L_{In} = 5.5 \times 10^{-14}$ mbar l/s is determined. The maximum shift variation of $\sim$110 Hz, allowed by the error bars, provides an upper limit for the leak rate at a maximal value of $L_{In_{Max}} = 1.5 \times 10^{-13}$ mbar l/s. This leak rate limit is already one order of magnitude smaller than the limits of the N_2O and the membrane deflection methods reported in [1].
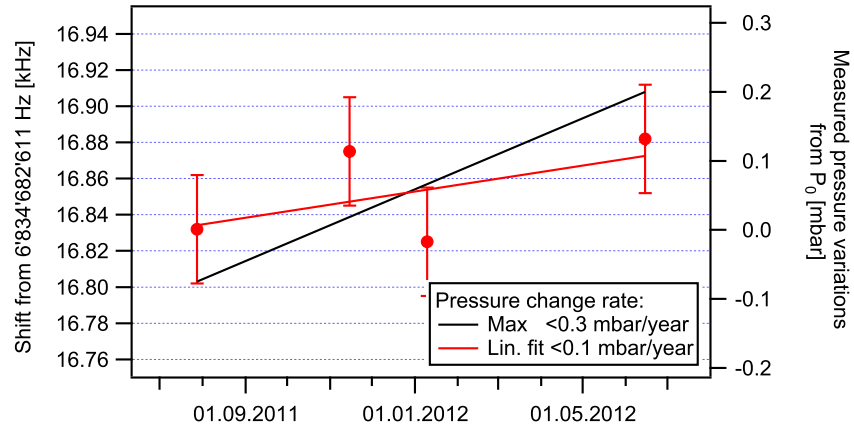
FIGURE 4.6: DR intrinsic frequency shifts of the In-bonded BG filled cell (Left axis) over 11 months, and the corresponding BG pressure variations (right axis).

Potentially, this limit could be further improved by exploiting the DR clock mode. As seen in the section 2.3.1, the DR clock mode offers 2×10^{-3} mbar resolution for the argon pressure at one day (assuming a frequency instability of $\sigma_y(1d) \sim 10^{-11}$). This resolution is improved down to 2×10^{-4} mbar for nitrogen. The resulting leak rate limit of this method in the In-bonded BG cell would correspond to 3.5×10^{-14} mbar l/s after one day only. This represents already two orders of magnitude improvement, with respect to the N_2O method [1]. Moreover, the DR clock mode does not require a vacuum chamber nor a pressurized N_2O atmosphere, and is achieved within one day only. Exploiting the coherent population trapping (CPT) instead of the DR of alkali atoms could add simplicity of operation to this fast, extremely efficient and non-destructive method for precise leak rate measurements of MEMS sealing methods. Moreover, since the microwave cavity is not required for CPT the error bars arising from the positioning uncertainty would be significantly reduced.

4.2.4.3   Gas permeation

Gas permeation through the walls of the vapour cells is an additional process that can drive pressure variations of the cell's inner atmosphere. Helium permeation was already considered by Camparo [109] as a cell ageing process for glass-blown alkali vapour cells. The permeation is considered as a leak process, as it induces a gas income. Nevertheless, the process is different to a leak: instead of passing through a channel, external gases are adsorbed on the outer part of the cell, they diffuse through the material and then desorb inside the cell [172]. It is commonly expressed as a total atomic flux q, in m^3s^{-1} at standard conditions defined as follow [174]:

$$\frac{dq}{dP} = K\frac{A}{d} \tag{4.11}$$

where K is the permeation constant (in $m^2s^{-1}Pa^{-1}$), also called permeation velocity constant depending on the gas and the membrane material. A is the area of exposed membrane, and d the membrane thickness. The link to a leak rate is straight forward using the law of perfect gases:

$$L = K\frac{A}{d}P_{ref}^2 \tag{4.12}$$

The permeation of other atmospheric gases (Ne, Ar, N_2, O_2) can be neglected, since their permeation constants through glass are smaller than helium's by several orders of magnitude [172]. The same argument applies on helium permeation through silicon [134], and this process is also neglected. We focus this discussion on helium permeation through Pyrex only. Helium through Pyrex permeation constant is $K_{He-Pyrex} = 3 \times 10^{-19}$ $m^2s^{-1}Pa^{-1}$ [175], which leads to a leak rate of $L_{He} \equiv 2.4 \times 10^{-9}$ mbar l/s for the geometry of the In-bonded cell having two windows of 5 mm diameter and 0.5 mm thickness. This is four orders of magnitude bigger than the leak rate limit measured in the previous section. However, the maximal inner helium pressure cannot exceed the partial atmospheric helium pressure of $P_{ext} = 5.3 \times 10^{-3}$ mbar. Since helium has a pressure shift coefficient for the clock transition of 540 Hz/mbar, the maximal induced shift is <3 Hz, with an initial clock frequency drift of 0.04 Hz/day or 5.9×10^{-12} (see equation 4.8), well below the resolution of this DC DR spectroscopic method.

The permeation induced drift can present issues for clocks applications. However, this effect is limited in time under a stable external atmosphere. Indeed, the evolution of the inner helium pressure has an exponential behaviour (see equation 4.2) to balance the external and internal

pressures. For a given cell volume, V_{cell}, the typical time constant τ_{He}, or time required for the pressure to reach 63% of the external pressure, is given by:

$$\tau_{He} = \frac{V_{cell}P_{ref}}{L_{He}}.$$ (4.13)

In the case of the In-bonded cell, this time constant is $\tau_{In_{He}} = 72$ days, which is of the same order as reported for glass-blown cells in [109]. 500 days are required to balance the internal and external pressure within 0.1 %. For the thick glass-core, or 3D cells, the time constant becomes $\tau_{3D_{He}} = 51$ days, and a full year is required to balance the pressures. As a general rule for helium permeation through cells walls, a time of $7\tau_{He}$ is required until the pressures are balanced within 0.1 % and the drift reaches a value below 1×10^{-13} /day.

4.2.4.4 Consuming the rubidium

For a leak small enough, the oxidation of the rubidium has no significant effects on the spectroscopic properties of the cell, since every alkali atom reacting with the oxygen is directly replaced by a new one from the metallic bulk to equilibrate the vapour pressure. The consequences are simply a slow consumption of the metallic rubidium reservoir, and after a certain amount of time (depending on the leak size) all the metallic rubidium will have reacted, resulting in a "dead" cell containing no rubidium vapour any more. But, the effect of the nitrogen pressure increase is visible way before the cell dies by oxidation: a potential and significant increase of 1 mbar of nitrogen pressure (inducing a 400 Hz shift or 6×10^{-8} relative shift) would come along with an income of 0.3 mbar of oxygen. In a 50 mm^3 cell (equivalent to the 3D cell), this corresponds to < 3 μmol that would burn only 0.3 μg of Rb, while the cell is commonly filled with more than 100 μg.

Other processes, such as reaction with indium [1], diffusion through the glass, also dry up the rubidium source. But these processes are relatively slow and thanks to the continuous equilibration of the vapour pressure, the rubidium density may be expected to be constant; it is therefore difficult to observe it spectroscopically. A dynamic reduction of the absorption strength could only be observed when solely Rb vapour exists in the cell. Compared to the lifetime of the cell this time is short, and we were not able to observe the reduction of the vapour density, but only the two steady-state phases where the vapour pressure is constant or null.

4.3   Evaluation of the BG filling in anodic bonded cell

We assumed for the In-bonding technique that the percentage of buffer gases filled in the cells had a $\pm 2\%$ uncertainty. In order to validate this statement, a similar cell was fabricated with an initial buffer gas filling of 60 mbar mixture of 57% of argon and 43% of nitrogen. This cell was anodically bonded to ensure its resistance at temperature up to 100°C. Moreover the cell was thicker (2 mm) and with the reduced buffer gas pressure, a sufficient absorption contrast, even at temperature as low as 55°C, was observed. Laser-pumped double-resonance spectroscopy in DC mode was also used to analyse this buffer gas filled cell. The experimental setup and method are identical to the one presented in the section 2.3. The intrinsic shift of the cell was measured at several temperatures between 65 and 100°C (See Figure 4.7). From a quadratic fit, the extremum abscissa stands at 76(3)°C, which corresponds, using equation 1.112 inverted, to an argon percentage of the buffer gas of 58.0(6)%. Similar measurement was performed using CPT spectroscopy of ^{85}Rb in the D1 line [29], using a setup similar to the one described in [5][1]. For a better comparison on figure 4.7, the intrinsic shifts obtained with the ^{85}Rb were rescaled to the ^{87}Rb frequency by multiplying them by the ratio of the hyperfine frequencies of the ^{87}Rb and ^{85}Rb [93]. The inversion temperature obtained with CPT was 73(3)°C, corresponding to an argon percentage of 58.6(6)%. Both results match within 2% the nominal percentage of argon in the mixture. This shows a relatively good control of the buffer gas mixture, in spite of the potentially large temperature gradients present in the filling chamber during the sealing procedure. The equivalence between the two drastically different spectroscopic methods and the independence of the buffer gas shift to the method of interrogation also validates the data obtained adapting a 14 mm microwave resonator to micro-fabricated cells (see section 2.5).

---

[1]This methods has also been employed by Boudot et al. to characterize a Ne-Ar mixture in Cs cells [96].
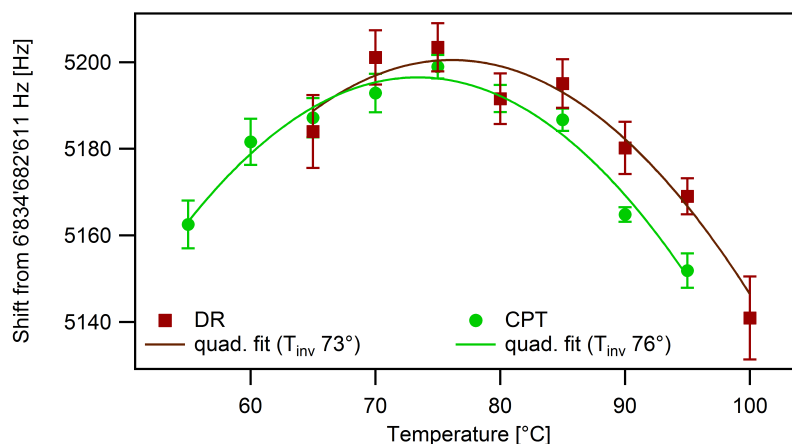
FIGURE 4.7: Intrinsic temperature shift of a buffer gas-filled anodic-bonded cell, measured independently with DR on ^{87}Rb, and CPT on the ^{85}Rb content.

4.4 Conclusion

In this chapter, we used the various spectroscopic methods described in the Chapter 2 as non-destructive methods for the characterization of the content of rubidium vapour cells. The resolution and applications of each method were discussed and are recalled here. The linear absorption in combination with the basic theoretical model presented in Chapter 1 allows the determination of a total inner buffer gas pressure with a resolution of few tens of mbar. It is compatible with any types of cells and serves as a go/no-go test for further analysis. The saturated absorption and DR spectroscopy demonstrated better precisions but their use is restricted to certain types of cells only. While the saturated absorption is dedicated for the measure of *small* contaminations in an evacuated cells only, DR is for the evaluation of a buffer gas pressure of at least few tens of mbar. Hyperfine DR spectroscopy of alkali atoms is demonstrated to potentially reach an unrivalled leak rate detection limit for N$_2$ at the level of 3.5×10^{-14} mbar l/s after one day only.

A contamination level below 1 mbar and a leak rate $L_{In} < 1.5 \times 10^{-13}$ mbar l/s associated to an innovative sealing method were measured using sub-Doppler saturated absorption and DC mode DR spectroscopy, respectively. These results demonstrate the hermeticity and the cleanliness of the innovative low temperature In-bonding sealing process developed by the SAMLAB and LTF, as well as its compatibility with the realization of alkali vapour cells in view of miniaturized atomic clocks. The low temperature of the sealing allows to envisage the combination of MEMS

technology and wall-coating (see Chapter 5). A systematic bias of more than 30% in the nominal buffer gas pressure of microfabricated cell is also identified. Originating from the temperature gradients present during the sealing process, the nominal pressure overestimation can be easily corrected.

The permeation process through silicon and pyrex was also treated as a leak. The permeation of other gases than helium through Pyrex, as well as the permeation of helium through silicon could be neglected based on their insignificant permeation rates reported in the literature. Only helium permeation through pyrex is retained and discussed in detail. The clock frequency drift induced by helium permeation remains below 1×10^{-11} /day for the microfabricated cells considered in this manuscript. Pressure equilibration time constants are calculated to be several tens of days.

Finally, a method to characterize the buffer gas mixture ratio is presented. Based on the inversion of the temperature coefficient of the clock transition, it allows the determination of the mixture percentage with a resolution of $\pm 2\%$. An excellent control of the buffer gas mixture during the filling and sealing process of the microfabricated cells is demonstrated for the dispensing method and the sealing technique based on anodic bonding described in Chapter 3. The measurement of the inversion temperature using DR spectroscopy on ^{87}Rb was also compared to the one using CPT on ^{85}Rb. Both methods gives similar results.

Chapter 5

Anti-relaxation wall coatings for atomic clocks

This chapter describes the spectroscopic studies performed on the various types of anti-relaxation wall-coated cells fabricated in Neuchâtel. At first a brief introduction on the state-of-the-art of wall coating and their application fields is given. Four types of coating have been tested: (1) tetracontane in glass blown cells, (2) OTS in a microfabricated wall-coated cell, and preliminary spectroscopic studies on (3 & 4) Parylene N & C as wall coating in glass-blown cells are presented in section 5.2. An update of the glass-blown cell filling system (see Figure 3.1a) has allowed the fabrication at LTF of high quality tetracontane-coated cells. The spectroscopic study of these cells is presented in section 5.3. An original observation of the coating's ripening process using DR is presented and interpreted. It is followed by the measurement of the tetracontane's intrinsic properties and the consequences on clock applications. Finally, the proof of principle for a micro-fabricated wall coated cell showing reduced relaxation rates is given in section 5.4. The origins (buffer gas or coating) of the reduced relaxation rates are discussed and effective anti-relaxation properties of the coating in this cell are demonstrated.

5.1 Introduction

Anti-relaxation wall coatings present an interesting alternative to the buffer gas for the preservation of the atomic coherence and ground state polarization of the alkali vapour in a cell. Since the first paper published on a paraffin coating presenting anti-relaxation properties in 1958 [176], several studies, based on a detailed theoretical description developed by Bouchiat et al. to describe the alkali spin surface relaxation process [38][1], have been undertaken to understand the origin of the anti relaxation properties: Camparo et al. studied the interactions between a rubidium vapour and a dichlorodimethylsilane coating [177], Stephens et al. measured the adsorption energy, outgassing, and chemical reaction rates between a caesium vapour and an octadecyl-trichlorosilane (OTS) coating [178], Seltzer et al. studied potassium polarization lifetimes in the presence of OTS, alkyltrichlorosilane monolayers and octadecylphosphonic acid monolayers [179]. Yi et al. tested Rb on OTS self-assembled monolayers [75], Ulanski measured the dwell times of rubidium on OTS and paraffin coated surfaces [180], and Seltzer published an alternative analysis of paraffin coatings based on surface science techniques [76], but currently the details of the anti-relaxation processes are still not fully understood [180]. Some authors like to define the application of a surface coating as *a rather laborious process with some degree of "black magic" that does not always yield reproducible results* [181]. However several studies have exploited these coatings and their anti-relaxation properties in various fields of physics: atomic clocks [78], [122], [182], [183], atomic magnetometers [149], [150], [184], [185], electromagnetically induced transparency (EIT) and slow-light [186], fundamental symmetry studies [187] magneto-optical traps [178], spin squeezing [188], long-lived entanglement [189] and quantum memory [190].

All the reported efficient coatings for alkali metals have in common an organic chain to which are attributed the anti-relaxation properties. They can be split into three categories, organosilane, alkane and alkene:

Organosilane compounds are composed of an hydrocarbon tail (hydrophobic) and a highly reactive silane head which can either bind to the -OH endings on a surface or to each other [1]. Organosilanes have the particularity to form on glass self-assembling mono- or multi- layers, which depends on the deposition method. The first report on this type of coating dates from

---

[1]We recall its main formulae in the Chapter 1.

1961 using dimethyldichlorosilane under the commercial name of Dri-Film [191]. The most effi-
cient organosilane, as anti-relaxation coating, reported so far is OTS. It can preserve the rubidium
atomic hyperfine polarization during up to 900 collisions, and can be operated at up to $160°C$
before its anti-relaxation properties are degraded [133][1]. An OTS coating in a micro-fabricated
anodic-bonded cell for a miniature clock has already been reported [192], but no conclusive proof
of anti-relaxation properties being due to the coating and not to a buffer gas was given. Al-
ternative coatings with a similar tail group structure, but different head groups have also been
reported: octadecylphosphonic acid monolayers [179] and nonadecylbenzene [193], but only the
nonadecylebenzene exhibited anti-relaxation properties. These coatings are commercially avail-
able from standard chemistry suppliers.

Alkane compounds, or paraffins, are saturated hydrocarbon chains of chemical formula C_nH_{2n+2}.
Commercially, they are also known as Paraflint. Alkanes are probably the most widely used coat-
ings, given the majority of the alkane-based studies found in the literature. Eicosane ($C_{20}H_{42}$)
was the first coating successfully tested with alkali atoms and could preserve the rubidium atomic
spin during up to 600 collisions [176]. For Rb on paraffin, up to 10 000 polarization-maintaining
collisions have been reported by Bouchiat et al. [73]. They also mentioned an improvement of
30% for shorter hydrocarbon chains and a five times improvement for deuterated polyethylene.
Since the alkanes' maximal temperatures of operation are dictated by their melting tempera-
tures [73], [79]: $96 - 100°C$ for hexacontane ($C_{60}H_{122}$), $80.5°C$ for tetracontane ($C_{40}H_{82}$) and
$35 - 37°C$ for eicosane ($C_{20}H_{42}$), longer chains appear preferable for higher operation tempera-
ture. Alkenes have been extensively used for basic alkali-coating interaction studies [38], [176],
[180], [194], rubidium clocks [63], [78], potassium-[184] and caesium-based magnetometers [149],
[153], light induced atomic desorption (LIAD) of potassium, rubidium, caesium [148], [195], and
sodium [196], [197], and slow-light experiments with rubidium [198]. Rubidium clock short-term
stabilities down to $2.8 \times 10^{-12}\tau^{-1/2}$ from a 14 mm diameter cell [122] and magnetic sensitivi-
ties down to $10 \text{ fT}/\sqrt{\text{Hz}}$ with a potassium cell of 15 cm diameter [184] and $4 \text{ pT}/\sqrt{\text{Hz}}$ with a
spherical glass-blown cells of only 3 mm diameter [153] have been reported. Alkane coatings are
commercially available from standard chemistry suppliers.

Alkene compounds, or olefins, are unsaturated (one C=C double-bond exists in the molecule)
hydrocarbon chains of chemical formula C_nH_{2n}. They have been recently proven to be the most
efficient anti-relaxing coatings, allowing up to 10^6 Zeeman polarization-maintaining collisions of

---

[1]2000 collisions are reported in the same article for potassium.

rubidium atoms in a spin exchange relaxation free (SERF) magnetometer configuration [72], [150]. In this case, the coating material was AlphaPlus® C20-24 normal alpha olefin from Chevron Phillips. It has a relatively low melting temperature which limits its anti-relaxation properties to temperatures below 33°C, and its intrinsic properties such as stability of the coating remain to be studied. However, higher temperatures of operation might be achieved with AlphaPlus® C30+ normal alpha olefin from Chevron Phillips, having a melting temperature of 71°C. To our knowledge, this material has only been reported in [76], without any spectroscopic data.

Recently, another material was also proposed and patented by Abbink et al. as anti-relaxation coating for NMR gyroscopes: the Parylene [166]. It is a polymer with a cyclic alkene group which presents excellent properties. It is transparent, has a melting temperature of 290°C for Parylene N or above for Parylene C, is chemically resistant and its deposition process is similar to CVD (Chemical Vapour Deposition). The coating is completely uniform, without pinholes, and conforms perfectly to even the most complex structures. It is usually used as a protective layer in harsh environments and for packaging applications and doesn't outgas[1]. In their patent, Abbink et al. state that *"Parylene coating minimizes interaction of the excited state of the alkali metal, increases lifetime of the excited state, and minimizes interaction of nuclear spin states with the cell walls"*, but no detailed results have been published. Its efficiency as anti-relaxing coating remains to be demonstrated.

The purpose of this chapter is triple:

1. To validate the updates of our cell filing facility to enable the production of wall coated cells and our fabrication recipe described in the Chapter 3. Initially, our facility allowed for the fabrication of buffer gas and evacuated cells only. The choice of tetracontane came naturally as a benchmark for successful realization of wall coated cells.

2. To deepen and extend our understanding of Parylene and tetracontane coatings: spectroscopic studies on Parylene coated alkali vapour cells were not reported in the literature. Also, the choice of Parylene as an alternative coating was motivated by its extremely interesting proven properties, and its chemical structure similarities with the alkenes. The anti-relaxing coatings are known to be of poor quality right after the production phase, and need to go through a so-called ripening process to show efficient anti-relaxation properties and a stable clock signal. This process is usually mentioned as a required step in the production phase but it has not been

---

[1]see www.comelec.ch

120

studied in details and is not yet fully understood. Producing the cells in our laboratory gave us the opportunity to observe the evolution of the DR signal of a coated cell during this ripening process.

3. To demonstrate the anti-relaxation properties of the OTS coating in our first wall-coated MEMS cell. The realization of such a cell was allowed by the excellent hermeticity and the low sealing temperature achieved by the In-bonding (see Chapter 4).

5.2   Parylene N/C

As shown in Table 3.1 two runs of 14 mm diameter cells coated with Parylene were produced. The fabrication process is described in section 3.2.5. The first ramp consisted of 4 cells coated with Parylene N, 4 with Parylene C and 2 uncoated cells serving as a references for the batch. Before being filled with Rb, the coated cells were clearly distinguishable with their milky white look (see Figure 5.1). One also sees the brown traces left by the Parylene that was oxydized or burnt during the soldering of the cells onto the ramp. After the Rb filling, the Parylene N cells were lightly purple coloured, while the neck of the Parylene C cells was strongly darkened. This was an unexpected reaction, since Parylene is supposed to be biocompatible and very chemically resistant. The cells were nevertheless sealed off the ramp as they still contained metallic rubidium in their reservoirs.

No optical absorption of the rubidium lines could be retrieved from the Parylene C cells, although the temperature of the reservoir was raised up to 80°C and metallic rubidium still visible in the reservoir. The impossibility to build up a vapour pressure sufficient to allow spectroscopy of the Parylene C cells, is interpreted as an indication of a rapid reaction between rubidium atoms and Parlene C. Moreover, after few days, all the visible metallic rubidium in the reservoir had disappeared and the neck turned to black. Since no spectroscopy was possible, and the rubidium consumed within few days, the studies on Parylene C were not continued.

In contrast, linear and saturated absorption could be achieved in the Parylene N cells, although the cell body was slightly purple coloured (see Figure 5.3). The consumption of the rubidium cannot be excluded, but the 33 MHz linewidth of the $|F_g = 2\rangle \rightarrow |F_e = 3\rangle$ transition of the ^{87}Rb is a strong indication for a below 1 mbar BG pressure potentially present inside the cell, and

validates the non-outgasing property expected for Parylene. A DR spectroscopy was attempted but no signal could be recorded. The Parylen appears to show no anti-relaxation properties for rubidium which is in contradiction with the claim from Abbink's patent [166].

The cell fabrication method was suspected to be responsible for the non anti-relaxation properties and another ramp was produced using Parylene N only. The following modifications to the procedure were applied:

- On the ten produced cells, eight were coated, among them six had an additional plasma etching treatment before being mounted on the ramp. The purpose of this etching was to remove the coating present in the reservoir. Among the six plasma treated cells, two were additionally annealed at 250°C.

- The rubidium distillation process was also modified so that the cells are not heated during the whole filling process.

Visually, these modifications appeared to be efficient. The plasma etching solved the Parylene burning issue during the soldering onto the ramp, while the modified distillation process did not colour the cells (see Figure 5.4). Saturated absorption spectra were similar to the one presented on Figure 5.3 for all the cells but the annealed one, which showed no absorption at all.

The setup used to obtain a DR clock signal spectrum with the cells showing an absorption signal is described in section 2.3. The cells were kept at room temperature ($\sim$21°C). A D1 laser head was used for the optical pumping. A detection of the DR signal in DC mode (see section 2.3.1) was not possible since the signal-to-noise ratio was too small. For the AC mode, a frequency modulation with a deviation of 9 kHz and a Lock-In integration time constant up to 1.5 seconds was required to extract the DR signal from the noise (see Figures 5.5). The measured linewidths are the same within the uncertainties for coated and uncoated cells, and are comprised between 25 and 34 kHz. These linewidths are three times larger than the theoretical 11 kHz broadening for bare glass cells of same geometry (see Table 1.5). We attribute this factor of three to the significant RF and optical power broadening as no signal could be measured at low light intensity and low RF power. The fact that no significant difference is observed between coated and uncoated cells, is a strong indication that the coating does not present any anti-relaxation properties. Moreover,

FIGURE 5.1: Parylene ramp before being filled with rubidium.
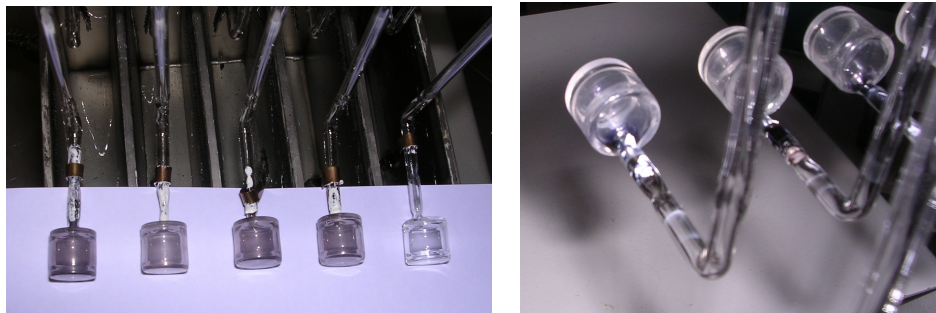
(A) Parylene N cells.

(B) Parylene C cells.

FIGURE 5.2: Parylene cells after Rb distillation.

although the cells showed no colouration at their early stage, a strong black colouration occured after few months kept at ambient temperature. All the rubidium appeared consumed, and no absorption signal could be retrieved any more. The nature of the reaction, chemical or physical, between rubidium and Parylene at the origin of this rubidium consumption and the colouration was not determined. However the conclusion that Parylene is not a suitable anti-relaxing wall coating for hyperfine microwave-optical DR spectroscopy in rubidium vapour cells is evident.
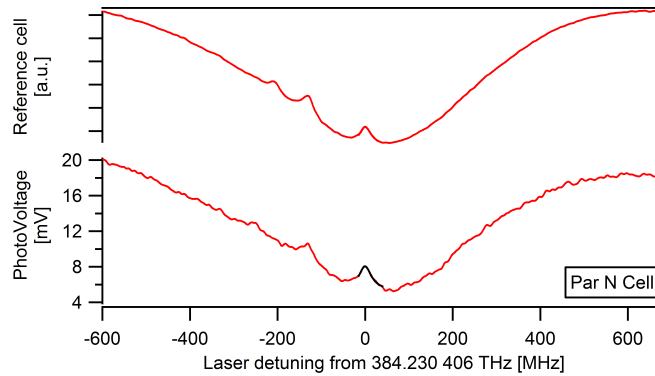
FIGURE 5.3: Saturated absorption spectroscopy of a Parylene N coated cell.
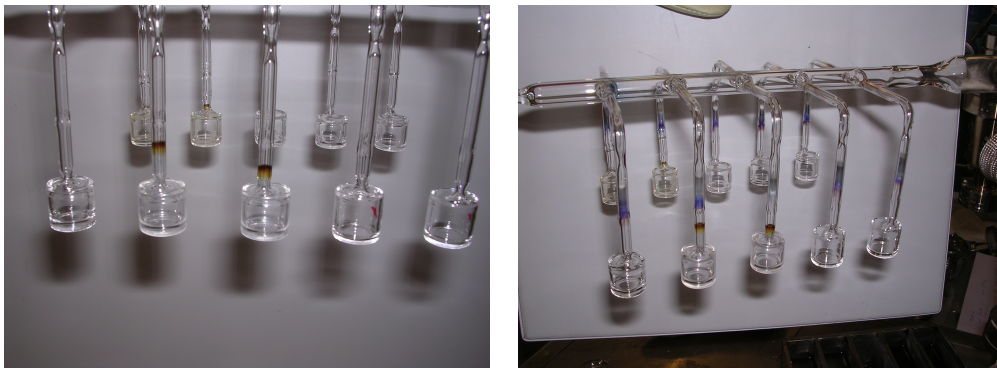
(A) Second Parylene ramp before being filled with Rb.

(B) Second Parylene ramp after being filled with Rb.

FIGURE 5.4: Second Parylene ramp during production.

5.3 Glass-blown Tetracontane coated cells

We present here the spectroscopic characterizations made on the tetracontane coated cells produced at LTF (see section 3.2.6). The first goal of these cells was to validate the update of the cell filling system and the method employed for their fabrication, but they also allowed the time-resolved observation of the ripening process by DR spectroscopy shown in section 5.3.1. The cell's intrinsic properties and some metrological aspects are also discussed the sections 5.3.2 and 5.3.3.

(A) First uncoated evacuated cell.

(B) Second uncoated evacuated cell.

(C) Parylene N coated without treatment.

(D) Parylene N coated with plasma treatment.
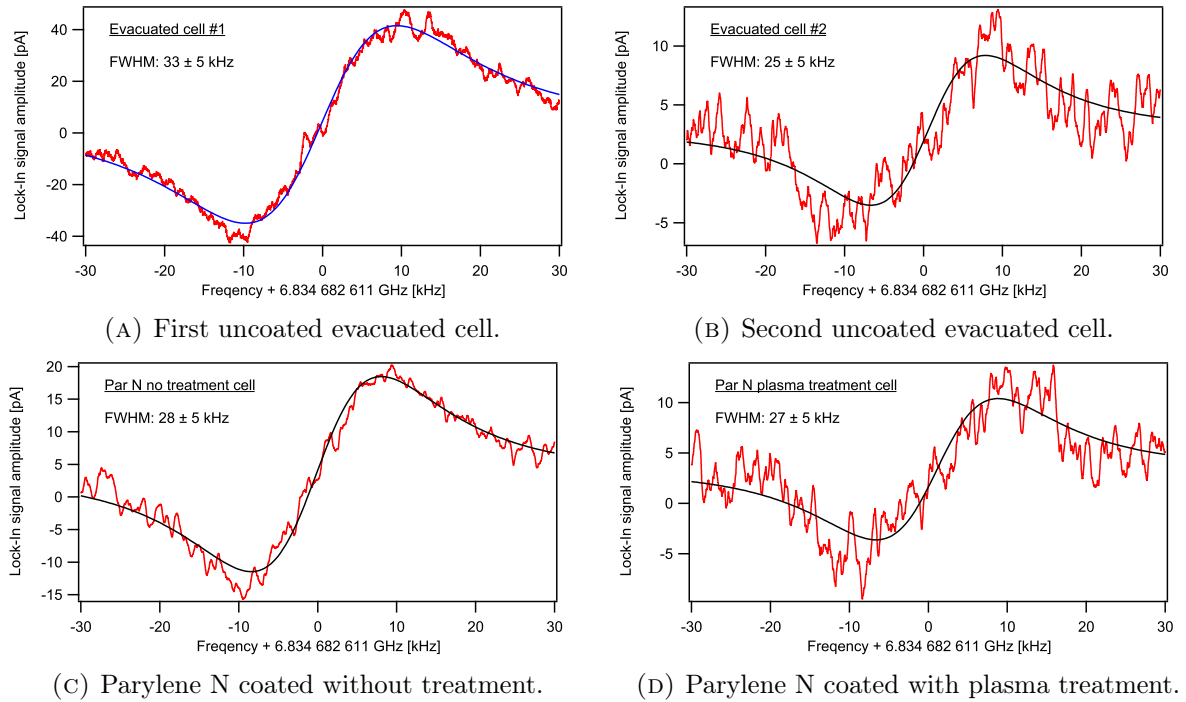
FIGURE 5.5: DR spectra of the Parylene N-coated cells obtained in AC mode (see section 2.3.1)

(A) initial state in 2011.

(B) actual state in 2014.
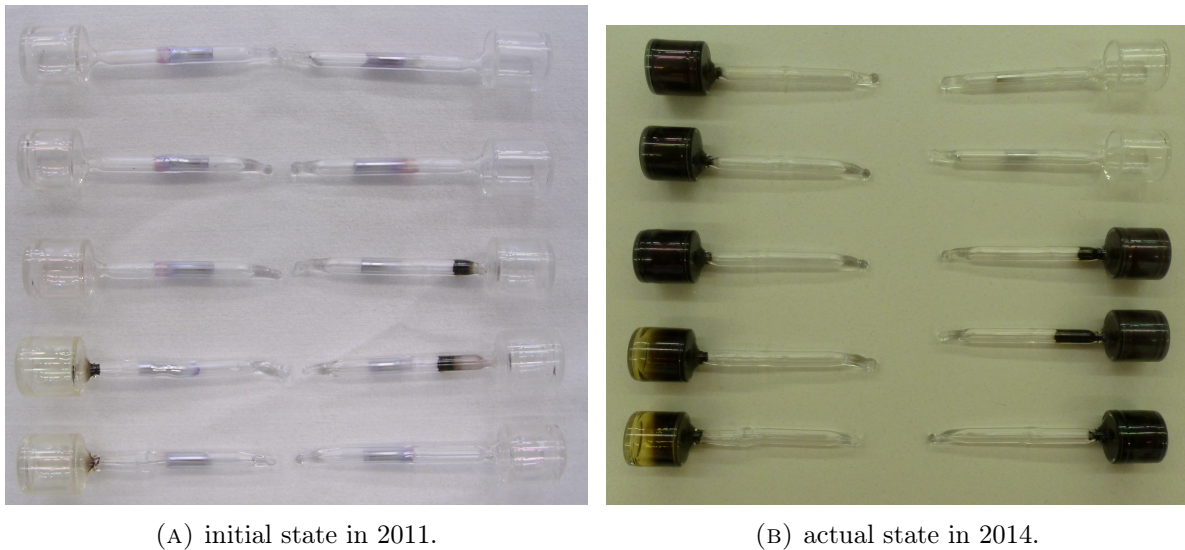
FIGURE 5.6: Colour evolution of the Parylene N coated cells. The two upper right cells are evacuated cells serving as references. In these two cells the presence of metallic rubidium is still clearly visible on the picture (B).

5.3.1 Ripening process

The spectroscopic observations on the ripening process of the tetracontane coated cells were performed on one cell at a time. The measurement started right after the cell was sealed off the production ramp, and placed inside the PP described in section 2.5. The cell's body was heated up to 70°C and the reservoir kept at room temperature without thermal control. The DR signal of the clock transition was recorded in DC mode (see section 2.3.1.1) every minute during the whole ripening process. The laser frequency was locked to the $F_g = 2 \rightarrow F_e = 2 - 3$ crossover of the laser head's reference cell, and a 7 mm diameter laser beam was sent through the cell. The light intensity and RF power were chosen sufficiently small (< 0.2 µW/mm^2, -11 dBm, respectively) so that the induced power broadenings (see equation 1.76 and 1.78) did not dominate the measured linewidth. Total power broadening was of the order of 100 Hz only for both effects combined.

All the tetracontane cells measured showed an evolution of the DR clock signal parameters similar to the ones shown on the Figures 5.7 throughout the ripening process. A slight reduction of the total clock signal frequency shift, a significant improvement of its linewidth and its amplitude along with an increase of its background level were observed. The relatively large scattering in the shifts and linewidths measured at the early times of the ripening process are due to the extremely small signal-to-noise-ratio of the recorded DR clock signals.

A qualitative interpretation of this evolution can be made using the basic three-level system, and the theoretical aspects presented in the Chapter 1. We recall here the steady state solution for the reduction of transmitted light intensity in the case of a DR interrogation of a rubidium vapour (see section 1.6):

$$\Delta I_{out} \approx I_0 \alpha \Delta z \left(-\frac{1}{2} + \frac{\Gamma_{L_1}}{4\Gamma_1} - \frac{S}{4} \frac{\Gamma_{L_1}}{\Gamma_1'} \frac{(\Gamma_2')^2}{2\pi(\nu_M - \nu_{12}')^2 + (\Gamma_2')^2(S+1)} \right). \tag{5.1}$$

In absence of a microwave field or out of magnetic resonance, only the two first members of the equation (5.1) remain, contributing to the background level:

$$Bck = 1 - I_0 \alpha \Delta z \left(\frac{1}{2} - \frac{\Gamma_{L_1}}{4\Gamma_1} \right). \tag{5.2}$$

Since the light intensity is maintained constant, the increase of the background level observed on Figure 5.7b is thus a direct consequence of the reduction of the longitudinal relaxation rate, Γ_1, that develops during ripening. Note that a potential increase of the vapour pressure during the ripening process as reported by Alexandrov [148] would have an opposite effect on the background level (i.e. a decrease of the background level), and is not observed here.

The third member of equation (5.1) is the clock signal itself. Its linewidth, in Hz, for small microwave power can be approximated by:

$$FWHM_\nu \approx \frac{\left(\Gamma_2 + \frac{\Gamma_{L_1}}{2}\right)}{\pi}. \tag{5.3}$$

Thus, for a constant optical pumping rate, Γ_{L_1}, Figure 5.7c shows the evolution of the coherence relaxation rate, Γ_2, only.

The clock signal frequency shift induced by the coating is obtained combining equations 1.115 and 1.93:

$$\Delta\nu_{coat} = \frac{\overline{\Phi}_{coat}}{2\pi\overline{\tau}_w} = \frac{\delta\omega_{ad}\tau_{ad}}{2\pi\overline{\tau}_w}. \tag{5.4}$$

We neglect here the spin-exchange shift, as it is calculated to be less than 1 Hz at the densities imposed by the reservoir temperature. Therefore, the 20% reduction of the clock signal frequency shift shown on Figure 5.7d is a consequence of a 20% reduction of the dwell time, τ_{ad} or of the average hyperfine frequency shift, $\delta\omega_{ad}$, experienced by the Rb atoms while they are adsorbed. Complementary measurement, like the explicit measurement of the dwell time proposed by Zhao [199], would be required to clearly identify the origin of this clock frequency shift reduction.

As seen in Chapter 1, the total relaxation rates have multiple origins, Spin-Exchange [65], adiabatic or electron randomization [78], that add up to the total relaxation rate:

$$\Gamma_{tot} = \Gamma_{SE} + \Gamma_{ad} + \Gamma_{er}. \tag{5.5}$$

- The spin exchange relaxation rate, Γ_{SE}, contributes to the linewidth at a constant level $FWHM_{SE} < 20$ Hz (equation 1.84), thanks to the low density imposed by the reservoir temperature that is kept at ambient temperature.

- The adiabatic coherence relaxation rate, $\Gamma_{2_{ad}}$, originates from the the average phase shift $\overline{\Phi}_{coat} = 2\pi\overline{\tau}_w\Delta\nu_{coat}$ experienced by the atoms at each collision with the coating (see section

1.7.2.3). It is estimated by [78]:

$$\Gamma_{2_{ad}} = 2\frac{(\overline{\Phi}_{coat})^2}{\overline{\tau}_w}.$$

(5.6)

The corresponding broadening, $FWHM_{ad} = \Gamma_{2_{ad}}/\pi$, is calculated to be 40 ± 2 Hz at the beginning and 23 ± 2 Hz at the end of the ripening process, which results in a ~ 17 Hz reduction of the DR signal linewidth throughout the ripening process.

- The electron randomization relaxation rate, Γ_{er}, can be of three different, but experimentally undistinguishable, origins:

  – Polarized atoms can enter the reservoir and be replaced by *new* unpolarized atoms from the reservoir (hole effect), this contribution can be estimated using equation 1.96, and gives a broadening of $FWHM_{hole} = 20 \pm 10$ Hz for a reservoir hole diameter estimated at 1.2 ± 0.4 mm. This effect is constant throughout the ripening process.

  – Atoms from the vapour can be adsorbed for a sufficiently long time on the coating, being as well replaced by new unpolarized atoms from the reservoir, or re-emitted from the coating (adsorption losses).

  – Collisions with uncoated glass surfaces (covering factor losses).

It is interesting to note that none of the predictable broadening mechanisms (spin-exchange, adiabatic, reservoir effect) can explain the comparatively large initial linewidth and its significant reduction by more than 400 Hz observed during the ripening process. We conclude that this improvement is dominated by a substantial reduction of the electron randomization relaxation rate, Γ_{er}. The most probable explanation is the reduction of the consumption of the rubidium atoms by long adsorption[1] on the coating throughout the ripening process. This process must also induce a modification of the interaction potential between the coating and the rubidium vapour in order to explain simultaneously the variation of the shift of the clock transition.

5.3.2 Intrinsic properties

After the first few days of ripening, the cells were kept at 70°C, and the intrinsic shifts and linewidths of each cell were obtained by extrapolating to zero light intensity and at low RF power the respective shifts and linewidths of the clock signals. These are presented on figures

---

[1]the chemical reaction hypothesis has been rejected by Seltzer et al. [76]
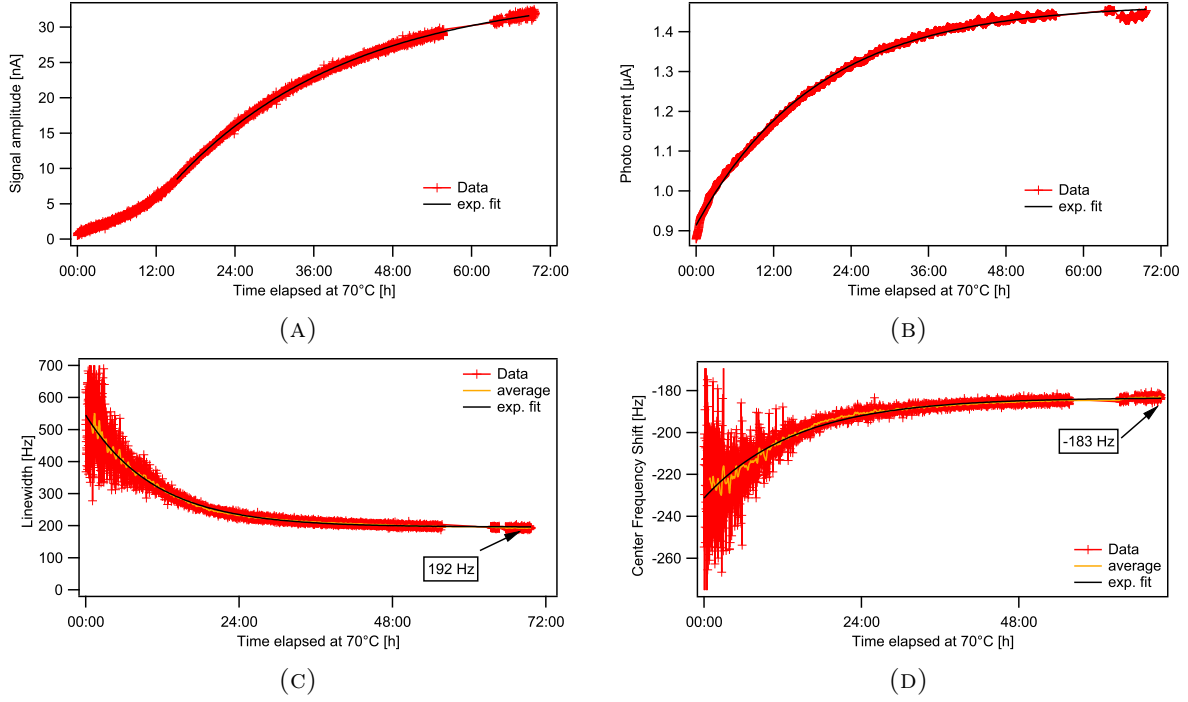
FIGURE 5.7: Evolution of the clock signal parameters during the ripening process of the tetra-contane cells. A) amplitude; B) background level; C) Linewidth; D) clock frequency shift.

5.8. Over the whole set of cells produced, the average intrinsic broadening is around 114 Hz with a standard deviation of 40 Hz. We explain this scattering by the limited reproducibility of the holes sizes inherent to the glass blowing technique. The average intrinsic shift is -187 ± 10 Hz, for which the scattering could be explained by a similar scattering in the dwell times or interaction potentials. Indeed, the reproducibility of coated cells is known to be highly variable [133]. Our best cell exhibits an intrinsic linewidth as small as 65 Hz, which is well explained by the various calculable broadening mechanisms (see Table 5.1). An efficient method to reduce the hole effect is to use a lockable reservoir [72], but this method significantly complicates the fabrication of the cells and was not employed here. The slightly reduced performances, in terms of intrinsic linewidth, of the other cells could also be explained by 99% coverage of the cell internal walls.

As mentioned at the end of the Chapter 1, the intrinsic properties of a wall coated cell strongly depend on the average collision rate, which is imposed by its geometry. In order to compare objectively similar coatings in different cell geometries, we scale down the total shifts to an average single collision. From the total shifts of figure 5.8a, the average phase shifts per collision

are calculated using equation 5.4. The value obtained over the produced cells is -33 mrad/coll with a standard deviation of 2 mrad/coll. This corresponds, within a factor of two, to the data found in the literature and listed in Table 5.2. The temperature dependency of the intrinsic shift allows the calculation of the activation energy (equation 1.116). From the temperature coefficient (TC) obtained with two cells of the batch (see Figure 5.9) the activation energy is found to be 0.053 eV, also in good agreement with the literature values for paraffin coatings (see Table 5.2).

(A)   (B)
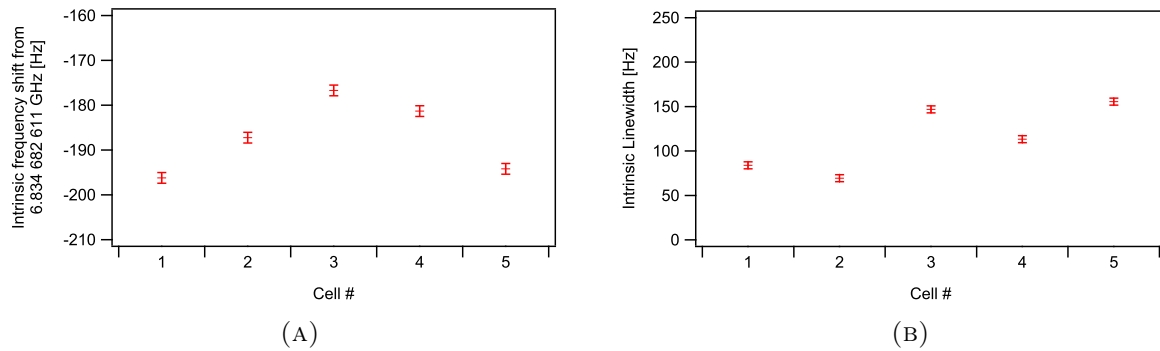
FIGURE 5.8: Intrinsic (A) shift and (B) linewidth of the produced tetracontane coated cells.
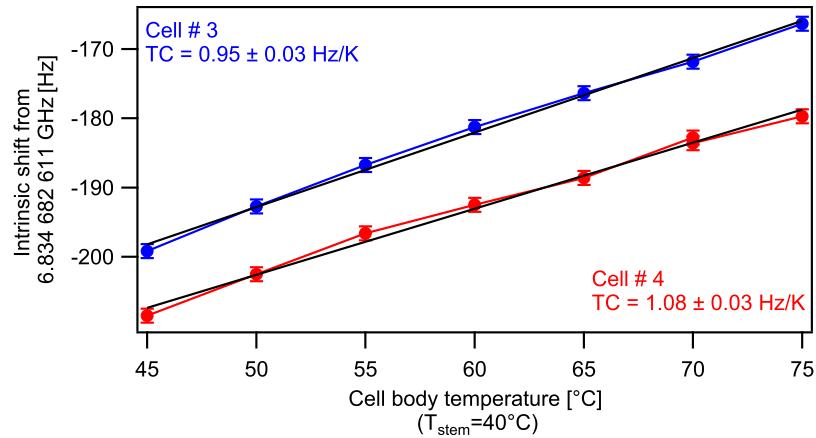
FIGURE 5.9: Clock signal frequency shift as a function of the cell temperature for two produced tetracontane coated cells.

TABLE 5.1: Summary of the calculable broadening mechanisms in our tetracontane wall coated cells after ripening.

Broadening mechanism	Parameter	Relaxation rate [s^{-1}]	Linewidth contribution [Hz]
Adiabatic (eq: 1.94)	$\Delta\nu_{\text{clock}} = -190 \pm 10$ Hz	78.5 ± 9	25 ± 3
Spin Exchange (eq: 1.84)	$\text{T}_{\text{cell}} = 70°\text{C}$	<65	<20
Hole effect (eq: 1.96)	$\varnothing_{\text{hole}} = 1.2 \pm 0.4$ mm	190 ± 100	60 ± 30
Total			105 ± 36

TABLE 5.2: Coating properties comparison for ^{87}Rb. "n.c." is for non communicated.

Author	Coating	Interrogation	Φ [mrad/coll]	TC [Hz/K]	E$_{\text{a}}$ [eV]
Brewer [200]	paraflint	DR	-40	n.c.	0.1
Vanier [37]	paraflint	DR	-45	+0.7	0.081
Risley [80]	paraffin	DR	-49	+2	0.06
Robinson [63]	Tetracontane	DR	-58	n.c.	n.c.
Budker [78]	Tetracontane	DR	-7	n.c.	0.06
Bandi [7]	Tetracontane	DR	-65	+1.39	0.036
Breschi [194]	Tetracontane	CPT	-55	+1.4	n.c.
Yi [75]	OTS	DR	-69	$\sim$+3	0.065
This study	Tetracontane	DR	-33 $\pm$ 2	+1	0.053

5.3.3 Metrological aspects

The optimization of the clock signal was performed on the D2 line, with the laser frequency stabilized to the crossover dip of the $|F_g = 2\rangle \rightarrow |F_e = 2\rangle$ and $|F_g = 2\rangle \rightarrow |F_e = 3\rangle$ transitions of the laser head reference cell. This choice was driven by the lowest α-LS coefficient obtained at that optical frequency. The temperatures of the cell body and reservoir were varied from 40 to 80° always keeping the reservoir temperature inferior to the body's one to avoid rubidium condensation in the coated volume. For every set of temperatures, the microwave power and the

light intensity were varied as well and the clock signal was recorded. A typical data sheet obtained at the optimal reservoir and volume temperatures is shown on figure 5.10. The optimized signal obtained at 0.7 μW/mm^2 and -45 dBm of light intensity and microwave power, respectively, presents a linewidth of 355 Hz with an amplitude and contrast of 0.2 µA and 20% respectively. The calculated shot-noise limit for the clock stability is $< 1 \times 10^{-13}\tau^{-1/2}$. Nevertheless, the cell body temperature affects significantly the shift of the clock transition (see figure 5.9). The temperature sensitivity of the clock transition frequency is of the order of 1 Hz/K or 1.5×10^{-10} /K. This severely limits the medium- to long-term clock frequency stability at a level of $\sigma_y \sim 10^{-12}$ assuming a challenging temperature control within ± 10 mK.

A very interesting behaviour was observed during the reservoir temperature optimization and is shown on figure 5.12: as a function of the reservoir temperature and thus the rubidium vapour density, the α-LS coefficient changes sign, and is therefore null for a certain reservoir temperature, or density of rubidium. A frequency shift of the optical transition induced by Rb-Rb collisions could be at the origin of this effect. Indeed, we saw in the section 1.7.2.5 that the α-light-shift coefficient depends explicitly on the laser frequency detuning with respect to the optical transitions of the interrogated rubidium atoms (see equation 1.126 and Figure 5.11a), and could be cancelled for a given laser detuning (see Figure 5.11b). In the present case, as the laser was frequency stabilized to the crossover dip of the $|F_g = 2\rangle \rightarrow |F_e = 2\rangle$ and $|F_g = 2\rangle \rightarrow |F_e = 3\rangle$ transitions of the laser head reference cell, its frequency fluctuations could not exceed ± 3 kHz at all time scale (see Table 2.1). Therefore these fluctuations cannot explain the equivalent observed detuning variation of ~ 150 MHz. An alternative way to explain this detuning with respect to the atoms of the coated cell would be to consider a shift of their optical transitions frequencies. However, such explanation appears highly improbable considering the huge optical shift involved; this would be equivalent to a buffer gas filling of ~ 30 mbar of N$_2$. Further studies are required to clearly identify the origin of this effect. In view of a clock application, this presents a strong interest since the α-light-shift coefficient can be cancelled without the fragile and cumbersome use of an AOM (see section 2.4.2) to shift the laser frequency off its reference frequency.
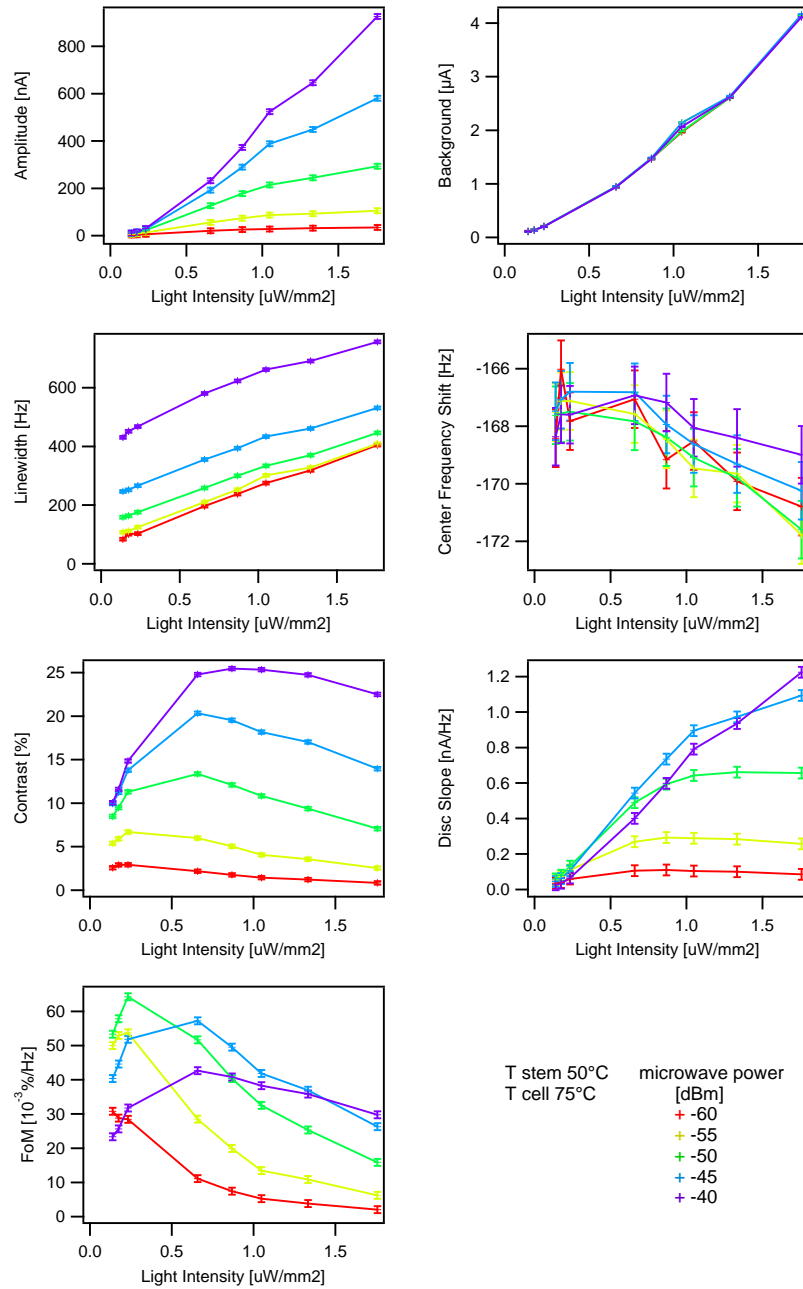
FIGURE 5.10: Tetracontane coated cell clock signal parameters as a function of light intensity and RF power. The reservoir and cell volume temperatures are fixed at 50°C, respectively, 75°C. Contrast, Discriminator slope and FoM are calculated from the measured Amplitude, Background level and Linewidth.

(A)

(B)
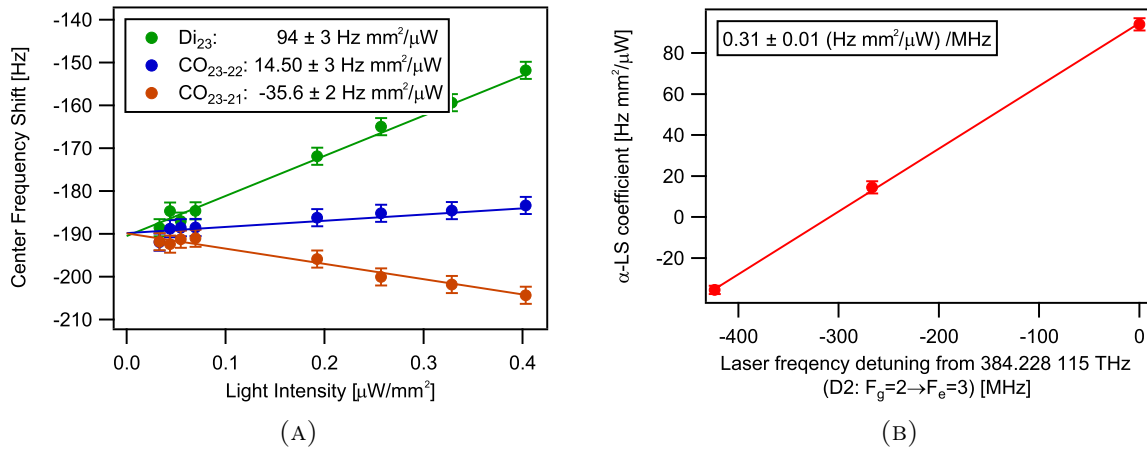
FIGURE 5.11: Clock frequency light shifts as a function of the laser intensity and frequency. (A) Intensity light shift for the three different laser frequency references; (B) α-LS coefficients as a function of the laser frequency detuning.
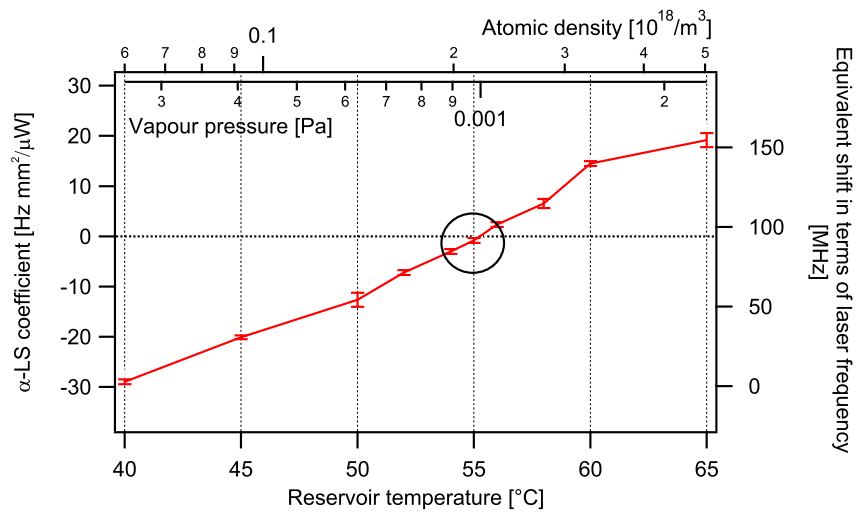
FIGURE 5.12: Intensity light shift coefficient as a function of the reservoir temperature in a tetracontane wall coated cell. The circle indicates the reservoir temperature at which the α-LS coefficient is zero. The scaling coefficient of Figure 5.11b was used to draw the right hand axis.

5.4   Microfabricated OTS coated cell

In this section we present the spectroscopic evaluation and study of the first micro-fabricated rubidium cell featuring an operational anti-relaxation wall coating. These presented studies have also been submitted for publication in *Applied Physics Letters* [171]. The fabrication of such a cell was enabled by the successful low-temperature In-bonding [134] validated in the Chapter 4, and has been briefly described in section 3.3.2.1. It consists of an evacuated KOH-etched double-chamber cell of which only one chamber, the interrogation chamber, is OTS coated. The other chamber, uncoated, is called the reservoir and contains the liquid Rb droplets acting as the atomic reservoir for the rubidium vapour. Each chamber has a decahedron shape (two base-to-base truncated square based pyramids) with a 4.2 mm^3 volume and 17.3 mm^2 wall area. The chambers volumes are connected by a 100 µm x 100 µm channel. The cell is shown on figure 3.9, and its fabrication was performed by R. Straessle. A thorough description of the cell and its fabrication can be found in her thesis [1].

The characterization of this cell follows the same approaches previously described in Chapter 4: linear absorption spectroscopy to prove the presence of a rubidium vapour, sub-Doppler saturated absorption spectroscopy to quantify the level of a potential buffer gas contamination, and finally, DR spectroscopy to evaluate the anti-relaxation properties of the OTS coating. The cell was mounted in a 14 mm cavity resonator using two glass cylinders to tune the microwave cavity (see figure 2.9b). The operation temperature was 70°C, and a D2 line laser head (see section 2.4) was employed for optical absorption spectroscopy and optical pumping. To allow the interrogation of a single chamber at a time, the laser beam was collimated and had a diameter of 0.56 mm. Its intensity was reduced by the mean of neutral density filters.

Linear absorption spectroscopy was performed on both, reservoir and interrogation chambers of the cell. The laser power was reduced down to 2.3 µW ($\sim$10 µW/mm^2) to avoid optical pumping effects. Initially, the coated chamber showed no absorption signal, while the reservoir did (see Figure 5.13a). The absence of a Rb vapour in the interrogation chamber is most likely attributed to the coating obstructing the channel or the ripening process. Therefore, the cell was kept over one night at 60°C; not too hot, in order to maintain the cell alive as long as possible, but warm enough to favour the diffusion of the rubidium vapour through the channel. The following day, the cell was heated up again at 70°C, and identical measurements were performed. Figure 5.13b confirms the presence of a rubidium vapour, this time in both chambers: The channel

FIGURE 5.13: Linear absorption spectra of (bottom traces) the microfabricated wall coated cell along with (upper trace) the reference spectrum. (A) The first day; (B) after one night heating at $60°$C.

obstruction was not tight, and after one night heating, a sufficient vapour pressure built up in the interrogation chamber. Nonetheless, a 50% reduced vapour pressure is observed in the interrogation chamber. This is most likely due to the fact that the measurement was performed during the equilibration process, or by a slow consumption of the rubidium atoms through the formation of Rb-clusters [201] or passivation of the coating [202]. An excellent fit is obtained for both chambers' spectra using Voigt profiles for every optical transition. This fit gives an upper limit for a potential gas contamination of 10 ± 5 mbar of N_2.

The sub-Doppler saturated absorption spectrum obtained from the coated chamber is shown on Figure 5.14. Sub-Doppler dips are clearly visible, and prove a collision less regime, thus confirm the low buffer gas contamination of the cell. A Lorentzian fit of the dip corresponding to the cyclic transition $|F_g = 2\rangle \rightarrow |F_e = 3\rangle$ gives a total linewidth of 110 MHz; with respect to the reference spectrum, this correspond to an additional broadening of 80 MHz. Since He and N_2, the most probable contaminants through the permeation process (see section 4.2.4.3), respectively the leak process (see section 4.2.2), have broadening coefficients of 15 MHz/mbar, the gas contamination of the cell is estimated to be of the order of 6 mbar (see Table 1.3). From the dimensions of the cell and equation 1.89, such pressure may reduce the DR linewidth from 95 kHz down to $\sim$20.1 kHz only.

A DR signal was successfully obtained out of the interrogation chamber solely, but could not be retrieved from the reservoir chamber. Since its contrast was very small (less than 0.5%), the DR AC mode was employed (see section 2.3.1.2). The microwave was frequency modulated at
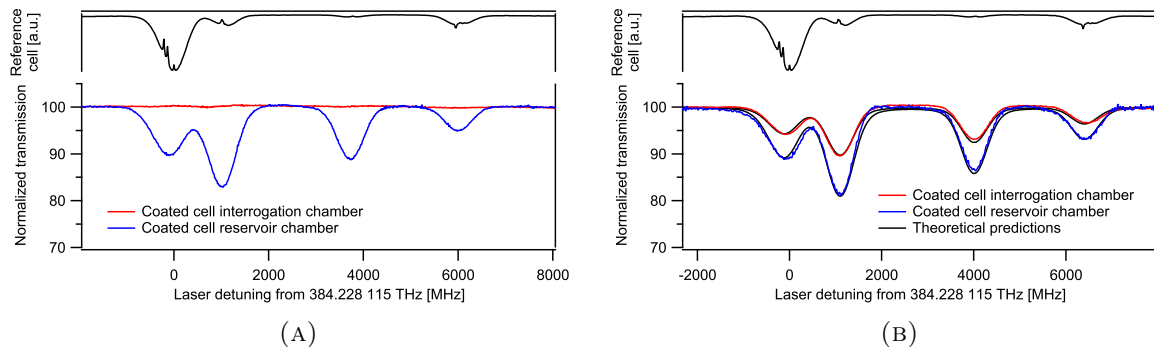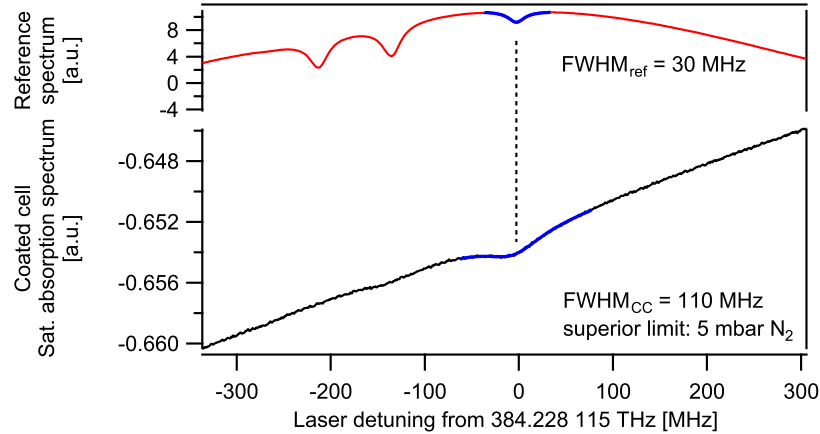
FIGURE 5.14: Saturated absorption spectra of (bottom trace) the microfabricated wall coated cell along with (upper trace) the reference spectrum.

687 Hz with a frequency deviation of 1500 Hz. Since the in-phase signal can be assimilated to the derivative of the DR signal for small deviation with respect to the linewidth, a "derivative lorentzian" fit of the AC signal, scaled in amplitude with respect to the frequency deviation used (see Figure 5.15), provides the characteristic parameters of the DR signal. These parameters are reported on Figures 5.16 and 5.17 for various RF power and light intensities. An extrapolation to zero light intensity provides an intrinsic linewidth of 8.9 ± 0.1 kHz. This linewidth cannot be explained by the potential gas contamination of 6 mbar which would reduce the theoretical 93.9 kHz line broadening issued from a bare and evacuated cell down to 20.1 kHz only. This is a strong indication for non-depolarizing wall collisions due to the coating. Moreover, if the linewidth reduction was a consequence of the BG contamination, a DR signal would have been measurable in the reservoir chamber as well.

The 8.9 kHz linewidth of the DR signal obtained corresponds to an average polarization life time of 35.8 µs equivalent to ~ 11 wall collisions. Assuming a perfect coating with uncoated area, this would correspond to a 90.5% coverage of the surface (see equation 1.95). This is consistent with the results from ellipsometric and contact angle measurements showing a covering factor of $\sim 90\%$ [1]. The reservoir effect, or hole effect is calculated to be 55 Hz (equation 1.96), which represents a negligible contribution to the experimental value of the linewidth.

Another strong argument points towards a reduction of the linewidth due exclusively to the wall coating, and excludes the nitrogen contamination contribution: the negative sign of the clock
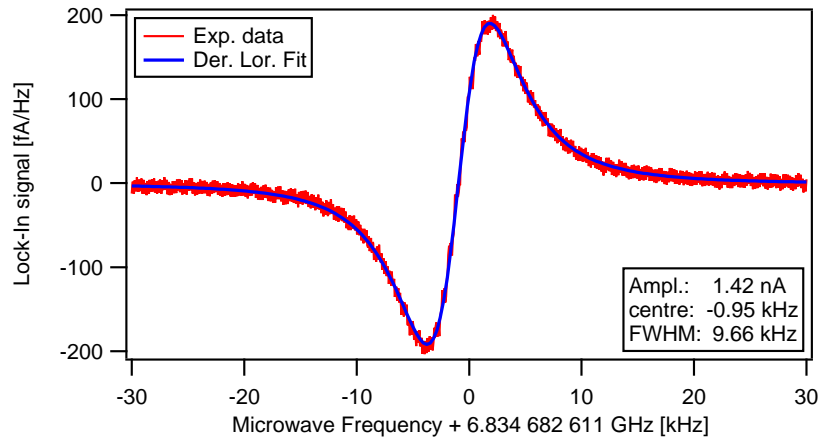
FIGURE 5.15: Derivative DR signal (see section 2.3.1.2) obtained from the microfabricated wall coated cell.

signal frequency shift: $\Delta\nu = -884 \pm 10$ Hz. Indeed, the supposed 6 mbar nitrogen contamination would induce a positive shift of 2.4 kHz to the clock transition. Only gases like Argon or Krypton, of which, contamination is highly improbable due to their rarity, induce negative shifts. Moreover, a negative shift is a typical signature of most of the coated cells studied [37]. The -884 Hz shift of the clock transition frequency corresponds to a collisional phase shift of $\Phi_{coat} = -18.8 \pm 0.2$ mrad/coll (see equations 1.86 and 1.115) which is of the same order but significantly smaller than the value of $\Phi = -69$ mrad/coll found in the literature [75]. Such difference is not yet understood and would require further investigation.

Table 1.16 summarizes the parameters of this cell and its theoretical broadening predictions. A comparison with the measured 14 mm tetracontane coated cells' properties (see section 5.3.2) and a hypothetical OTS-coated 3D cell (see section 3.3.1) is also given.

A clock operation was not carried out. Nevertheless, from the achievable shot noise limit $\sigma_{shot}(\tau) < 3 \times 10^{-10} \tau^{-1/2}$ shown on Figures 5.16 and 5.17, a stability $\sigma_y(\tau) < 1 \times 10^{-9} \tau^{-1/2}$ could be envisaged. Currently, the main limit is imposed by the relative large linewidth but also by the tiny (few 10^{-5}) figure of merit resulting from the small optical thickness (small cell thickness and low vapour density imposed by the temperature limit of the In-seal).
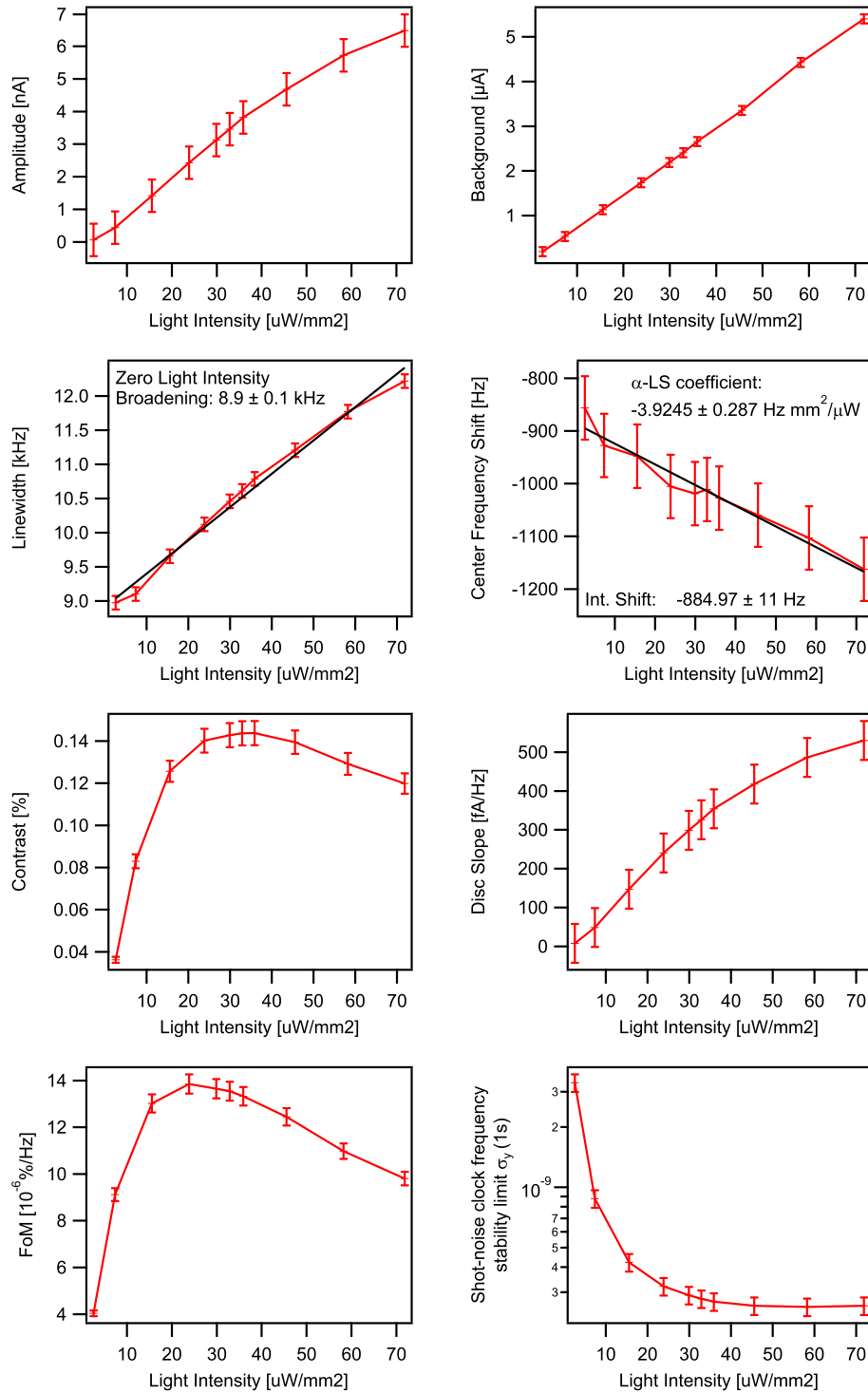
FIGURE 5.16: Microfabricated coated cell clock signal parameters as a function of light intensity. The microwave power is fixed at 0 dBm. Contrast, Discriminator slope, FoM and Shot Noise limit are calculated from the measured Amplitude, Background level and Linewidth.
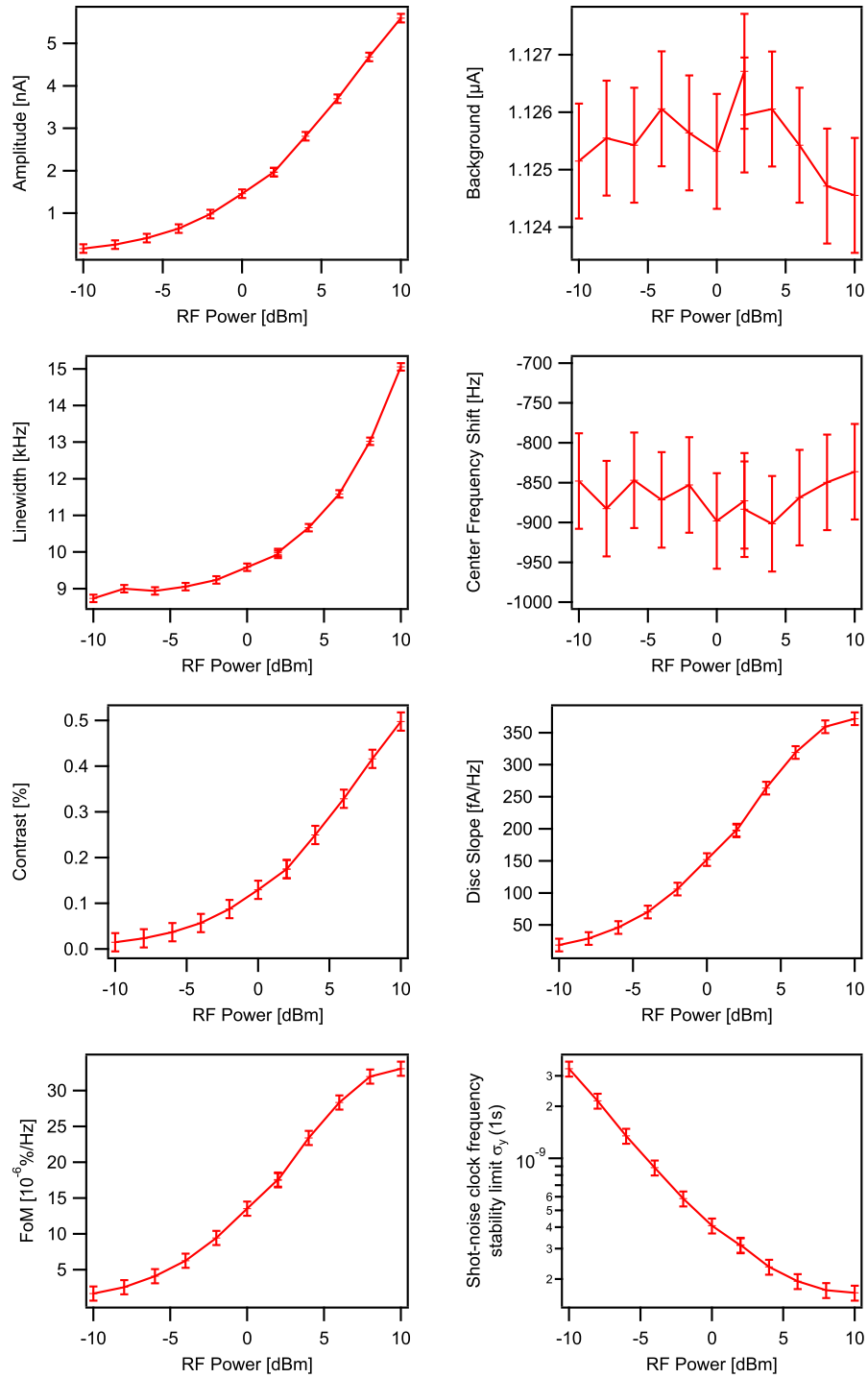
FIGURE 5.17: Microfabricated coated cell clock signal parameters as a function of RF power. The light intensity is fixed at 15.5 µW/mm^2. Contrast, Discriminator slope, FoM and Shot Noise limit are calculated from the measured Amplitude, Background level and Linewidth.

5.5   Conclusions

Coated 14-mm scale cells as well as a microfabricated coated cell were succesfully produced and tested in our laboratories. Parylene coating is found to be inadequate for any type of cell: it consumes all the rubidium present in the cell and from our studies, does not show any anti relaxation properties at all. However, the update of our cell filling facilities at LTF and our production method for tetracontane coated 14-mm scale was demonstrated to be successful by the comparable intrinsic properties of the cells compared to what is found in the litterature. Linewidths below 100 Hz could be retrieved, mostly dominated by the hole effect. In terms of clock applications, this corresponds to a shot-noise limit below $1 \times 10^{-13} \tau^{-1/2}$ under optimized conditions.

The in-situ production of the tetracontane coated cells allowed the observation of the dynamics of the ripening process through DR spectroscopy; it is observed that the ripening affects the evolution of all the parameters of the DR clock signal over time in a similar exponential way: the amplitude and the background level increase, while the frequency shift and the linewidth are reduced. The evolutions of the linewidth, amplitude and background level are attributed to a clear reduction of both the population and the coherence relaxation rates, and the evolution of the shift shows a modification of the physical interactions between the coating and the rubidium atoms during their adsorption period.

A dependency of the DR α-LS coefficient to the vapour density was observed in tetracontane coated cells optically pumped by a fixed frequency laser. Within the operable temperatures of the coating a inversion is observed, allowing a complete cancellation of this coefficient. Such effect offers an very simple and interesting alternative solution to the laser frequency shifting [7] or modulation [99] for light shift cancellation, based on the rubidium reservoir temperature only. A similar effect was previously reported by Miletic but in a cesium buffer-gas cell based CPT clock [203]. However in her case, the laser was frequency referenced on the Doppler absorption line of the clock cell, providing a temperature sensitive and significantly less stringent reference for the laser frequency.

Finally, we demonstrated for the first time that a micro-fabricated OTS coated cell shows efficient anti-relaxation properties. The buffer gas contamination was estimated below 6 mbar, allowing a potential reduction of the DR clock signal linewidth from 95 kHz down to 20.1 kHz only. The

measured DR signal linewidth in the coated chamber was below 9 kHz, and cannot be explained by the buffer gas contamination. Indeed, a pressure of at least 25 mbar would be required to reach such a low linewidth. Moreover, the negative frequency shift of the clock transition (known typical behavior for coatings [37]), and the impossibility to retrieve a DR signal in the reservoir chamber, are strong arguments in favour of efficient anti-relaxation properties of the cell. The 9 kHz broadening can be explained by a 90% coverage of the wall by the coating, as partial coverage is a known issue from OTS coatings [75]. These results provide the proof of concept for efficient anti-relaxing wall-coated micro fabricated cells, and opens the way to further studies. Improving the coverage factor, and analysing the frequency stability of the cells remain to be explored. However, this technology could already be used in combination with the BG technique to significantly improve the relaxation rates of a low BG pressure [86] or to lower the high pressures currently required in mm-scale cells, while improving at the same time, the performances of the cell [204].

Chapter 6

Miniature double-resonance atomic clock

In this chapter, we report on the metrological investigations of the miniature atomic resonator developed in the frame of the MACQS project (see page xxix). At first, a brief introduction on the state-of-the-art of miniature atomic clocks and their application fields is given. It is followed by a detailed description of the laboratory experimental setup and the micro-fabricated atomic resonator (cell and microwave resonator). We then present our investigations on the clock performances: the optimization of the DR clock signal and its short-term stability limits, and the characterization of the medium- to long-term limiting factors, or shift coefficients. A comparison between the theoretical LS model developed in section 1.7.2.5 and the experimental data is given. Finally, the clock frequency measured over six months is presented and a stability analysis from 1 s to 10^5 s is performed and compared to existing commercial clocks. Indications for future optimization are given and an alternative interrogation method is finally proposed.

6.1 Introduction

Currently, most of the commercial miniature atomic clocks are still exploiting the DR principle and use a discharge lamp to optically pump the rubidium atoms. These clocks have a large variety of applications: from the synchronisation of various telecommunication networks such as

TV and radio (DVB, DAB), cellular phone base stations and internet, to the time tagging in financial markets, smart grids, or as a scientific equipment for precise time measurement. These applications have a constantly increasing need for smaller and cheaper clocks.

Several experiments have shown that the use of lasers instead of lamps can significantly improve the performances, in terms of stability, size and power consumption, of an atomic clock. Replacing the lamp by a laser for optical pumping in DR based clocks allows one orders of magnitude improvement of short-term frequency stability [205], and stabilities of $1.4 \times 10^{-13} \tau^{-1/2}$ have been recently reported for a compact laser pumped DR atomic clock [7]. Nevertheless, for commercial applications, issues related to the lasers, such as reliability, ageing and cost are still problematic.

In terms of miniaturization, most of the researches focused on the CPT scheme [206] for it allows a significant size reduction as the microwave cavity, considered as a size limiting factor, is not required [25], [30], [31]. The CPT scheme allowed an extreme miniaturization of the PP and led to the smallest commercially available atomic clock, the Symmetricom's chip scale atomic clock (CSAC) SA.45s[1] [25]. However, the DR was also studied for sub-miniature atomic clocks [39], [207], as it presents additional advantages compared to CPT: in identical conditions, the short-term stability of the DR based clock is five times better than that of CPT [36]; lower microwave power requirements (-30 dBm has been reported for a double-resonance clock using a resonant microwave cavity [81] against -3 dBm [5] and -14 dBm [208] for a CPT clock); a lower background level and relaxed requirements on the light source.

These findings therefore motivated the studies and evaluations of this chapter towards a sub-miniaturized DR based vapour cell clock. In the context of this thesis, the miniaturization of the cell was developed in collaboration with the SAMLAB[2], EPFL [164]. The choice of a buffer gas filling and anodic bonding was driven by the maturity and reliability of the fabrication process. Alternative techniques such as towards wall-coated microfabricated cells were also investigated, see section 5.4. Modelling and fabricating a dedicated microwave cavity of dimensions well below the wavelength of the rubidium atomic transition ($\sim$4.3 cm) was developed in collaboration with the LEMA[3], EPFL, and resulted in the realization of a miniaturized loop-gap microwave resonator, the μ-LGR [209]. For the light source, both the laser [154] and the microfabricated discharge lamp [210] were envisaged.

---

[1]see www.symmetricom.com/products/frequency-references/chip-scale-atomic-clock-csac/SA.45s-CSAC/
[2]Sensors, Actuators and Microsystems Laboratory
[3]Laboratory of Electromagnetics and Acoustics

6.2 Experimental setup

The experimental setup realizes the functionalities of a classical DR scheme (see Figure 2.3) and is depicted in Figure 6.1. The pumping light is produced by the LTF in-house made laser heads (LH) described in section 2.4. The two versions were employed for the lines of interest: the 795 nm LH for the light-shift (see section 1.7.2.5) measurement on the rubidium D1 line, and the 780 nm AOM-LH for the light-shift measurement on the D2 line as well as for the realization of the clock exploiting its additional laser frequency detuning. At the output of the laser head, a part of the linearly polarized beam is sent to a wavelength meter (HighFinesse WSU/30), the remainder, is used as the optical pump for the DR. Its intensity is varied using ND filters, and the Gaussian spatial distribution of the beam intensity is flattened through a beam diffuser. Inside the PP, the beam propagation vector is parallel to the static magnetic field (C-Field), or the quantization axis. The light is therefore sigma-polarized (see Figure 1.6), and doesn't allow optical π-transitions. Such a configuration imposes in equation (1.127): $\epsilon_{\pm 1} = 0.5$ and $\epsilon_0 = 0$. The 6.834 GHz microwave radiation is produced from the 2.278 GHz output of a commercial synthesizer (Rohde&Schwartz SMA100A), via a frequency tripler.
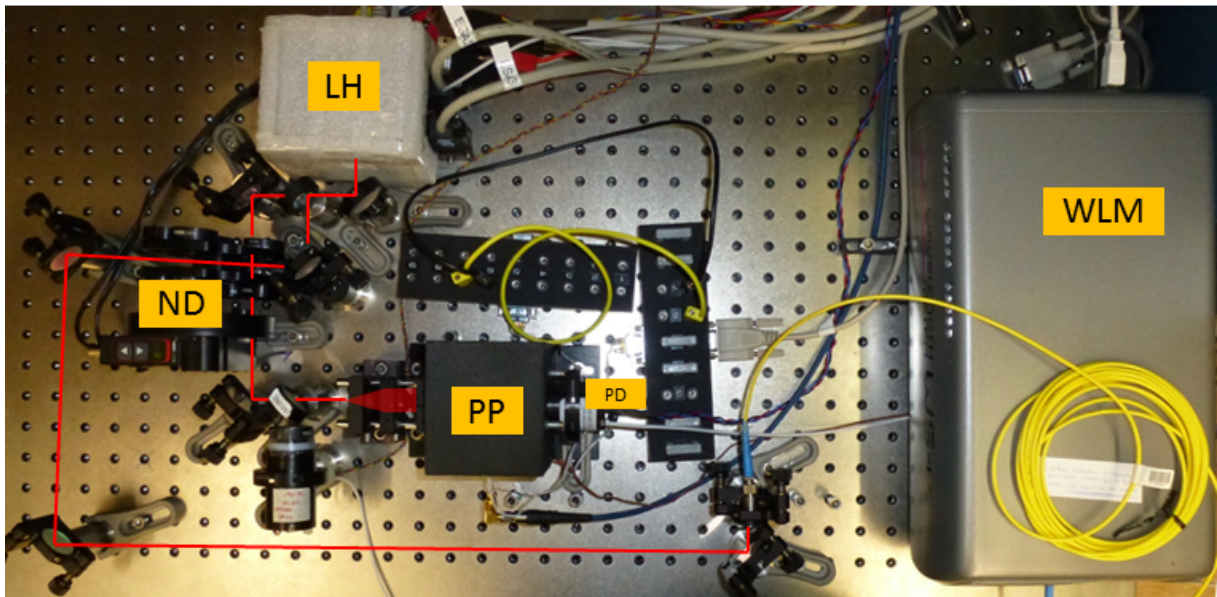
FIGURE 6.1: Experimental setup of the miniature DR atomic clock. LH, Laser Head; ND, Neutral Density Filters; PP, Physics Package; PD, Photo Detector; WLM, Wavelength Meter.
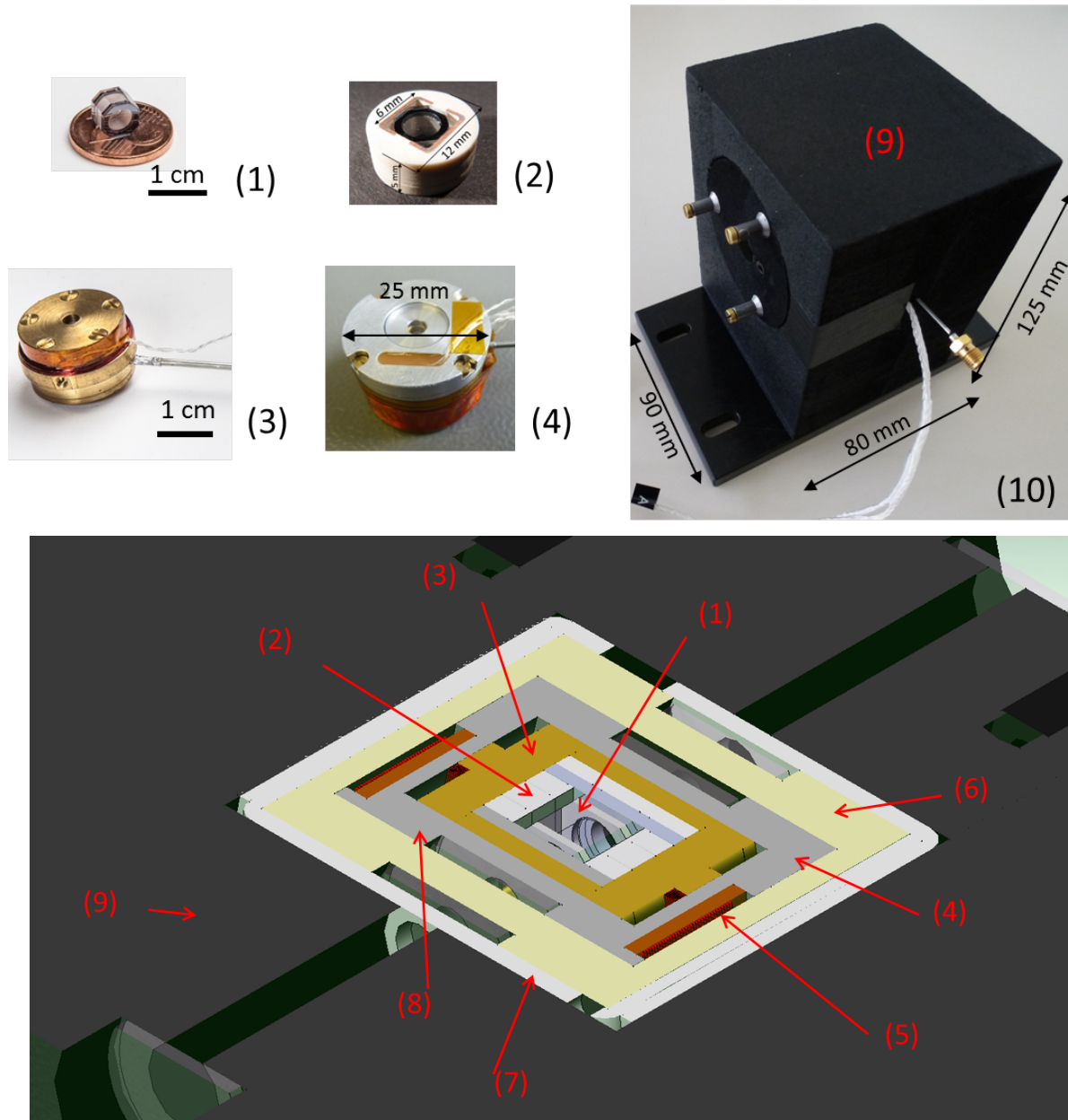
FIGURE 6.2: μ-LGR based physics package. (1) 3D cell; (2) µ-LGR (*photo: courtesy of LEMA-EPFL*); (3) Brass enclosure (design optimized for flexibility); (4) Heating cavity, NTC's and resistive heater are not visible; (5) C-field coil, 35 turns and 7 mm length; (6) Thermal isolation; (7) µ-metal magnetic shield; (8) Additional NTC's, independent from temperature servo loop, for temperature monitoring; (9) Thermal isolation: extruded polystyrene with low thermal conductivity, $\lambda = 0.035$ Wm^{-1}K^{-1}; (10) Fully assembled PP for table top spectroscopy.

6.2.1 Atomic resonator or 3D cell-µLGR assembly

The heart of the PP is the atomic resonator. It consists of a microfabricated cell, and a new type of miniaturized microfabricated microwave resonator. The various components, assembly steps and CAD diagram of the PP are shown in Figure 6.2.

The cell is a microfabricated rubidium vapour cell with a thick glass core [164], also called the 3D cell. Its fabrication and geometry are described in section 3.3.1. The cell is filled with an enriched ^{87}Rb vapour and nominally 60 mbar of a 58%/42% Ar/N$_2$ buffer gas mixture.

The microwave resonator is a micro loop-gap resonator or µ-LGR [211]. It was developed and realized at LEMA, EPFL by M. Violetti in collaboration with the LTF, and is the subject of a patent application [209]. A detailed description can be found in her thesis [2]. It consists of a multi-layer stack of four planar loop-gap electrodes. The electrodes are printed on cylindrical dielectric layers, and electrically connected by means of metallic vias. The dielectric layers have central openings adjusted to fit and hold the 3D cell within the loop-gap electrodes. The stacked structure is inductively coupled by a printed loop that is coaxially fed, and the whole is placed inside a brass enclosure of inner cavity volume $V_{int} < 1$ cm^3. Since a versatile and fully demountable atomic resonator was desired for the experiment, the brass enclosure was not miniaturized. The μ-LGR has a loaded Quality Factor $Q_L = 30$ with a good coupling efficiency. Its resonance frequency is tunable over a 140 MHz wide range around 6.834 GHz to compensate for the fabrication irregularities. The advantages of such a cavity are:

- an excellent field geometry favouring the magnetic π-transitions, therefore the clock transition (see section 6.2.1.1).

- a low RF power need, only -20 dBm, or even less, are required.

- an easy and low cost fabrication with an excellent reproducibility, thanks to the microfabrication process.

6.2.1.1 Field orientation factor

The quality of the resonator's field mode, in terms of efficiency for clock application, can be quantified by the field orientation factor (FOF) ξ defined by [212]:

$$\xi_{th} = \frac{\int_{V_{\text{cell}}} B_{||}^2 dV}{\int_{V_{\text{cell}}} |\mathbf{B}|^2 dV} \tag{6.1}$$

It gives, over the active cell volume V_{cell}, the fraction of microwave magnetic field power that is oriented parallel to the C-field direction and thus is useful for interrogation of the clock transition. Recalling section 1.4.3:

(1) At low RF power, the amplitude of the DR signal is proportional to the square of the Rabi frequency (equation 1.74), that is proportional to the square of the RF field amplitude.

(2) The magnetic dipole selection rules relate exclusively the π-transitions to the RF-field component parallel to the C-field ($B_{||}$), respectively the σ-transitions to the orthogonal ($B_{\perp}$) component. Moreover, equation 1.24 shows that neither the σ nor the π-transitions are intrinsically favoured, thus only the orientation of the RF magnetic field compared to the C-field weights these transitions.

The integral over all DR strengths related to the $\pi(\sigma)$-transitions, $S_{\pi(\sigma)}$, over the full spectrum range, is proportional to the square of the parallel(orthogonal) RF field amplitude integrated over the whole cell volume. Therefore,

$$\xi_{\text{exp}} = \frac{\int d\nu S_{\pi}}{\int d\nu S_{\pi} + \int d\nu S_{\sigma}} = \frac{\int dV |B_{||}|^2}{\int dV |B_{||}|^2 + \int dV |B_{\perp}|^2}, \tag{6.2}$$

defines the experimental FOF.

From Figure 6.3, we find an experimental value of $\xi_{\text{exp}} = 0.7$ for the FOF of the μ-LGR, which is close to the FOF of $\xi_{\text{sim}} = 0.8$ found from the numerical simulations [2]. The difference between the simulated value and the experimental one is attributed to inhomogeneities in the C-field induced by the finite length of the C-field coil, as for the simulated value the C-field was assumed to be exclusively z-oriented.
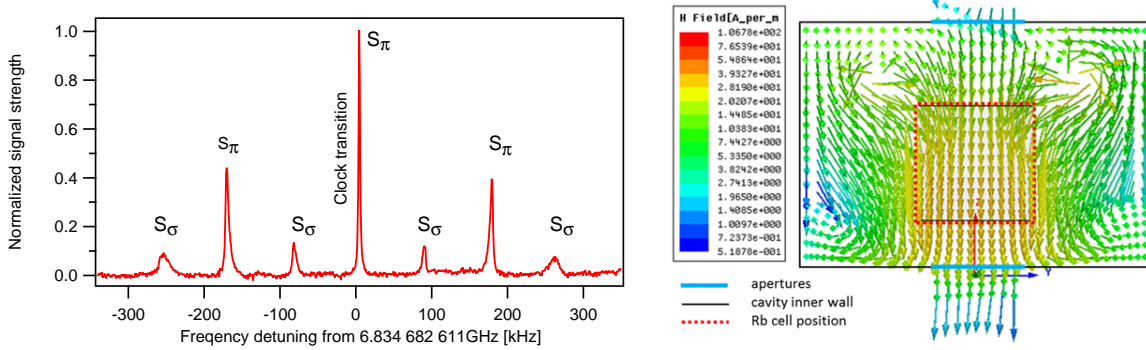
FIGURE 6.3: Experimental and theoretical determination of the field orientation factor. Left: DR spectrum of the clock and all the Zeeman transitions measured using the μ-LGR. Right: simulation of the microwave magnetic field lines; the cell volume is represented by the dotted lines [211]. *Simulation courtesy: M. Violetti.*

TABLE 6.1: Summary of the most relevant parameters of the μ-LGR cavity based physics package.

Parameter	Symbol & units	Value
Magn. Shield. factor	S_L	∼110
C-field coil turns	N_{sp}	35
LGR cavity		
quality factor	Q_L	∼ 30
Resonance frequency temp. coeff.	TC_{cavity} [MHz/K]	0.4
$FOF_{exp}(FOF_{sim})$	$\xi_{exp}(\xi_{sim})$	0.7(0.8)
Typ. cell volume	V_{cell}[cm^3]	0.15
Internal cavity volume	V_{int} [cm^3]	0.95
External cavity volume	V_{ext} [cm^3]	2.9

6.3 Clock stability optimization

Optimizing the operating conditions involves several parameters such as cell temperature, light intensity, microwave power, or light spectral properties (spectrum, intensity, frequency). Each parameter has a significant influence on both the short term and the long term stability regimes. In addition, the optimal parameters are interdependent. For example, the optimal light intensity depends, among others, on the applied RF power and the cell temperature. Therefore, each

parameter must be optimized, and compromises made so that both regimes are "optimal" simultaneously. The following stability analysis is split into two regimes, the short-term ($1\text{ s} < \tau < 100\text{ s}$) and the medium- to long-term ($100\text{ s} < \tau < 10^5\text{ s}$), as the instabilities have different origins: while in the short term regime, the stability is limited by the detection noise and the lineshape of the clock signal (see equation 1.101), the slow fluctuations of the environmental parameters affect the medium to long term regime (see equation 1.105).

6.3.1   Limits of short term frequency stability

The lineshape of the clock signal was optimized as a function of the light intensity and RF power. The cell temperature and the laser frequency were chosen to optimize the medium- to long-term optimizations at 67°C (see section 6.3.2.3) and 384.227 771 THz (see section 6.3.2.1), respectively. The pump beam is frequency stabilized at -130 MHz optical frequency offset from the CO21-23 transition in the D2 line using the AOM laser head (see section 2.4.2). Given its size, the use of the AOM laser head is obviously not compatible with a miniature atomic clock. However, it is motivated here by the desire to determine the ultimate performances of the ensemble 3D cell-µ-LGR. A potential interrogation scheme to circumvent its use is shown in Figure 6.25.

Figures 6.4 and 6.5 show the measured amplitudes, linewidths and background levels of the DR clock signal along with the calculated contrasts, discriminator slopes, figure of merit (see section 1.6) and shot-noise stability limits (see equation 1.103) as a function of the light intensity and microwave power.
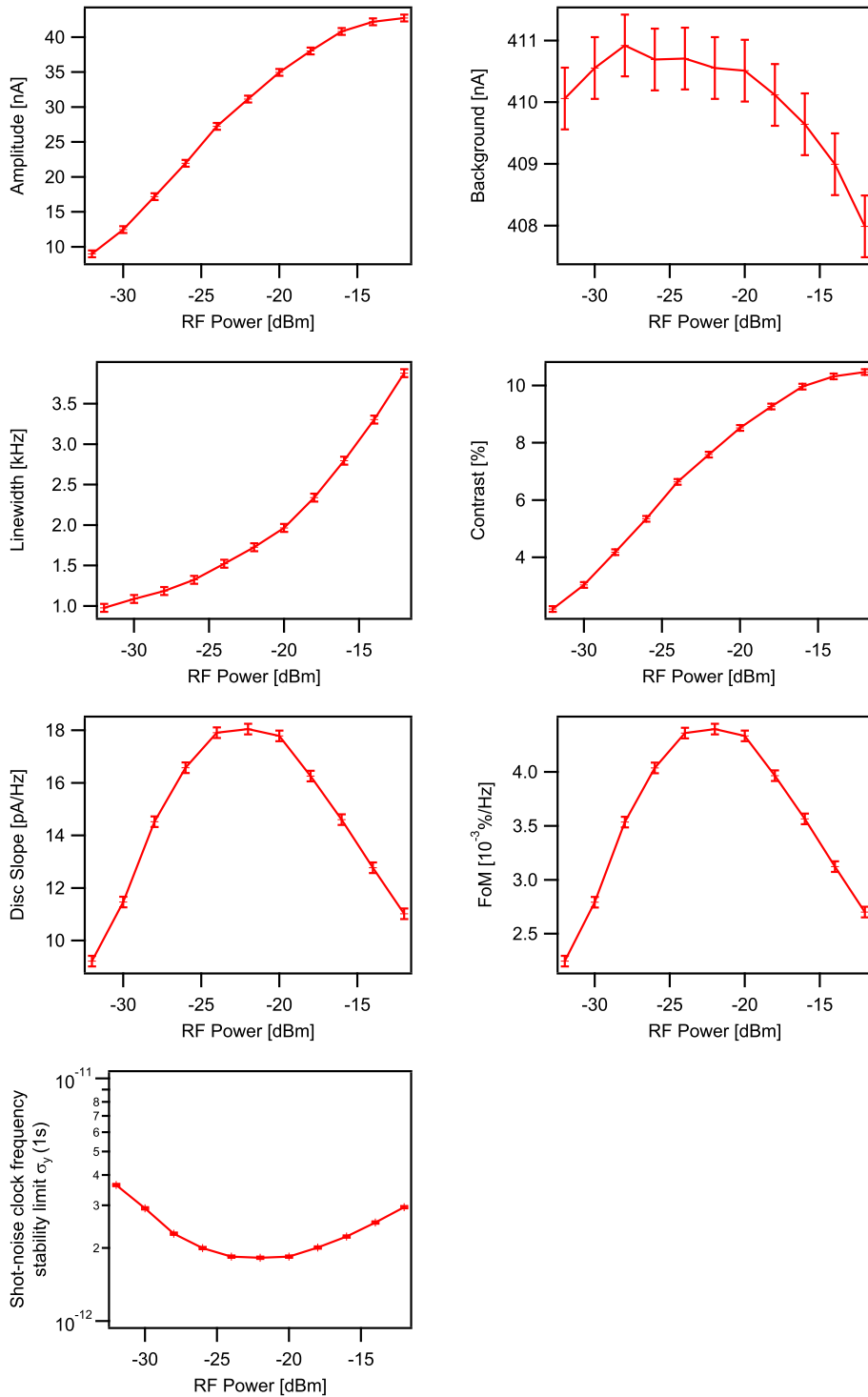
FIGURE 6.4: Clock signal parameters as a function of microwave power. The light intensity is fixed at 1 $\mu W/mm^2$. Contrast, Discriminator slope, figure of merit (FoM) and Shot Noise limit are calculated from the measured Amplitude, Background level and Linewidth.
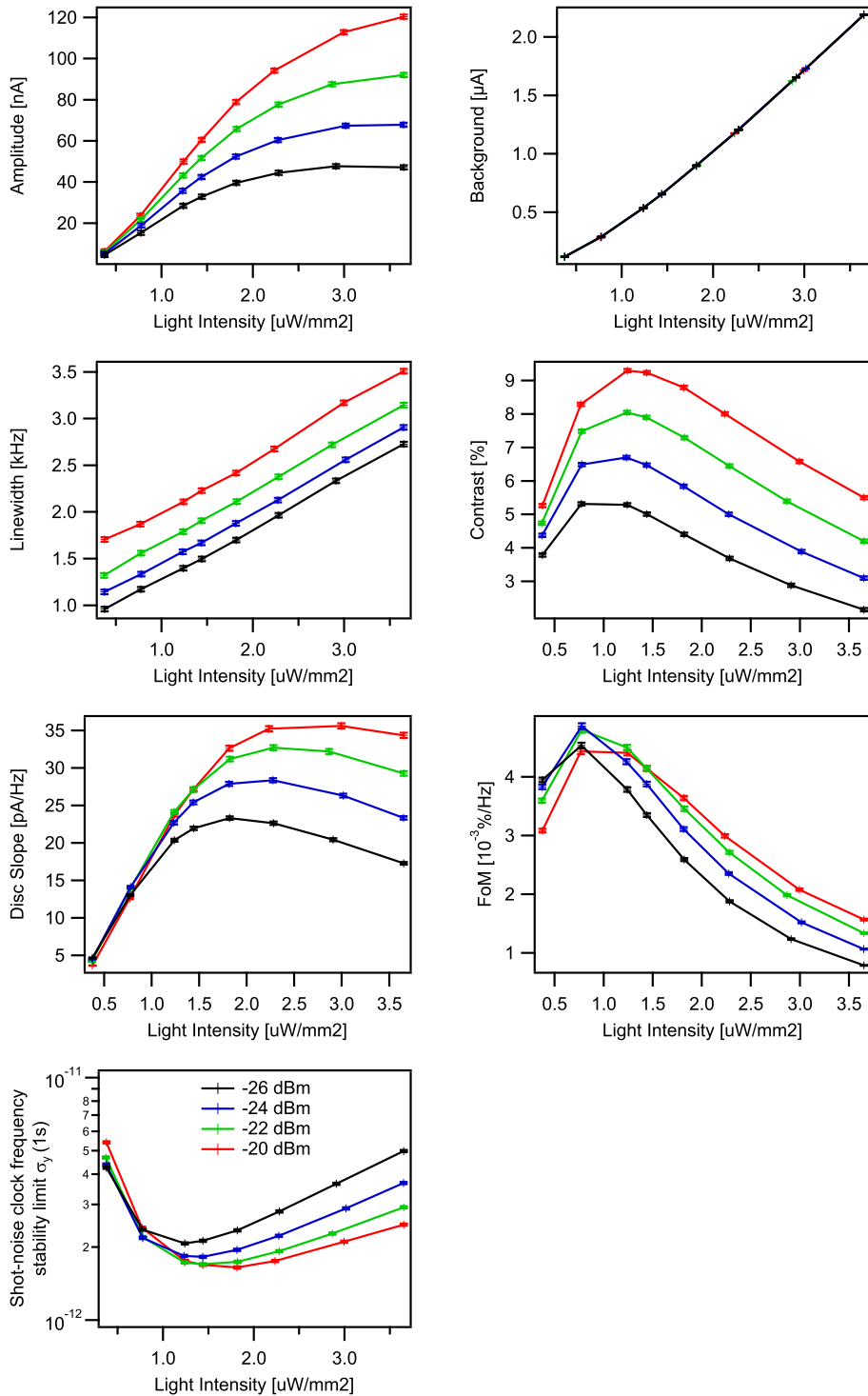
FIGURE 6.5: Clock signal parameters as a function of incident laser intensity. Contrast, Discriminator slope, FoM and Shot Noise limit are calculated from the measured Amplitude, Background level and Linewidth.

By extrapolating the clock signal linewidth to zero light intensity at low microwave power, we obtain an intrinsic linewith of $FWHM_{intr}^{exp} = 650 \pm 30$ Hz. This value is in excellent agreement with the theoretical prediction of $FWHM_{intr}^{th} = 635 \pm 1$ Hz, obtained using equation 1.89 and the experimental BG pressure and mixture determined in section 6.3.2.3. Contrasts above 10% and discriminator slopes up to 35 pA/Hz could be achieved. However, these parameters do not necessarily guarantee the best clock short term performances, and we used the shot-noise limit as optimisation criterion. Based on this parameter, a laser intensity of 1.2 μW/mm^2 along with a microwave power of -20 dBm were chosen. The laser intensity is chosen lower than the optimal value in terms of shot-noise stability limit to minimize the light shift effect. Indeed, the losses in terms of short term performances are negligible compared to the almost two-fold reduction factor for the frequency light shift coefficient (see section 6.3.2.1). Figure 6.6 shows the chosen DR signal for the clock realization. It has an amplitude of 50 nA, a linewidth of $FWHM_{clock} = 2110 \pm 25$ Hz, and a shot-noise stability limit of $\sigma_{y_{shot}}(\tau) = 1.8 \times 10^{-12}\tau^{-1/2}$. The overall detection noise in closed-loop clock operation was measured at a level of $N_{clock} = 1.85$ pA/$\sqrt{\text{Hz}}$, inducing a signal-to-noise limit of $\sigma_{y_{S/N}}(\tau) = 1.0 \times 10^{-11}\tau^{-1/2}$.
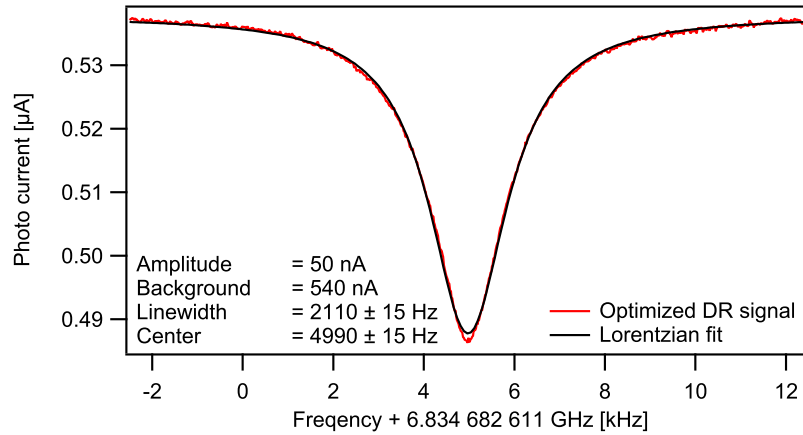
FIGURE 6.6: Optimized double resonance signal.

Considering only the short-term for optimization, higher temperatures up to 80 °C were used, and slightly better performances (Shot-Noise limit $< 10^{-12}\tau^{-1/2}$) were achieved, see appendix C. Though an improvement by a factor of 1.4 for the short-term clock frequency stability ($\sim 7 \times 10^{-12}$ at 1 s) was achieved, the measured medium- to long-term stability was limited at a level of $\sigma_y(10^4) \sim 1 \times 10^{-11}$ due to the increased temperature sensitivity. Figure 6.7 shows a comparison of the obtained clock frequency stabilities obtained in both configurations.
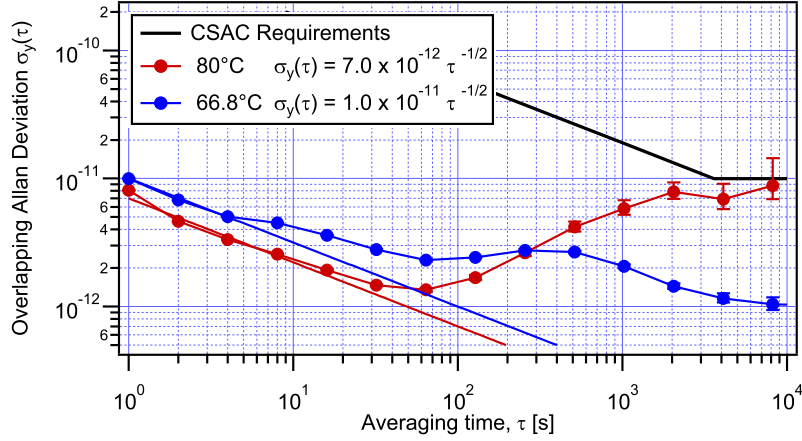
FIGURE 6.7: Comparison of clock frequency stabilities achieved at $80°C$ and $66.8°C$.

6.3.2 Shifts characterizations and medium- to long- term limits

We present in this section quantitative measurements of several sources of instabilities, their corresponding shift coefficients, and their direct consequences on the clock frequency stability, $\sigma_{y_i}(\tau)$. These coefficients and their respective induced limits are summarized at the end of the section in Table 6.2.

6.3.2.1 Light shift

This effect was treated theoretically in the Chapter 1, section 1.7.2.5. Experimentally, the DR spectra were acquired and fitted at given optical frequencies and for different laser intensities. The central frequencies were plotted as a function of the laser intensity, and the experimental α-LS coefficient is given by the slope of the linear fit (see Figure 6.8).

Figures 6.9 and 6.10 show the theoretical and experimental intensity light shift coefficients (α-LS$(\nu_L) = \frac{\partial \Delta \nu_{clock}}{\partial I}(\nu_L)$) as a function of the laser frequency over the whole D1, respectively D2, line. For the D1 line, the laser zero detuning frequency corresponds to the direct transition $|F_g = 2\rangle \rightarrow |F_e = 1\rangle$ (respectively $|F_g = 2\rangle \rightarrow |F_e = 3\rangle$ for the D2 line), called Di21 (Di23), of the unperturbed ^{87}Rb atom. The laser locked to these transitions was used as a reference for the calibration of the wavelength meter. This calibration was validated over the whole D line frequencies, by locking the laser to the other patterns of the sub-Doppler spectrum (crossover
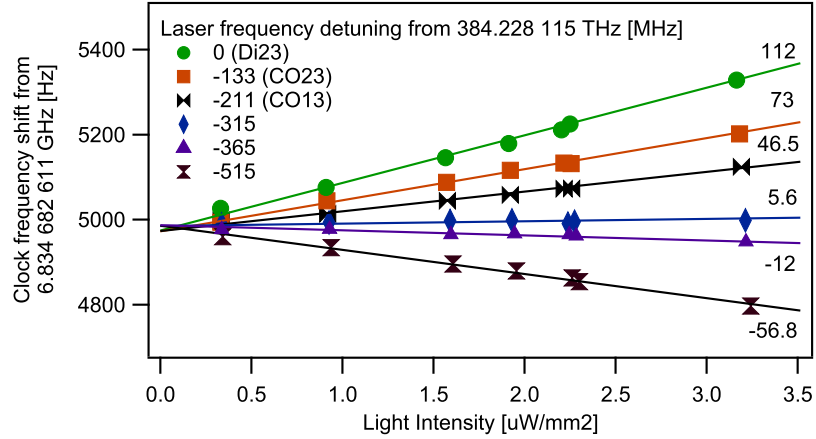
FIGURE 6.8: Subset of experimental light shifts as a function of the incident laser intensity, in the D2 line. The numbers on the right hand side are the α-LS coefficients in [Hz mm^2/µW] of the respective traces.

dips) of the reference cell. The measured optical frequencies match within 1 MHz the theoretical values. For the laser in free running mode, its frequency fluctuations during the measurement time imposes abscissa error bars of the order of ± 5 MHz. Both modes (free running and locked laser) were tested at the lockable frequencies in order to validate the α-LS coefficients obtained with the laser in free running mode. Similar coefficients are obtained with only 4% difference.

An excellent agreement is observed between experimental data and the model (equation 1.131), in both D1 and D2 lines. The model is not a fit, as no parameter is free, and all values are calculated based on parameters measured independently for the clock operation. Note that the α_{LS} coefficients measured in the D2 line (Figure 6.10) are well described by both Mathur's [101] and our models, and that both theoretical curves are extremely similar. The reason of this similarity comes from the fact that the hyperfine splitting of the $5^2P_{3/2}$ state is much smaller than the broadening mechanisms present in the cell. This similarity also explains the excellent agreement observed by Arditi [103] between Mathur's theoretical model and his experimental data, since the hyperfine splitting of the Caesium $6^2P_{3/2}$ state is also unresolved.

The D1 line case (see Figure 6.9) is much more interesting, since experimental data are well matched with our model but cannot be explained by Mathur's one [101]. The main reason for the failure of his model comes from the fact that it considers the hyperfine states only. From our model, Mathur's one is equivalent to average all the transition probabilities of the
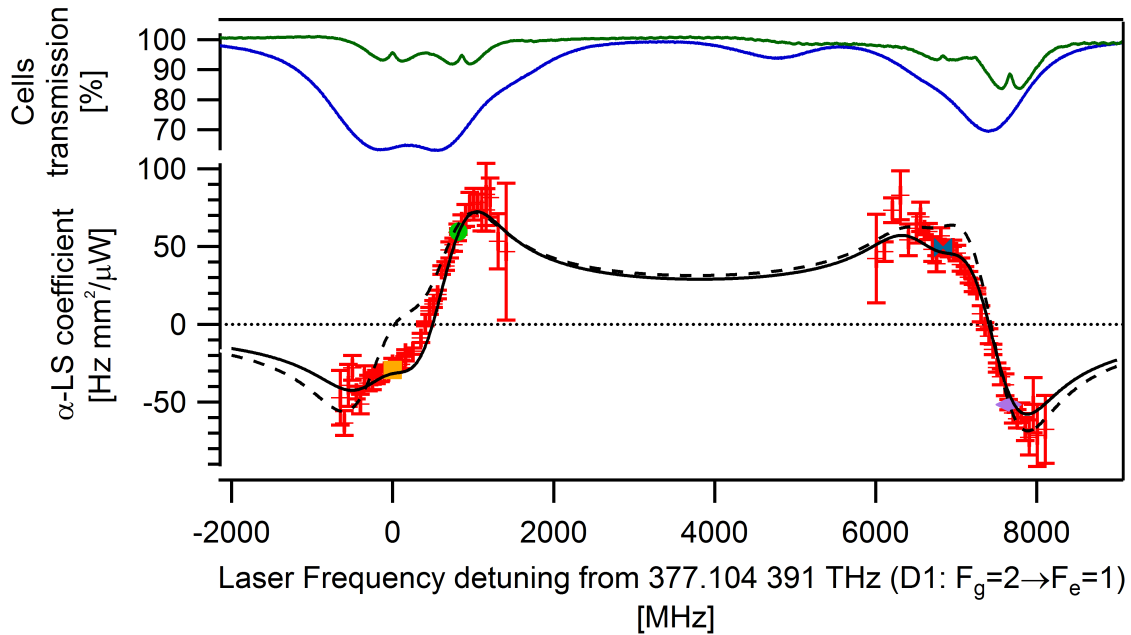
FIGURE 6.9: Light shift in the D1 line: upper part, sub-Doppler absorption spectrum of the reference cell (green) and absorption spectrum of the clock cell (blue); lower part: experimental (markers) and theoretical (lines) α_{LS} coefficients as a function of the laser frequency. The solid line corresponds to our model. The dashed line is calculated using the coefficients (see equation 1.125) of Mathur's model [101].

Zeeman substates considering an isotropic light (see equation 1.128), which is not the case in our experiment. Nonetheless, as seen for the D2 case, this approximation appears valid for optical transitions of which the hyperfine structure of the excited state is truly unresolved due to Doppler broadening or BG broadening.

Intensity light shift coefficient and clock operation:

For the clock operation, we focus now on the optical frequencies inducing transitions from $|F_g = 2\rangle$ state in the D2 line; the laser frequency offset is relative to the Di23 transition frequency. From the data of Figures 6.8 and 6.10, the α-LS coefficient changes sign between -315 and -365 MHz laser frequency offset, it must therefore be null in between. The use of the AOM laser head (see section 2.4.2) allowed to produce a pumping laser beam detuned from the reference frequencies provided by the sub-Doppler patterns and with a good frequency stability. Locking the AOM frequency shifted laser beam to the CO21-23 of the reference cell (-211.7 MHz offset)
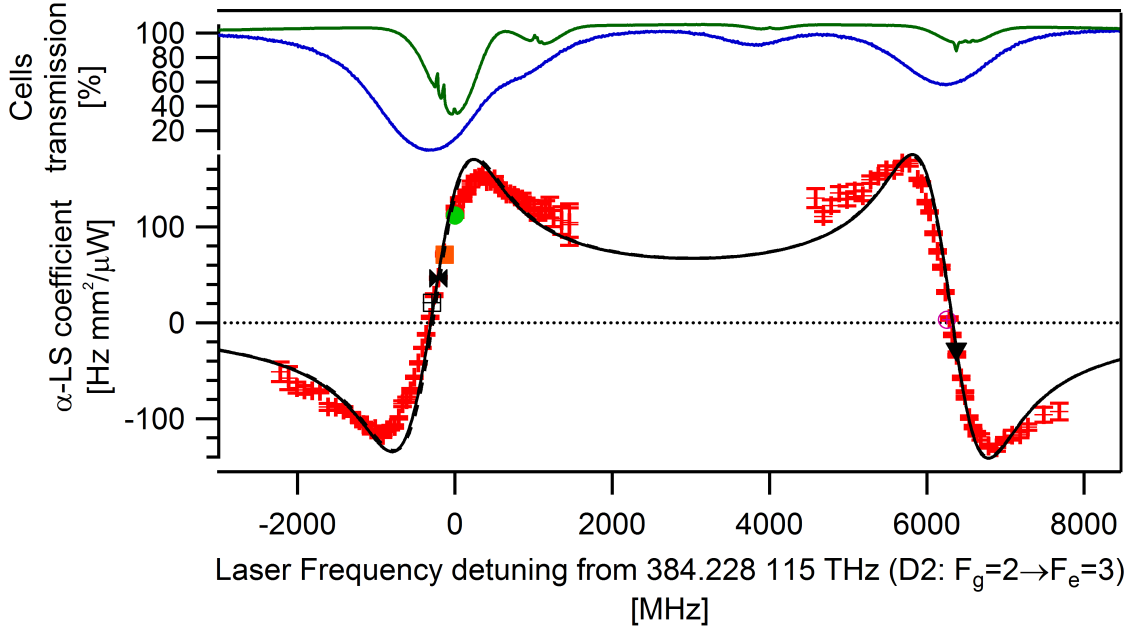
FIGURE 6.10: Light shift in the D2 line: upper part, sub-Doppler absorption spectrum of the reference cell (green) and absorption spectrum of the clock cell (blue); lower part: experimental (markers) and theoretical (solid line) α_{LS} coefficients as a function of the laser frequency. The solid line corresponds to our model. The dashed line, calculated using the coefficients (see equation 1.125) of Mathur's model [101], cannot be distinguished from the solid line.

enabled a frequency range from -346.7 to -296.7 MHz; the AOM allows $\pm 110 \pm 25$ MHz frequency shifts.

The light shifts obtained at an optical frequency offset of -341.7 MHz are shown on Figure 6.11 for different cell temperatures. They are measured in clock mode (see section 2.3.1.3). Thanks to the small light induced shift, two interesting phenomena can be observed. Non linearities, hidden by the strong α-LS coefficient at other laser frequency offsets, appear, and the α-LS coefficient has a dependency on the cell temperature. The non linearities are most likely due to light intensity gradients in the cell [213]. Concerning the temperature dependency and especially the sign inversion of the α-LS coefficient, this effect is highly similar to the effect observed in the tetracontane wall coated cell (see section 5.3.3), and the question of its physical origin remains open. A similar behaviour with an optical pumping from $|F_g = 1\rangle$ state would help to answer this question.

Based on the data of Figure 6.11 and the intensity light shift coefficient inversion observed, the
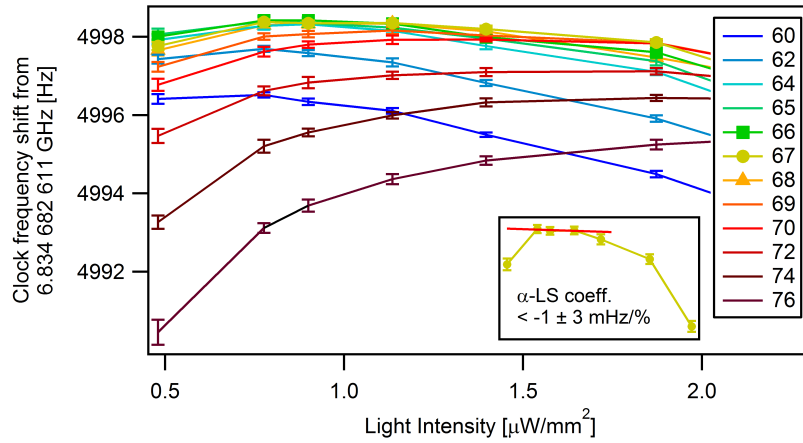
FIGURE 6.11: Clock frequency shift as a function of the laser intensity for different cell temperatures.

α-LS coefficient can be arbitrarily small. A value of $\alpha_L S < 1\pm3$ mHz/% at 1μW/mm^2 and at a temperature of $67°$C is obtained (see inset of Figure 6.11).

The Allan deviation of the incident (to the clock cell) light intensity fluctuations recorded over a period of 20 days is shown on Figure 6.12. On the same figure is also shown the potential effect on the clock instability using equation 1.105 and the measured α-LS coefficient. The clock instabilities induced by light intensity fluctuations stay below 3×10^{-14} up to one day.
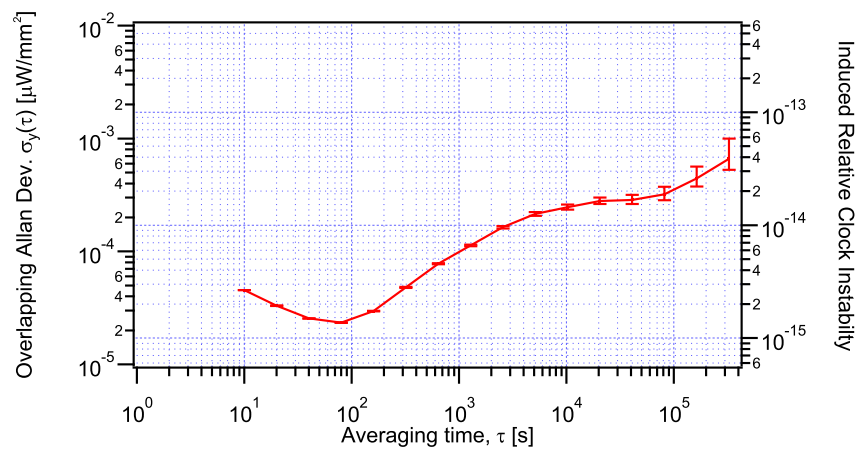
FIGURE 6.12: Light intensity fluctuation in terms of Allan deviation. The right axis shows the potential limitation on the clock instability.
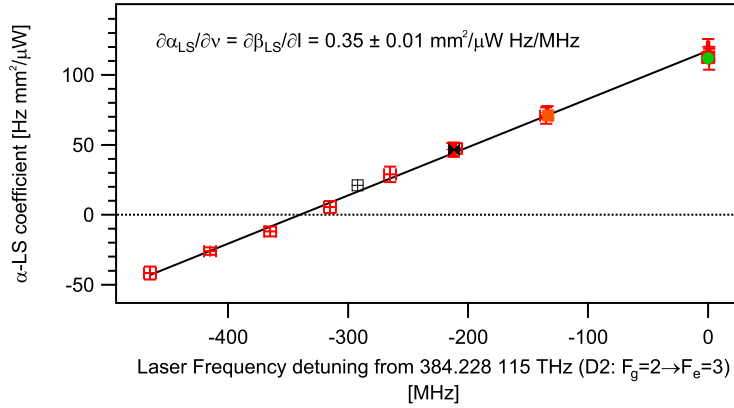
FIGURE 6.13: Close view of Figure 6.10 around operating optical frequency.

Frequency light shift:

Since the total light shift is proportional to the light intensity, the frequency light shift coefficient, or β-LS coefficient, can also be expressed as follow:

$$\beta_{LS} = \frac{\partial \Delta \nu}{\partial \nu_{opt}} = I \frac{\partial}{\partial \nu_{opt}} \left(\frac{\partial \Delta \nu}{\partial I} \right) \tag{6.3}$$

$$= I \frac{\partial}{\partial \nu_{opt}} (\alpha\text{-LS}), \tag{6.4}$$

where ν is the microwave clock frequency, and ν_{opt} the laser frequency. The measurement presented on Figure 6.10 contains therefore all the information on the light-shift effect, and a linear fit of the data points (see Figure 6.13) gives the β-LS coefficient with respect to the light intensity. At an intensity of $1\mu W/mm^2$ this coefficient is $\beta_{LS} = 0.35 \pm 0.01$ Hz/MHz.

The Allan deviation of the light frequency of the AOM laser head is shown on Figure 6.14. It results from the frequency stability of a beat note between the AOM laser head and another standard laser head. Each laser frequency was locked on a different atomic transition, distant of several MHz, and the beat note was detected by a fast photo-detector. The operating conditions were chosen to optimize the AOM laser frequency stability and a limit at a level of 2×10^{-11} at 10^4 s could be reached. The measurement details are explained in [11]. In our experimental configuration, the operating conditions were not chosen to optimize the laser frequency stability but to reduce the α-LS coefficient. This can potentially degrade the achievable AOM laser frequency stability. Indeed, the laser frequency was stabilized to the less stable crossover, the
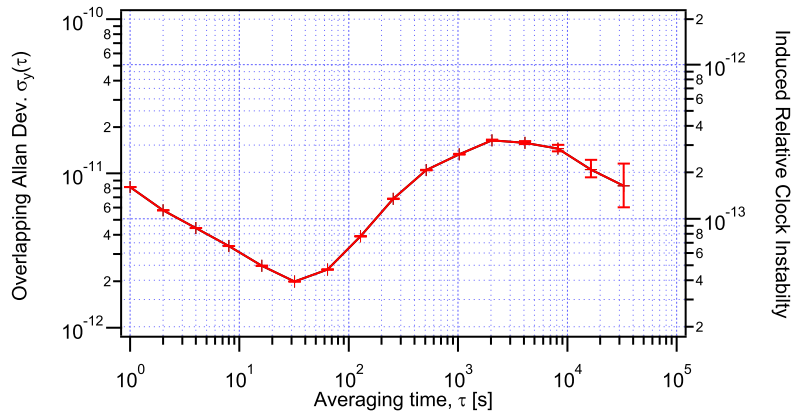
FIGURE 6.14: AOM Laser frequency fluctuation in terms of Allan deviation from [11]. The right axis shows the corresponding limitation due to the frequency light shift coefficient on the clock instability.

CO21-23, and the offset at which the α-LS coefficient is cancelled required to drive the AOM at 130 MHz, close to the upper edge of its bandwidth. Assuming a degradation of the laser frequency stability due to these modifications by a factor of 3 only, the laser frequency instabilities limit the clock stability at a level of 1.2×10^{-12}.

6.3.2.2 Microwave power shift

As seen in Chapter 1, no detailed theory has been developed to predict the power dependency of the clock transition frequency along with the power of the microwave field. Nevertheless, this shift can be quantified experimentally. For a fixed laser intensity of 1 μW, and laser frequency offset of -341.7 MHz nullifying the α-LS coefficient (see section 6.3.2.1), the clock frequency is measured as a function of the microwave power (see Figure 6.15). A linear fit in the vicinity of the optimal RF power gives a microwave power shift (PS) coefficient of -0.17(3) Hz/dBm (equivalent to $(2.5 \pm 0.4) \times 10^{-11}$ /dBm or -75 mHz/μW). Combining this coefficient with the fluctuations reported on Figure 6.16 (the RF power was measured using a calibrated Low-Barrier Schottky Diode Detector) a maximal instability contribution is estimated between 10^4 and 10^5 seconds at a level of 1.3×10^{-12}.
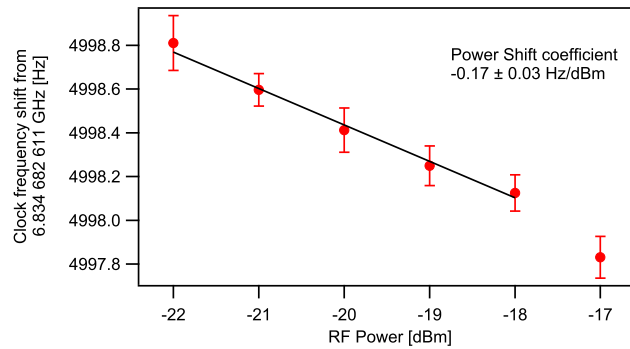
FIGURE 6.15: Clock frequency shift as a function of the microwave power.
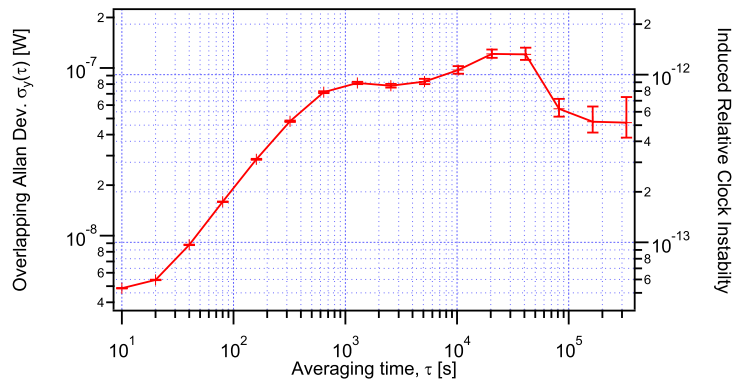
FIGURE 6.16: Microwave power fluctuation in terms of Allan deviation. The right axis shows the potential limitation due to the microwave power shift coefficient on the clock instability.

6.3.2.3   Temperature shift

The temperature shift coefficients for a buffer-gas cell were treated in section 1.7.2.2.   The measurement of the clock frequency shift as a function of the cell temperature is shown in 6.17.   The inversion temperature is $T_{inv} = 66.8°$C, corresponding to a buffer gas mixture of $59.8 \pm 0.2\%/40.2 \pm 0.2\%$ of Ar/N$_2$ (see equation 1.113). From this mixture and the total shift, the internal pressure is calculated to be 38.2 ± 0.1 mbar, using equation 1.107 and the coefficients of Table 1.9. Similarly to the observation made in Chapter 4, the effective buffer gas pressure is smaller ($\sim 40\%$) than the nominal value. At the chosen operating temperature of 67°C, the linear and quadratic temperature coefficients were measured to be $TC_{BG}^{(1)} = 52 \pm 22$ mHz/K and $TC_{BG}^{(2)} = 48 \pm 1$ mHz/K^2, respectively.

The PP temperature was measured using two NTCs independent from the temperature servo loop (see Figure 6.2); thermal fluctuations well below the mK are observed. The figure 6.18 shows the corresponding Allan deviation, and the theoretically induced instabilities to the clock frequency using equation 1.105 and the linear temperature shift coefficient, $TC_{BG}^{(1)}$. The induced clock instabilities are limited well below 1×10^{-14} up to one day, and below 1×10^{-18} up to one day using the quadratic temperature coefficient $TC_{BG}^{(2)}$.
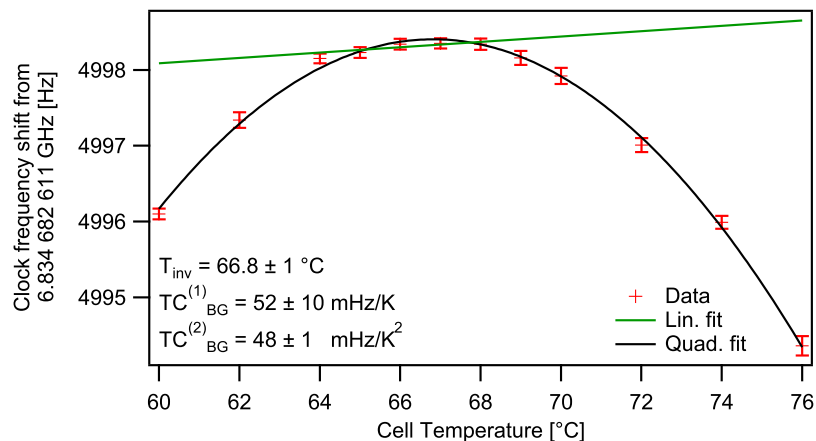
FIGURE 6.17: Clock frequency shift as a function of the PP temperature.
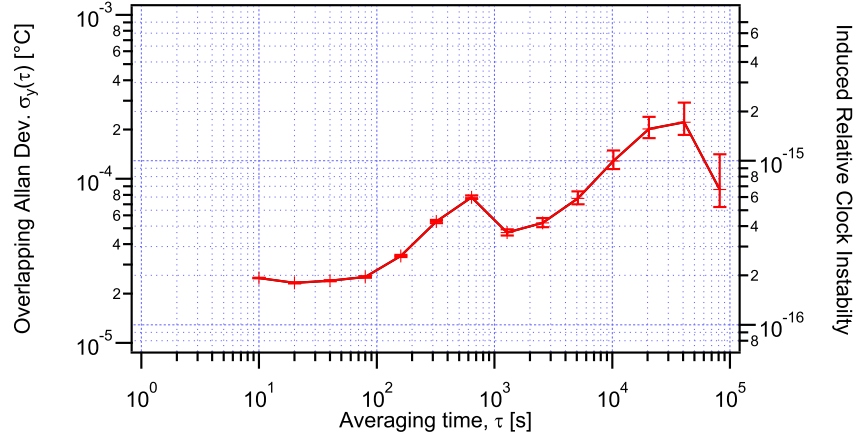
FIGURE 6.18: Physics package temperature fluctuation in terms of Allan deviation. The right axis shows the potential limitation due to the linear temperature shift coefficient, $TC_{BG}^{(1)}$, on the clock instability.

The other temperature dependant shifts, such as spin-exchange and cavity pulling, are experimentally indistinguishable and are therefore already included in the measurement of Figure 6.17. We estimate here below their individual and hidden contributions.

Spin exchange shift:

We use the derivative of equation 1.106 at the operating temperature of 67°C as the spin exchange shift coefficient. A value of $TC_{SE} = -0.17\,\mathrm{Hz/K}$ is calculated. As a stand alone process, and combined with the measured temperature fluctuations of the PP shown in Figure 6.18, the consequences on the clock stability would be of the order of 5×10^{-15}. But as mentioned earlier, it cannot be experimentally dissociated from the other thermal shifts, and is therefore compensated by other thermal shifts and already included in the data presented in Figures 6.17 and 6.18.

This effect might question the buffer gases pressures and percentages calculated in section 4.3. But the absolute spin exchange shift (SE) is relatively small ($\sim$ 2 Hz at 340 K) and almost linear within the temperature range considered. It shifts the inversion temperature of the cell by less than three Kelvin, equivalent to 0.6% error in the buffer gases percentages determination: 59.1(6)% Ar including SE shift and 59.8(6)% otherwise. Concerning the pressure determination, the effect is also small, and we calculate 37.4(6) mbar including SE shift and 38.2(6) mbar otherwise. Therefore, the analysis of section 4.2.4 remains still valid.

Cavity pulling:

We recall the cavity pulling temperature coefficient from section 1.7.2.6:

$$TC_{pulling} = \frac{\mathrm{d}\Delta\nu_{CP}}{\mathrm{d}T} \approx 3 \times 10^{-3} \frac{Q_L}{Q_a} \frac{\mathrm{d}\Delta\nu_{cavity}}{\mathrm{d}T} \tag{6.5}$$

For the micro loop-gap resonator (µ-LGR) considered here, the measured cavity resonance shift coefficient is $\frac{\mathrm{d}\Delta\nu_{cavity}}{\mathrm{d}T} \approx 0.4$ MHz/K [2]. From its relatively low quality factor ($Q_L \approx 30$) compared to the atomic one ($Q_a \approx 1.14 \times 10^6$), the cavity pulling temperature coefficient is $TC_{CP} = 32$ mHz/K. Similarly to the SE shift, the cavity pulling effect is already included in the experimental data of Figure 6.17, and doesn't induce any additional temperature sensitivity to the clock frequency shift.

6.3.2.4   DC magnetic field shift

In section 1.7.2.4, we identified two independent magnetic instability sources, the longitudinal magnetic field fluctuation and the C-field current fluctuations. For a non null C-field strength of $C_0 = 125$ mG, the linear magnetic sensitivity factor of the clock frequency was given by:

$$MS = 2 \cdot 575 \cdot C_0 = 144 \mathrm{Hz/G}. \tag{6.6}$$

As the earth magnetic field's daily fluctuations are of the order of 250 μG [214], they can potentially induce a clock frequency instability of the order of 5.3×10^{-12}. With the use of proper magnetic shields, these fluctuations can be significantly reduced. Bandi measured a magnetic field attenuation factor, or shielding factor, of $S = 3000$ for two concentric μ-metal cylindrical shields [7]. This configuration would allow a clock frequency instability of $< 2 \times 10^{-15}$. In our configuration, only a single cylindrical shield of 35 mm diameter and similar to the one used by Bandi is employed. Since in our configuration the cylinder has holes to allow the light to interact with the atoms and be detected, a theoretical prediction based on a closed cylinder would provide an overestimated value for the shielding factor. Although we did not measure it, we estimate our shielding factor based on the fact that in the case of two shields, the shielding factors of the

individual shields, S_i, are multiplied together as follow[1]:

$$S = 2S_1 S_2 \frac{a_2 - a_1}{a_2} \tag{6.7}$$

where

$$S_i \propto \frac{1}{a_i}, \tag{6.8}$$

and a_i are the diameters of the shields. Since diameters of $a_2 = 98$ mm and $a_1 = 36$ mm were employed by T. Bandi, we obtain a shielding factor of $S \approx 80$. This reduces the clock frequency instability at a level of 6.6×10^{-14}.

In our configuration, the 2 mA C-field current induces linear C-field current sensitivity factor for the clock frequency of $CC_{Zeem} = 9.1$ Hz/mA (see Table 1.11). Since our electronics guarantees a relative current instability inferior to 10^{-5} from 1 s up to one day, the induced instability to the clock frequency remains below 2.6×10^{-14} at all time scales.

6.3.2.5 Atmospheric pressure effect

The estimation of the atmospheric pressure effect was discussed in section 1.7.2.8. A relative pressure shift coefficient of $PrC_{Atm} = 1 \times 10^{-14}$/hPa was deduced. The Allan deviation of the atmospheric pressure recorded over a period of 20 days[2] is shown on Figure 6.19. On the same figure is also shown the potential effect on the clock instability using equation 1.105 and the calculated atmospheric pressure shift coefficient, PrC_{Atm}. The induced instability stays below 5×10^{-14} up to one day.

---

[1]The formulae are taken from http://www.magneticshields.co.uk/fr/faq
[2]The pressure data were provided by MétéoSuisse
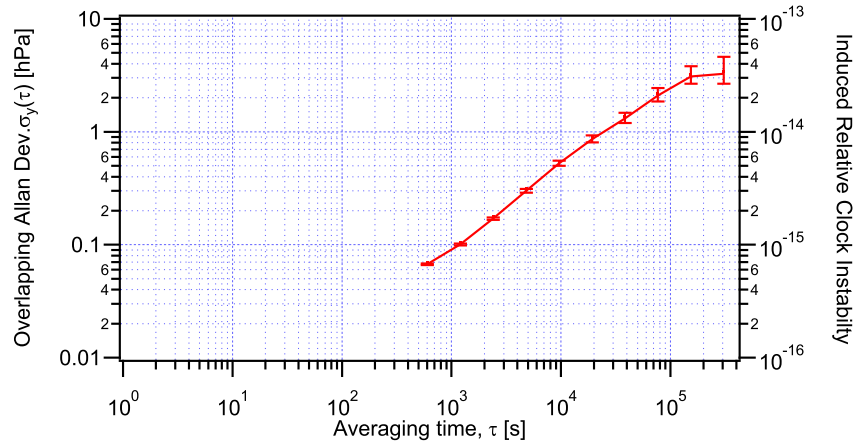
FIGURE 6.19: Pressure fluctuation in terms of Allan deviation. The right axis shows the potential limitation on the clock instability. Pressure data source: MétéoSuisse.

TABLE 6.2: Summary of the instability contributions in medium to long term time scales. PS, power shift; LS, light shift; TS, temperature shift; PrS, pressure shift.

Physical effect	Coefficient	Parameter Variation at 10^4-10^5 s	Absolute Instability	Relative Instability
Microwave PS	-0.17 Hz/dBm -75 mHz/μW	5×10^{-2} dBm 0.12 μW	9 mHz	**1.3$\times$ 10^{-12}**
Frequency LS Intensity LS	0.35 Hz/MHz[a] 0.4 Hz/$\frac{\mu W}{mm^2}$	23 kHz[b] 3.2×10^{-4} $\frac{\mu W}{mm^2}$	8 mHz 0.13 mHz	**1.2 $\times$ 10^{-12}** 1.9×10^{-14}
Measured. TS	52 mHz/K 48 mHz/K^2	<1 mK	<0.05 mHz < 48 nHz	$< 7 \times 10^{-15}$ $< 1 \times 10^{-17}$
Spin Exchange *Cavity Pulling*	-0.17 Hz/K 32 mHz/K	<1 mK	<0.17 mHz <0.03 mHz	$< 2.5 \times 10^{-14}$ $< 5 \times 10^{-15}$
C-Field Current Atmosph. PrS DC Magn. Field	9.1 Hz/mA 68.3 uHz/hPa 144 Hz/G	< 0.02 μA 3 hPa 3.1 μG	0.18 mHz 0.2 mHz 0.5 mHz	$< 2.6 \times 10^{-14}$ $< 5.0 \times 10^{-14}$ 6.6×10^{-14}
Total instabilities at $\tau = 10^4 - 10^5$ seconds:				$\sim 1.8 \times 10^{-12}$

[a]at 1 μW/mm^2
[b]estimated as thrice the value from [7]

6.4   Clock frequency stability

Figure 6.20 shows the relative clock frequency obtained over the course of several months, by frequency comparison with an active hydrogen Maser. The clock was operated at the optimized conditions deduced from the previous section: a PP temperature of 67 °C, a laser intensity of 0.9 μW/mm^2, -20 dBm of microwave power injected into the cavity and the laser frequency offset of -130 MHz from the CO21-23 using the AOM laser head. The microwave frequency was square modulated at 187 Hz with a modulation depth of 540 Hz.
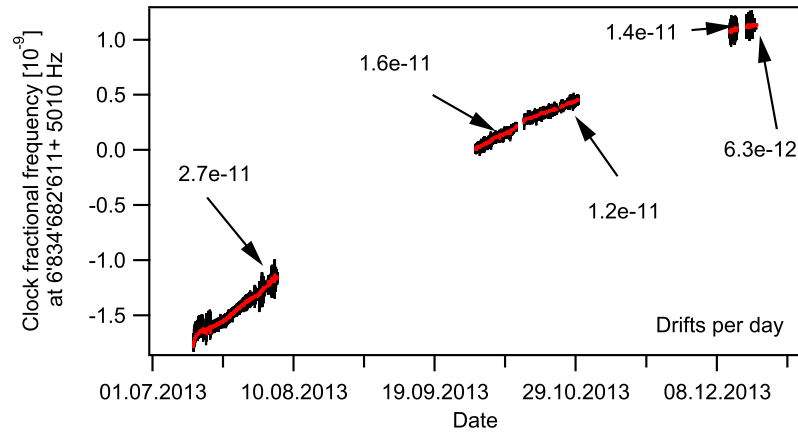
FIGURE 6.20: 3D cell-μ-LGR clock fractional frequency over a 6 month period. In black: $\tau = 1$ s, red: $\tau = 1000$ s. The numbers at the arrows give the local linear drift per day.

A clock frequency drift of the order of 1×10^{-11}/Day is observed, inducing a total clock frequency shift of more than 2.5×10^{-9} over 6 month. A similar behaviour was also observed for a Symmetricom's CSAC prototype after several weeks of operation [25], but hypothesises on physical origins are not discussed. For our case, the drift is ten times bigger than the potential drift induced by the ageing of the DFB (see Matthey [215]) through the measure of α-LS coefficient. It is also 10-100 bigger than the reported frequency equilibriation and/or linear frequency ageing rate by Camparo [109]. It cannot either be explained by the helium permeation effect that can induce a maximal total shift of 4.4×10^{-10} only (see section 4.2.4.3). However, the origin of this drift could be attributed to a Nitrogen leak of 1.32×10^{-13} mbar l/s (see equation 4.9 in section 4.2.4), but would require further analysis and much longer observation times to validate

this hypothesis. Note also that the 3D cell has not been subject to an accelerated ageing process at elevated temperatures, and the initial ageing process could also explain the drift observed.

The overlapping Allan deviation of the October data set (10 days starting from 14th October) is shown on Figure 6.21 along with the calculated shot-noise and signal to noise limits. The shot-noise limit of $\sigma_{y_{Shot}}(\tau) = 1.8 \times 10^{-12} \tau^{-1/2}$ and the signal-to-noise limit of $\sigma_y(\tau) = 1 \times 10^{-11} \tau^{-1/2}$ are calculated using equation 1.104 and 1.101, respectively and the parameters of the DR clock signal shown in Figure 6.6. Figure 6.22 shows the same stability along with the estimated contributions from the most significant shifts studied in section 6.3.2. The parameters were recorded simultaneously to the clock frequency, except the laser frequency taken from [11], and every Allan deviation is calculated with the possible drift included. The clock frequency drift observed at $\tau > 10^4$ s in Figure 6.21 corresponds to the linear drift measured in Figure 6.20, but cannot be explained by any measured parameter drift. This hints that the clock frequency drift is intrinsic to the cell only. Most probably, an internal ageing process is responsible for the drift, as the helium or neon permeation, and the nitrogen leak, can be excluded:

- In Figure 6.20, the total shift of the clock frequency due to the drifts after 6 months is $\Delta\nu > 17$ Hz. Such a shift could be explained by an increase of 0.03 mbar of the helium internal pressure, but this is incompatible with the atmospheric helium partial pressure of 5.3×10^{-3} mbar (see section 4.2.4.3).

- In Figure 6.20, the total shift of the clock frequency due to the drifts after 6 months is $\Delta\nu > 17$ Hz. Such a shift could be explained by an increase of 0.063 mbar of the neon internal pressure[1], but this is incompatible with the atmospheric neon partial pressure of 1.8×10^{-2} mbar (see section 4.2.4.3). Moreover, the permeation rate of neon through glass is 50 times less than helium through glass [172], leading to an equilibration time of $\tau_{Ne} = 50$ years (see section 4.2.4.3). Such time is not compatible with the observed equilibration time of ~ 1 year.

- In Figure 6.20, the drift coefficient is reduced by at least a factor of two after 6 month. Considering equation (4.9), such reduction could be explained by a significant internal nitrogen pressure increase of at least half of the initial internal-external pressures difference, *i.e.* > 450 mbar, inducing a total shift of 180 kHz. This is clearly incompatible with the total shift observed.

---

[1]The neon pressure shift coefficient is 269.7 Hz/mbar [92]

Up to 5 seconds, the clock frequency stability corresponds well to the signal-to-noise limit but is then degraded by two distinct cyclic frequency fluctuations, around 10^1 and 10^3 seconds. The precise physical effects at the origin of these fluctuations could not be identified yet, though a thermal effect affecting the laser frequency and not the microwave power is highly suspected. This statement is based on the following arguments:

- The laser frequency is the only parameter considered as a source of instability that was not measured simultaneously to the clock frequency.

- Its sensitivity coefficient, $\beta_{LS} = 0.35$ Hz/MHz, in combination with the ultimate frequency stability of the AOM laser head represents already the second most important clock stability limiting factor at a level of 4×10^{-13} (see Figure 6.22).

- No clear correlation is observed between the fluctuations of the measured parameters and the fluctuations of the clock frequency, as shown in Figure 6.23. Especially the microwave power fluctuations do not seem to correlate with the clock frequency fluctuations.

- The air conditioning system of our laboratory has a temperature cycle of typically 20-30 minutes period, responsible for the "bump" observed on the clock stability between 10^2 and 10^3 seconds in Figure 6.21. Such feature is not observed on any measured parameter stability, but the cell temperature which has only a negligible influence on the clock stability (see Table 6.2).
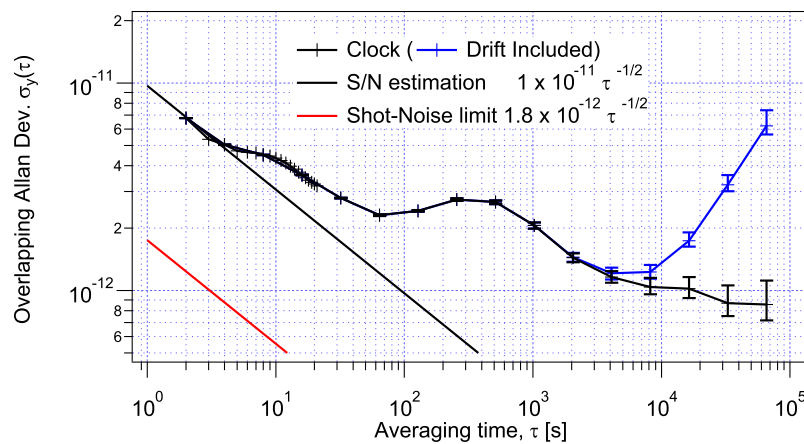
FIGURE 6.21: 3D cell-μ-LGR clock frequency stability in terms of Allan deviation.
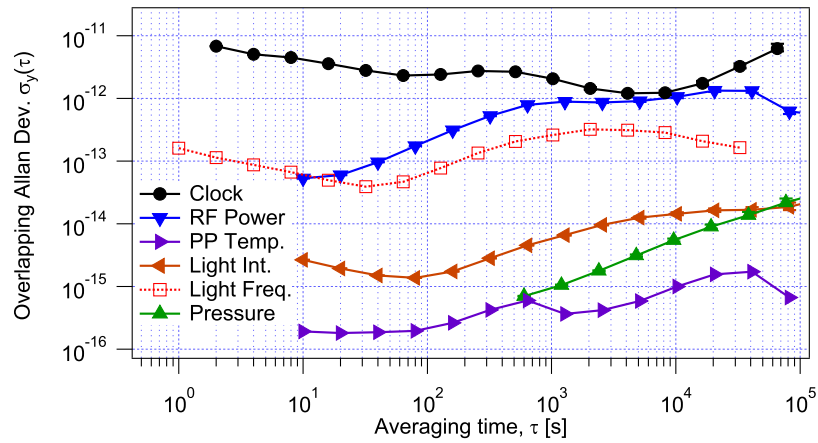
FIGURE 6.22: Clock frequency in terms of Allan deviation and estimated contribution from the most significant shifts.
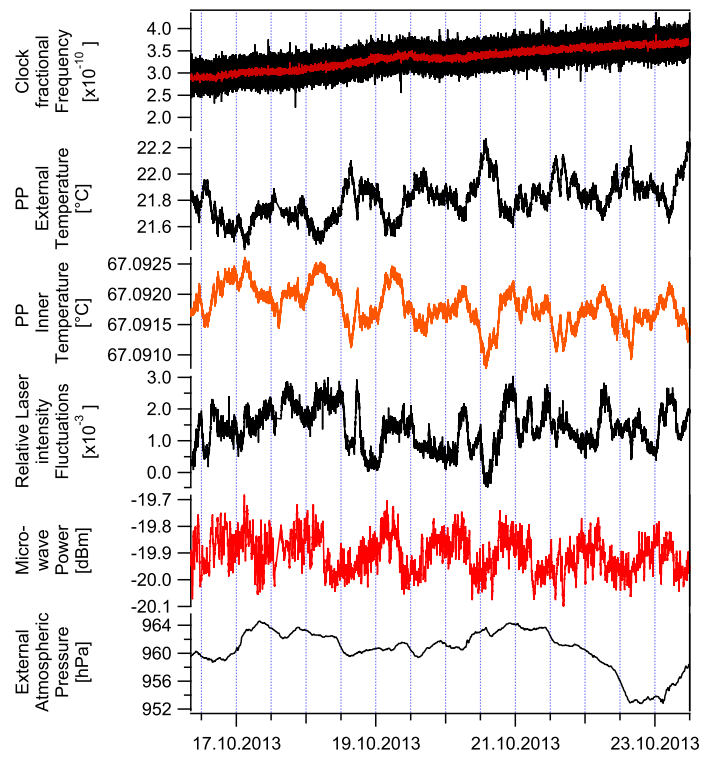
FIGURE 6.23: Clock fractional frequency and simultaneously measured varying parameters potentially affecting the clock frequency stability. No correlation is found between the clock frequency fluctuations and the parameters ones.

6.5   Suppressing the light shift effect

The light-shift effect is one of the main contributors to the clock frequency instabilities. In the past years, several techniques have been proposed to suppress or reduce significantly this effect in vapour cell based atomic clock:

- Deng proposed a method in the D1 line exploiting the selective pumping due to the polarization of the light. Two lasers of orthogonal polarizations pump simultaneously the two hyperfine ground states. The second laser with a π-polarization is used to compensate the light shift effect of the first laser and also to increase the contrast of the DR signal [104]. To our knowledge no experimental data reports on this method.

- Camparo proposed the use of higher buffer gas pressure (100 Torr) exploiting the reduced light-shift effect for broadened optical transition (see equation (1.131)). Both sensitivity coefficients could be simultaneously reduced. The reported values are: $\beta_{LS} = 6 \times 10^{-13}$ /MHz and $\alpha_{LS} = 0.9 \times 10^{-11}$ /% [216]. The operating intensities were not given.

- Another approach, used by Affolderbach et al., consists of a multi-frequency pump light field produced by the frequency modulation of a single frequency pump laser. Simulations and experiment demonstrate the existence of a "smooth spot" at which α_{LS} and β_{LS} coefficients are suppressed by factors of 80 and 45 respectively. The reported coefficients are $\beta_{LS} = 2.3 \times 10^{-12}$ /MHz and $\alpha_{LS} = 6 \times 10^{-13}$ /% at 40 µW of laser power [99].

- Recently McGuyer [217] proposed an innovative laser frequency locking scheme for a DR clock minimizing the intensity light shift coefficient only. The method uses the out-of-phase lock-in detection of the DR signal, to lock the laser frequency [218]. No explicit measure of the shift coefficients is reported, but a fractional frequency stability below 10^{-11} at 10^4 s is obtained based on this method.

- Bandi exploits the predicted zero α_{LS} coefficient (see Figures 1.19) and reduces the β_{LS} with a reduced laser intensity. The reported coefficients are $\beta_{LS} = 1.2 \times 10^{-11}$ /MHz and $\alpha_{LS} = 1 \times 10^{-12}$ /% at 35 µW/mm^2 of laser intensity [7]. In this study, we followed the same approach (see Chapter 6) and our measured coefficients are: $\beta_{LS} = 5.1 \times 10^{-11}$ /MHz and $\alpha_{LS} = 5.9 \times 10^{-13}$ /% at 1 µW/mm^2 of laser intensity.

Table 6.3 summarizes all these coefficients.

TABLE 6.3: Comparison of the reduced intensity- and frequency light-shift coefficients reported in the literature.

	α_{LS} [%$^{-1}$]	β_{LS} [MHz^{-1}]
Camparo [216]	0.9×10^{-11}	6×10^{-13}
Affolderbach [99]	6×10^{-13}	2.3×10^{-12}
Zhu [106]	$< 1 \times 10^{-12}$	$< 1 \times 10^{-12}$
Bandi [7]	1×10^{-12}	1.2×10^{-11}
This study	5.9×10^{-13}	5.1×10^{-11}

The most promising method was proposed by Zhu, in which he exploits the light polarization and buffer gas pressure dependency of the light shift effect. He demonstrated that for a single laser source with a given light polarization and an adapted buffer gas pressure both sensitivity coefficients are significantly reduced [106], [219]. No numerical value of the shift coefficients is reported, and the resolution of the graphics allows only a poor estimation of the light shift coefficients within one order of magnitude. Nevertheless, these are estimated to be $\beta_{LS} < \times 10^{-12}$ /MHz and $\alpha_{LS} < 1 \times 10^{-12}$ /% at 10 µW of laser power [106]. Following the same method, our theoretical model also predicts these observations (as shown on Figure 6.24), and the simultaneous suppression of both α-LS and β-LS coefficients over a wide frequency range (> 100 MHz) is predicted for a pumping light source having a 44% π- and 56% σ- polarization and a BG pressure of 30 mbar. This method is particularly interesting since an isoclinic point[1] (see [220]) is also located within this frequency range. Experimentally, such a DR interrogation configuration is achieved with: a D1 laser locked on the isoclinic point, propagating orthogonally to the C-field, and of which the linear polarization makes an angle of $\sim 48.5°$ with respect to the C-field (see Figure 6.25). Although the laser stabilization to the isoclinic point may reduce significantly the laser frequency stability (roughly two orders of magnitude at 10^4 s [120]), this is compensated by the arbitrarily small β-LS coefficient that can be theoretically achieved.

This method was already proven to be extremely efficient by Miao Zhu [106], [219], who demonstrated clock frequency stabilities below 10^{-13} at 10^4 seconds. In terms of complexity, cost and volume it also presents significant advantages: it allows a simple and compact locking scheme for the laser frequency. Moreover since the laser is frequency locked on the clock cell, the diode

---

[1]in other words, a laser stabilization point of which the frequency doesn't change at the first order with the temperature and the buffer gas pressure.
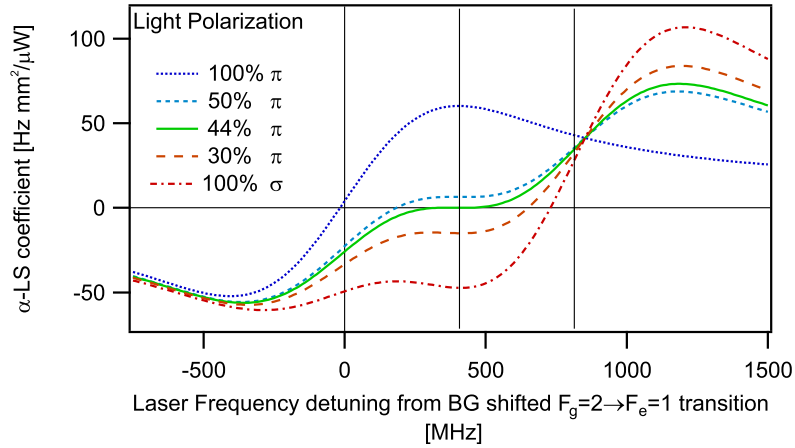
FIGURE 6.24: Predicted α_{LS} coefficients as a function of the light frequency and for different polarization mixing in a 30 mbar BG cell. The vertical external lines, at 0 and 814.5 MHz detuning, correspond to the optical frequencies of the direct transitions Di21 and Di22 ($|F_g = 2\rangle \rightarrow |F_e = 1\rangle$, resp. ($|F_g = 2\rangle \rightarrow |F_e = 2\rangle$ transitions); the central one to the optical frequency of Rb D1 isoclinic point [220].
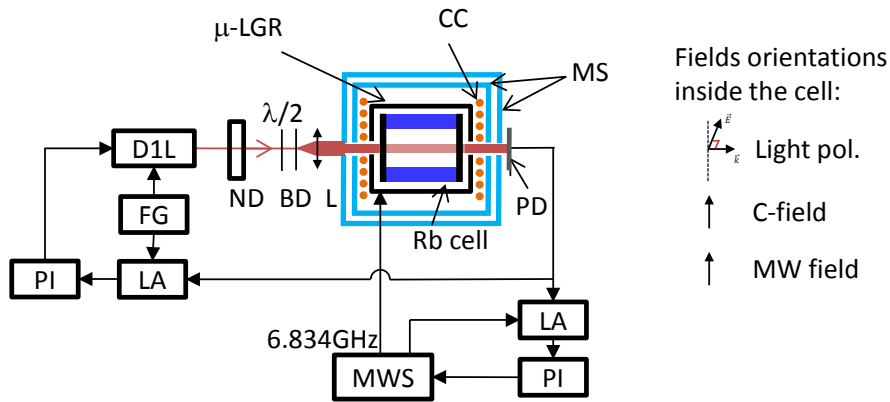
FIGURE 6.25: Clock setup exploiting the zero LS coefficients. D1L, D1 Laser; LA, Lock-in Amplifier; PI, PI controller; FG, Frequency Generator; $\lambda/2$, half-wave plate; MW, microwave. Other acronyms are given in Figure 6.1. Half-wave plate serves for light polarization control.

can be directly integrated in the PP and the laser head becomes obsolete. Finally, a cheaper light source with a larger emission spectrum (e.g. VCSEL) can also be envisaged, for the optical reference line used for laser frequency stabilization is much wider than the sub-Doppler patterns and doesn't require the narrow emission spectrum of a DFB to be observed.

6.6 Comparison with commercially available clock

Figure 6.26 shows and compares the measured stabilities of various types of commercial clocks with our miniature 3D-µ-LGR clock. Except for the SA3xm and the 3D-LGR clocks, the data presented in Figure 6.26 were measured on a dedicated test bench developed during a three-months stay at the European Space Research and Technology Centre (ESTEC) in 2012 in Noordwijk, Netherlands. This test bench allows the simultaneous measurement of three different clock frequency stabilities along with all their available operating parameters.

As compared to the other miniature commercial clock (LPFRS), the performances achieved with the 3D cell-µLGR atomic resonator look very promising. Indeed, with a significantly smaller volume, our atomic resonator, exhibits similar, or even better short-term stabilities than commercially available miniature atomic clocks (see Figure 6.26 and Table 6.4). In spite of the cyclic fluctuations, the stability starts at, and remains below 10^{-11} up to 1 day. Drift removed, it reaches 1×10^{-12} at 4000 seconds and remains at this level up to one 10^{5} s. This demonstrates the potential of our 3D-µ-LGR clock to significantly reduce the size of miniature atomic clocks without degrading the excellent stability performances already achieved.
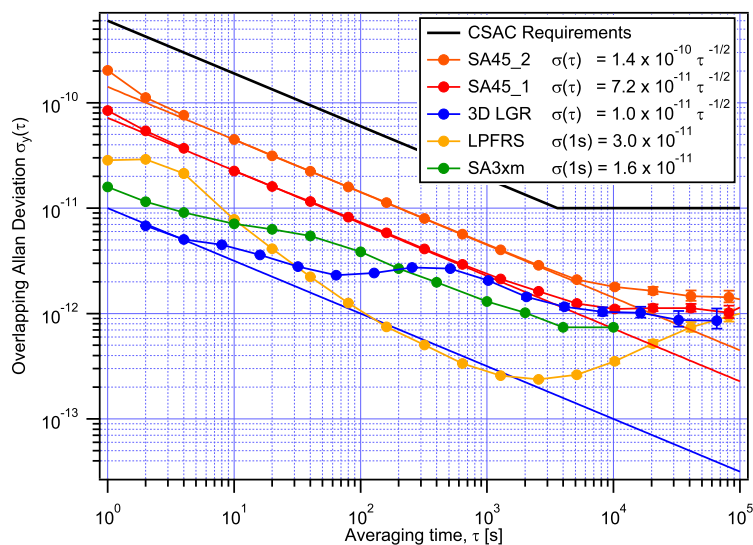
FIGURE 6.26: Comparison of the stability of the μ-LGR clock with three other commercially available clocks. All the clock stabilities, but the SA.3xm taken from [221], were experimentally measured within this thesis work.

TABLE 6.4: Comparison of the µ-LGR atomic resonator with commercially available miniature atomic clocks in terms of clock frequency stabilities, volume and power consumption. Data obtained from the respective clock datasheets, except for the Spectratime's LPFRS and Symmetricom's CSAC which were measured.

Company	Model	$\sigma_y(1s)$	drift [day^{-1}]	Power [W]	Dimensions [mm]	Volume [cm^3]
Lamp pumped DR						
SRS	PRS10	2×10^{-11}	2×10^{-11}	14	102 x 76 x 51	395
Frequency Electronics	FE-5680A	1.4×10^{-11}	2×10^{-11}	11	125 x 86 x 25	270
Spectratime	LPFRS	3×10^{-11}	4×10^{-12}	10	76 x 77 x 36.5	214
Accubeat	AR133A	2×10^{-11}	2×10^{-12}	n.a.	77 x 77 x 25.4	151
Symmetricom	X72	3×10^{-11}	5×10^{-11}	8	75 x 89 x 18	125
CPT						
Quartzlock	E10-MRX	8×10^{-11}	5×10^{-12}	6	51 x 51 x 25	65
Symmetricom	CSAC	7×10^{-11}	2×10^{-12}	0.120	41 x 35 x 11	16
This study	µ-LGR only	1×10^{-11}	7×10^{-12}	Heating only: (1)	($\varnothing$ 20.3 x 11.3)	(3)

6.7 Conclusions

We presented a detailed metrological characterization of a new type of microfabricated atomic resonator of 0.9 cm^3 volume, the µ-LGR. This resonator presents the particularity of having dimensions smaller than half the rubidium hyperfine transition wavelength while still showing a TE011 like mode. The resonator's microwave field has a very high homogeneity (orientation parallel to the C-field) over the cell volume, which is expressed by the high field orientation factor measured as 0.7, in good agreement with the simulated value of 0.8. The cell, sealed by anodic bonding is buffer gas filled with a Nitrogen-Argon mixture. The optimized operating conditions allow clock signals having a 10% contrast, and a discriminator slope of 15 pA/Hz. The corresponding shot-noise and signal-to-noise limit are $2 \times 10^{-12} \tau^{-1/2}$ and $1 \times 10^{-11} \tau^{-1/2}$, respectively. A detailed study of the systematic shifts affecting the clock stability was provided. A special attention was dedicated to the light-shift study and an excellent match is obtained between the intensity light shift coefficients predicted by our theoretical model of the Chapter 1 and the experimental data. Frequency light shift and microwave power shifts are demonstrated to be the main contributors to the long term clock instability at a level of few 10^{-12} at one day of integration time. The other instability sources such as temperature shift, spin exchange shift, cavity pulling, atmospheric pressure shift and DC magnetic field shift appear to contribute at a level of 7×10^{-14} or below. The measured stability of the physics package starts and stays below 1×10^{-11} from 1 second up to one day, in excellent agreement with the predicted short-term stability limit. In the short-term regime, the achieved performances are similar, even better than the ones of commercially available miniature rubidium clocks. A drift of 1×10^{-11}/day is observed. It is attributed to an ageing process. The existing methods minimizing the light shift effect were discussed and compared, and a promising method (in terms of cost, volume and complexity) was identified. Proposed first by Zhu [106], this method allows a simultaneous suppression of both the intensity and frequency light-shift coefficients with the use of a single laser diode and a single rubidium vapour cell. This would allow the realization of a clock limited in size only by the µ-LGR and the electronics. The experimental demonstration still remains to be addressed on our setup.

Summary and conclusions

This thesis presents the realization and the experimental and theoretical spectroscopic studies of innovative cells and other components for a miniature rubidium atomic clock. This research took place within the frame of four projects: MACQS, NPI, FNS-Rb and FNS-REQUIP (see page xxix).

Theoretically, a new empirical model describing precisely the light-shift effect in buffer gas cells has been developed. Its predictions were experimentally tested and validated. The principal experimental results are summarized in Table 6.5 in terms of cell types and sizes. These are summarized in the following paragraphs.

A first update of the LTF cell filling facility allowed the production of high quality glass-blown buffer-gas or evacuated cells. The excellent reproducibility of the buffer gas mixture achieved permits a control of the inversion temperature within ± 2 K [155], and the produced BG cells were used for the realization of high performances compact rubidium atomic clocks. These clocks presented state-of-the-art frequency stabilities: $\sigma_y(\tau) = 5 \times 10^{-13} \tau^{-1/2}$ for a 14 mm diameter cell [6] and $\sigma_y(\tau) < 2 \times 10^{-13} \tau^{-1/2}$ for 25 mm diameter cells [8], [119]. The evacuated cells were employed in the realization of various laser frequency stabilization systems developed in those as well as in other projects. Optical frequency instabilities down to $\sigma_y(\tau) < 7 \times 10^{-12}$ for τ up to 10^4 s were demonstrated for our laser head [11].

A second update of the LTF cell filling facility allowed the fabrication of glass-blown wall-coated cells. Previously known Tetracontane and Parylen coatings were implemented using two different deposition methods, *in-situ* and *ex-situ*. The non-compatibility of parylen as well as its non-efficiency as anti-relaxing coating with Rb were demonstrated. The successful in-house production of Tetracontane coated cells allowed a continuous DR spectroscopic measurement of the ripening process, which shows an exponential reduction of the population, coherence relaxation rates, and of the frequency shift per collision during the process. These results bring additional information for the understanding of this known but not well understood process. The Tetracontane cells were also characterized post ripening and intrinsic linewidths below 100 Hz were

measured. This corresponds to a coherence lifetime of more than 3 ms (or more than 100 collisions), which is mostly limited by the reservoir effect. The measured average shift per collision and the temperature coefficients are $\Phi = -32 \pm 2$ mrad/coll and $TC_{coat} = 1 \pm 0.1$ Hz/K, respectively. The comparison with the data found in the literature validates our own fabrication process. More detailed laser-pumped DR spectroscopy of a Tetracontane coated cell, put in evidence the Rb-density dependency of the intensity light-shift coefficient. It is not only reduced but can be inverted by changing the cell temperature, without shifting the laser frequency. This effect potentially offers a simple method for intensity light shift suppression, essential for improving the clock frequency stability. However, it needs further investigations.

The micro-fabricated cells[1] studied used two sealing techniques: anodic- and innovative low-temperature indium-bonding. Various spectroscopic studies were presented to evaluate the tightness of the low-temperature In bonding. The build-up of a sufficient Rb vapour pressure for spectroscopic studies and the presence of buffer gas were confirmed by linear absorption spectroscopy. A maximal contamination level of ~ 1 mbar of inert gas was determined by sub-Doppler saturated absorption spectroscopy. An novel method, based on DR spectroscopy, was employed to evaluate the sealing leak rate. Exploiting the hyperfine buffer-gas frequency shift of the Rb atoms allowed the measurement of an upper leak rate limit at a level of $< 1.5 \times 10^{-13}$ mbar l/s for the anodic bonded cell by using DR spectroscopy. This leak rate measurement technique, using CPT instead of DR spectroscopy, could allow a fast, real-time, continuous and low-cost leak rate measurement tool for certain types of MEMS sealing compatible with alkali atoms; on the contrary to leak rate analysis based on N_2O Fourier transform infrared (FTIR) spectroscopy [222] in which the spectroscopic analysis is made sequentially after bombarding in a pressurized chamber the sample, our alternative method is possible inside the pressurized chamber.

Thanks to the low sealing temperatures achieved with the In-bonding, the first micro-fabricated wall-coated cell showing effective anti-relaxing properties could be produced. It already shows very promising anti-relaxing features, such as an intrinsic linewidth below 9 kHz for a volume of 5.9 mm^3, and proves the feasibility of such a cell.

Finally we presented the spectroscopic and clock studies of a miniaturized physics package. The cell was a thick core anodic bonded cell filled with enriched ^{87}Rb and buffer gas mixture [164],

---

[1]produced by R. Straessle and Y. Pétremand using the micro-fabricated cell filling system co-owned by LTF and SAMLAB.

and the resonator, a µ-LGR developed and realized in collaboration with LEMA-EPFL by M. Violetti [223]. DR signal optimization and studies on the medium-term instability sources such as light intensity, microwave power, and temperature fluctuation were presented. Excellent short-term clock frequency stabilities of $\sigma_y(\tau) \sim 1 \times 10^{-11} \tau^{-1/2}$ showing a flicker floor at 10^{-12} were demonstrated with a PP's internal cavity volume of only ~ 1 cm^3. The frequency light shift as well as the microwave power shift were identified as the main limiting factors at a level of few 10^{-12}. The good short term frequency stability and a careful metrological analysis have allowed to identify and quantify a cell's intrinsic frequency drift, of the order of 1×10^{-11} /day, due to some ageing process in the cell. Our theoretical model for the light shift was also validated using this physics package by a thorough measure of the light shift coefficients over the whole D1 and D2 lines. An excellent match between experiments and the model predictions is observed. The validity of the model allows to explain and predict quantitatively the experimental conditions required for the realization of the interrogation scheme proposed by M. Zhu [219]. This scheme allows a significant and simultaneous suppression of the intensity and the frequency light shifts, thus reducing the intensity and frequency stability requirements for the optical source.

Future research directions

Our cell filling facility update allows now the fabrication of high quality buffer-gas cells and wall-coated cells. The study of alternative coatings, such as for example C30+ normal alpha olefin, is of high interest and could also be implemented in bigger glass-blown cells. For clock application, the temperature coefficient of the tetracontane, of the order of 1 Hz/K, remains a significant limit, but the use of a complementary low pressure buffer gas mixture might allow to compensate for this sensitivity, although the interaction mechanisms are different.

The cell micro-fabrication, and more particularly the In-bonding, is now proven to be compatible with the use of OTS as anti-relaxation coating. Further investigations on such type of cells, especially on the currently limited lifetime, and in view of clock, or other applications, have to be done. The use of a coating in addition to a low buffer gas pressure has also to be studied. It is already proven to significantly improve the relaxation rates of the cell [204], but given the small volume of the chamber, other effects related to the atoms being trapped near the walls [86] could be put in evidence.

The miniature double-resonance atomic clock based on the µ-LGR presents several potential further investigation lines. Currently, the identified stability limiting factors are the microwave power-shift, and the laser frequency light-shift. A detailed study of the microwave power shift as well as a measurement of the laser frequency in parallel with the clock frequency would allow a better understanding of the current limitations of the clock frequency stability. The long term drift has also to be further studied to identify and understand its origin; for the current cell, as well as for other cells that would have been subject to an accelerated ageing process. A residual gas analysis of these cells broken under vacuum could also bring additional informations on the ageing process. The miniature discharge lamp technology, proven to be efficient for Zeeman pumping, [4], has also to be tested as an optical hyperfine pumping light source.

Finally, the theoretical predictions on the light-shift effect with mixed light polarizations should be experimentally validated. Then, the actual high-performance, cumbersome and costly laser-head could be replaced by a simple and cheap VCSEL diode [224], without degrading the excellent clock frequency stability; the realization of a DR sub-miniature atomic clock having a $1 \times 10^{-11} \tau^{-1/2}$ frequency stability with a PP volume of few cm^3 at a moderate cost appears feasible. A preliminary verification looks realistic with the actual µ-LGR thanks to its non perfect field orientation factor. Indeed, a fraction of the microwave field components orthogonal to symmetry axis of the µ-LGR will induce π-transition, thus a DR clock signal, under a C-field orthogonal to the same symmetry axis. But eventually, a new µ-LGR would have to be redesigned to allow the required condition for a strong 0-0 clock transition, i.e.: a good field orientation factor (FOF) with respect to a C-field orthogonal to the laser propagation vector (see Figure 6.25).

TABLE 6.5: Global overview of the achievements realized within this thesis from a cells sizes and types point of view.

	Glass blown (GB)[a]	μ-fabrication (μ-fab)	
		Anodic bonding[b]	Indium bonding[c]
Buffer Gas (BG)	Evaluation of Cell filling update for buffer gas: -Excellent reproducibility of buffer gas filling is demonstrated. Realization of High performances clocks.	Evaluation of buffer gas filling of the μ-fabrication process (2D, 3D). Realization of a miniature PP for miniature atomic clock.[d] Validation of the Light-shift model.	Preliminary validation of the innovative sealing method : -Determination of the leak rate of the sealing by linear absorption and DR spectroscopy.
Wall Coating (WaCo)	Evaluation of Cell filling update for wall coating, and two deposition methods for the production of wall coated cell. Test of innovative coatings: Parylen N & C.[e] Spectroscopic evaluation of Tetracontane: - Observation of the ripening process by DR spectroscopy; - Measurement of an α-LS coeficient inversion.	Currently incompatible technologies.	First ever MEMS OTS wall-coated cell. Validation of the antirelaxing properties by spectroscopic evaluation.
Evacuated (Evac.)	Improvement of the cell cleaning procedure. Realization of optical frequency references for laser stabilization.	Not studied here. For a realization, of such a cell see [169].	Preliminary validation of the innovative sealing method : -Determination of the leak rate of the sealing by sub-Doppler absorption spectroscopy.

[a]Cells fabricated by M. Pellaton
[b]Cells fabricated by R. Straessle & Y. Pétremand
[c]Cells fabricated by R. Straessle
[d]μ-wave resonator realized by LEMA, EPFL
[e]Cells fabricated by M. Pellaton & R. Straessle

Appendix A

Spin composition: Clebsch-Gordan Coefficients

This appendix gives the Clebsch-Gordan coefficients describing the combination of two angular momenta (electron spin and nuclear spin). The new representation is expressed as follow:

$$|F, m_F\rangle = C^{F,m_F}_{J,I,m_J,m_I} |J, I, m_J, m_I\rangle, \qquad (A.1)$$

where C^{F,m_F}_{J,I,m_J,m_I} are the Clebsch-Gordan coefficients given in table A.1.

TABLE A.1: Clebsch-Gordan coefficients for ^{87}Rb ($I = 3/2$, $S = 1/2$)

m_S	m_I	F=2 m_F=2	F=2 m_F=1	F=2 m_F=0	F=2 m_F=-1	F=2 m_F=-2	F=1 m_F=1	F=1 m_F=0	F=1 m_F=-1
1/2	3/2	1							
-1/2	3/2		$\sqrt{1/4}$				$\sqrt{3/4}$		
1/2	1/2		$\sqrt{3/4}$				$-\sqrt{1/4}$		
-1/2	1/2			$\sqrt{1/2}$				$\sqrt{1/2}$	
1/2	-1/2			$\sqrt{1/2}$				$-\sqrt{1/2}$	
-1/2	-1/2				$\sqrt{3/4}$				$\sqrt{1/4}$
1/2	-3/2				$\sqrt{1/4}$				$-\sqrt{3/4}$
-1/2	-3/2					1			

Appendix B

Magnetic transition probabilities in terms of intensity

In Chapter 1 we decomposed the RF magnetic field as follow

$$\vec{B}_{RF}(t) = (\vec{B}_\parallel + \vec{B}_\perp)\cos(\omega_M t) \text{ with } \begin{cases} \vec{B}_\parallel = \frac{\vec{B}_{RF} \cdot \vec{C}_0}{||\vec{C}_0||} \frac{\vec{C}_0}{||\vec{C}_0||} \\ \vec{B}_\perp = \vec{B}_{RF} - \vec{B}_\parallel \end{cases} \quad \text{(B.1)}$$

considering the amplitudes of the field known and a static geometry (no rotating field). Switching now in term of known intensities of electromagnetic waves, one can decompose the RF field in the local orthonormal basis $\{\vec{e}_z, \vec{e}_+, \vec{e}_-\}$ induced by the C-field, as follow:

$$\vec{B}_{RF}(t) = \left(B_\parallel \vec{e}_z + B^+ \vec{e}_+ + B^- \vec{e}_-\right)\cos(\omega_M t) \text{ with } \begin{cases} \vec{e}_z = \frac{\vec{C}_0}{||\vec{C}_0||} \\ \vec{e}_\pm = \frac{1}{\sqrt{2}}(\vec{e}_x \pm i\vec{e}_y) \end{cases} \quad \text{(B.2)}$$

$B_\parallel \vec{e}_z$ correspond to the magnetic field of a π_M polarized RF field, $B^+ \vec{e}_+$ and $B^- \vec{e}_-$ to the magnetic fields of σ^+ and σ^- polarized RF fields, respectively. Figure 1.6 schemes these polarizations.

with the same argumentation as in Chapter 1, we obtain the following pumping rates:

$$\Gamma_{M_{if}}(\omega_M) = \begin{cases} \left(\frac{B_z \mu_B}{\hbar}\right)^2 2\pi g(\omega_M - \omega_{if}) \underbrace{|\langle f| \, \boldsymbol{S}_z \, |i\rangle|^2}_{(\mu_{if}^\pi)^2} \\[2em] \left(\frac{B_+ \mu_B}{\hbar}\right)^2 2\pi g(\omega_M - \omega_{if}) \underbrace{|\langle f| \, \frac{1}{\sqrt{2}} \boldsymbol{S}_+ \, |i\rangle|^2}_{(\mu_{if}^+)^2} \\[2em] \left(\frac{B_- \mu_B}{\hbar}\right)^2 2\pi g(\omega_M - \omega_{if}) \underbrace{|\langle f| \, \frac{1}{\sqrt{2}} \boldsymbol{S}_- \, |i\rangle|^2}_{(\mu_{if}^-)^2} \end{cases} \tag{B.3}$$

with $\boldsymbol{S}_\pm = \vec{\boldsymbol{S}} \cdot \vec{e}_\pm = (\boldsymbol{S}_x \pm i\boldsymbol{S}_y)$, the spin ladder operators. The matrix elements, $\mu_{if}^{\pi,\pm}$ are given in Table B.1. One can notice this time that:

$$\frac{1}{(B_\parallel)^2} \sum_i (\Omega_{M_{ii}}^\pi)^2 = \frac{1}{(B_+)^2} \sum_{i,j} (\Omega_{M_{ij}}^+)^2 = \frac{1}{(B_-)^2} \sum_{i,j} (\Omega_{M_{ij}}^-)^2 \tag{B.4}$$

TABLE B.1: Magnetic dipole matrix elements, μ_{if}^{π}, top table, μ_{if}^{-}, lower left table and μ_{if}^{+}, lower right table, within the ground state $5^2\mathrm{S}_{1/2}$. We use: $i \leftrightarrow m_1$, and $f \leftrightarrow m_2$.

$m_{F=1}$ \ $m_{F=2}$	-2	-1	0	1	2
-1		$\frac{\sqrt{3}}{4}$			
0			$\frac{1}{2}$		
1				$\frac{\sqrt{3}}{4}$	

m_1 \ m_2	-2	-1	0	1	2
-1	$-\frac{\sqrt{3}}{2\sqrt{2}}$				
0		$-\frac{\sqrt{3}}{4}$			
1			$-\frac{1}{4}$		

m_1 \ m_2	-2	-1	0	1	2
-1			$\frac{1}{4}$		
0				$\frac{\sqrt{3}}{4}$	
1					$\frac{\sqrt{3}}{2\sqrt{2}}$

Appendix C

Lineshape optimization at 80 °C

In Chapter 6 we gave the optimization of the 3D8 cell and µ-LGR resonator clock signal as a function of light intensity and microwave power at a temperature of 67°C, imposed by the desire to minimize the temperature sensitivity. Here, we show for comparison a similar optimization at a higher temperature of 80°C for the same setup.
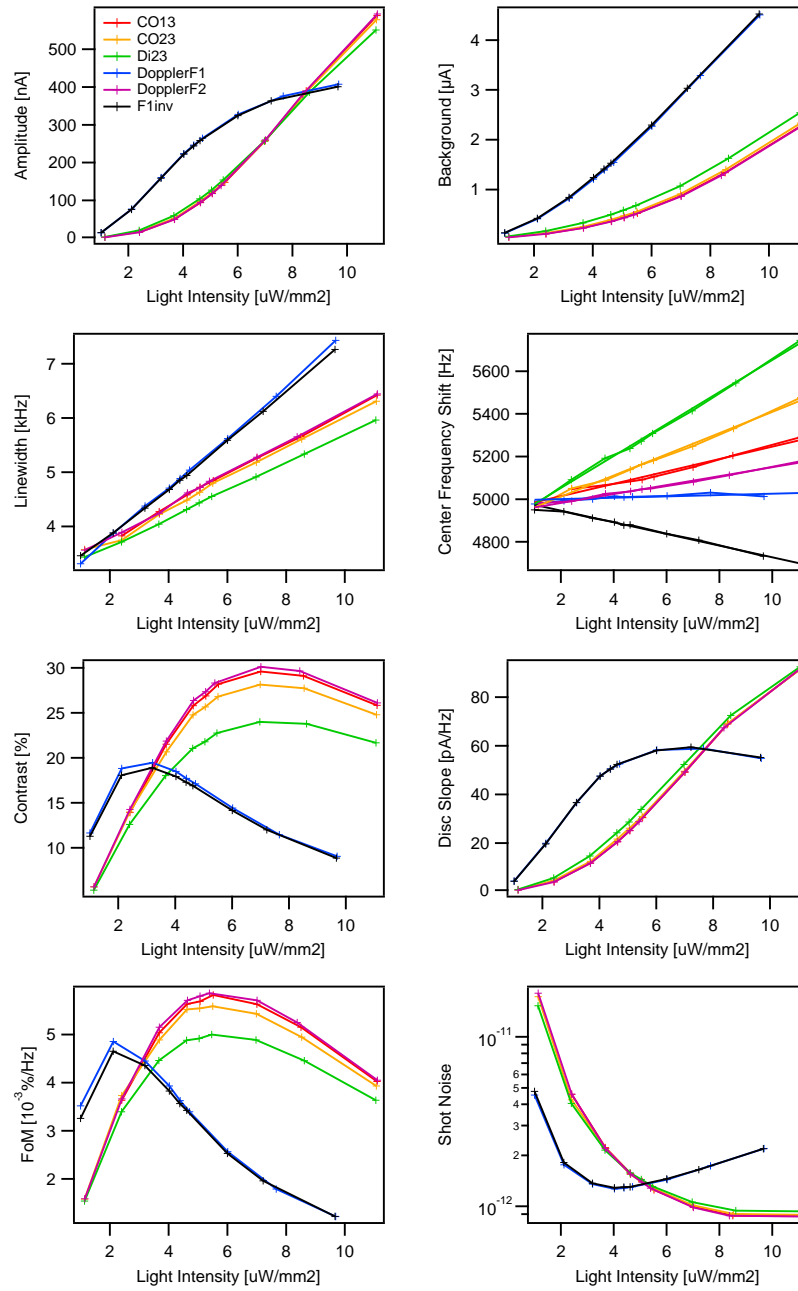
FIGURE C.1: 3D8 cell and µ-LGR resonator clock signal lineshape optimization as a function of the light intensity in the D2 line. Temperature is set to T=80 °C, and microwave power $P_{\mu W}$=-15 dBm.

Appendix D

Relative optical transition strengths of ^{87}Rb atoms for D1 and D2 lines
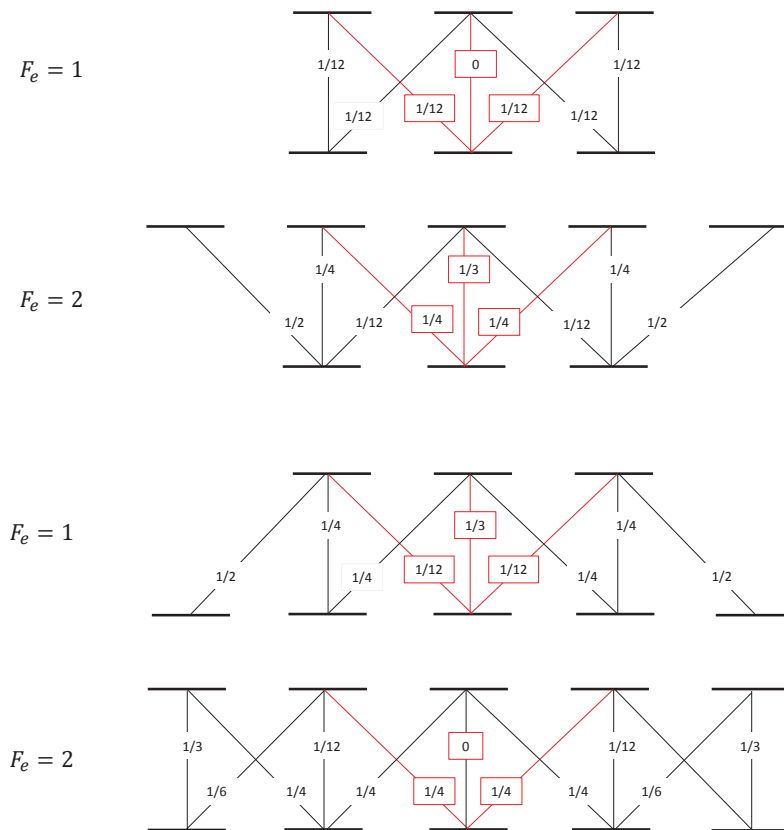
FIGURE D.1: Relative optical transition strengths of ^{87}Rb atoms for the D1 line, expressed as multiple of $|\langle J_e = 1/2| |e\boldsymbol{r}| |J = 1/2\rangle|^2$ [13].
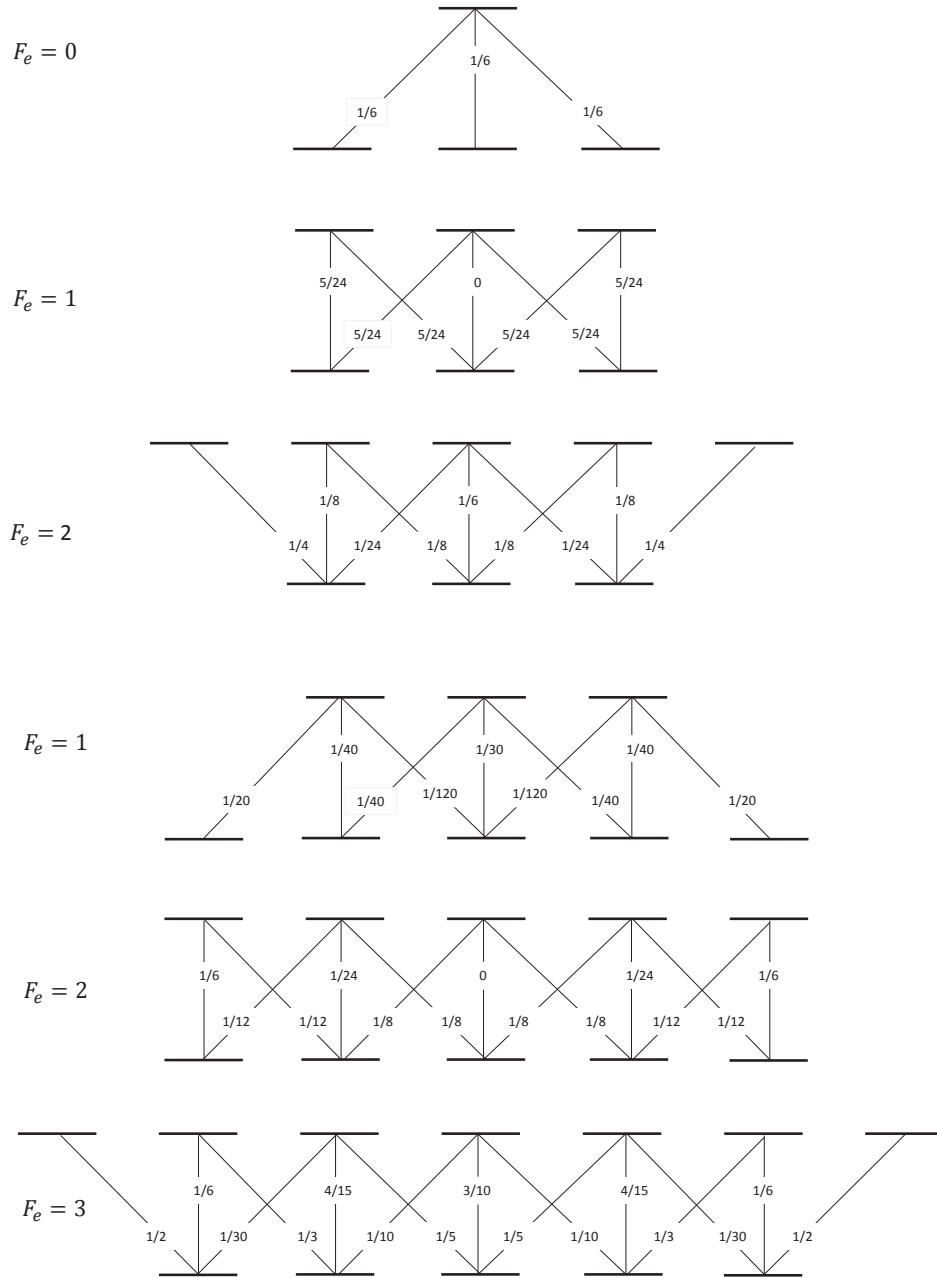
FIGURE D.2: Relative optical transition strengths of ^{87}Rb atoms for the D2 line, expressed as multiple of $|\langle J_e = 3/2 | |e\boldsymbol{r}| |J = 1/2 \rangle|^2$ [13].

Bibliography

[1]   R. Straessle, "Low temperature hermetic wafer bonding and microfabrication of wall-coated alkali vapor cells for chip-scale atomic clocks," PhD thesis, Ecole Polytechnique Fédérale De Lausanne, 2013.

[2]   M. Violetti, "Miniaturized microwave cavities for industrial applications," PhD thesis, Ecole Polytechnique Fédérale De Lausanne, 2012.

[3]   F. Vecchio, "Integrated packaging solutions and hotplates for a miniature atomic clock and other microsystems," PhD thesis, Ecole Polytechnique Fédérale De Lausanne, 2013.

[4]   V. L. Venkatraman, "Microfabricated rubidium dielectric barrier discharge light sources for portable atomic clocks," PhD thesis, Ecole Polytechnique Fédérale De Lausanne, 2013.

[5]   C. Schori, G. Mileti, B. Leuenberger, and P. Rochat, "CPT Atomic Clock based on Rubidium 85," in *Proc. of the 24th European Frequency and Time Forum (EFTF)*, 2010.

[6]   C. Affolderbach, T. Bandi, R. Matthey, F. Gruet, M. Pellaton, and G. Mileti, "Compact, high-stability rb atomic clocks for space," in *Proc. of 3rd Int. Colloquium - Scientific and Fundamental Aspects of the Galileo Programme*, 3rd Int. Colloquium - Galileo Science, Copenhagen, Denmark, Sep. 2011.

[7]   T. Bandi, "Double resonance studies on compact, high performance rubidium cell frequency standards," PhD thesis, University of Neuchâtel, 2013.

[8]   S. Micalizio, A. Godone, C. Calosso, F. Levi, C. Affolderbach, and F. Gruet, "Pulsed optically pumped rubidium clock with high frequency-stability performance," *IEEE Trans. Ultrason., Ferroelectr., Freq. Control*, vol. 59, no. 3, pp. 457–462, Mar. 2012.

[9]   L. Stauffer, F. Walti, U. Vokinger, and K. Siercks, "High-precision surface mount assembly of micro-optical components per laser reflow soldering: positioning accuracy and thermal stability," in *Proc. of SPIE Vol. 5454*, vol. 5454, 2004, pp. 85–95.

[10] R. Matthey, G. Mileti, L. Stauffer, P. Giaccari, A. Pollini, and L. Balet, "Assembly technique for miniaturized optical devices: towards space qualification," in *Proc. of the International Conference on Space Optics (ICSO)*, Ajaccio, 2012.

[11]   F. Gruet, M. Pellaton, C. Affolderbach, T. Bandi, R. Matthey, and G. Mileti, "Compact and frequency stabilised laser heads for rubidium atomic clocks," in *Proc. of the International Conference on Space Optics (ICSO)*, ICSO 2012, Ajaccio, Corse, France, Oct. 2012.

[12]   P. J. Mohr, B. N. Taylor, and D. B. Newell, "CODATA recommended values of the fundamental physical constants: 2010," *Rev. Mod. Phys.*, vol. 84, no. 4, 2012.

[13]   D. A. Steck. (2007). Rubidium 87 d line data, [Online]. Available: `http://steck.us/alkalidata`.

[14]   M. Lombardi, "First in a series on the evolution of time measurement: celestial, flow, and mechanical clocks," *Instrumentation Measurement Magazine, IEEE*, vol. 14, no. 4, pp. 45–51, 2011.

[15]   J. W. Horton and W. A. Marisson, "Precision determination of frequency," in *Proc. of the Institute of Radio Engineers*, vol. 16, 1928, pp. 137–154.

[16]   H. Lyons, "The atomic clock," *Instruments*, vol. 22, pp. 133–135, Dec. 1949.

[17]   L. Essen and J. V. L. Parry, "An atomic standard of frequency and time interval: a caesium resonator," *Nature*, vol. 176, pp. 280–282, Aug. 1955.

[18]   L. Devenoges, "Évaluation métrologique de l'étalon primaire de fréquence à atomes froids de césium focs-2," PhD thesis, Université de Nuechatel, 2012.

[19]   T. M. Fortier, N. Ashby, J. C. Bergquist, M. J. Delaney, S. A. Diddams, T. P. Heavner, L. Hollberg, W. M. Itano, S. R. Jefferts, K. Kim, F. Levi, L. Lorini, W. H. Oskay, T. E. Parker, J. Shirley, and J. E. Stalnaker, "Precision atomic spectroscopy for improved limits on variation of the fine structure constant and local position invariance," *Phys. Rev. Lett.*, vol. 98, p. 070 801, 7 Feb. 2007.

[20]   A. Shelkovnikov, R. J. Butcher, C. Chardonnet, and A. Amy-Klein, "Stability of the proton-to-electron mass ratio," *Phys. Rev. Lett.*, vol. 100, p. 150 801, 15 Apr. 2008.

[21]   M. W. N. K. Pavlis, "The relativistic redshift with 3×10^{-17} uncertainty at NIST Boulder Colorado USA," *Metrologia*, vol. 40, no. 2, p. 66, 2003.

[22]   R. Lutwak, *Principles of atomic clocks*, San Francisco, CA: Tutorial of the Joint Conference of the IEEE International Frequency Control Symposium (IFCS) and European Frequency and Time Forum (EFTF), May 2011.

[23] G. Mileti, C. Affolderbach, E. Breschi, C. Schori, P. Scherler, and P. Thomann, "Recherches sur les horloges atomiques miniatures et optiques," in *Actes du Congrès International de Chronométrie 2007: Horlogerie et automobile*, Colombier, Switzerland, Sep. 2007.

[24] F. Droz, P. Rochat, and Q. Wang, "Performance overview of space rubidium standards," in *Proc. of the 24th European Frequency and Time Forum (EFTF)*, 2010, pp. 1–6.

[25] R. Lutwak, A. Rashed, M. Varghesea, G. Tepolt, J. LeBlanc, M. Mescher, D. K. Serkland, K. M. Geib, G. M. Peake, and S. Römisch, "The chip-scale atomic clock - prototype evaluation," in *Proc. of the 39th Annual Precise Time and Time Interval (PTTI) Meeting*, 2007.

[26] S. Fossi, *Introduction to Symmetricom's QUANTUM Chip Scale Atomic Clock SA.45s CSAC*, Institute of Navigation, Jan. 2012.

[27] J. Kitching, S. Knappe, and L. Hollberg, "Miniature vapor-cell atomic-frequency references," *Appl. Phys. Lett.*, vol. 81, no. 3, pp. 553–555, Jul. 2002.

[28] N. Cyr, M. Tetu, and M. Breton, "All-optical microwave frequency standard: a proposal," *IEEE Trans. Instrum. Meas.*, vol. 42, pp. 640–649, 1993.

[29] J. Vanier, "Atomic clocks based on coherent population trapping: a review," *Appl. Phys. B*, vol. 81, pp. 421–442, 4 2005.

[30] D. W. Youngner, L. Lust, D. R. Carlson, S. T. Lu, L. J. Forner, H. M. Chanhvongsak, and T. D. Stark, "A manufacturable chip-scale atomic clock," in *Proc. of the IEEE intenational Solid-State Sensors, Actuators and Microsystems Conference, TRANSDUCERS*, 2007, pp. 39–44.

[31] J. F. DeNatale, R. L. Borwick, P. A. Stupar, R. A. Newgard, and M. Zhu, "Compact, low-power atomic time and frequency standards," DTIC Document, Tech. Rep., 2008.

[32] D. Miletic, "Light-shift and temperature-shift studies in atomic clocks based on coherent population trapping," PhD thesis, Université de Neuchâtel, 2013.

[33] J. Haesler, J. Bennes, T. Overstolz, J. Pierer, R. James, D. Ruffieux, and S. Lecomte, "Swiss miniature atomic clock: first prototype and preliminary results," in *Proc. of the 26th European Frequency and Time Forum (EFTF)*, 2012, pp. 312–315.

[34] J. Vanier and C. Mandache, "The passive optically pumped Rb frequency standard: the laser approach," *Appl. Phys. B*, vol. 87, pp. 565–593, 2007.

[35] G. Mileti, J. Deng, F. Walls, D. Jennings, and R. Drullinger, "Laser-pumped rubidium frequency standards: new analysis and progress," *IEEE Journal of Quantum Electronics*, vol. 34, no. 2, pp. 233–237, 1998, ISSN: 0018-9197.

[36] R. Lutwak, D. Emmons, W. Riley, and R. M. Garvey, "The chip-scale atomic clock - coherent population trapping vs. conventional interrogation," in *Proc. of the 34th Annual Precise Time and Time Interval (PTTI) Meeting*, 2002.

[37] J. Vanier and C. Audoin, *The Quantum Physics of Atomic Frequency Standards*. Adam Hilger, 1989.

[38] M.-A. Bouchiat-Guiochon, "Etude par pompage optique de la relaxation d'atomes de rubidium," PhD thesis, Université de Paris, Jun. 1964.

[39] S. Wang, L. Lin, and H. Guo, "Analysis and design of a micromachined rb-85 filter in passive rubidium atomic clock," in *Proc. 4th IEEE Int. Conf. on Nano/Micro Engineered and Molecular Systems (NEMS)*, Jan. 2009, pp. 911–914.

[40] V. Venkatraman, H. Shea, Y. Pétremand, N. F. de Rooij, C. Affolderbach, and G. Mileti, "Low-power chip-scale rubidium plasma light source for miniature atomic clocks," in *Proc. of the 2011 Joint Conference of the IEEE International Frequency Control Symp. (IFCS) and the European Frequency and Time Forum (EFTF)*, 2011.

[41] C. Cohen-Tannoudji, B. Diu, and F. Laloë, *Mecanique Quantique vol. I and II*. Hermann, 2000.

[42] D. A. Steck. (2013). Quantum and Atom Optics, [Online]. Available: `http://steck.us/teaching`.

[43] A. Corney, *Atomic and Laser Spectroscopy*. Oxford University Press, 1977.

[44] S. Bize, Y. Sortais, M. S. Santos, C. Mandache, A. Clairon, and C. Salomon, "High-accuracy measurement of the 87 rb ground-state hyperfine splitting in an atomic fountain," *Europhysics Letters*, vol. 45, no. 5, p. 558, 1999.

[45] G. Breit and I. I. Rabi, "Measurement of Nuclear Spin," *Phys. Rev.*, vol. 38, pp. 2082–2083, 11 Dec. 1931.

[46] C. Kittel, *Thermal Physics*. Wiley, 1969.

[47] G. Mileti, "Etude du pompage optique par laser et par lampe spectrale dans les horloges à vapeur de rubidium," PhD thesis, Université de Neuchâtel-Faculté des Sciences, 1995.

[48] J. J. Olivero and R. L. Longbothum, "Empirical fits to the voigt line width: a brief review," *J. Quant. Spectrosc. Radiat. Transfer*, vol. 17, no. 2, pp. 233–236, 1977.

[49] C. B. Alcock, V. P. Itkin, and M. K. Horrigan, "Vapor Pressure Equations for the Metallic Elements: 298-2500K," *Canadian Metallurgical Quarterly*, vol. 23, no. 309, 1984.

[50] G. D. Domenico and A. Weis. (). Spectra of the d-lines of alkali vapors from the wolfram demonstrations project, [Online]. Available: `http://demonstrations.wolfram.com`.

[51] B. E. King, *Angular momentum coupling and rabi frequencies for simple atomic transitions*, 2008.

[52] C. Ottinger, R. Scheps, G. W. York, and A. Gallagher, "Broadening of the Rb resonance lines by the noble gases," *Phys. Rev. A*, vol. 11, pp. Pp. 1815–1828, 1975.

[53] S. L. Izotova, A. I. Kantserov, and M. S. Frish, "Study of perturbation of hyperfine components of the ^{87}RbD1 line by inert gases using a compound Fabry-Perot interferometer," *Opt. Spektrosk.*, vol. 46, pp. 646–648, 1979.

[54] ——, "Determination of the shifts and broadening of the hyperfine components of the 87RbD2 line due to collisions with atoms of the inert gases He and Ar," *Opt. Spektrosk.*, vol. 49, pp. 546–547, 1980.

[55] ——, "Constants for broadening and shift of d1 and d2 rubidium-87 lines by inert gases," *Opt. Spektrosk.*, vol. 51, pp. 107–109, 1981.

[56] P. Y. Kantor and L. N. Shabanova, "Profiles of the rb1 794.7- and 780.0-nm lines in the presence of inert gases; parameters of interatomic potentials," *Opt. Spektrosk.*, vol. 58, pp. 614–619, 1985.

[57] M. Têtu, B. Villeneuve, N. Cyr, P. Tremblay, S. Thériault, and M. Breton, "Multiwavelength source using laser diodes frequency-locked to atomic resonances," *J. Lightwave Technol.*, vol. 7, pp. 1540–1548, 1989.

[58] M. D. Rotondaro, "Collisional Dynamics Of The Rubidium 5^2P Levels," PhD thesis, Air Force Institute of Technology of Air University, 1995.

[59] M. D. Rotondaro and G. P. Perram, "Collisional broadening and shift of the Rubidium D1 and D2 lines (52S1/2 $\rightarrow$ 52P1/2, 52P3/2) by rare gases, H2, D2, N2, CH4 and CF4," *J. Quant. Spectrosc. Radiat. Transfer*, vol. 57, pp. 497–507, 1997.

[60] M. V. Romalis, E. Miron, and C. D. Cates, "Pressure broadening of Rb D1 and D2 lines by ^{3}He, ^{4}He, N$_2$, and Xe: Line cores and near wings," *Phys. Rev. A*, vol. 56, pp. 4569–4578, 1997.

[61] S. Micalizio, A. Godone, F. Levi, and C. Calosso, "Pulsed optically pumped ^{87}Rb vapor cell frequency standard: A multilevel approach," *Phys. Rev. A*, vol. 79, p. 013 403, 1 Jan. 2009.

[62] R. H. Dicke, "The Effect of Collisions Upon the Doppler Width of Spectral Lines," *Phy. Rev.*, vol. 89, pp. 472–473, Jan. 1953.

[63] H. G. Robinson and C. E. Johnson, "Narrow ^{87}Rb hyperfine-structure resonances in an evacuated wall-coated cell," *Appl. Phys. Lett.*, vol. 40, no. 9, pp. 771–773, May 1982.

[64] W. Happer, "Optical Pumping," *Rev. Mod. Phys.*, vol. 44, no. 2, p. 169, 1972.

[65] S. Micalizio, A. Godone, F. Levi, and J. Vanier, "Spin-exchange frequency shift in alkali-metal-vapor cell frequency standards," *Phys. Rev. A*, vol. 73, p. 033 414, 3 Mar. 2006.

[66] ——, "Erratum: spin-exchange frequency shift in alkali-metal-vapor cell frequency standards [phys. rev. a 73, 033414 (2006)]," *Phys. Rev. A*, vol. 74, p. 059 905, 5 Nov. 2006.

[67] S. Grafström and D. Suter, "Interaction of spin-polarized atoms with a surface studied by optical-reflection spectroscopy," *Phys. Rev. A*, vol. 54, pp. 2169–2179, 3 Sep. 1996.

[68] H. N. de Freitas, M. Oria, and M. Chevrollier, "Spectroscopy of cesium atoms adsorbing and desorbing at a dielectric surface," English, *Applied Physics B*, vol. 75, no. 6-7, pp. 703–709, 2002.

[69] A. Horsley, G.-X. Du, M. Pellaton, C. Affolderbach, G. Mileti, and P. Treutlein, "Imaging of relaxation times and microwave field strength in a microfabricated vapor cell," *Phys. Rev. A*, vol. 88, p. 063 407, Dec. 2013.

[70] P. J. Oreto, Y.-Y. Jau, A. B. Post, N. N. Kuzma, and W. Happer, "Buffer-gas-induced shift and broadening of hyperfine resonances in alkali-metal vapors," *Phys. Rev. A*, vol. 69, p. 042 716, 2004.

[71] J. Vanier, J.-F. Simard, and J.-S. Boulanger, "Relaxation and frequency shifts in the ground state of Rb^{85}," *Phys. Rev. A*, vol. 9, no. 3, pp. 1031–1040, Mar. 1974.

[72] M. V. Balabas, T. Karaulanov, M. P. Ledbetter, and D. Budker, "Polarized Alkali-Metal Vapor with Minute-Long Transverse Spin-Relaxation Time," *Phys. Rev. Lett.*, vol. 105, p. 070 801, Aug. 2010.

[73] M. Bouchiat and J. Brossel, "Relaxation of Optically Pumped Rb Atoms on Paraffin-Coated Walls," *Phys. Rev.*, vol. 147, pp. 41–54, 1966.

[74] S. J. Seltzer, P. J. Meares, and M. V. Romalis, "Synchronous optical pumping of quantum revival beats for atomic magnetometry," *Phys. Rev. A*, vol. 75, p. 051 407, 5 May 2007.

[75] Y. W. Yi, H. G. Robinson, S. Knappe, J. E. Maclennan, C. D. Jones, C. Zhu, N. A. Clark, and J. Kitching, "Method for characterizing self-assembled monolayers as antirelaxation wall coatings for alkali vapor cells," *Journal of Applied Physics*, vol. 104, no. 2, 023534, p. 023 534, 2008.

[76] S. J. Seltzer, D. J. Michalak, M. H. Donaldson, M. V. Balabas, S. K. Barber, S. L. Bernasek, M.-A. Bouchiat, A. Hexemer, A. M. Hibberd, D. F. J. Kimball, C. Jaye, T. Karaulanov, F. A. Narducci, S. A. Rangwala, H. G. Robinson, A. K. Shmakov, D. L. Voronov, V. V. Yashchuk, A. Pines, and D. Budker, "Investigation of antirelaxation coatings for alkali-metal vapor cells using surface science techniques," *The Journal of Chemical Physics*, vol. 133, no. 14, 144703, p. 144 703, 2010.

[77] H. M. Goldenberg, D. Kleppner, and N. F. Ramsey, "Atomic Beam Resonance Expriments with Stored Beams," *Phy. Rev.*, vol. 123, pp. 530–537, 1961.

[78] D. Budker, L. Hollberg, D. F. Kimball, J. Kitching, S. Pustelny, and V. V. Yashchuk, "Microwave transitions and nonlinear magneto-optical rotation in anti-relaxation-coated cells," *Phys. Rev. A*, vol. 71, p. 012 903, 1 Jan. 2005.

[79] C. Rahman and H. G. Robinson, "Rb 0-0 Hyperfine Transition in Evacuated Wall-coated Cell at Melting Temperature," *IEEE J. Quantum Elect.*, vol. 23, no. 4, pp. 1533–1539, Apr. 1987.

[80] A. Risley, S. Jarvis, and J. Vanier, "The Dependence of Frequency Upon Microwave Power of Wall-coated and Buffer-gas-filled Gas Cell Rb87 Frequency Standards," *J. Appl. Phys.*, vol. 51, no. 9, pp. 4571–4576, 1980.

[81] T. Bandi, C. Affolderbach, and G. Mileti, "Study of Rb 0-0 hyperfine double-resonance transition in a wall-coated cell," in *Proc. of the 24th European Frequency and Time Forum (EFTF)*, Apr. 2010.

[82] M. Pellaton, R. Straessle, C. Affolderbach, D. Briand, N. F. de Rooij, and G. Mileti, "Wall-coated cells for rb atomic clocks: study of the ripening process by double-resonance spectroscopy," in *Proc. of the 26th European Frequency and Time Forum (EFTF)*, Göteborg, Apr. 2012.

[83] H. G. Robinson, "Evacuated, wall-coated, sealed, alkali atom cell for an atomic frequency standard," U. S. Patent 4 596 962, Jun. 1986.

[84] F. Masnou-Seeuws and M.-A. Bouchiat, "Étude théorique de la relaxation d'atomes alcalins par collisions sur une paroi et sur un gaz," *J. Physique*, vol. 28, no. 5-6, 1967.

[85] J. S. Boulanger, PhD thesis, Université Laval, Québec, 1975.

[86] S. Knappe and H. G. Robinson, "Double-resonance lineshapes in a cell with wall coating and buffer gas," *New Journal of Physics*, vol. 12, no. 6, p. 065 021, 2010.

[87] W. Riley and D. A. Howe, *Handbook of Frequency Stability Analysis*. NIST Spec. Pubs., Jul. 2008.

[88] D. W. Allan, "Statistics of atomic frequency standards," in *Proc. of the IEEE*, vol. 54, 1966, pp. 221–230.

[89] T. Bandi, C. Affolderbach, C. E. Calosso, and G. Mileti, "High-performance laser-pumped rubidium frequency standard for satellite navigation," *Electron. Lett.*, vol. 47, no. 12, pp. 698–699, 2011.

[90] G. Missout and J. Vanier, "Pressure and temperature coefficients of the more commonly used buffer gases in rubidium vapor frequency standards," *IEEE Transactions on Instrumentation and Measurement*, vol. 24, no. 2, pp. 180–184, 1975.

[91] B. L. Bean and R. H. Lambert, "Temperature dependance of hyperfine density shifts. III. ^{23}Na, ^{39}K, and ^{85}Rb in He, Ne, Ar, and N$_2$," *Phys. Rev. A*, vol. 12, no. 4, pp. 1498–1502, Oct. 1975.

[92] ——, "Temperature dependance of hyperfine density shifts. IV. ^{23}Na, ^{39}K, and ^{85}Rb in He, Ne, Ar, and N$_2$ at low temperatures," *Phys. Rev. A*, vol. 13, p. 492, 1976.

[93] J. Vanier, R. Kunski, N. Cyr, J. Y. Savard, and M.Têtu, "On hyperfine frequency shifts caused by buffer gases: Application to the optically pumped passive rubidium frequency standard," *J. Appl. Phys.*, vol. 53, no. 8, pp. 5387–5391, Aug. 1982.

[94] J. Vanier, R. Kunski, P. Paulin, J. Y. Savard, M. Têtu, and N. Cyr, "On the light shift and buffer gas shift in passive Rubidium frequency standards," in *Proc. of the 36th Annual Frequency Control Symposium (FCS)*, Philadelphia (PA), USA, Jun. 1982, pp. 348–354.

[95] F. Gong, Y.-Y. Jau, and W. Happer, "Nonlinear pressure shifts of alkali-metal atoms in inert gases," *Phys. Rev. Lett.*, vol. 100, p. 233 002, 23 Jun. 2008.

[96] R. Boudot, D. Miletic, P. Dziuban, C. Affolderbach, P. Knapkiewicz, J. Dziuban, G. Mileti, V. Giordano, and C. Gorecki, "First-order cancellation of the cs clock frequency temperature-dependence in ne-ar buffer gas mixture," *Optics Express*, vol. 19, no. 4, pp. 3106–3114, 2011.

[97] O. Kozlova, "Caractérisation d'une horloge à piègeage cohérent de population dans une vapeur thermique de césium. Principaux effets pouvant affecter la stabilité de fréquence à moyen-long terme.," PhD thesis, Université Paris VI Pierre et Marie Curie, 2012.

[98] B. H. McGuyer, "Atomic physics with vapor-cell clocks," PhD thesis, Princeton University, 2012.

[99] C. Affolderbach, C. Andreeva, S. Cartaleva, T. Karaulanov, G. Mileti, and D. Slavov, "Light-shift suppression in laser optically pumped vapour-cell atomic frequency standards," *Appl. Phys. B: Lasers Opt.*, vol. 80, pp. 841–848, 2005.

[100] J. Camparo, "The rubidium atomic clock and basic research," *Physics Today*, vol. 60, no. 11, pp. 33–39, Nov. 2007.

[101] B. S. Mathur, H. Tang, and W. Happer, "Light shifts in the alkali atoms," *Phys. Rev.*, vol. 171, pp. 11–19, 1 Jul. 1968.

[102] W. Happer and B. S. Mathur, "Effective operator formalism in optical pumping," *Phys. Rev.*, vol. 163, pp. 12–25, 1 Nov. 1967.

[103] M. Arditi and J.-L. Picque, "Precision measurements of light shifts induced by a narrow-band GaAs laser in the 0-0 133 Cs hyperfine transition," *J. Phys. B*, vol. 8, no. 14, p. L331, 1975.

[104] J. Deng, "Light shift compensation in a rb gas cell frequency standard with two-laser pumping," *IEEE Trans. Ultrason., Ferroelectr., Freq. Control*, vol. 48, no. 6, pp. 1657–1661, 2001.

[105] D. Miletic, T. Bandi, C. Affolderbach, and G. Mileti, "Ac stark shift in double resonance and coherent population trapping in a wall-coated cell for compact rb atomic clocks," *Physica Scripta*, vol. 2012, no. T149, p. 014 012, 2012.

[106] M. Zhu, "Optical pumping method to reduce light shift in a vapor cell atomic frequency standard," in *Proc. of the 2007 Joint Conference of the IEEE International Frequency Control Symp. (IFCS) and the European Frequency and Time Forum (EFTF)*, 2007, pp. 1334–1338.

[107] A. Risley and G. Busca, "Effect of line inhomogeneity on the frequency of passive rb 87 frequency standards," in *Proc. of the 32nd Annual Frequency Control Symposium (FCS)*, 1978, pp. 506–513.

[108] G. Mileti, I. Ruedi, and H. Schweda, "Line inhomogeneity effects and power shift in miniaturized rubidium frequency standard," in *Proc. of the 6th European Frequency and Time Forum (EFTF)*, 1992.

[109] J. C. Camparo, C. M. Klimcak, and S. J. Herbulock, "Frequency equilibration in the vapor-cell atomic clock," *IEEE Transactions on Instrumentation and Measurement*, vol. 54, no. 5, pp. 1873–1880, Oct. 2005.

[110] W. J. Riley, "The physics of the environmental sensitivity of rubidium gas cell atomic frequency standards," *IEEE Trans. Ultrason., Ferroelectr., Freq. Control*, vol. 39, no. 2, pp. 232–240, 1992.

[111] C. Lemarchand, "Mesure de la constante de Boltzmann par spectroscopie laser : vers une contribution au futur Système International d'unités," PhD thesis, Université Paris 13, 2012.

[112] T. W. Hänsch, I. S. Shahin, and A. L. Schawlow, "High-Resolution Saturation Spectroscopy of the Sodium D Lines with a Pulsed Tunable Dye Laser," *Phys. Rev. Lett.*, vol. 27, pp. 707–710, 11 Sep. 1971.

[113] W. Demtröder, *Laser Spectroscopy Basic Concepts and Instrumentation*. Springer, 1998.

[114] D. W. Preston, "Doppler-free saturated absorption: laser spectroscopy," *Am. J. Phys.*, vol. 64, no. 11, pp. 1432–1436, 1996.

[115] A. L. Schawlow, "Spectroscopy in a new light," *Rev. Mod. Phys.*, vol. 54, no. 3, pp. 697–709, Jul. 1982.

[116] M. Himsworth and T. Freegarde, "Rubidium pump-probe spectroscopy: comparison between *ab initio* theory and experiment," *Phys. Rev. A*, vol. 81, p. 023 423, 2 Feb. 2010.

[117] D. A. Smith and I. G. Hughes, "The role of hyperfine pumping in multilevel systems exhibiting saturated absorption," *American Journal of Physics*, vol. 72, no. 5, pp. 631–637, 2004.

[118] C. P. Pearman, C. S. Adams, S. G. Cox, P. F. Griffin, D. A. Smith, and I. G. Hughes, "Polarization spectroscopy of a closed atomic transition: applications to laser frequency locking," *Journal of Physics B: Atomic, Molecular and Optical Physics*, vol. 35, no. 24, p. 5141, 2002.

[119] T. Bandi, C. Affolderbach, C. Stefanucci, F. Merli, A. K. Skrivervik, and G. Mileti, "Medium- to long-term frequency stability of high-performance cw double-resonance rb standard," in *proc. of the 2013 Joint UFFC, EFTF and PFM Symp.*, 2013.

[120] C. Affolderbach and G. Mileti, "Tunable, stabilised diode lasers for compact atomic frequency standards and precision wavelength references," *Optics and Lasers in Engin.*, vol. 43, pp. 291–302, Jul. 2004.

[121] ——, "A compact laser head with high-frequency stability for rb atomic clocks and optical instrumentation," *Rev. Sci. Instrum.*, vol. 76, no. 7, 073108, p. 073 108, 2005.

[122] T. Bandi, C. Affolderbach, and G. Mileti, "Laser-pumped paraffin-coated cell rubidium frequency standard," *J. Appl. Phys.*, vol. 111, no. 12, 124906, p. 124 906, 2012.

[123] A. Godone, S. Micalizio, F. Levi, and C. Calosso, "Microwave cavities for vapor cell frequency standards," *Rev. Sci. Instrum.*, vol. 82, no. 7, pages, Jul. 2011.

[124] W. N. Hardy and L. A. Whitehead, "Split-ring resonator for use in magnetic resonance from 200-2000 mhz," *Review of Scientific Instruments*, vol. 52, no. 2, pp. 213–216, 1981.

[125] G. Busca and L. Johnson, "Passive frequency standard," U. S. Patent 4 947 137, 1990.

[126] G. H. Mei, D. Zhong, S. F. An, J. T. Liu, and X. H. R. 2. M. M. C. for Atomic Frequency Standard U S Patent No.6 225 870 B1, "Miniaturized microwave cavity for atomic frequency standard," U. S. Patent 6 225 870 B1, 2001.

[127] B. Xia, D. Zhong, S. An, and G. Mei, "Characteristics of a novel kind of miniaturized cavity-cell assembly for rubidium frequency standards," *IEEE Trans. on Instrum. and Measurement*, vol. 55, no. 3, pp. 1000–1005, 2006.

[128] D. Zhong, B. Xia, S. An, H. Wu, Q. Wang, F. Zhao, F. Qi, F. Wang, and G. Mei, "Investigation on physics package with slotted-tube microwave cavity for rubidium atomic frequency standard," in *Proc. of the 2009 Joint Conference of the IEEE International Frequency Control Symp. (IFCS) and the European Frequency and Time Forum (EFTF)*, 2009, pp. 1019–1022.

[129] L. Guo-Bin, Z. Feng, and G. Si-Hong, "Study of a low power dissipation, miniature laser-pumped rubidium frequency standard," *Chinese Physics B*, vol. 18, no. 9, pp. 3839–3843, Sep. 2009.

[130] J. Deng, "Subminiature microwave cavity for atomic frequency standards," in *Proc. of the IEEE International Frequency Control Symp. (IFCS)*, 2001, pp. 85–88.

[131] H. S. Schweda, G. Busca, and P. Rochat, "Atomic frequency standard," U. S. Patent 5 387 881, 1995.

[132] Y. Shiyu, C. Jingzhong, T. Jianhui, and L. Yaoting, "A kind of magnetron cavity used in rubidium atomic frequency standards," *Journal of Semiconductors*, vol. 32, no. 12, p. 122 001, 2011.

[133] S. J. Seltzer and M. V. Romalis, "High-temperature alkali vapor cells with antirelaxation surface coatings," *Journal of Applied Physics*, vol. 106, no. 11, 114905, p. 114 905, Dec. 2009.

[134] R. Straessle, M. Pellaton, C. Affolderbach, Y. Pétremand, D. Briand, G. Mileti, and N. F. de Rooij, "Low-temperature indium-bonded alkali vapor cell for chip-scale atomic clocks," *Journal of Applied Physics*, vol. 113, no. 6, 064501, p. 064 501, 2013.

[135] G. Singh, P. Dilavore, and C. O. Alley, "A Technique for Preparing Wall Coated Cesium Vapor Cells," *Rev. Sci. Instrum.*, vol. 43, no. 9, pp. 1388–1389, 1972.

[136] D. F. Phillips, A. Boca, and R. L. Walsworth, "Evaporative coating of rb maser cells," Jun. 1999.

[137] L. A. Liew, S. Knappe, J. Moreland, H. G. Robinson, L. Hollberg, and J. Kitching, "Microfabricated alkali atom vapor cells," *Appl. Phys. Lett.*, vol. 84, no. 14, pp. 2694–2696, Apr. 2004.

[138] F. Vecchio, V. Venkatraman, H. R. Shea, T. Maeder, and P. Ryser, "Dispensing and hermetic sealing rb in a miniature reference cell for integrated atomic clocks," *Sensors and Actuators A: Physical*, vol. 172, no. 1, pp. 330–335, 2011.

[139]   S. Knappe, "MEMS Atomic Clocks," *Comprehensive Microsystems*, vol. 3, Y. B. Gian-
        chandani, O. Tabata, and H. Zappe, Eds., pp. 571–612, Sep. 2007.

[140]   S. Knappe, V. Gerginov, P. D. D. Schwindt, V. Shah, H. G. Robinson, L. Hollberg, and
        J. Kitching, "Atomic vapor cells for chip-scale atomic clocks with improved long-term
        frequency stability," *Opt. Lett.*, vol. 30, no. 18, pp. 2351–2353, Sep. 2005.

[141]   L.-A. Liew, J. Moreland, and V. Gerginov, "Wafer-level filling of microfabricated atomic
        vapor cells based on thin-film deposition and photolysis of cesium azide," *Applied Physics
        Letters*, vol. 90, no. 11, 114106, p. 114 106, 2007.

[142]   T. Overstolz, J. Haesler, and V. Passov, "Method for producing a microfabricated atomic
        vapor cell," U. S. Patent 2012/0301631 A1, 2012.

[143]   F. Gong, "New Physics And Technology For Spin-polarized Alkali-metal Atoms," PhD
        thesis, Princeton University, 2008.

[144]   P. Knapkiewicz, J. Dziuban, R. Walczak, L. Mauri, P. Dziuban, and C. Gorecki, "MEMS
        caesium vapour cell for european micro-atomic-clock," *Procedia Engineering*, vol. 5, pp. 721–
        724, 2010.

[145]   S. Radhakrishnan and A. Lal, "Alkali metal-wax micropackets for chip-scale atomic
        clocks," in *Proc. of the 13th International Conference on Solid-State Sensors, Actuators
        and Microsystems*, vol. 1, 2005, 23–26 Vol. 1.

[146]   A. Lal and S. Radhakrishnan, "Alkali metal-wax micropackets for alkali metal handling,"
        English, U. S. Patent 7 666 485 B2, 2010.

[147]   D. J. Clack and J. M. Stanley, "The manufacture of alkali vapour cells for optical pumping
        experiments," *Journal of Physics E: Scientific Instruments*, vol. 4, no. 10, p. 758, 1971.

[148]   E. B. Alexandrov, M. V. Balabas, D. Budker, D. English, D. F. Kimball, C.-H. Li, and
        V. V. Yashchuk, "Light-induced desorption of alkali-metal atoms from paraffin coating,"
        Phys. Rev. A, vol. 66, no. 4, p. 042 903, Oct. 2002.

[149]   N. Castagna, G. Bison, G. Di Domenico, A. Hofer, P. Knowles, C. Macchione, H. Saudan,
        and A. Weis, "A large sample study of spin relaxation and magnetometric sensitivity of
        paraffin-coated cs vapor cells," *Applied Physics B: Lasers and Optics*, vol. 96, pp. 763–
        772, 4 2009.

[150] M. V. Balabas, K. Jensen, W. Wasilewski, H. Krauter, L. Madsen, J. Müller, T. Fernholz, and E. S. Polzik, "High quality anti-relaxation coating material for alkali atom vapor cells," *Opt. Express*, vol. 18, no. 6, pp. 5825–5830, 2010.

[151] B. Patton, K. Ishikawa, Y.-Y. Jau, and W. Happer, "Intrinsic impurities in glass alkali-vapor cells," *Physical Review Letters*, vol. 99, no. 2, p. 027 601, Jul. 2007.

[152] S. Knappe, V. Velichansky, H. G. Robinson, J. Kitching, and L. Hollberg, "Compact atomic vapor cells fabricated by laser-induced heating of hollow-core glass fibers," *Review of Scientific Instruments*, vol. 74, no. 6, pp. 3142–3145, 2003.

[153] M. V. Balabas, D. Budker, J. Kitching, P. D. D. Schwindt, and J. E. Stalnaker, "Magnetometry with millimeter-scale antirelaxation-coated alkali-metal vapor cells," *J. Opt. Soc. Am. B*, vol. 23, no. 6, pp. 1001–1006, Jun. 2006.

[154] M. Pellaton, C. Affolderbach, Y. Pétremand, N. F. de Rooij, and G. Mileti, "Study of laser-pumped double-resonance clock signals using a microfabricated cell," *Physica Scripta*, vol. 2012, no. T149, p. 014 013, 2012.

[155] C. Affolderbach, F. Gruet, R. Matthey, and G. Mileti, "A compact laser-pumped Rb clock with $5 \times 10^{-13} \tau^{-1/2}$ frequency stability," in *Proc. of the 2011 Joint Conference of the IEEE International Frequency Control Symp. (IFCS) and the European Frequency and Time Forum (EFTF)*, 2011.

[156] L. Lin, "Mems post-packaging by localized heating and bonding," *IEEE Transactions on Advanced Packaging*, vol. 23, no. 4, pp. 608–616, 2000.

[157] G. Wallis, "Field assisted glass sealing," *ElectroComponent Science and Technology*, vol. 2, no. 1, pp. 45–53, 1975.

[158] S. Knappe, V. Velichansky, H. G. Robinson, L. Liew, J. Moreland, J. Kitching, and L. Hollberg, "Atomic vapor cells for miniature frequency references," in *Proc. of the 2003 Joint Conference of the IEEE International Frequency Control (IFCS) and the European Frequency and Time Forum (EFTF)*, 2003.

[159] F. Gong, Y.-Y. Jau, K. Jensen, and W. Happer, "Electrolytic fabrication of atomic clock cells," *Review of Scientific Instruments*, vol. 77, no. 7, 076101, p. 076 101, 2006.

[160] E. J. Eklund, A. M. Shkel, S. Knappe, E. Donley, and J. Kitching, "Glass-blown spherical microcells for chip-scale atomic devices," *Sensors and Actuators A: Physical*, vol. 143, no. 1, pp. 175–180, 2008.

[161] A. Douahi, M. Hasegawa, L. Nieradko, J. Boy, C. Gorecki, and V. Giordano, "Advanced vapor cell technologies for chip scale atomic clock," in *Proc. of the 22nd European Frequency and Time Forum (EFTF)*, Toulouse, Apr. 2008.

[162] S. Juan, D. Ke, G. Deng-Zhu, W. Zhong, C. Jing, Z. Geng-Min, and C. Xu-Zong, "Stable ^{85}Rb micro vapour cells: fabrication based on anodic bonding and application in chip-scale atomic clocks," *Chinese Physics B*, vol. 19, no. 11, p. 110 701, 2010.

[163] K. Deng, X. Chen, and Z. Wang, "A 85rb coherent population trapping atomic clock," in *Proc. of the IEEE International Frequency Control Symp. (IFCS)*, IFCS, Jun. 2010, pp. 459–461.

[164] Y. Pétremand, C. Affolderbach, R. Straessle, M. Pellaton, D. Briand, G. Mileti, and N. F. de Rooij, "Microfabricated rubidium vapour cell with a thick glass core for small-scale atomic clock applications," *J. Micromech. Microeng.*, vol. 22, no. 2, p. 025 013, 2012.

[165] K. Tsujimoto, Y. Hirai, K. Sugano, T. Tsuchiya, and O. Tabata, "Sacrificial microchannel sealing by glass-frit reflow for chip scale atomic magnetometer," *Electronics and Communications in Japan*, vol. 96, no. 5, pp. 58–66, 2013.

[166] H. C. Abbink, E. Kanegsberg, K. D. Marino, and C. H. Volk, "Micro-cell for nmr gyroscope," U. S. Patent 7 292 031, 2007.

[167] H. Dong, J. Fang, B. Zhou, J. Qin, and S. Wan, "Review of atomic mems: driving technologies and challenges," English, *Microsystem Technologies*, vol. 16, no. 10, pp. 1683–1689, 2010.

[168] M. Pellaton, C. Affolderbach, Y. Pétremand, G. Mileti, and N. F. de Rooij, *Laser-pumped double-resonance clock using a micro-fabricated cell*, San Francisco, California, USA: Joint Conference of the IEEE International Frequency Control Symposium (IFCS) and European Frequency and Time Forum (EFTF), May 2011.

[169] S. A. Knappe, H. G. Robinson, and L. Hollberg, "Microfabricated saturated absorption laser spectrometer," *Optics express*, vol. 15, no. 10, pp. 6293–6299, May 2007.

[170] Y. Pétremand, C. Schori, R. Straessle, G. Mileti, N. de Rooij, and P. Thomann, "Low temperature indium-based sealing of microfabricated alkali cells for chip scale atomic clocks," in *Proc. of the 24th European Frequency and Time Forum (EFTF)*, 2010, pp. 1–3.

[171] R. Straessle, M. Pellaton, C. Affolderbach, Y. Pétremand, D. Briand, G. Mileti, and N. de Rooij, "Microfabricated alkali vapor cell with antirelaxation coatings," *accepted for publication in Appl. Phys. Lett.*, 2014.

[172] J. Norton, "Permeation of gases through solids," *Journal of Applied Physics*, vol. 28, no. 1, pp. 34–39, 1957.

[173] M. Hasegawa, R. K. Chutani, R. Boudot, L. Mauri, C. Gorecki, X. Liu, and N. Passilly, "Effects of getters on hermetically sealed micromachined cesium-neon cells for atomic clocks," *J. Micromech. Microeng.*, vol. 23, no. 5, p. 055 022, 2013.

[174] G. J. V. Amerongen, "The permeability of different rubbers to gases and its relation to diffusivity and solubility," *Journal of Applied Physics*, vol. 17, no. 11, pp. 972–985, 1946.

[175] K. Kawasaki and K. Senzaki, "Permeation of helium gas through glass," *Japanese Journal of Applied Physics*, vol. 1, no. 4, pp. 223–226, 1962.

[176] H. G. Robinson, E. S. Ensberg, and H. G. Dehmelt, "Preservation of spin state in free atom-inert surface collisions," *Bull. Am. Phys. Soc*, vol. 3, p. 9, 1958.

[177] J. C. Camparo, "Alkali $< I \cdot S >$ Wall relaxation in Dichlorodimethylsilane Coated Resonance Cells," *J. Chem. Phys.*, vol. 86, pp. 1533–1539, 1987.

[178] M. Stephens, R. Rhodes, and C. Wieman, "Study of wall coatings for vapour-cell laser traps," *J. Appl. Phys.*, vol. 76, no. 6, pp. 3479–3488, Sep. 1994.

[179] S. J. Seltzer, D. M. Rampulla, S. Rivillon-Amy, Y. J. Chabal, S. L. Bernasek, and M. V. Romalis, "Testing the effect of surface coatings on alkali atom polarization lifetimes," *Journal of Applied Physics*, vol. 104, no. 10, 103116, p. 103 116, 2008.

[180] E. Ulanski and Z. Wu, "Measurement of dwell times of spin polarized rubidium atoms on octadecyltrichlorosilane- and paraffin-coated surfaces," *Appl. Phys. Lett.*, vol. 98, no. 20, 201115, p. 201 115, 2011.

[181] D. Budker and M. Romalis, "Optical magnetometry," *Nature Physics*, vol. 3, pp. 227–234, 2007.

[182] H. G. Robinson and C. E. Johnson, "A New Heart for Rb Frequency Standards: The Evacuated, Wall-coated Sealed Cell," *IEEE T. Instrum. Meas.*, vol. 32, no. 1, p. 198, 1983.

[183] C. Rahman and H. G. Robinson, "Frequency Stability in Wall-coated Evacuated Cell: Preliminary Results," in *Proc. of the 18th Annual Precise Time and Time Interval (PTTI) Meeting*, Proc. of the 18th Annual Precise Time and Time Interval (PTTI) Meeting, Dec. 1986, pp. 559–564.

[184] E. B. Alexandrov, M. V. Balabas, A. S. Pasgalev, A. K. Vershovskii, and N. N. Yakobson, "Double-resonance atomic magnetometers: from gas discharge to laser pumping," *Laser Phyiscs*, vol. 6, no. 2, pp. 244–251, 1996.

[185] D. Budker, V. Yashchuk, and M. Zolotorev, "Nonlinear magneto-optic effects with ultra-narrow widths," *Phys. Rev. Lett.*, vol. 81, pp. 5788–5791, 26 Dec. 1998.

[186] M. Klein, M. Hohensee, D. F. Phillips, and R. L. Walsworth, "Electromagnetically induced transparency in paraffin-coated vapor cells," *Physical Review A*, vol. 83, no. 1, pages, Jan. 2011.

[187] W. C. Griffith, M. D. Swallows, T. H. Loftus, M. V. R. B. R. Heckel, and E. N. Fortson, "Improved Limit on the Permanent Electric Dipole Moment of ^{199}Hg," *Phys. Rev. Lett.*, vol. 102, p. 101 601, 10 Mar. 2009.

[188] A. Kuzmich, L. Mandel, and N. P. Bigelow, "Generation of spin squeezing via continuous quantum nondemolition measurement," *Phys. Rev. Lett.*, vol. 85, pp. 1594–1597, 8 Aug. 2000.

[189] B. Julsgaard, A. Kozhekin, and E. S. Polzik, "Experimental long-lived entanglement of two macroscopic objects," *Nature*, vol. 413, pp. 400–403, 2001.

[190] B. Julsgaard, J. Sherson, J. I. Ciraca, J. Fiurasek, and E. S. Polzik, "Experimental demonstration of quantum memory for light," *Nature*, vol. 432, pp. 482–486, 2004.

[191] C. O. Alley, "Wall Coatings of Alkyl-Chloro-Silanes for the Inhibition of Spin Relaxation," *Advances in Quantum Electronics*, p. 120, 1961.

[192] M. Hasegawa, P. Dziuban, L. Nieradko, A. Douahi, C. Gorecki, and V. Giordano, "Fabrication of wall-coated cs vapor cells for a chip-scale atomic clock," in *Optical MEMs and Nanophotonics, 2008 IEEE/LEOS Internationall Conference on*, 2008, pp. 162–163.

[193] M. V. Balabas and O. Y. Tretiak, "Comparative study of alkali-vapour cells with alkane-, alkeneand 1-nonadecylbenzene-based antirelaxation wall coatings," *Quantum Electronics*, vol. 43, no. 12, p. 1175, 2013.

[194] E. Breschi, G. Kazakov, C. Schori, G. D. Domenico, G. Mileti, A. Litvinov, and B. Matisov, "Light effects in the atomic-motion-induced ramsey narrowing of dark resonances in wall-coated cells," *Phys. Rev. A*, vol. 82, p. 063 810, 6 Dec. 2010.

[195] T. Karaulanov, M. T. Graf, D. English, S. M. Rochester, Y. Rosen, K. Tsigutkin, D. Budker, E. B. Alexandrov, M. V. Balabas, D. F. J. Kimball, F. A. Narducci, S. Pustelny, and V. V. Yashchuk, "Controlling Atomic Vapor Density in Paraffin-coated Cells Using Light-Induced Atomic Desorption," *Phys. Rev. A*, vol. 79, p. 012 902, 2009.

[196] S. Gozzini, A. Lucchesini, L. Marmugi, and G. Postorino, "Light-induced sodium desorption from paraffin film," English, *The European Physical Journal D*, vol. 47, no. 1, pp. 1–5, 2008.

[197] A. Bogi, C. Marinelli, A. Burchianti, E. Mariotti, L. Moi, S. Gozzini, L. Marmugi, and A. Lucchesini, "Full control of sodium vapor density in siloxane-coated cells using blue led light-induced atomic desorption," *Opt. Lett.*, vol. 34, no. 17, pp. 2643–2645, Sep. 2009.

[198] M. Klein, M. Hohensee, A. Nemiroski, Y. Xiao, D. F. Phillips, and R. L. Walsworth, "Slow light in narrow paraffin-coated vapor cells," *Applied Physics Letters*, vol. 95, no. 9, 2009.

[199] K. F. Zhao, M. Schaden, and Z. Wu, "Method for measuring the dwell time of spin-polarized rb atoms on coated pyrex glass surfaces using light shift," *Phys. Rev. Lett.*, vol. 103, p. 073 201, 7 Aug. 2009.

[200] R. G. Brewer, "Study of atom-wall collisions by optical pumping," *J. Chem. Phys.*, vol. 38, no. 12, pp. 3015–3020, 1963.

[201] D. M. Rampulla, N. Oncel, E. Abelev, Y. W. Yi, S. Knappe, and S. L. Bernasek, "Effects of organic film morphology on the formation of Rb clusters on surface coatings in alkali metal vapor cells," *Applied Physics Letters*, vol. 94, no. 4, p. 041 116, 2009.

[202] A. M. Hibberd, "Alkali metal atom - wall coating interactions in atomic vapor cells," PhD thesis, Princeton university, 2011.

[203] D. Miletic, C. Affolderbach, M. Hasegawa, R. Boudot, C. Gorecki, and G. Mileti, "Ac stark-shift in cpt-based cs miniature atomic clocks," English, *Applied Physics B*, vol. 109, no. 1, pp. 89–97, 2012.

[204] W. Happer, Y.-Y. Jau, and G. Walker, *Optically Pumped Atoms*. Wiley -VCH, 2010.

[205] G. Mileti, "Study of the S/N performance of passive atomic clocks using a laser pumped vapour," in *Proc. of the 9th European Frequency and Time Forum (EFTF)*, 1995, pp. 271–276.

[206] G. Alzetta, A. Gozzini, L. Moi, and G. Orriols, "An experimental method for the observation of r.f. transitions and laser beat resonances in oriented Na vapour," *Il Nuovo Cimento*, vol. 36, pp. 5–20, 1976.

[207] A. M. Braun, T. J. Davis, M. H. Kwakernaak, J. J. Michalchuk, A. Ulmer, W. K. Chan, J. H. Abeles, Z. A. Shellenbarger, Y.-Y. Jau, W. Happer, T. McClelland, H. Fruehauf, R. Drap, W. Weidemann, and M. Variakojis, "RF-interrogated end-state chip-scale atomic clock," in *Proc. of the 39th Annual Precise Time and Time Interval (PTTI) Meeting*, 2007.

[208] S. Knappe, P. D. D. Schwindt, V. Gerginov, V. Shah, L. Hollberg, J. Kitching, L. Liew, and J. Moreland, "Microfabricated Atomic Clocks At NIST," in *Proc. of the 36th Annual Precise Time and Time Interval (PTTI) Meeting*, 2004.

[209] M. Violetti, C. Affolderbach, F. Merli, G. Mileti, and A. K. Skrivervik, "Microwave resonator, quantum sensor, and atomic clock," European Patent application 12 155 696, Feb. 16, 2012.

[210] V. Venkatraman, Y. Pétremand, C. Affolderbach, G. Mileti, N.-F. de Rooij, and H. Shea, "Microfabricated chip-scale rubidium plasma light source for miniature atomic clocks," *IEEE Trans. Ultrason., Ferroelectr., Freq. Control*, vol. 59, no. 3, pp. 448–456, 2012.

[211] M. Violetti, F. Merli, J.-F. Zürcher, A. Skrivervik, M. Pellaton, C. Affolderbach, and G. Mileti, "New Miniaturized Microwave Cavity for Rubidium Atomic Clocks," in *proceedings of IEEE Sensors conference*, proc. IEEE Sensors 2012, 2012.

[212] C. Stefanucci, T. Bandi, F. Merli, M. Pellaton, C. Affolderbach, G. Mileti, and A. K. Skrivervik, "Compact microwave cavity for high performance rubidium frequency standards," *Rev. Sci. Instrum.*, vol. 83, no. 10, 104706, p. 104 706, 2012.

[213] J. C. Camparo, R. P. Frueholz, and C. H. Volk, "Inhomogeneous light shift in alkali-metal atoms," *Phys. Rev. A*, vol. 27, pp. 1914–1924, 4 Apr. 1983.

[214] J. Stepisnik, "Spectroscopy: nmr down to earth," *Nature*, vol. 439, pp. 799–801, 2006.

[215] R. Matthey, C. Affolderbach, and G. Mileti, "Methods and evaluation of frequency aging in distributed-feedback laser diodes for rubidium atomic clocks," *Opt. Lett.*, vol. 36, no. 17, pp. 3311–3313, Sep. 2011.

[216] J. Camparo, J. Coffer, and J. Townsend, "Laser-pumped atomic clock exploiting pressure-broadened optical transitions," *J. Opt. Soc. Am. B*, vol. 22, no. 3, pp. 521–528, Mar. 2005.

[217] B. H. McGuyer, Y.-Y. Jau, and W. Happer, "Simple method of light-shift suppression in optical pumping systems," *Appl. Phys. Lett.*, vol. 94, no. 25, 251110, p. 251 110, Jun. 2009.

[218] ——, "Method for suppressing light shift in optical pumping systems," U. S. Patent 7 825 736, Nov. 2010.

[219] M. Zhu and J. DeNatale, "Application of reduced light shift optical pumping method to chip scale atomic clock," in *Proc. of the 2009 Joint Conference of the IEEE International Frequency Control Symp. (IFCS) and the European Frequency and Time Forum (EFTF)*, 2009, pp. 1183–1186.

[220] N. P. Wells and J. C. Camparo, "^{87}Rb D_1 isoclinic point," *Phys. Rev. A*, vol. 82, p. 062 505, 6 Dec. 2010.

[221] J. Deng, P. Vlitas, D. Taylor, L. Perletz, and R. Lutwak, "A commercial CPT rubidium clock," in *Proc. of the 22nd European Frequency and Time Forum (EFTF)*, Toulouse, France, 2008.

[222] D. Lellouchi, J. Dhennin, X. Lafontan, D. Veyrie, J.-F. L. Neal, and F.Pressecq, "A new method for the hermeticity testing of wafer-level packaging," *Journal of Micromechanics and Microengineering*, vol. 20, no. 2, p. 025 031, 2010.

[223] M. Violetti, M. Pellaton, C. Affolderbach, F. Merli, J. F. Zürcher, G. Mileti, and A. K. Skrivervik, "The micro loop-gap resonator: a novel miniaturized microwave cavity for double-resonance rubidium atomic clocks," *submitted to IEEE sensors Journal*, 2013.

[224] J. D. Francesco, F. Gruet, C. Schori, C. Affolderbach, R. Matthey, G. Mileti, Y. Salvadé, Y. Pétremand, and N. D. Rooij, "Evaluation of the frequency stability of a VCSEL locked to a micro-fabricated Rubidium vapour cell," in *Proc. of SPIE Vol. 7720*, 2010.